DISSERTATION

FAULT RESPONSE OF INVERTER-BASED RESOURCES AND THEIR IMPACT ON GRID PROTECTION SYSTEMS

Submitted by

Rasel Mahmud

Department of Systems Engineering

In partial fulfillment of the requirements

For the Degree of Doctor of Philosophy

Colorado State University

Fort Collins, Colorado

Spring 2026

Doctoral Committee:

Advisor: James Cale

Gaofeng Jia
Daniel Herber
Dan Zimmerle

ABSTRACT

FAULT RESPONSE OF INVERTER-BASED RESOURCES AND THEIR IMPACT ON GRID PROTECTION SYSTEMS

Inverter-based resources (IBRs) now supply a substantial portion of modern power systems, yet their short-circuit behavior during grid faults differs fundamentally from that of synchronous machines. These differences challenge traditional protection schemes and motivate the need for models that capture the essential physics of IBR fault response while remaining tractable for large-scale studies. This dissertation develops a physics-informed, data-driven reduced-order model (ROM) of IBR fault current tailored for protection applications.

The work begins with requirements analysis that translates interconnection standards, fault ride-through (FRT) requirements, and protection needs into modeling targets. These requirements specify the necessary outputs (sequence-domain currents and voltages), behaviors (current limiting, negative-sequence control), interfaces (compatibility with short-circuit and coordination tools), and quality metrics (relay-relevant timing and magnitude accuracy). Guided by these requirements, detailed electromagnetic transient (EMT) models are developed in Simulink and PSCAD to generate IBR fault responses under diverse control modes, grid strengths, and fault conditions.

A theoretical analysis of IBR behavior during grid faults is then performed to characterize the inverter fault response. This includes temporal decomposition into subtransient, transient, and steady-state regimes; dq- and sequence-frame current trajectory analysis; and harmonic and inter-harmonic studies under PWM saturation, current limiting, PLL and sequence-extractor imperfections, and grid-code reference-current policies. These investigations show that IBR fault currents follow a structured sequence of event-driven dynamic regimes.

Based on these insights, a parameterized ROM architecture is formulated in which the total current is represented as the sum of subtransient, transient, and steady-state components with physically interpretable parameters. A data-driven generalizability layer allows these parameters to vary systematically with pre-fault operating point and sequence-voltage depression using empirically fitted sensitivity coefficients. The ROM is implemented across multiple platforms (Python, Simulink, PSCAD) to support interoperability with EMT tools and protection-oriented short-circuit programs.

A validation framework is developed using experimental data from a commercial off-the-shelf (COTS) inverter, detailed EMT simulations, and relay-based assessments. Quantitative metrics such as cumulative error, RMSE, phase-shift alignment, and a composite performance metric demonstrate that the ROM reproduces EMT and experimental waveforms with acceptable accuracy, especially beyond the first cycle after fault inception. Relay studies indicate that the ROM captures key protection behaviors, including distance and overcurrent element operation, negative-sequence directional response, and voltage supervision, with timing differences generally within one cycle.

The ROM of the IBR presented in this dissertation was developed using a systems-engineering approach, beginning with requirements-based problem formulation, followed by a theoretical analysis of inverter fault dynamics, and concluding with the construction of a reduced-order model intended for use in protection studies and grid-level applications.

ACKNOWLEDGEMENTS

I would like to express my sincere gratitude to my advisor, Dr. James Cale, and to my committee members, Dr. Gaofeng Jia, Dr. Daniel Herber, and Dr. Dan Zimmerle, for their guidance, feedback, and support throughout this dissertation.

I am grateful to my colleagues and collaborators at the National Renewable Energy Laboratory (NREL) for their valuable discussions, modeling insights, and experimental assistance, all of which contributed significantly to the technical development of this work. I also acknowledge the support of the U.S. Department of Energy, whose programs and research environment enabled key aspects of this research.

I extend heartfelt thanks to my friends and peers for their encouragement throughout this journey. Above all, I am deeply thankful to my wife and daughter for their patience, sacrifices, and unwavering support. Their continuous encouragement made the completion of this dissertation possible.

Finally, I acknowledge the use of OpenAI's ChatGPT as an auxiliary tool for language editing and organizational refinement during the preparation of this manuscript. All scientific conclusions, technical content, analyses, and interpretations are solely my own.

DEDICATION

To my mother, whose inspiration guided me, and to my wife and daughter, whose love, strength, and unwavering support made this journey possible.

TABLE OF CONTENTS

LIST OF TABLES

LIST OF FIGURES

Chapter 1

Introduction and Background

1.1 Context and Overview

The electric–power sector is undergoing its fastest technology turnover since the dawn of the synchronous-machine era [2]. Global capacity additions of inverter-based resources (IBRs)—solar photovoltaic (PV), land-based and offshore wind, battery energy storage, and emerging bidirectional electric vehicles—reached about 666 GW in 2024 [3]. Within the United States, IBRs taken as wind plus solar supplied about 20% of total net generation in early 2025, up from roughly 19% a year earlier[1] [4]. Penetrations at the balancing-authority level are even more striking: California Independent System Operator (CAISO) recorded a five-minute interval on 6 April 2024 in which renewable production reached 117%[2] of internal load [5]. Similarly, Electric Reliability Council of Texas (ERCOT) reached a renewable share of 75.67% at 14:13, CST on 29 March 2024, with 34,958 MW of combined wind and solar generation online [6]. Unlike synchronous machines, IBRs possess virtually no electromechanical inertia, have limited thermal overload capability, and rely on cascaded digital controls operating from µs to s scales. Two pivotal departures from traditional short-circuit behavior follow:

1. *Current-limited injections:* hardware and control logic typically cap fault current to 1-2 pu, whereas synchronous machines deliver 5-8 pu subtransiently.

2. *Controller-imposed sequencing:* phase-locked loop (PLL) resynchronization, negative-sequence regulators, and ride-through logic introduce implementation-specific state changes.

[1] EIA does not publish an "IBR" category. Shares are derived from wind and solar net generation in Electric Power Monthly Table 1.01 (utility-scale plus estimated small-scale solar) divided by total net generation. See [4]. Independent summaries of these same EIA data report wind+solar at ≈20.3% in 1H 2025 and 18.6% in 1H 2024.

[2] Exports exceeded internal demand.

These characteristics have precipitated an escalating regulatory response. The foundational IEEE Std 2800-2022 stipulates fault-ride-through (FRT) envelopes, negative-sequence limits, and post-fault recovery ramps for transmission-connected plants [7]. The North American Electric Reliability Corporation (NERC) followed with a Level 2 Alert on IBR model-quality deficiencies in 2024 [8] and had earlier published a detailed Reliability Guideline on IBR performance issues in 2023 [9]. Most recently—marking its highest alert tier—NERC issued a Level 3 Essential Actions Alert on IBR Performance and Modeling (initial distribution 20 May 2025) [10], requiring Transmission Owners, Planners, and Generator Owners to acknowledge receipt within seven days and to report implementation progress by 18 August 2025. The alert's eight "essential actions" mandate (*i*) enhanced interconnection-study criteria with explicit reactive-power and frequency-response parameters, (*ii*) uniform data-retention practices, and (*iii*) transparent publication of IBR performance expectations—underscoring the industry's urgent need for accurate, parameter-transparent models.

Planners and protection engineers thus face a conundrum: vendor black-box EMT models capture the physics but are opaque and computationally prohibitive at scale, whereas simplified root-mean-square (RMS) blocks omit precisely the timing and sequence phenomena that determine relay performance. Recent EPRI projects have produced promising reduced-order representations, yet these remain proprietary or are limited to grid-forming topologies [11]. A transparent, physics-informed, computationally efficient modeling framework is therefore essential to (*i*) demonstrate compliance with emerging FRT standards and alerts, (*ii*) safeguard distance, differential, and sensitive inverter protections, and (*iii*) enable bulk-system planning studies that now analyse thousands of contingencies per scenario.

This dissertation addresses that gap through a systems engineering approach in which stakeholder requirements from grid codes, standards, and alerts are systematically captured, structured, and linked to a hierarchical suite of truth, reduced-order, and RMS models. The framework maintains full traceability between verification and validation artifacts, ensuring that every timing parameter and fault-current envelope can be directly associated with its governing document.

1.1.1 Role of Symmetrical Components in Power System Protection

The method of symmetrical components has served as a cornerstone of power system analysis and protection for more than a century. Since its introduction by Fortescue in 1918, the decomposition of three-phase electrical quantities into positive-, negative-, and zero-sequence components has enabled systematic representation and analysis of unbalanced operating conditions. This framework provided protection engineers with a powerful and intuitive tool for understanding fault behavior, coordinating protective devices, and ensuring system reliability [12].

In conventional power systems dominated by synchronous machines and passive network elements, the sequence networks exhibit largely linear and decoupled behavior. The positive-sequence component represents the normal operating condition and governs electromagnetic torque production in synchronous generators, while the negative- and zero-sequence components characterize system unbalance and ground fault phenomena, respectively. This predictable structure enabled the development of widely adopted protection principles, including distance protection, directional elements, negative-sequence relays, and ground fault detection schemes, all of which rely on well-defined relationships between sequence voltages and currents.

The increasing penetration of inverter-based resources fundamentally alters this classical picture. Unlike synchronous machines, inverter-based resources inject currents determined by embedded control systems, current limiters, modulation constraints, and internal protection functions. During large disturbances, these control systems may enter multiple layers of saturation, including pulse-width modulation saturation, current-controller saturation, and dc-link voltage constraints. These nonlinear mechanisms introduce strong coupling between sequence components and violate the traditional assumptions of linearity and independence that underpin classical protection theory.

As a result, while symmetrical components remain a valuable analytical framework, the interpretation of positive- and negative-sequence behavior in modern power systems becomes significantly more complex, particularly under severe fault conditions where controller saturation dominates the inverter response. This shift motivates the need for revised modeling approaches and protection concepts that explicitly incorporate inverter control dynamics and saturation phenomena.

1.2 Problem Statement and Motivation

Modern IBR studies are constrained by two fundamentally different modeling paradigms. Vendor EMT "truth" models capture device-level physics in great detail but embed proprietary source code, providing no visibility into control states, sequence parsing, or protection logic. A single credible-contingency case can take 20 min–1 h to solve on a workstation, and a full NERC screening set exceeds 2,000 scenarios [13], making such runtimes infeasible for regional planning where thousands of contingencies must be evaluated routinely. Conversely, RMS phasor models—used widely for transient-stability studies—assume balanced conditions and neglect fast control dynamics. As a result, they cannot reproduce negative-sequence current injections or phase-locked-loop (PLL) loss of synchronism, now required reporting metrics under the 2025 NERC Level 3 Alert [10]. This fidelity gap forces planners to either over-simplify protection and ride-through assessments or over-invest computational resources in black-box EMT runs that still lack parameter transparency.

The reliability implications of this modeling shortfall are no longer theoretical. The Odessa II event in Texas (4 June 2022) led to 1.7 GW of solar PV tripping when PLL loss-of-synchronism and AC over-current functions activated within 120 ms of a normally cleared phase-to-ground fault [14, 15]. Pre-event EMS studies had no mechanism to represent such sequence-specific dynamics. NERC's 2024 EMT guideline warns that "flat-start" RMS cases can underestimate IBR negative-sequence currents by more than 40% because PLL and current-limiter states are omitted [13]. Laboratory tests further show that grid-following inverters can misoperate for phase-angle jumps as small as 8° when PLL bandwidths and negative-sequence regulators interact [16]. These incidents highlight a persistent mismatch between the models used for grid studies and the actual inverter behaviors observed during field disturbances.

In response, standards bodies and regulators have tightened compliance requirements. IEEE Std 2800–2022 codifies explicit limits on negative-sequence current, detection delays, and post-fault recovery ramps—parameters absent from most RMS models. The NERC Level 3 Essential Actions Alert (2025) mandates verifiable timing data for every inverter plant by 18 August 2025 and requires updated interconnection studies [10]. Meanwhile, the DOE i2X Forum reports that many legacy IBR fleets cannot demonstrate IEEE 2800 compliance without software or control upgrades, noting that appropriate study tools remain "presently lacking" [17]. These developments, combined with international efforts such as ENTSO-E's Requirements for Generators [18], signal a global shift toward transparency and accountability in inverter performance modeling.

At the same time, practical and operational demands continue to intensify. Regional planners must screen tens of thousands of contingencies per base case—WECC's 2032 anchor-data-set alone includes over 19,000 single-line-to-ground events across 16 snapshots [19]. Running these scenarios with detailed EMT models would consume long CPU-hours, an untenable cost even for modern HPC resources. Faster, reduced-order models (ROMs) that maintain key control and protection dynamics are therefore essential to enable bulk-system risk assessments, Monte-Carlo studies, and real-time decision support.

Beyond computational efficiency, transparency and knowledge transfer are equally critical. Open, physics-informed models accelerate peer review, collaborative validation, and regulatory acceptance. Initiatives such as pvlib-python for PV performance analysis [20] and NREL's open efforts on grid-forming control architectures [21] illustrate how shared, validated tools can catalyze both research and standardization.

Taken together, these regulatory, operational, and technical pressures define a clear research gap. The power industry needs a transparent, physics-informed reduced-order model that reproduces both symmetrical and asymmetrical inverter behavior during and after grid faults, captures sub-cycle control and protection transitions, exposes parameters directly tied to grid-code clauses, and executes orders of magnitude faster than detailed EMT models [22, 23]. No existing model satisfies all of these requirements simultaneously. This dissertation therefore aims to develop such a model, integrate it within a structured systems engineering framework, and validate its performance against high-fidelity EMT simulations and experimental data.

1.3 Literature Review and State of the Art

Traditional bulk-power-system short-circuit tools were developed during an era dominated by synchronous-machine generation, where fault currents were primarily governed by subtransient reactances and electromechanical dynamics. As a result, most commercial short-circuit programs rely on the classical voltage-source–behind–impedance (Thévenin-equivalent) representation. This framework is computationally efficient and well-suited for traditional protection studies because it assumes *i*) a strong coupling between voltage and current through fixed machine parameters, *ii*) large electromechanical inertia, and *iii*) predictable subtransient and transient current envelopes. When applied to IBRs, however, these assumptions no longer hold [24, 25].

A broad set of studies has shown that fixed Thévenin representations of IBRs are inadequate for capturing behaviors that directly influence protection performance [26–28]. Grid-following IBR responses are strongly shaped by fast digital control loops such as PLLs, current-limiters, vector current controllers, and ride-through logic [29, 30]. These controls introduce fast dynamics, sequence coupling, and current-saturation characteristics that cannot be represented by fixed impedance. Further, modern IBR controllers couple positive- and negative-sequence behavior, making current injection dependent on instantaneous terminal voltages, imbalance conditions, and internal controller states [31–33]. During deep voltage depressions, IBR current injection is dictated almost entirely by software and hardware current limits and their associated slew-rate constraints, producing fault-current signatures that fixed-impedance or steady-state current-source models cannot reproduce [32, 34, 35]. Collectively, these limitations motivate the need for modeling approaches capable of representing control-driven inverter behavior with sufficient accuracy for protection studies.

EMT models implemented in tools such as PSCAD, EMTP-RV, or RTDS are often used to address these limitations. EMT models provide detailed, time-domain representations of switching behavior, inner- and outer-loop controllers, PLL dynamics, negative-sequence regulators, saturation phenomena, and current-limiter transitions [36–38]. This fidelity enables EMT models to accurately reproduce protection-relevant characteristics such as subcycle transients, momentary cessation, high-frequency interactions, and post-fault recovery behavior. For these reasons, EMT simulation is widely considered the benchmark for evaluating IBR short-circuit response under both symmetrical and asymmetrical faults [26,35,39,40].

Despite their accuracy, EMT models face several practical limitations that hinder routine use in planning and protection workflows. First, EMT simulations are computationally intensive: time steps on the order of tens of microseconds are required, and simulation time scales poorly with system size [41]. Large-scale contingency studies can require minutes to hours per scenario [42,43]. Second, EMT models typically rely on proprietary controller data supplied by manufacturers, limiting transparency and the ability to perform independent verification [9]. Third, many utilities lack sufficient computational resources, licenses, or personnel trained in EMT modeling [41,44]. Survey results from NERC's EMT modeling adoption white paper indicate that a significant fraction of utilities cite process delays and workflow bottlenecks as major barriers to EMT adoption, while others highlight hardware and computational limitations as key constraints [39,44]. Academic studies similarly show that EMT–RMS co-simulation reduces some burden but still inherits significant computational cost and interface complexity [45,45,46].

These challenges have motivated the development of intermediate modeling approaches that can bridge the gap between conventional phasor-domain models and full EMT simulation. Current practice includes *i*) vendor-provided black-box EMT models, *ii*) semi-transparent or "real-code" white-box implementations, *iii*) tabular voltage-controlled current-source (VCCS) representations, *iv*) parametric reduced-order models, and *v*) data-driven or machine-learning-based surrogates.

Black-box EMT models are widely distributed by manufacturers and provide high fidelity but limited transparency. Internal control logic is encapsulated in compiled libraries, restricting parameter access, sensitivity studies, and cross-tool portability [45]. Similar concerns have been noted in small-signal stability analysis, where black-box models impede interpretability and controller tuning [47]. White-box or real-code models alleviate these issues by exposing the underlying equations and, in some cases, aligning them with firmware-level implementations [41]. These models facilitate parameter transparency, validation, and order reduction, but their adoption is limited by intellectual-property constraints and the effort required to maintain versions across tools and firmware updates.

Tabular VCCS models have emerged as a practical alternative for short-circuit programs. In this approach, positive- and negative-sequence current injections are defined as functions of terminal voltage magnitude and other operating conditions [48, 49]. These tables can be imported into commercial tools such as ASPEN, CAPE, and CYME [50]. Iterative solvers incorporating VCCS characteristics have demonstrated robust convergence even in networks with multiple IBRs [51]. However, VCCS models remain quasi-steady-state approximations and cannot capture fast transient phenomena, controller mode switching, or detailed current-limiter behavior [35]. Their accuracy also degrades when multi-dimensional dependencies (e.g., pre-fault power, grid strength) must be represented.

Reduced-order parametric models offer another path toward tractable yet controller-aware representations. Mahmud et al. propose a reduced-order short-circuit model that explicitly incorporates current-limiter behavior and key control time constants, calibrated using experimental data. [52]. Similar approaches have been extended to bulk-system inverters by tuning reduced-order models to EMT-derived positive- and negative-sequence envelopes [53–55]. These models balance fidelity and efficiency, maintain a clear link to physical parameters, and can be integrated into standard short-circuit tools without revealing detailed firmware logic.

Data-driven and machine-learning-based surrogates represent an emerging class of models for short-circuit analysis. Neural-network-based inverter models have been shown to reproduce steady-state and dynamic responses in distribution networks [56], while ML-based short-circuit prediction frameworks have demonstrated high accuracy without requiring disclosure of proprietary control details [57]. Although promising, these techniques remain exploratory for bulk-system protection studies, where questions of generalization, interpretability, and regulatory acceptance are still open.

Overall, conventional short-circuit tools are computationally efficient but lack controller awareness, whereas EMT tools offer full fidelity but are expensive, proprietary, and difficult to scale. Intermediate methods—black-box EMT, white-box models, VCCS tables, reduced-order models, and data-driven surrogates—each address parts of this gap but introduce trade-offs among fidelity, transparency, computational effort, and workflow compatibility. In particular, existing reduced-order models either remain closely tied to specific EMT implementations, rely on curve-fitting with limited physical interpretability, or do not explicitly capture the internal saturation and mode-transition behavior that governs inverter fault response.

The parametric reduced-order modeling framework developed in this dissertation advances the state of the art by introducing a protection-oriented representation that explicitly decomposes inverter fault currents into physically meaningful subtransient, transient, and steady-state components in the sequence domain, while directly incorporating controller saturation and nonlinear dynamics. Unlike quasi-steady-state VCCS models or black-box surrogates, the proposed approach preserves the dominant physical mechanisms driving fault behavior, supports systematic calibration from EMT simulation or experimental data, and enables scalable integration into existing short-circuit and protection-study tools without reliance on proprietary controller implementations.

1.4 Research Methodology

The research methodology adopted in this thesis is grounded in systems engineering principles, providing a structured and iterative approach to analyzing the behavior of IBRs and their impact on grid protection systems. Systems engineering principles emphasize a comprehensive and holistic view of the system, ensuring that all components, interactions, and feedback loops are considered throughout the research process. This methodology enables the integration of modeling, simulation, and validation processes in a coherent framework that addresses the complexity of modern power grids with high IBR penetration.

1.4.1 A systems engineering Perspective

A systems engineering framework provides the methodological foundation for this dissertation. Rather than treating models as stand-alone artifacts, this approach situates them within a connected design and verification process that begins with stakeholder needs and extends through requirement definition, system architecture, modeling, and validation [58, 59]. In the present work, the stakeholder hierarchy spans from enterprise-level reliability and regulatory concerns (e.g., NERC and standards bodies) to utility-level planning and protection requirements, and finally to inverter plant subsystems and their control behaviors. Requirements derived from these stakeholder needs are structured in a manner that ensures traceability across all implementation tiers.

Although a complete digital system model is beyond the scope of this dissertation, the work identifies how the EMT and ROM models developed here—and a future RMS-level representation—could be embedded within an integrated systems framework in subsequent research. Figure 1.1 conceptually situates the proposed ROM within the left leg of the systems engineering V-model, with the corresponding verification and validation activities aligned on the right leg.

Stakeholder and Requirements Capture

Grid-code clauses and standards discussed in Section 1.2 are represented as measurable requirements derived from stakeholder needs. The Level 3 NERC Alert [10] is treated as a compliance constraint with defined timelines. This structure supports bidirectional traceability, ensuring that any future revision to grid standards automatically identifies the corresponding simulation artifacts impacted by those changes..

Functional Decomposition

The inverter plant is partitioned into four functional domains: Source, Controls, Filter, and Protection. Each domain includes parameter definitions and dynamic relationships such as energy-flow and timing equations. For example, the Controls domain includes PLL bandwidth (ω_{PLL}) and current-limiter logic. This decomposition follows established systems engineering best practice for "separation of concerns," enabling modular refinement of the ROM [58].

Model Tiers and Allocation Strategy

To support scalable studies across different analysis environments, four fidelity tiers are defined, each representing a distinct level of abstraction and analytical depth:

a) *Tier 0—Theoretical Analysis:* foundational analytical formulation of inverter behavior during grid faults, including sequence decomposition, control-loop interactions, and protection response mechanisms. This tier establishes the governing equations and physical interpretations that guide model development and parameter identification in higher tiers.

b) *Tier 1—EMT Truth Model* (vendor black-box or PSCAD): high-fidelity electromagnetic transient representations that capture detailed device-level physics and serve as validation benchmarks for reduced-order modeling.

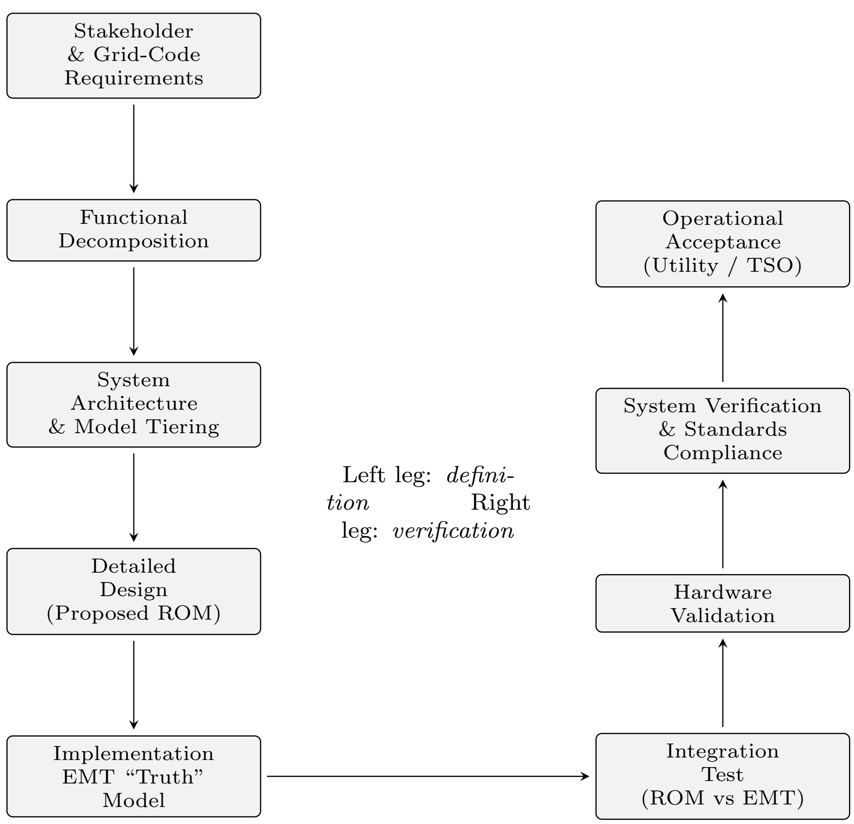

Figure 1.1: Placement of the proposed ROM within a simplified V-model systems engineering lifecycle.

c) *Tier 2—Proposed ROM* (MATLAB/Simulink, PSCAD, Python): reduced-order dynamic models derived from EMT simulations, offering computationally efficient surrogates for extensive scenario studies while preserving essential inverter dynamics and post-fault behavior.

d) *Tier 3—RMS Proxy* (PSS®E, PowerFactory): positive-sequence phasor-domain models envisioned to embed ROM characteristics into conventional planning tools for bulk-system studies. This tier is not developed within the scope of this dissertation but is identified as a logical extension of the framework for future research.

Allocation strategies maintain consistency in power balance and sequence impedance across tiers. Automated scripts transfer parameters from Tier 1 to Tier 2 for characterization and sensitivity studies, while Tier 0 provides the theoretical basis for interpreting those relationships. The Tier 3 layer, though not implemented here, represents the future integration of reduced-order dynamics into grid-planning and interconnection study environments.

Verification and Validation

A structured requirement–test matrix links each requirement to specific verification artifacts across model tiers and environments. Verification was primarily performed by comparing the proposed ROM against the high-fidelity EMT "truth" model across a comprehensive set of fault scenarios, including symmetrical and asymmetrical disturbances. These tests ensured that the ROM accurately reproduced key inverter behaviors such as fault-current magnitude, phase dynamics, and recovery transitions.

In addition, several response datasets obtained from commercial off-the-shelf (COTS) inverters through hardware experiments were used to further validate the tuned ROM parameters. These comparisons confirmed that the reduced-order model could represent realistic post-fault dynamics observed in physical hardware.

A detailed protection-relay model, incorporating multiple protection elements, was also used to process current and voltage waveforms from both the EMT and ROM models. The resulting relay responses were compared to assess consistency in event detection, trip timing, and coordination behavior, providing an additional layer of verification relevant to protection studies.

Overall, the validation framework integrates:

- *Model-in-the-loop* tests in Python for automated regression of control functions and parameter updates,
- *EMT–ROM waveform overlays* to evaluate dynamic fidelity under a wide range of grid-fault conditions,
- *Hardware-based response comparisons* to ensure alignment with COTS inverter behavior, and
- *Protection-relay response validation* to confirm that both models produce consistent relay operation signatures.

This verification chain follows established systems engineering validation practices [58], ensuring reproducibility, consistency, and compliance. Automated continuous-integration workflows execute these tests at each update, aligning with the NERC Alert's Essential Action 7 on model maintenance and sustained validation of inverter-based resource models [10].

Chapter 2

System Description – Part I: Requirement Analysis

2.1 Protection Study Context and Stakeholder Needs

Protection engineering decisions (settings, coordination, logic selection, and risk assessment) depend on relay-seen quantities during faults: the magnitude and phase angle of current relative to terminal voltage, positive- and negative-sequence content, and the timing of control-driven events (e.g., current limiting, momentary cessation, and recovery). In IBR plants these quantities are shaped by converter controls and limits, not by synchronous-machine electromechanics, which makes control-aware models essential for credible protection studies [60–62].

Distance protection (reach and polarization), negative-sequence directional elements, phase and ground overcurrent protection—both instantaneous (IOC) and time-delayed (TOC)—line differential, breaker-failure timing, and power-swing blocking are particularly sensitive to the IBR fault response. Key sensitivities include (*i*) the angle of on-fault current (often not purely inductive), (*ii*) the engagement and priority of current limiters, (*iii*) explicit negative-sequence behavior (controller objective, commanded angle, and saturation/suppression rules), and (*iv*) ride-through behavior including momentary cessation and zone timers [60, 63]. Peer-reviewed studies further show that simplifications of negative-sequence behavior can materially alter directional decisions and coordination outcomes [64].

Protection studies must resolve the early fault window (sub-cycle to a few cycles), the transient window (first few cycles to several cycles), and the post-transient recovery where ride-through logic and ramping determine relay margins. Standards-aligned guidance recommends using EMT models to establish behavior in these windows and to generate truth data for protection assessment and tool calibration [61, 62, 65]. Short-circuit tools used for settings and coordination can then consume control-aware abstractions that preserve time-sliced magnitude/angle and sequence quantities [66].

Protection engineers require model artifacts that directly inform element reach, directional torque angle, pickup timing, and restraint behavior (including negative/zero-sequence access driven by plant grounding and transformer vector groups). Planners and interconnection engineers need models that scale to broad scanning of operating points and grid strengths while remaining traceable to EMT truth. Operators and commissioning teams benefit from models that can replay observed disturbance behavior to verify settings and mitigation measures. Regulatory direction (e.g., NERC alerts and EMT guidance) emphasizes verified model fidelity, traceability, and the availability of protection-relevant data products [62, 67].

Credible protection assessments must span balanced and unbalanced faults (SLG, LL, LLG, LLL), a range of fault resistances and locations (near-end, remote, behind-infeed), pre-fault operating points (P, Q) and control modes (GFL vs. GFM), as well as grid-strength variation (e.g., SCR/impedance). Ride-through and reactive current injection requirements (e.g., IEEE Std 2800) must be evaluated in combination with limiter behavior and negative- sequence control [68], because these interactions set relay-observed trajectories and timers [62, 63]. Regional practices (e.g., ERCOT interconnection modeling expectations) reinforce the need for high-quality, facility-specific EMT models and supporting verification [65].

For use in planning/protection toolchains, IBR models should provide (*i*) EMT cases for representative scenarios to establish ground truth and (*ii*) reduced artifacts consumable by short-circuit/coordination tools, such as VCCS tables of positive/negative-sequence current magnitude and angle versus terminal voltage, segmented into early, transient, and post-transient time slices. These artifacts should include flags for limiter and ride-through states to support relay analytics and settings traceability [62, 66]. At the fleet and system level, NERC's reliability assessments highlight the operational importance of maintaining reactive support and model quality for IBR-rich systems—further motivating protection-grade modeling and verification [69].

2.2 Regulatory and Standards Landscape

In North America, the policy direction is set by the Federal Energy Regulatory Commission (FERC) and implemented by the North American Electric Reliability Corporation (NERC) through Reliability Standards, reliability guidelines, alerts, and task-force outputs. Industry standards (e.g., IEEE Std 2800) and regional implementation guidance (e.g., ERCOT) further specify performance and modeling expectations with direct implications for protection studies.

FERC's Order No. 901 directs NERC to develop new or modified Reliability Standards addressing identified IBR reliability gaps in the areas of data sharing, model validation, planning and operational studies, and performance requirements [70]. Since then, FERC has approved Reliability Standards applicable to inverter-based generators consistent with the Order 901 directive, reinforcing mandatory expectations on entities to provide validated models and support credible planning and protection analyses [71]. These actions elevate modeling—including fault-response fidelity—from a recommended practice to a standards-backed obligation for registered entities involved in interconnection and planning.

NERC has published detailed guidance on EMT modeling and simulations, explicitly recommending EMT models be required for all newly connecting BPS-connected IBRs and providing study scoping, model-content, and verification practices [72]. A companion reliability guideline on Recommended Practices for Performing EMT System Studies for IBRs provides end-to-end practices for screening, modeling, scenario design, and verification, with emphasis on protection-relevant phenomena such as unbalance, weak-grid conditions, and ride-through interactions [62]. In May 2025, NERC issued a Level 3 Alert titled Essential Actions for IBR Performance and Modeling, directing Transmission Owners (TOs), Transmission Planners (TPs), Planning Coordinators (PCs), and Generator Owners (GOs) to enhance minimum technical requirements, study practices, and verification processes—further tightening expectations on model fidelity and traceability [67]. The NERC Electromagnetic Transient Modeling Task Force (EMTTF) has defined scope and deliverables aimed at model quality, availability of facility-specific EMT models, and consistent study procedures [73]. NERC's earlier guidance on integrating IBRs into low short-circuit strength systems remains relevant to protection because it frames grid-strength dependencies that influence relay-observed behavior [74].

IEEE Std 2800™–2022 defines transmission-interconnection performance requirements for large-scale IBRs—including dynamic reactive current injection during faults, momentary cessation, and ride-through zone timers [75]—that materially affect relay-observed trajectories and timing. These parameters must therefore be represented accurately in study models used for protection analysis [63, 76]. The IEEE PES Power System Relaying and Control Committee (PSRC) report on Protection Challenges and Practices for Interconnecting IBRs documented specific protection functions and modeling behaviors of concern, such as current-limiting priority, negative-sequence control, and polarization effects, providing a reference baseline for protection-oriented modeling requirements [60].

Regional practices have operationalized these expectations. For example, ERCOT's Inverter-Based Resource Task Force (IBRTF) published EMT modeling and simulation guidance aimed at Transmission Planners and Planning Coordinators, highlighting model-quality requirements and their adoption in interconnection and planning studies. ERCOT's planning documents and task-force reports formally incorporate these expectations into regional study processes [77, 78]. Such regional materials typically specify deliverables (e.g., EMT models, validation artifacts) and usage contexts (e.g., screening, weak-grid analysis) that are directly relevant to protection applications.

Across these regulatory and standards sources, several convergent requirements emerge for models used in protection studies: (*i*) provision of EMT models and supporting validation documentation; (*ii*) inclusion of control-driven fault-response behaviors such as current limiting, negative-sequence control, dynamic reactive current injection, and momentary cessation with hysteresis and timers; (*iii*) treatment of operating-point and grid-strength dependence; and (*iv*) exportable artifacts suitable for integration with planning and short-circuit analysis tools. These shared expectations are summarized in Table 2.1, which consolidates the main regulatory and standardization sources alongside their modeling implications for protection studies.

Table 2.1: Regulatory and standards sources with derived modeling implications for protection studies.

Source	Stakeholder Needs	Model Requirements
FERC Order 901 and subsequent approvals [70, 71]	Develop and implement standards for data sharing, model validation, planning and operational studies, and performance requirements	Provide validated, standards-compliant models (including fault response) and documentation traceable to studies used for protection
NERC EMT guidelines and practices [62, 72]	Recommend EMT models for newly connecting BPS IBRs; define study scope, model content, and verification practices	Include control-driven behaviors; cover weak-grid and unbalanced conditions; provide EMT truth cases and verification artifacts for protection analysis
NERC Level 3 Alert (May 2025) [67]	Define essential actions for IBR performance and modeling across TO/TP/PC/GO	Establish minimum technical requirements, protection-relevant studies, and model traceability
IEEE Std 2800 (overview materials) [63, 76]	Specify fault ride-through, dynamic reactive current, and momentary cessation with timing envelopes	Ensure models reproduce on-fault current magnitude, angle, and timing consistent with IEEE 2800 behavior for relay analysis
IEEE PSRC TR-81 [60]	Identify protection functions and IBR behaviors of concern; recommend modeling practices	Represent current-limiting priority, negative-sequence paths, and polarization effects; provide sequence-domain observability
ERCOT IBRTF and Planning Guide [77, 78]	Establish regional EMT model adoption, quality, and interconnection-study usage	Deliver region-compliant EMT models and validation artifacts suitable for protection and weak-grid studies

2.3 Requirements for IBR Models Used in Protection Studies

This section defines the essential capabilities that IBR models must provide to support credible protection studies. These requirements are distilled from North American regulatory and standards guidance, as well as from established protection-engineering practice. In summary, models used for protection applications must expose time-resolved sequence-domain current magnitude and angle during fault events, represent control-driven behaviors such as current limiting, negative-sequence control, and ride-through or cessation logic, account for operating-point and grid-strength dependence, and produce artifacts compatible with planning and protection analysis tools [60, 62, 67, 72].

2.3.1 Functional Behaviors the Model Shall Reproduce

F1: *Time-dependent fault current magnitude and angle by sequence.* The model shall provide positive- and negative-sequence currents, $\{|I_1|, \angle I_1, |I_2|, \angle I_2\}$, as a function of PCC voltage during fault conditions, resolved over three characteristic intervals: (*i*) subtransient (0.5 cycles), (*ii*) transient (3–10 cycles), and (*iii*) post-transient. Protection functions such as distance reach and polarization depend primarily on these quantities [60, 62].

F2: *Current limiting and priority arbitration.* The model shall represent current ceilings, reactive-versus-active current priority (I_q vs. I_p), rate limits, and anti-windup behavior, since limiter engagement significantly alters both the magnitude and phase of fault currents as observed by protective relays [60, 62].

F3: *Negative-sequence control behavior.* An explicit negative-sequence control path shall be included, representing control objectives, commanded angles, limiter interactions, and any vendor-specific suppression features, as these directly influence the performance of negative-sequence directional and polarization elements [60].

F4: *Ride-through and momentary cessation logic.* The model shall reproduce dynamic reactive current injection versus voltage, momentary cessation and hysteresis behavior, zone timers, and recovery ramps consistent with transmission-interconnection standards such as IEEE Std 2800. These behaviors shape the relay-observed current trajectory and timing during fault and recovery intervals [62, 63].

F5: *Operating-point and grid-strength dependence.* Model parameters shall be expressed as functions of the pre-fault operating point (P, Q, and control mode—grid-following or grid-forming) and a grid-strength proxy (e.g., short-circuit ratio or Thévenin impedance). Weak-grid conditions and inverter operating modes substantially affect relay-observed fault responses [62, 72].

F6: *Collector system and grounding effects.* The model shall represent transformer vector groups, grounding configurations, and zero-/negative-sequence current access paths necessary for ground and sequence-based elements. Current and voltage measurement points (CTs and PTs) should be aligned with study conventions [60, 62].

The relationship between protection functions and the corresponding model phenomena that must be represented is summarized in Table 2.2.

2.3.2 Verification and Data Expectations

V1: *Verification traceability and evidence.* Verification shall provide disturbance-based or test-based evidence that the model reproduces protection-relevant behaviors, including sequence current magnitudes and angles, limiter and cessation timing, and ride-through state transitions. Provenance, acceptance criteria, and version traceability shall be maintained in accordance with NERC guidance [62, 67].

V2: *Scenario coverage.* Model validation shall include a diverse set of fault conditions, single line to ground (SLG), line to line (LL), double line to ground (LLG), and three phase (LLL), as well as variation in fault resistance, fault location, operating point (P, Q), control mode (grid-following/forming), and grid strength. Validation should include both ride-through/cessation active and inactive cases, and explicit tests of negative-sequence behavior [62, 72].

V3: *Exportable artifacts for protection studies.* The model shall produce time-sliced voltage-controlled current source (VCCS) tables, including, where supported, $\{|I_1|, \angle I_1, |I_2|, \angle I_2\}$, and associated state or flag signals (e.g., limiter active, cessation active, ride-through zone, recovery). All outputs shall include units, reference points, and interpolation rules documented for integration with relay-analysis and planning tools [62, 79].

2.4 From Protection Needs to a Reduced-Order Model: Rationale and Derived Requirements

Sections 2.1–2.3 established that credible protection studies require models capable of revealing time-resolved, sequence-domain fault currents (magnitude and angle), capturing control-driven

Table 2.2: Protection functions and associated model phenomena that must be represented.

Protection Function	Modeling Requirement
Distance (reach, polarization)	Time-resolved $\angle I_1$ and $\lvert I_1\rvert$ vs. $\lvert V_1\rvert$; current-limiter priority and rate limits; reactive current injection per ride-through profile; dependence on grid strength.
Negative-sequence directional/polarization	Explicit I_2 control path (commanded angle, limiter or suppression behavior); transformer and grounding representation for sequence access; accurate I_2/I_1 ratio.
Overcurrent (IOC/TOC) and breaker-failure timing	Realistic $\lvert I\rvert$ magnitude trajectories; limiter and cessation timing; recovery ramps.
Line differential	Subtransient and transient sequence components; realistic collector-system modeling and CT/PT placement.
Ground elements	Representation of zero- and negative-sequence paths through transformers and grounds; residual current observability.

behaviors (current limiting with priority arbitration, negative-sequence control, and ride-through or cessation with timers), accounting for operating-point and grid-strength dependence, and representing plant and grounding effects. High-fidelity EMT models are therefore indispensable as the "truth" source for understanding and validating inverter fault behavior [60, 62, 67, 72].

However, practical protection-engineering workflows—such as relay setting, coordination, and sensitivity analyses—require thousands of scenarios spanning diverse pre-fault operating points, fault types and locations, fault resistances, and system strengths. Running such large-scale simulations solely in EMT environments becomes computationally prohibitive, while traditional phasor-domain short-circuit (SC) models lack the fidelity needed to capture the control-driven phenomena identified above [62, 80, 81].

To bridge this gap, a reduced-order, protection-grade surrogate model is needed—one that retains the essential inverter dynamics relevant to protection studies while achieving the computational efficiency required for large-scale coordination and planning tasks. The key motivations driving the development of such a reduced-order model are summarized below.

2.4.1 Drivers for a Reduced-Order, Protection-Grade Surrogate

D1: *Scale and speed for settings and coordination.* Protection engineers must evaluate numerous combinations of operating point (P, Q), system strength (e.g., SCR), and fault condition.

Comprehensive EMT sweeps are prohibitively slow, and even phasor-domain solutions experience significant slowdowns as the number of detailed IBR models increases [82].

D2: *Interoperability with planning and short-circuit tools.* Modern short-circuit and coordination tools increasingly support voltage-controlled current-source (VCCS) abstractions with time-sliced, tabular magnitude and angle (and, where available, sequence-domain) outputs. These interfaces require models that can populate such tables while preserving relay-critical behavior [79].

D3: *Fidelity gaps in generic short-circuit models.* Comparative analyses show notable deviations between generic phasor-domain IBR models and EMT "truth" responses, particularly in negative-sequence current behavior and current-limiting transitions [64, 80].

D4: *Intellectual property and data-sharing constraints.* OEM control algorithms embedded in EMT models are often proprietary and cannot be shared broadly. A reduced-order model can provide the necessary external behavior for protection analysis without revealing vendor-specific control implementations [62, 81].

D5: *Regulatory and industry momentum.* Emerging standards and regulatory guidance place increasing emphasis on verified model fidelity and traceability, particularly for protection-relevant studies. This trend reinforces the need for a validated, shareable surrogate model that can be deployed at scale [60, 62, 67].

2.4.2 Definition of "Accuracy" for Protection-grade ROM

For protection applications, accuracy is defined in terms of quantities that protective relays actually measure and respond to—rather than point-by-point waveform matching. Accordingly, the ROM must accurately reproduce, for each characteristic time window (e.g., first $\frac{1}{2}$ cycle, 1–3 cycles, and beyond 3 cycles), the following aspects: (*i*) the positive- and negative-sequence current magnitudes and angles, $\{|I_1|, \angle I_1, |I_2|, \angle I_2\}$, as functions of PCC voltage; (*ii*) limiter engagement, priority arbitration, and rate-limit behavior; and (*iii*) operating-point and grid-strength dependence.

All of these quantities must be benchmarked against EMT "truth" simulations and, where available, validated against disturbance data or hardware-based observations [62, 72, 79, 81].

2.4.3 Architectural Implications for the ROM

The need to reproduce relay-relevant behavior without full electromagnetic detail imposes specific architectural requirements on the ROM. These requirements ensure that the model remains both computationally efficient and compatible with existing protection and planning tools. The key architectural implications are outlined below.

A1: *Sequence-domain, time-sliced outputs.* The ROM shall provide positive- and negative-sequence current magnitudes and angles, segmented into subtransient, transient, and post-transient windows. This aligns directly with relay decision horizons and short-circuit tool interfaces [79, 83].

A2: *Control-aware behavior.* The model shall embed explicit representations of current limiting with I_q/I_p priority arbitration, anti-windup, rate limits, and negative-sequence control objectives, as these govern the relay-observed current trajectories in both magnitude and phase [60, 64].

A3: *Parametric dependence.* Model parameters shall vary with pre-fault operating point (P, Q), control mode (GFL/GFM), and grid-strength indicators such as SCR, acknowledging the documented sensitivity of protection outcomes to these factors [72, 80].

A4: *Exportable artifacts.* The ROM shall generate voltage-controlled current-source (VCCS) tables or sequence-resolved surfaces with clearly documented units, interpolation rules, and event flags for limiters, cessation, and ride-through states. These artifacts enable drop-in integration with protection and coordination tools [79, 82].

2.4.4 Derived Requirements for the ROM

The protection-driven considerations above translate into the following consolidated requirements for a reduced-order model suitable for large-scale protection studies:

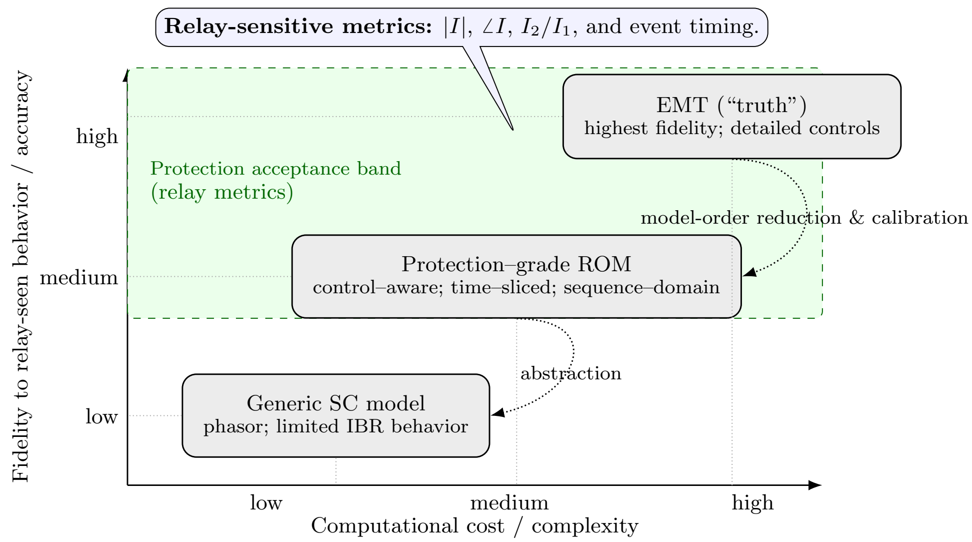

Figure 2.1: Illustration of the accuracy–complexity trade-off motivating a protection-grade reduced-order model.

- *Outputs:* time-sliced $\{|I_1|, \angle I_1, |I_2|, \angle I_2\}$ vs. $\{|V_1|, \angle V_1, |V_2|, \angle V_2\}$.
- *Behaviors:* accurate representation of current limiting with I_q/I_p priority, negative-sequence control, ride-through dynamics with hysteresis and timers, and explicit dependence on operating point and grid strength.
- *Interfaces:* ability to export VCCS tables or sequence-resolved surfaces, including metadata and event indicators, for compatibility with short-circuit and coordination tools. The ROM should also include EMT cross-validation packages and disturbance-matching evidence consistent with PPMV (performance, provenance, maintenance, validation) practices.
- *Quality targets:* accuracy defined in relay-metric time slices (magnitude, angle, and sequence ratios), with explicit timing accuracy for limiter and cessation transitions.

Chapter 3

System Description – Part II: Hardware and Control Architecture

This chapter describes the system chosen for modeling, analysis, and verification in this dissertation. The objective is to investigate inverter fault behavior, ride-through performance, and converter-driven dynamic responses in a representative IBR used in transmission-connected renewable generation.

A utility-scale wind turbine was selected as the reference system model for several reasons. First, wind energy is among the most widely deployed forms of grid-connected renewable generation globally, with Type-IV wind energy conversion systems (WECS) now predominant in new installations due to their superior controllability and grid-support capability [84–86]. Second, unlike photovoltaic (PV) resources—which have no mechanical inertia—wind turbines incorporate both mechanical and electrical energy-conversion stages, enabling examination of interactions among aerodynamic torque, generator dynamics, DC-link stabilization, and converter current control [87, 88]. Finally, the Type-IV or Full-Scale Converter (FSC) architecture places the grid entirely behind a back-to-back converter, allowing complete decoupling between generator and grid and enabling fault-response mechanisms and IEEE 2800 compliance to be examined in isolation from machine-electromagnetics [89, 90].

For these reasons, a Type-IV WECS was used in this research. The following sections describe the major hardware components and control layers of the system under study.

3.1 Type-IV WECS Overview

A notional depiction of a Type-IV WECS, connected to a medium-voltage distribution system, is shown in Fig. 3.1. As illustrated, the system consists of: (*i*) the aerodynamic rotor extracting kinetic energy from the wind; (*ii*) a permanent-magnet synchronous generator (PMSG) converting

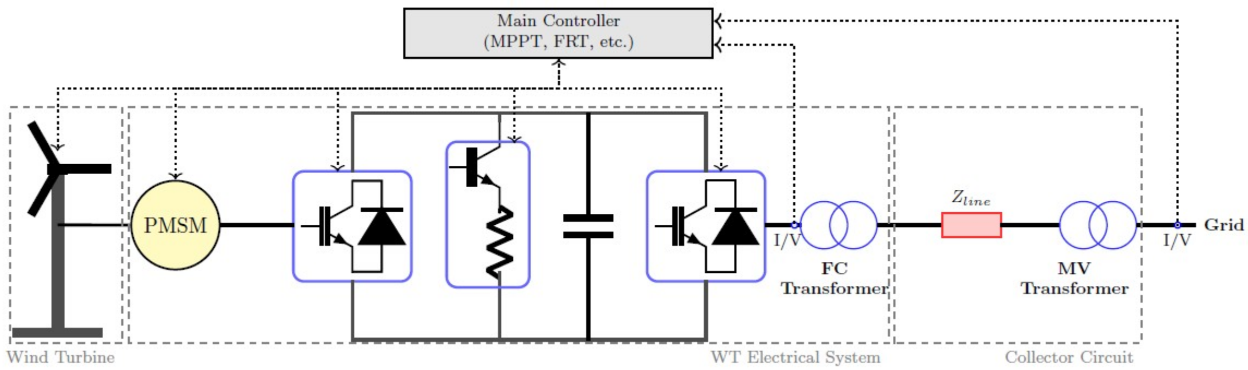

Figure 3.1: Schematic of the Full-Size Converter (FSC) Wind Turbine Electrical System.

mechanical torque into electrical power; (*iii*) a full-scale back-to-back converter with a regulated DC-link; (*iv*) step-up transformer(s) and park collection circuits; and (*v*) the point of interconnection (POI) to the grid [91, 92].

3.1.1 Mechanical Subsystem

The mechanical subsystem converts kinetic wind energy into mechanical shaft power that ultimately drives electrical generation. As depicted in Fig. 3.2, this chain begins with aerodynamic energy capture by the turbine rotor, continues through the flexible turbine–generator drivetrain, and terminates at the PMSG, whose torque is governed by the converter. The system is excited by two exogenous inputs:

- the instantaneous wind speed V, which represents the sole external energy source, and
- the blade-geometry vector $\left[\vartheta_B(r),\, t_B,\, c_B,\, c_w\right]$, which parameterizes the local twist angle $\vartheta_B(r)$, thickness t_B, chord length c_B, and lift-to-drag behavior c_w.

These variables jointly determine the aerodynamic power-coefficient surface $C_p(\lambda, \beta)$, which governs aerodynamic energy extraction as a function of tip-speed ratio λ and pitch angle β.

The turbine controller closes the mechanical loop by issuing two actuator-relevant inputs:

- a collective-pitch command β_{ref}, which regulates aerodynamic loading, and
- an electromagnetic torque reference T_g^*, or equivalently a power-setpoint $P_{\text{set}} = T_g^*\,\omega_g$, which determines generator loading.

The aerodynamic rotor extracts mechanical power,

$$P_t = \tfrac{1}{2}\rho A C_p(\lambda, \beta) V^3, \tag{3.1}$$

where ρ is air density, $A = \pi R^2$ is rotor swept area, R is rotor radius, and $C_p(\lambda, \beta)$ is the turbine power coefficient. The corresponding aerodynamic torque is

$$T_t = \frac{P_t}{\omega_t}, \tag{3.2}$$

where ω_t is the rotor angular speed. The tip-speed ratio,

$$\lambda = \frac{\omega_t R}{V}, \tag{3.3}$$

relates turbine rotational speed to the incoming wind speed.

The rotor and generator are modeled as two inertias coupled by a flexible shaft. The rotor side is characterized by inertia J_t and damping D_t, while the generator side exhibits inertia J_g and damping D_g. The shaft stiffness K_{tg} and mutual damping D_{tg} permit torsional deflection $\theta_t - \theta_g$, enabling transient energy exchange between the two masses.

Let θ_t and θ_g denote rotor and generator angular positions, and ω_t and ω_g their angular velocities. The drivetrain dynamics follow:

$$J_t \dot{\omega}_t = T_t - K_{tg}(\theta_t - \theta_g) - D_{tg}(\omega_t - \omega_g) - D_t \omega_t, \tag{3.4}$$

$$J_g \dot{\omega}_g = K_{tg}(\theta_t - \theta_g) + D_{tg}(\omega_t - \omega_g) - T_g - D_g \omega_g, \tag{3.5}$$

where T_t accelerates the rotor and T_g decelerates the generator in accordance with electromagnetic torque demands from the converter.

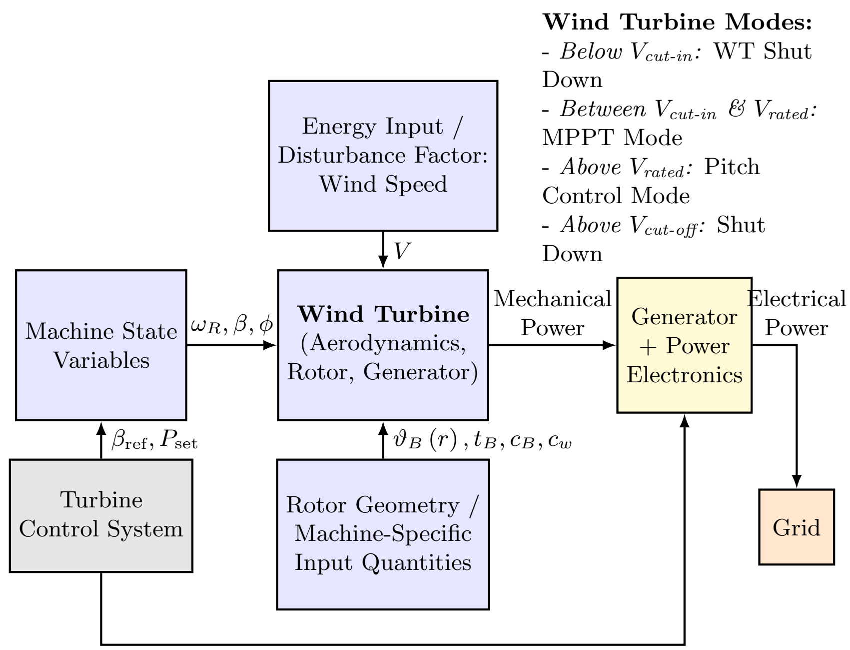

Figure 3.2: Signal flow in the mechanical chain.

3.1.2 Electrical Subsystem

The electrical subsystem converts mechanical shaft torque into regulated electrical power and interfaces the turbine with the transmission system. As shown in Fig. 3.3, the electrical chain consists of:

- a PMSG,
- a full-scale back-to-back converter, comprising
  - a machine-side converter (MSC),
  - a DC-link energy storage stage, and
  - a grid-side converter (GSC),
- a step-up transformer connecting to the medium-voltage collection system,
- and the final interface transformer connecting the plant to the transmission-level grid at the point of interconnection (POI).

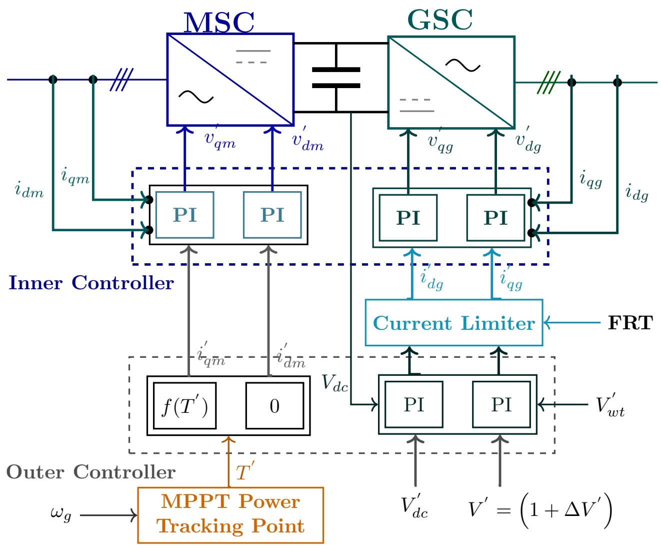

Figure 3.3: Electrical subsystem architecture of a full-scale-converter wind turbine.

The PMSG converts mechanical torque T_g into three-phase stator currents i_{abc}. Because the generator is fully decoupled from grid frequency by the back-to-back converter, its electrical frequency is proportional strictly to mechanical speed,

$$\omega_g = \frac{d\theta_g}{dt}, \tag{3.6}$$

rather than being constrained by grid synchronization. This enables variable-speed operation, which enhances energy capture and reduces mechanical stress.

The MSC rectifies the generator's AC output to a controlled DC link voltage. It regulates generator electrical torque by commanding the current component aligned with the generator's q-axis. On this side of the system, the electrical environment is isolated from grid imbalances, harmonics, or asymmetric faults, and all quantities are referenced to the generator synchronous frame.

The DC link—consisting of capacitor energy storage—acts as an intermediate energy reservoir between the two converters. It absorbs short-term power imbalance between generator torque and grid power flow. Its voltage V_{dc} reflects real-power transfer:

$$P_{\text{grid}} \approx P_{\text{gen}} - \frac{dE_{dc}}{dt}, \tag{3.7}$$

where E_{dc} is stored DC-link energy. During grid faults, when active-power transfer is temporarily restricted, the stored DC-link energy rises until electrical torque is shed at the MSC or the turbine power is curtailed.

The GSC synthesizes three-phase voltages v^*_{abc} to control current injection into the grid. The GSC is the sole interface where the wind turbine "observes" the grid: voltage magnitude, imbalance, unbalance, and frequency deviations appear only on this side. The GSC determines the positive- and negative-sequence current components at the POI and ensures that the inverter satisfies grid requirements, including reactive power support and fault ride-through capability.

After conversion, the generated power flows through:

1. a low-voltage stator circuit,
2. a step-up transformer to the medium-voltage collector system (e.g., 33 kV),
3. an aggregation of multiple turbine outputs, and finally
4. a transmission-level step-up transformer (e.g., 138 kV) connecting the plant to the bulk power grid.

3.2 Control

Figure 3.1 illustrates the schematic of the system considered in this study—a FSC wind turbine system—comprising the aerodynamic rotor, PMSG, full-scale back-to-back converter with DC-link, step-up transformers, collector circuit, and the grid POI.

3.2.1 System-level Controls

Figure 3.4 presents the high-level structure used throughout this work.

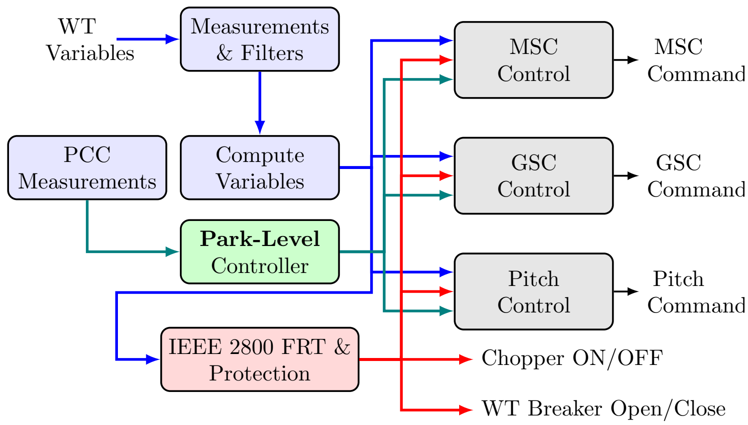

Figure 3.4: High-level control hierarchy adopted for the FSC wind-turbine model.

1. *Signal-conditioning layer* Local measurements from each turbine and from the POI are filtered and transformed, providing clean speed, current, and voltage signals for the inner loops.

2. *Turbine-level loops* Each turbine executes three nested regulators: (*i*) a torque loop for maximum power point tracking, (*ii*) a DC-link loop that governs active power, and (*iii*) a reactive-power or terminal-voltage loop.

3. *Park-level supervisor* A plant-wide controller compares POI measurements with grid-operator targets (voltage, power factor, or reactive-power schedule) and issues a common bias to all turbines so the aggregate response satisfies network requirements.

4. *Compliance and protection layer* Functions mandated by IEEE Std 2800—voltage and frequency ride-through, current-priority logic, rate-limited power recovery, and internal protection—are implemented as supervisory states. When a threshold is crossed, this layer temporarily overrides lower layers to inject dynamic current or, if self-damage is imminent, to trip the unit.

3.2.2 Turbine Controls

Wind turbine operation is governed by a hierarchical supervisory control strategy that adjusts aerodynamic torque, rotor speed, and generator torque demand according to the prevailing

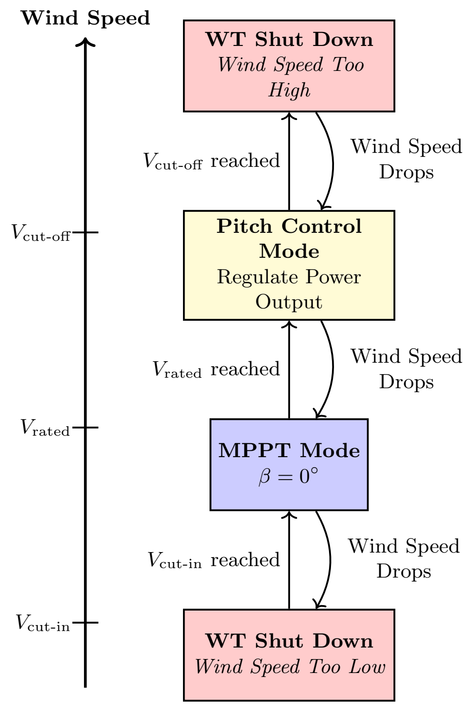

Figure 3.5: Wind-turbine operating regions.

wind conditions. As shown in Fig. 3.5, the controller transitions between shutdown, MPPT, pitch-limited, and high-wind cut-out modes based on the filtered wind speed V. Each operating region imposes a different control objective and determines the corresponding targets for rotor speed ω_t, aerodynamic torque T_t, and generator torque reference T_g^*. Aerodynamic power extraction is computed from the available wind energy and the turbine operating point, using the well-established nonlinear relationships

$$P_t = \tfrac{1}{2}\rho A C_p(\lambda, \beta) V^3, \qquad T_t = \frac{P_t}{\omega_t}, \qquad \lambda = \frac{\omega_t R}{V}, \tag{3.8}$$

where the power coefficient $C_p(\lambda, \beta)$ is obtained from a pre-tabulated look-up surface derived from manufacturer data. Tip-speed ratio λ and pitch angle β together determine the extracted aerodynamic torque. Linear interpolation of the C_p surface ensures a continuous torque response suitable for controller linearization and stability analysis (Fig. 3.6).

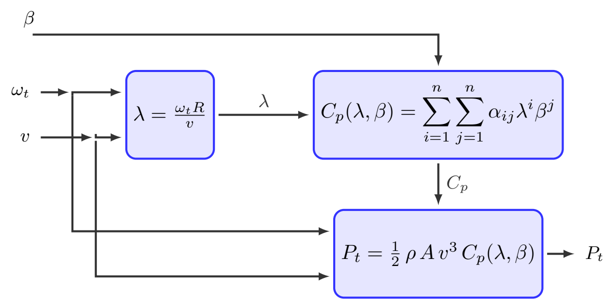

Figure 3.6: Wind-turbine power-coefficient and power-extraction model.

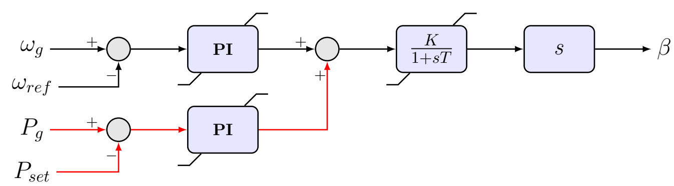

Figure 3.7: Wind-turbine pitch-control system with nested speed (ω_t) and power (P_g) regulators.

The conversion of these aerodynamic relationships into actionable actuator commands is performed by the pitch-control system shown in Fig. 3.7. This controller incorporates two nested objectives: a fast inner speed-regulation loop that maintains rotor speed at its rated value once $V \geq V_{\text{rated}}$, and a slower outer power-control loop that biases the commanded pitch angle to meet the desired generator power set-point P_{set}. Together, these layers ensure stable turbine operation across the full range of wind conditions while extracting maximum power during MPPT operation, limiting mechanical loads in high-wind regimes, and enabling seamless interaction with the electrical control systems described later.

3.2.3 Inverter Controls

The electrical conversion stage of the Type-IV wind turbine is governed by two coordinated voltage-source converters: the MSC, which interfaces the generator with the DC link, and the GSC, which governs the injection of positive- and negative-sequence currents into the grid. Although these converters share the DC-link interface, their operating objectives and control architectures are distinct, reflecting their different roles in the power-conversion chain.

The MSC regulates the electromechanical interaction between the PMSG and the DC link. Because the generator is electrically isolated from the grid, the MSC is not exposed to negative-sequence disturbances. A single coupled dq-frame current controller suffices, with MPPT realized via the standard K_{opt} torque–speed relationship. The outer loop computes the electromagnetic torque reference,

$$T_{\text{ref}} = K_{\text{opt}}\,\omega_g^2, \tag{3.9}$$

which is translated into a q-axis current command through a PI regulator,

$$i_{qm}^* = k_{p,T}(T_{\text{ref}} - T_e) + k_{i,T}\int (T_{\text{ref}} - T_e)\,dt, \tag{3.10}$$

while the d-axis reference is fixed at zero. The inner loop enforces the commanded currents via standard decoupled PI controllers with feed-forward cross-coupling terms, ensuring fast current tracking and stable generator torque control. During grid faults, when the GSC temporarily suspends active-power transfer and DC-link energy rises, the MSC automatically reduces generator torque, backing off i_{qm}^* to prevent DC-link overvoltage. Additionally, if generator current reaches thermal limits, the MSC proportionally scales both current references to preserve converter safety while cooperating with downstream current-limiting actions.

Complementing this, the GSC manages the interaction between the wind turbine and the external power system. Its controller is explicitly sequence-aware, using a PLL and a sequence-extraction algorithm (e.g., DSOGI) to decompose measured voltages and currents into positive- and negative-sequence components. Under normal operation, the outer loops regulate DC-link voltage via the d-axis current i_d^{+*} and reactive power or terminal voltage via the q-axis current i_q^{+*}, with all negative-sequence references held at zero. Upon activation of FRT conditions—indicated by a Boolean $FLAG_{fault}$—the reference policy changes: the active positive-sequence component is frozen, and reactive positive- and active negative-sequence currents are commanded based on voltage sag conditions using IEEE 2800-consistent k-factor logic [93]. A selector block chooses between normal-mode and FRT-mode reference currents, while a current-limiting stage enforces

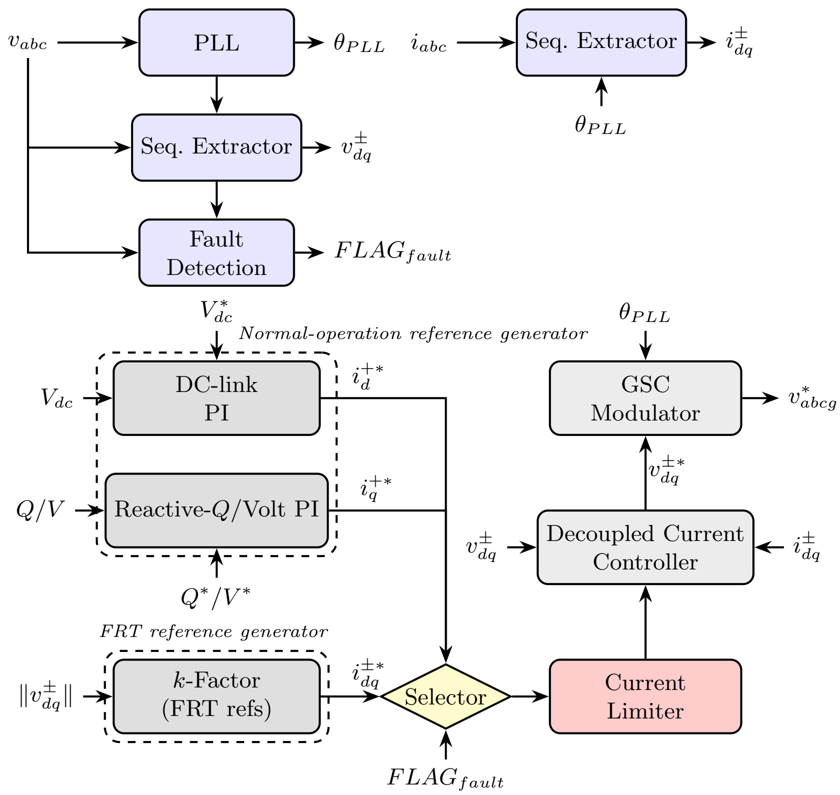

Figure 3.8: Positive-/negative-sequence GSC control with automatic switching of current references.

per-sequence magnitude constraints consistent with prioritization rules. Final control action is carried out by fully decoupled dq-frame PI current controllers that synthesize the commanded voltage $v_{dq}^{\pm*}$ for the GSC modulator (Fig. 3.8). The inner current-regulation layer is implemented using proportional–integral (PI) controllers, reflecting the most widely adopted structure in commercial grid-side converter designs and enabling direct alignment with prevailing industrial practice.

3.3 Grid Support Features

Figure 3.9 illustrates the supervisory control logic that oversees the MSC and GSC layers to ensure compliance with the mandatory requirements of IEEE Std 2800-2022. This standard establishes performance requirements for IBRs connected to transmission-level networks, and the modeling approach adopted here builds on the generic IEEE 2800-compliant framework presented in [75].. The converter-centric model developed in Sections 3.1.1–3.1.2 integrates all essential control functions required by the standard. A high-level mapping between IEEE 2800 clauses.

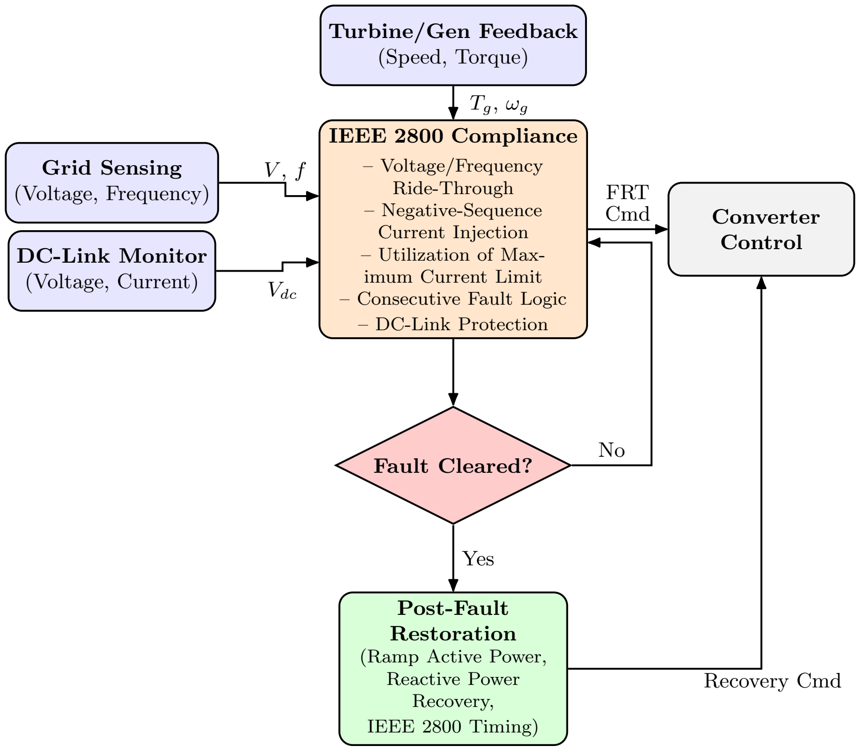

Figure 3.9: IEEE 2800 compliance coordination and post-fault control logic. The logic monitors grid, turbine, and DC-link conditions, manages fault ride-through compliance, and issues appropriate converter control commands based on fault status and restoration requirements.

3.3.1 Voltage Ride-Through (VRT) Logic

Voltage ride-through capability is implemented using a finite-state machine (Fig. 3.10) that monitors the per-phase voltage and transitions between operating states based on the disturbance voltage magnitude and the minimum ride-through duration prescribed in Tables 11 and 12 of Clause 7 of IEEE Std 2800-2022. During a disturbance:

- The model transitions to a RIDE-THROUGH state if the voltage drops below or exceeds the defined thresholds.
- The positive- and negative-sequence current references are adjusted according to the logic described in Section 3.1.2, ensuring compliance with IEEE 2800 injection and priority rules.
- Transient overvoltage events are also handled by incorporating the requirements of Table 13, with tuning of PI controller parameters to shape the voltage support response.

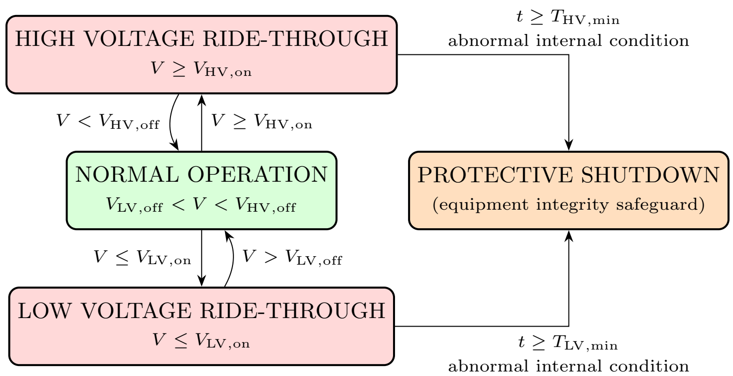

Figure 3.10: Finite-state machine implementing the IEEE 2800 voltage ride-through logic.

- A current limit logic ensures the IBR utilizes its full available current capability per phase during unbalanced conditions, enabling accurate positive and negative sequence current injection as dictated by the ride-through reference generator.

Since IEEE 2800 specifies only the minimum required ride-through times, a protective trip logic is also implemented. This logic monitors critical operating parameters such as DC-link overvoltage and excessive rotational speed to detect abnormal conditions and safeguard the integrity of the IBR hardware.

3.3.2 Frequency Ride-Through and Support

A parallel state machine handles frequency ride-through by monitoring grid frequency offset and rate of change (ROCOF). When frequency deviates from nominal, the model enters a FREQUENCY-SUPPORT mode.

3.3.3 Disturbance Tracking and Setpoint Management

During ride-through events, the pre-disturbance setpoints for active and reactive power are latched. Upon returning to normal grid conditions, the model either ramps back to the original setpoints at a default rate of 10%/s or accepts new commands from the plant-level controller if a significant change is detected—implementing the setpoint freeze/adjust logic described in Annex E, Step 8.

3.4 Wind-Park Reactive-Power Coordination Strategy

The regulation of reactive power at the POI is essential for ensuring grid code compliance, voltage stability, and optimal power system operation in modern wind power plants (WPPs). The centralized Wind Park Controller (WPC) supervises and coordinates the reactive power contribution of individual Wind Turbine Controllers (WTCs), employing a hierarchical voltage control strategy. Figure 3.11 illustrates the communication and control flow between WPC and WTCs, highlighting the transfer of voltage reference signals.

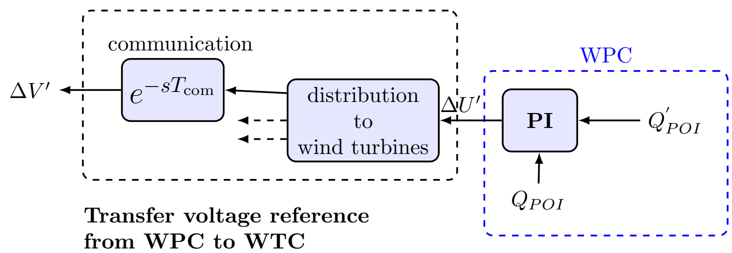

Figure 3.11: Wind Park Reactive Power Control: Communication between WPC and WTCs [1].

3.4.1 Hierarchical Reactive Power Control

Reactive power control in a wind park follows a hierarchical framework:

Primary Control: Local WTC Regulation

Each WTC regulates its positive-sequence terminal voltage V_{wt}^{+} via a proportional voltage regulator to ensure local stability and fast dynamic response. This control is executed independently at the wind turbine level.

Secondary Control: Centralized WPC Supervision

At the wind park level, the WPC monitors the reactive power exchange at POI (Q_{POI}) and adjusts the WTC reference voltage (V') via a proportional-integral (PI) reactive power regulator. The WPC computes the required voltage correction and distributes it to individual WTCs, ensuring compliance with grid requirements.

3.4.2 Voltage and Power Factor Control Modes

The WPC operates under different control modes depending on grid requirements:

Voltage Control Mode (V-control) In this mode, the reactive power reference Q'_{POI} is determined using an outer proportional voltage control law:

$$Q_{\text{POI}} = K_{V_{\text{POI}}} \left(V'_{\text{POI}} - V^{+}_{\text{POI}} \right) \tag{3.11}$$

where:

- V^{+}_{POI} is the positive-sequence voltage at POI.
- $K_{V_{\text{POI}}}$ is the WPC voltage regulator gain.

Power Factor Control Mode (PF-control) Alternatively, when the WPC operates under power factor control, the reactive power reference Q'_{POI} is determined based on the active power at POI:

$$Q'_{\text{POI}} = f(P_{\text{POI}}, pf_{\text{POI}}) \tag{3.12}$$

where:

- P_{POI} is the active power at POI.
- pf_{POI} is the desired power factor.

3.4.3 Fault Handling and Voltage Sag Response

During grid disturbances such as voltage sags at POI, it is crucial to stabilize the reactive power reference to prevent excessive fluctuations. The PI controller inside the WPC ensures smooth operation by keeping the output correction term ($\Delta U'$) constant, effectively blocking rapid changes in $(Q'_{\text{POI}} - Q_{\text{POI}})$. This prevents overvoltage following fault clearance and ensures system stability.

3.5 Model Evaluation

To validate the IEEE Std 2800-compliant wind park model, an EMT simulation was performed to evaluate its FRT and voltage regulation capabilities.

A detailed FSC wind turbine plant model was developed in PSCAD as described in this paper. A representative single inverter unit rated at 5 MVA was modeled to capture the plant-level dynamics. The inverter output is connected to a 0.69 kV/33 kV delta/wye transformer, which steps up the voltage to the medium-voltage plant collection level. A scaling factor of $N = 60$ was applied to represent the aggregate response of the entire wind plant. Finally, a 33 kV/138 kV wye/wye transformer interfaces the plant with the transmission grid. We present two representative use cases to demonstrate the performance of the converter model under IEEE Std 2800-2022 compliance: (1) steady-state power ramp and (2) asymmetrical fault response.

Steady-State Power Ramp

In the first case, the converter operates under nominal grid conditions and ramps up its active power from 0 MW to 250 MW over a duration of approximately 1.5 seconds. Figure 3.12 shows the simulated quantities at the POI. The top subplot shows the RMS line-to-line voltage at the POI, which remains stable at approximately 33.5 kV throughout the ramp.

The second subplot shows the wind turbine rotor speed ω_g and the DC-link voltage E_{dc}, both of which exhibit smooth and stable behavior during the ramp-up. The third subplot shows the line currents at the converter terminal, increasing proportionally with active power output, with all three phases remaining balanced.

Finally, the bottom subplot displays the real (P) and reactive (Q) power output of the plant. Active power increases steadily to the 250 MW target, while reactive power is regulated near zero, maintaining unity power factor as required under normal operation.

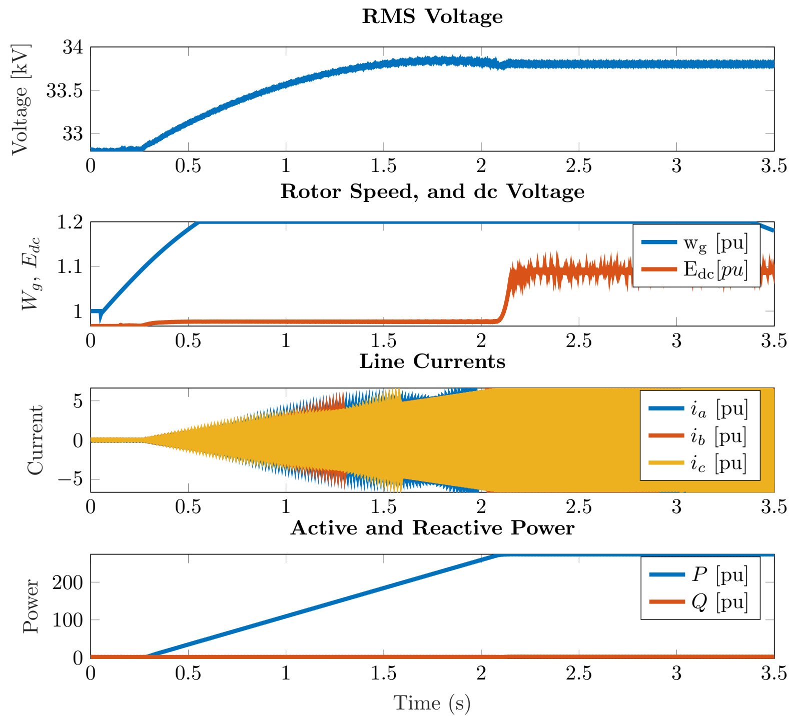

Figure 3.12: Steady-state operation showing POI voltage, rotor speed, DC voltage, converter terminal currents, and power output during an active power ramp.

Asymmetrical Fault Response

In the second case, a line-to-line (BC) fault is applied at the 33 kV collector bus at $t = 0.2$ s and cleared at $t = 0.4$ s. The converter is required to remain connected and provide fault ride-through support during the event.

Figure 3.13 shows the positive- and negative-sequence current magnitudes and angles during this disturbance. The top subplot illustrates the current magnitudes. Upon fault inception, the positive-sequence current $|i^+|$ sharply decreases, and the negative-sequence current $|i^-|$ rises in response to the voltage unbalance, consistent with IEEE 2800 sequence injection requirements. Both currents return to their pre-fault levels within four cycles after fault clearance, meeting the performance requirements for FRT specified in Clause 7 of IEEE Std 2800. The bottom subplot shows the current angles. Both the positive, and negative sequence angles $\angle i^{\pm}$ remains mostly stable, during fault. These behaviors confirm correct implementation of current prioritization logic and voltage ride-through performance as specified in Clauses 5.4.2, 5.4.3, and 5.5 of IEEE Std 2800-2022.

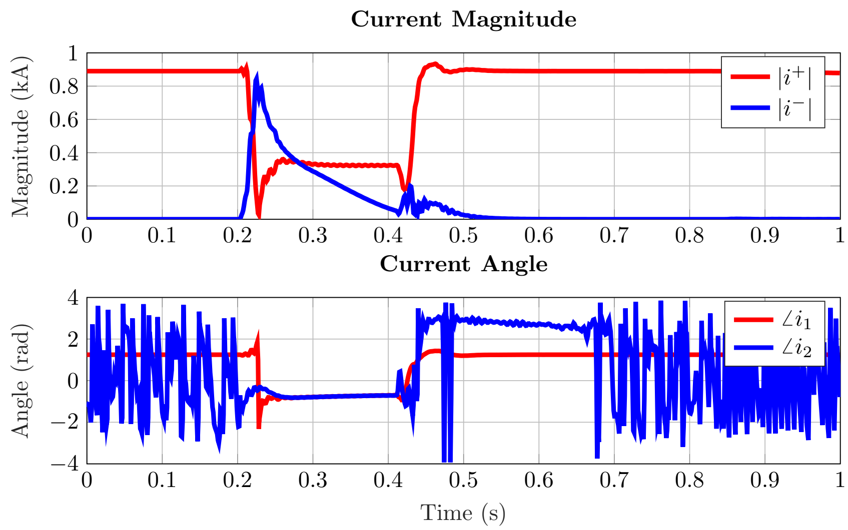

Figure 3.13: Converter output current magnitudes and angles during a BC fault at the 33 kV collector bus (fault applied at $t = 0.2$ s, cleared at $t = 0.4$ s).

Chapter 4

Analysis of IBR Fault Response– Part I: Subsystem-Level Temporal Behavior (Saturation Phase)

4.1 Introduction

Large-scale deployment of IBRs—including wind, solar PV, and battery systems—has fundamentally altered fault dynamics in power systems, replacing the predictable subtransient behavior of synchronous machines with fast, nonlinear control responses [52]. Modern interconnection standards require IBRs to remain connected during grid faults, with IEEE Std 2800-2022 mandating full reactive current injection within a few cycles to support transient voltage recovery at the transmission level, while IEEE Std 1547-2018 imposes voltage-support and ride-through requirements at the distribution level [94, 95]. Meeting this requirement in practice is complicated by four interacting nonlinearities that dominate the inverter's initial post-fault response: the always-active current limiter, saturation of the space-vector pulse-width modulation (SVPWM) modulator, saturation of the proportional-integral (PI) current controller, and the abrupt control-mode shift triggered by fault detection and substitution of ride-through setpoints [96–99]. The sequence and overlap of these nonlinearities unfold within a 5–15 ms window and dictate whether the inverter can stay within its current envelope, meet the step-response deadlines set by standards, or risk entering non-compliant or unstable operating modes. In particular, their interaction can momentarily drive fault currents beyond the typical controlled limit of 1.2 pu [100], violating grid-code expectations for well-regulated and predictable IBR responses during faults.

Early investigations into PWM saturation primarily emphasized its impact on harmonic distortion and dc-link utilization, demonstrating that the space-vector modulation (SVM) hexagon enforces a hard circular limit on the achievable $\alpha\beta$ voltage references [101]. Subsequent work by Cheng *et al.* extended the analysis to include inverter stability under PWM saturation, accounting for parameter uncertainty and its influence on system robustness [102]. On the control side, Bottrell *et al.* explored current and voltage limiting strategies in cascaded-loop inverter controllers, highlighting the importance of avoiding limiter latch-up and PI wind-up during fault transients [103]. More recently, Xu *et al.* derived how PI-controller saturation affects the transient behavior of short-circuit current (SCC) in grid-side converters of type-IV wind turbines, directly influencing peak SCC calculations used in protection studies [104]. Despite these contributions, PI and PWM saturation are still often analyzed in isolation, typically in stability-focused studies, with limited attention to their coupled dynamics or their interaction with control-mode shifts during fault ride-through.

Signal-processing research has produced a spectrum of detector latencies. Delayed-signal cancellation (DSC) and zero-cross tracking achieve preliminary sag confirmation in 3–5 ms, followed by a harmonic-filtered value in 10–15 ms [105]. Quadrature DSC refinements report worst-case 3.3 ms detection even with $6h \pm 1$ interharmonics [106]. Fast-amplitude estimation (FAE) yields 3.9–4.0 ms convergence without a phase-locked loop, robust to ± 1 Hz frequency drift [107]. By contrast, detectors that rely on half-cycle discrete Fourier transform (DFT) or PLL-notch filters require 8–20 ms, with the one-cycle window itself forming the dominant delay.

Grid codes indirectly bind detection and control latencies. IEEE 1547-2018 allows up to 0.083 s (Category III) for DERs to react to steep voltage deviations, but IEEE 2800-2022 tightens the step-response clock to ≤ 2.5 cycles ($\approx$ 41.7 ms at 60 Hz) and explicitly counts a one-cycle DFT window against that budget [94, 95]. Consequently, a realistic controller must allocate ~ 25 ms to ramp current, leaving $\lesssim 15$ ms for detection, filtering and qualification.

Despite rich, domain-specific advances, three critical voids remain:

(a) *Lack of a unified timing model.* Analyses of PWM saturation typically assume instantaneous fault detection, neglecting detection delays and their interaction with control saturation dynamics [101, 104]. Conversely, fault-detection algorithms are often studied using simplified, linear inverter models without accounting for saturation effects [105–107].

(b) *Insufficient analysis for PWM saturation duration.* While recent work has characterized PI controller saturation during fault transients [104], similar analysis for PWM saturation remains largely unexplored.

(c) *Limited validation at utility scale.* Most studies rely on $\leq$10 kVA laboratory testbeds or simulation-only setups. Experimental validation using commercial utility-scale inverters—where dc-link voltage dynamics, filter resonance, and digital signal processor (DSP) execution schedules affect the millisecond response—is scarce. Furthermore, few report time-resolved results at microsecond-level resolution [103].

In short, the literature still lacks an integrated, experimentally validated framework that (*i*) predicts the concurrent durations of PWM and PI saturation under realistic grid faults, and (*ii*) allocates the remaining millisecond budget to detection latency so that IBRs can meet the strictest ride-through clauses of modern standards.

This section bridges that gap by analyzing nonlinear saturation dynamics and detection latency jointly in grid-following IBRs. The specific contributions are:

(i) Derivation of an analytical expression for the PWM-clamp duration Δt_{PWM} as a function of the current-loop time constant τ_c and the initial overshoot ratio R_{v0}.

(ii) Closed-form characterization of the PI-clamp duration Δt_{PI} that incorporates proportional, integral, and anti-windup control parameters.

(iii) Development of an end-to-end timing budget framework that couples Δt_{PWM}, Δt_{PI}, and the detection delay $\Delta t_{\mathrm{detect}}$, yielding an upper bound of ≤ 15 ms for detection latency to comply with the 2.5-cycle response requirement in IEEE Std 2800-2022.

(iv) Validation through both EMT simulations of a detailed inverter model and experimental testing on a commercial 21 kW grid-following inverter, capturing real-world control and hardware interactions.

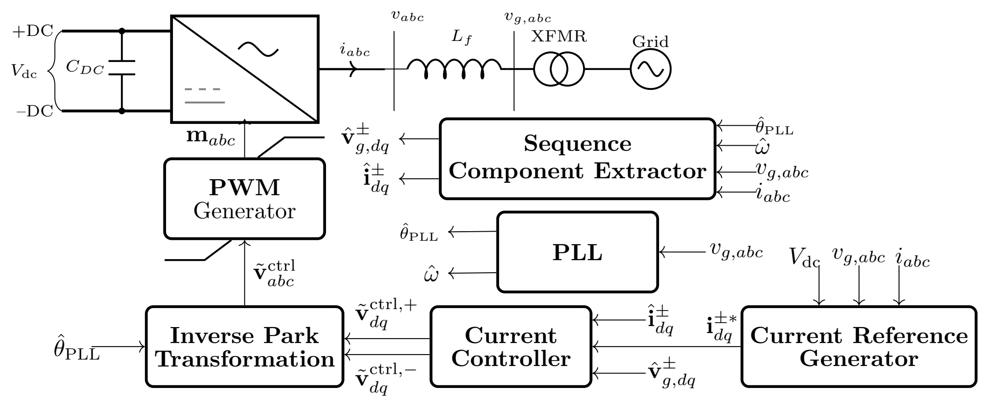

Figure 4.1: Control architecture for a grid-tied inverter. Internal signals with hats denote estimated quantities derived from PLL angle and sequence extraction.

Section 4.2 reviews the inverter control architecture and its response path. Section 4.3 introduces the key nonlinear saturation mechanisms. Section 4.3.1 derives an analytical expression for the PWM-clamp duration, while Section 4.3.2 develops a closed-form model for the PI-clamp. Section 4.3.3 surveys state-of-the-art fault detection methods and quantifies their timing contributions. Section 5.5 presents both EMT simulation results and hardware validation using a commercial inverter.

4.2 IBR Dynamics During Fault

Figure 4.1 illustrates the grid-following control architecture that forms the basis for the subsequent analysis. Signals measured at the inverter terminals, i_{abc} and $v_{g,abc}$, are transformed into synchronous reference frames using the PLL angle and a sequence extraction algorithm, producing the estimated positive- and negative-sequence quantities $\hat{\mathbf{i}}^{\pm}_{dq}$ and $\hat{\mathbf{v}}^{\pm}_{g,dq}$. These estimated variables drive the control system and are distinguished from the physical plant variables by the hat notation.

The reference-generation layer produces synchronous-frame current commands $\mathbf{i}^{*\sigma}_{dq} = [\, i^{*\sigma}_d,\, i^{*\sigma}_q \,]^{\mathsf{T}}$ for each sequence $\sigma \in \{+, -\}$, subject to the circular current rating

$$\|\mathbf{i}^{*}_{dq}\| \leq I_{\max}. \tag{4.1}$$

Under normal conditions, the positive-sequence d-axis reference regulates active power (typically via MPPT), while the q-axis controls reactive power or terminal voltage. Negative-sequence references are normally zero in balanced steady state.

Following a voltage sag, the controller transitions into reactive-priority LVRT mode, freezing the active current component $i_d^{*+} \to 0$ and commanding increased reactive current $i_q^{*+} > 0$, while optionally enabling negative-sequence current injection to satisfy IEEE 2800 ride-through and unbalance-support requirements.

Each sequence is regulated by an identical PI current controller,

$$\mathbf{v}_c^{\sigma}(s) = \Big(K_p + \frac{K_i}{s}\Big)\big(\mathbf{i}_{dq}^{*\sigma} - \hat{\mathbf{i}}_{dq}^{\sigma}\big), \qquad K_p, K_i > 0. \tag{4.2}$$

Because the negative sequence rotates opposite to the PLL reference frame, its cross-coupling term enters with opposite sign. Including feedforward of the estimated grid voltage, the controller-generated voltage commands are

$$\begin{aligned} \tilde{\mathbf{v}}_{dq}^{\text{ctrl},+} &= \mathbf{v}_c^{+} + \omega L_f \mathbf{J}\hat{\mathbf{i}}_{dq}^{+} + \hat{\mathbf{v}}_{g,dq}^{+}, \\ \tilde{\mathbf{v}}_{dq}^{\text{ctrl},-} &= \mathbf{v}_c^{-} - \omega L_f \mathbf{J}\hat{\mathbf{i}}_{dq}^{-} + \hat{\mathbf{v}}_{g,dq}^{-}, \end{aligned} \tag{4.3}$$

where $\mathbf{J} = \begin{bmatrix} 0 & -1 \\ 1 & 0 \end{bmatrix}$ implements the synchronous cross-coupling.

The positive- and negative-sequence control voltages superimpose in the phase domain. The total commanded inverter terminal voltage in the abc frame is therefore

$$\tilde{\mathbf{v}}_{abc}^{\text{ctrl}} = \text{Park}^{-1}\{\tilde{\mathbf{v}}_{dq}^{\text{ctrl},+}\} + \text{Park}^{-1}\{\tilde{\mathbf{v}}_{dq}^{\text{ctrl},-}\}. \tag{4.4}$$

This voltage request is normalized by the dc-link voltage and mapped to PWM duty cycles,

$$\mathbf{m}_{abc} = \frac{2}{V_{\text{dc}}}\,\tilde{\mathbf{v}}_{abc}^{\text{ctrl}}. \tag{4.5}$$

where $\mathbf{m}_{abc} = [m_a, m_b, m_c]^\mathsf{T}$. When the modulation remains in its linear region ($|m_{a,b,c}| < 1$), the inverter behaves approximately as a linear voltage source and the realized synchronous-frame voltage is

$$\mathbf{v}_{dq} = G_{\text{PWM}}\,\tilde{\mathbf{v}}_{dq}^{\text{ctrl}}, \qquad G_{\text{PWM}} = \frac{V_{\text{dc}}}{2V_{\text{base}}}.$$

The L_f–R_f filter dynamics for each sequence are therefore

$$L_f \dot{\mathbf{i}}_{dq}^{+} + R_f \mathbf{i}_{dq}^{+} = G_{\text{PWM}} \tilde{\mathbf{v}}_{dq}^{\text{ctrl},+} - \mathbf{v}_{g,dq}^{+}, \tag{4.6a}$$

$$L_f \dot{\mathbf{i}}_{dq}^{-} + R_f \mathbf{i}_{dq}^{-} = G_{\text{PWM}} \tilde{\mathbf{v}}_{dq}^{\text{ctrl},-} - \mathbf{v}_{g,dq}^{-}. \tag{4.6b}$$

In the remainder of this chapter, analysis is restricted to positive-sequence dynamics. For notational simplicity, all variables are therefore understood to be positive-sequence quantities unless explicitly stated otherwise, and the superscript "$+$" is omitted.

Two independent nonlinear constraints limit the commanded voltage. First, the controller saturation bound M restricts the PI output; once reached, the integrator is frozen to prevent wind-up, yielding an effectively open-loop RL current response. Second, the dc-link constraint $V_{\max}$ applies whenever

$$\|\tilde{\mathbf{v}}_{dq}^{\text{ctrl}}\| > V_{\max}, \tag{4.7}$$

in which case the PWM stage clips the voltage vector to the circle of radius $V_{\max}$, corresponding to the maximum achievable inverter phase voltage.

4.3 Inverter Saturation and Fault Detection Timing: Mechanisms and Interactions

Figure 4.2 presents a simplified view of the control path of an grid-following inverter, emphasizing the two key nonlinearities—the PI controller and the SV-PWM modulator—whose saturation governs the inverter's initial transient response during grid faults. Whenever a fault forces either bound to engage the usual closed-loop path is broken, the filter sees an effectively open-loop

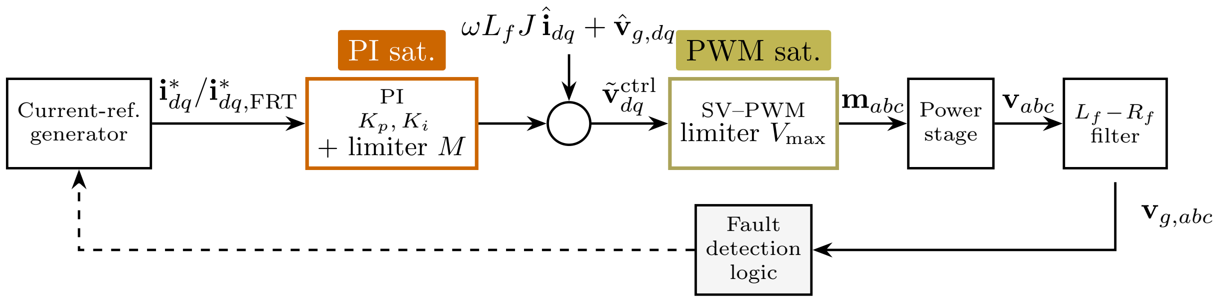

Figure 4.2: Simplified control path of a grid-tied inverter, highlighting the two key saturation points—PI-controller limit M and SV-PWM dc-link limit $V_{\max}$. When either bound is hit, the loop enters a nonlinear open-loop interval that dominates the initial fault response.

voltage, and the response is governed by the RL plant until the commanded vector re-enters both limits.

4.3.1 PWM Saturation: Entry and Duration

During steady-state operation each leg of the three-phase bridge behaves almost linearly: the instantaneous phase voltages are the dc- link half-bus scaled by the duty-ratio vector,

$$\mathbf{v}_{abc}(t) = \tfrac{V_{\mathrm{dc}}}{2}\,\mathbf{m}_{abc}(t), \qquad \mathbf{m}_{abc}(t) \in [-1,1]^3. \tag{4.8}$$

If the controller produces the reference $\tilde{\mathbf{v}}^{\mathrm{ctrl}}_{abc}$ and the duty ratio is well inside its limits ($|m_{a,b,c}| < 1$), the bridge looks like a constant small-signal gain,

$$\mathbf{v}_{abc}(t) = G_{\mathrm{PWM}}\,\tilde{\mathbf{v}}^{\mathrm{ctrl}}_{abc}(t), \qquad G_{\mathrm{PWM}} = \frac{V_{\mathrm{dc}}}{2V_{\mathrm{base}}}.$$

The dc-link voltage caps the maximum line-to-neutral amplitude:

$$v_{\mathrm{abc,max}} \approx \tfrac{V_{\mathrm{dc}}}{2}\,m_{\max}, \qquad 0 < m_{\max} \le 1. \tag{4.9}$$

In the $\alpha\beta$ (or equivalently the rotating dq) plane this limit is represented by the familiar SVPWM hexagon, conservatively circumscribed by the circle $v_{\alpha\beta,\max} = V_{\mathrm{dc}}/\sqrt{3}$. Hence every admissible voltage command must satisfy

$$\sqrt{v_d^2 + v_q^2} \le V_{\max}, \qquad V_{\max} = v_{\alpha\beta,\max}. \tag{4.10}$$

A deep voltage sag can force the current controller to demand $\|\tilde{\mathbf{v}}_{dq}^{\mathrm{ctrl}}\| > V_{\max}$. When any phase duty ratio hits ± 1 the linear relation breaks and the bridge enters PWM saturation: the requested voltage is projected onto the circular boundary of (4.10),

$$\mathbf{v}_{dq} = G_{\mathrm{PWM}} \cdot \begin{cases} \tilde{\mathbf{v}}_{dq}^{\mathrm{ctrl}}, & \|\tilde{\mathbf{v}}_{dq}^{\mathrm{ctrl}}\| \le V_{\max}, \\ V_{\max} \dfrac{\tilde{\mathbf{v}}_{dq}^{\mathrm{ctrl}}}{\|\tilde{\mathbf{v}}_{dq}^{\mathrm{ctrl}}\|}, & \text{otherwise.} \end{cases} \tag{4.11}$$

as detailed in [101, 102]. This hard clipping distorts the output waveform, decouples the current loop from its reference [102, 103], and initiates the nonlinear PWM-clamp interval.

Duration of PWM Saturation During Faults

During a PWM clamp the modulator replaces the unconstrained request $\tilde{\mathbf{v}}_{dq}^{\mathrm{ctrl}}$ with a fixed vector on the dc-link boundary,

$$\tilde{\mathbf{v}}_{dq}^{\mathrm{sat}} = V_{\max}\, \mathbf{e}_v, \qquad \mathbf{e}_v := \frac{\tilde{\mathbf{v}}_{dq}^{\mathrm{ctrl}}}{\|\tilde{\mathbf{v}}_{dq}^{\mathrm{ctrl}}\|}. \tag{4.12}$$

At that instant the actuator is saturated, and modern DSP firmware engages anti-wind-up protection:

(a) *Conditional integration:* the integrator input is forced to zero while the saturation flag is set; or

(b) *Back-calculation:* $\dot{C}_I = k_{\mathrm{bc}}\big(\tilde{\mathbf{v}}_{dq}^{\mathrm{ctrl}} - \mathbf{v}_{dq}^{\mathrm{sat}}\big)$, where C_I is the frozen integrator state.

Both schemes guarantee $\dot{C}_I \approx 0$ throughout the clamp interval [103], so the integral state may be treated as a constant bias $C_I = C_I(t_0)$. Even if anti–wind-up were disabled, the integrator could increase only by the area under its current-error input

$$\Delta \mathbf{C}_I \;=\; \int_{t_0}^{t_0+\Delta t} K_i\, \mathbf{e}_i(\tau)\, d\tau, \qquad \mathbf{e}_i := \mathbf{i}^*_{dq} - \mathbf{i}_{dq}. \tag{4.13}$$

The drift is bounded by $\|\Delta \mathbf{C}_I\| \;\leq\; K_i\, I_{\max}\, \Delta t$. The worst-case drift over a few-millisecond clamp would be an order of magnitude smaller than the voltage error caused by the dc-link clamp itself, and is therefore negligible. The total output feeding the modulator is the sum of the feed-forward term $\mathbf{v}_{\text{ff}} = \omega_s L_f \mathbf{J}\, \mathbf{i}_{dq} + \mathbf{v}_{g,dq}$, where $\mathbf{J} = \left[\begin{smallmatrix} 0 & -1 \\ 1 & 0 \end{smallmatrix}\right]$ is the 90° rotation matrix $[x,\, y]^\mathsf{T} \mapsto [-y,\, x]^\mathsf{T}$, and the regulator signal $K_p(\mathbf{i}^*_{dq} - \mathbf{i}_{dq}) + C_I$. During a fault the PCC voltage collapses to its new (faulted) value within a fraction of a cycle; if no further network events occur this vector remains practically unchanged for the next few milliseconds. Over the same short interval window the fundamental envelope of the filter current, $\mathbf{i}_{dq}(t)$, is still dictated by the RL pole $\tau_c = L_f/R_f$ (2-10 ms). Hence the *average* change of $\mathbf{i}_{dq}$ during a typical PWM-clamp window (<5 ms) is modest and its phasor merely rotates with the (almost constant) synchronous speed ω. Instantaneously, however, the full–bus step $\mathbf{v}^{\text{sat}}_{dq} = V_{\max} \mathbf{e}_v$ imposed by the clamp drives a large $\dot{\mathbf{i}}_{dq} = (\mathbf{v}^{\text{sat}}_{dq} - \mathbf{v}_{g,dq} - R_f \mathbf{i}_{dq})/L_f$, so phase currents can overshoot $I_{\max}$ and acquire harmonic side–bands even though the slowly varying feed-forward term $\omega_s L_f \mathbf{J} \mathbf{i}_{dq}$ can be regarded as quasi-constant for the analytical duration estimate. After subtracting this fixed bias, the part of the command that does evolve is therefore governed by the proportional path alone:

$$\tilde{\mathbf{v}}^{\text{ctrl}}_{dq}(t) \;=\; \underbrace{\mathbf{v}_{\text{ff}}(t_0)}_{\text{nearly constant}} \;+ K_p\big(\mathbf{i}^*_{dq} - \mathbf{i}_{dq}(t)\big) \;+\; C_I, \tag{4.14}$$

On the L_f–R_f filter side of the converter, PWM saturation fixes the d-axis terminal voltage at the clamp value $G_{\text{PWM}} V_{\max} e_{v,d}$, whereas the grid component $v_{g,d}$ has already collapsed to its faulted level. The net drive $\big(G_{\text{PWM}} V_{\max} e_{v,d} - v_{g,d}\big)$ is therefore much larger than the cross–coupling contribution $\omega L_f i_q$. Quantitatively $|G_{\text{PWM}} V_{\max} e_{v,d} - v_{g,d}| \;\gg\; \omega L_f |i_q|$, so the inductive coupling alters the right–hand side of the d-axis equation in (4.3) by only a few percent during the PWM clamp. Neglecting it yields a close approximation envelope for $i_d(t)$ while greatly simplifies the derivation of the clamp duration:

$$L_f \frac{di_d}{dt} = G_{\text{PWM}} V_{\max} e_{v,d} - v_{g,d} - R_f i_d, \tag{4.15}$$

whose solution is

$$i_d(t) = i_{d,\infty} + \left[i_d(t_0) - i_{d,\infty}\right] e^{-(t-t_0)/\tau_c}, \qquad \tau_c = \frac{L_f}{R_f}, \tag{4.16}$$

$$i_{d,\infty} = \frac{G_{\text{PWM}} V_{\max} e_{v,d} - v_{g,d}}{R_f}.$$

Because $\tilde{v}_d^{\text{ctrl}}$ in (4.14) is proportional to $i_d^* - i_d$, it inherits the same exponential factor, yielding

$$\tilde{v}_d^{\text{ctrl}}(t) = \tilde{v}_d^{\text{ctrl}}(t_0)\; e^{-(t-t_0)/\tau_c}, \quad \tau_c = L_f/R_f. \tag{4.17}$$

Similar analysis can be done for $\tilde{v}_q^{\text{ctrl}}(t)$. Once $\tilde{v}_{dq}^{\text{ctrl}}(t)$ decays below $V_{\max}$ at $t = t_{\text{PWM}}$, the clamp is lifted. Substituting this into the saturation condition, the saturation exit time t_{unsat} is estimated by solving:

$$\sqrt{\left(\tilde{v}_d^{\text{ctrl}}(t_0) \cdot e^{-(t-t_0)/\tau_c}\right)^2 + (\tilde{v}_q^{\text{ctrl}}(t_0) \cdot e^{-(t-t_0)/\tau_c})^2} = V_{\max}, \tag{4.18}$$

or equivalently:

$$\sqrt{(\tilde{v}_d^{\text{ctrl}}(t_0))^2 + (\tilde{v}_q^{\text{ctrl}}(t_0))^2} \cdot \exp\left(-\frac{t-t_0}{\tau_c}\right) = V_{\max}. \tag{4.19}$$

Solving for $t - t_0 = \Delta t_{\text{PWM}}$, we obtain:

$$\Delta t_{\text{PWM}} = \tau_c \cdot \ln\left(\frac{\sqrt{(\tilde{v}_d^{\text{ctrl}}(t_0))^2 + (\tilde{v}_q^{\text{ctrl}}(t_0))^2}}{V_{\max}}\right). \tag{4.20}$$

Figure 4.3 plots the analytical relation

$$\begin{aligned} \Delta t_{\mathrm{PWM}} = \tau_c \ln\Big(1 + R_{v0}\Big), \qquad \tau_c = L_f/R_f, \\ R_{v0} = \frac{\|\tilde{\mathbf{v}}^{ctrl}_{dq}(t_0)\|}{V_{\max}} - 1, \end{aligned} \tag{4.21}$$

as a function of the two governing parameters: the current-loop time-constant τ_c and the initial overshoot ratio R_{v0}. The surface reveals two complementary trends. First, for a fixed time-constant, every additional 10% of overshoot adds roughly 2-3 ms of clamping; e.g. increasing R_{v0} from 5% to 40% at τ_c =20 ms stretches Δt_{PWM} from about 1 ms to 10 ms. Second, for a fixed overshoot the duration scales nearly linearly with τ_c; with a 20% overshoot, a fast loop (τ_c =10 ms) yields a 3 ms clamp, whereas a slower loop (τ_c =30 ms) prolongs it to about 9 ms. Over the range typical of utility converters (τ_c =2-10 ms and R_{v0} =5-60%), the analytical map predicts Δt_{PWM} between 1 and 5 ms.

Initial voltage command and sources of overshoot.

Immediately after the dip, but before any PWM saturation, ($t = t_0 \approx t^+_{\mathrm{fault}}$), the inner current loop constructs its voltage command from three additive terms[3]

$$\begin{aligned} \tilde{\mathbf{v}}^{\mathrm{ctrl}}_{dq}(t_0) = \underbrace{\hat{\mathbf{v}}_{g,dq,f}}_{\substack{\text{measured}\\ \text{PCC voltage}}} + \underbrace{\omega_s L_f\, \mathbf{J}\, \mathbf{i}_{dq,0}}_{\text{inductive drop}} \\ + \underbrace{K_p\Big(\mathbf{i}^*_{dq,0} - \mathbf{i}_{dq,0}\Big) + K_i \int_{t_0}^{t} \Big(\mathbf{i}^*_{dq} - \mathbf{i}_{dq}\Big)\, d\tau}_{\approx 0 \text{ at } t=t_0}, \end{aligned} \tag{4.22}$$

where

[3]**Feed-forward term and time-scale separation.** When $\tilde{\mathbf{v}}^{\mathrm{ctrl}}_{dq}(t_0)$ is evaluated to test whether PWM saturation is *triggered*, the feed-forward voltage $\mathbf{v}_{\mathrm{ff}}(t_0) = \hat{\mathbf{v}}_{g,dq,f}(t_0) + \omega_s L_f \mathbf{J}\mathbf{i}_{dq,0}$ must retain the instantaneous PLL-tracking error; This lagged voltage estimate can overshoot the true PCC voltage by several-tens-of-percent, driving the commanded vector beyond the SVPWM circle at the instant of the fault. During the ensuing clamp the PLL error and the impedance drops decay with the comparatively slow poles $\sigma_{\mathrm{PLL}} \approx 5 - 10$ ms^{-1} and $\tau_c^{-1} = (R_f/L_f) \approx 0.5 - 10$ ms^{-1} [108]. Because the PWM-clamp interval itself lasts only a few milliseconds, $\mathbf{v}_{\mathrm{ff}}(t)$ is effectively constant over that window, justifying the simpler relaxation model of (4.14). Should the faulted grid voltage later experience large secondary changes (e.g. auto-reclosing), $\mathbf{v}_{\mathrm{ff}}(t)$ may shift again and a new PWM-saturation episode would begin—behaviour that is beyond the single-pulse analysis developed here.

- $\hat{\mathbf{v}}_{g,dq,f} = H_{\mathrm{PLL}}(s)\,\mathbf{v}_{g,dq,f}$ is the PCC voltage after ADC sampling, Clarke–Park transformation and PLL filtering. Because the PLL retains memory of the pre-fault magnitude [109], $\|\hat{\mathbf{v}}_{g,dq,f}\| \gtrsim \|\mathbf{v}_{g,dq,f}\|$ immediately after the dip.

- $\mathbf{i}^*_{dq,0}$ is the pre-fault current reference, and $\mathbf{i}_{dq,0} = \mathbf{i}_{dq}(t_0^-) \simeq \mathbf{i}^*_{dq,0}$ is the measured current just before the dip. Because the $L_f - R_f$ filter prevents an instantaneous change in current, the difference $\mathbf{i}^*_{dq,0} - \mathbf{i}_{dq,0}$ is essentially zero, so the proportional jump $K_p(\mathbf{i}^*_{dq,0} - \mathbf{i}_{dq,0})$ can be neglected at t_0.

- The remaining term is the instantaneous inductive drop $\omega_s L_f \mathbf{J}\mathbf{i}_0$.

Hence the initial overshoot arises from the sum of the lag-biased voltage estimate $\hat{\mathbf{v}}_{g,dq,f}$ and the filter-impedance drops. Taking the norm of (4.22) and normalising by the dc-link circle radius $V_{\max} = V_{\mathrm{dc}}/\sqrt{3}$ yields the dimensionless overshoot

$$R_{v0} = \frac{\left\|\hat{\mathbf{v}}_{g,dq,f} + \omega_s L_f \mathbf{J}\mathbf{i}^*_{dq,0}\right\|}{V_{\max}} - 1, \tag{4.23}$$

which depends on two physically separate contributions:

- *PLL memory bias,* $\hat{\mathbf{v}}_{g,dq,f}$. Right after the dip the PLL has not yet settled, so $\|\hat{\mathbf{v}}_{g,dq,f}\| > \|\mathbf{v}_{g,dq,f}\|$; a faster PLL (larger ω_{PLL}) therefore *reduces* R_{v0}.

- *Inductive drop,* $\omega_s L_f \mathbf{J}\mathbf{i}^*_{dq,0}$. Its magnitude scales with both the pre-fault current $\|\mathbf{i}^*_0\|$ and the filter inductance L_f; increasing either raises R_{v0}.

Accordingly, R_{v0} grows with (*i*) deeper voltage sags (smaller $\|\mathbf{v}_{g,dq,f}\|$), (*ii*) higher pre-fault current magnitudes, or (*iii*) a larger filter inductance L_f. Because the PWM-clamp duration satisfies $\Delta t_{\mathrm{PWM}} \propto \ln\bigl(1 + R_{v0}\bigr)$, each of these factors lengthens the saturation window predicted by Fig. 4.3.

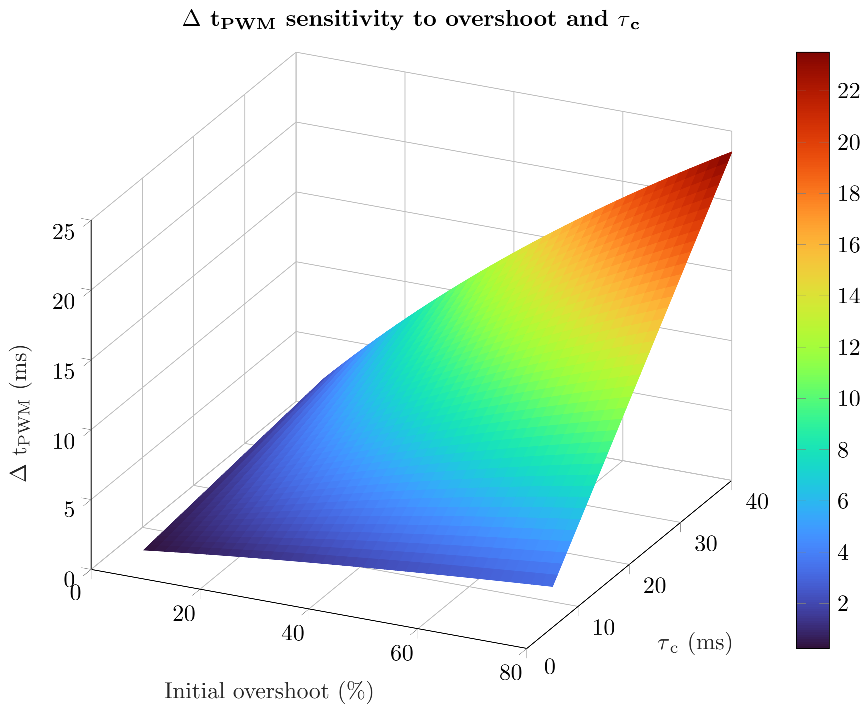

Figure 4.3: Analytical duration of the PWM clamp, Δt_{PWM}, versus initial overshoot ratio R_{v0} and current-loop time-constant τ_c.

4.3.2 PI Controller Saturation: Entry, and Duration

While PWM saturation arises due to the physical voltage limits imposed by the inverter's DC-link, PI controller saturation results from the internal limits of the control system itself. The current control loop computes voltage commands based on the difference between the reference current and the measured current. However, when this error becomes large—as is the case immediately after a reference current update—the controller output may exceed its configured bounds, initiating what is known as PI controller saturation or clamping.

Entry Conditions for PI Saturation

PI saturation may be triggered at two distinct instants:

(i) *Pre-detection step* $\left(t \approx t_{\text{fault}}^{+}\right)$*:* At the instant the fault occurs, the reference still frozen at its pre-fault value $\mathbf{i}_{dq,0}^{*} = \left[i_{d,0}^{*},\, i_{q,0}^{*}\right]^{\mathsf{T}}$ and the measured current equal to $\mathbf{i}_{dq,0} = \left[i_{d,0},\, i_{q,0}\right]^{\mathsf{T}}$,

$$\Delta i_{d,\text{pre}} = i_{d,0}^{*} - i_{d,0}, \quad \Delta i_{q,\text{pre}} = i_{q,0}^{*} - i_{q,0}. \tag{4.24}$$

The proportional branch delivers the instantaneous voltages

$$v_{dP,\text{pre}} = K_p\, \Delta i_{d,\text{pre}}, \qquad v_{qP,\text{pre}} = K_p\, \Delta i_{q,\text{pre}}, \tag{4.25}$$

while the integral branch is still dormant [104]. PI saturation is triggered as soon as either axis exceeds the controller bound M:

$$|v_{dP,\text{pre}}| > M \;\text{ or }\; |v_{qP,\text{pre}}| > M \;\implies\; \text{PI output frozen.} \tag{4.26}$$

(ii) *Post-detection step* $\left(t = t_{\text{detect}}^{+}\right)$*:* When the fault is confirmed, the ride-through coordinator substitutes a LVRT reference $\mathbf{i}_{dq,\text{FRT}}^{*} = \left[i_{d,\text{FRT}}^{*},\, i_{q,\text{FRT}}^{*}\right]^{\mathsf{T}}$. Hence a second error step occurs:

$$\begin{aligned} \Delta i_{d,\text{post}} &= i_{d,\text{FRT}}^{*} - i_d(t_{\text{detect}}^{-}), \\ \Delta i_{q,\text{post}} &= i_{q,\text{FRT}}^{*} - i_q(t_{\text{detect}}^{-}). \end{aligned} \tag{4.27}$$

The proportional outputs become

$$v_{dP,\text{post}} = K_p\, \Delta i_{d,\text{post}}, \qquad v_{qP,\text{post}} = K_p\, \Delta i_{q,\text{post}}. \tag{4.28}$$

A secondary PI clamp is engaged if either axis overruns the bound M:

$$|v_{dP,\text{post}}| > M \;\text{ or }\; |v_{qP,\text{post}}| > M \;\implies\; \text{PI output frozen,} \tag{4.29}$$

and it remains active until the magnitude of the corresponding current error falls below M/K_p or the integrator unwinds.

Duration of PI Saturation

When the proportional term in either axis exceeds the controller ceiling M,

$$v_{d,\mathrm{PI}}(t) \;=\; -M\;\mathrm{sgn}\big(\Delta i_d\big), \qquad v_{q,\mathrm{PI}}(t) \;=\; -M\;\mathrm{sgn}\big(\Delta i_q\big), \tag{4.30}$$

with $\Delta i_d = i_d^* - i_d,\; \Delta i_q = i_q^* - i_q$, the anti–wind-up logic freezes the integrator state and each clamped axis follows its open-loop $L_f - R_f$ dynamics. Let $\sigma \in \{+,-\}$ denote the sequence channel and $k \in \{d, q\}$ the axis. Adapting the derivation of [104], the clamp duration for each axis/sequence pair is

$$\Delta t^{\sigma}_{\mathrm{PI},k} = \frac{K^{\sigma}_{p,k}\,|\Delta i^{\sigma}_{k}| - M}{K^{\sigma}_{i,k}\,|\Delta i^{\sigma}_{k}| - \dfrac{K^{\sigma}_{p,k}}{L_f}\,M} \qquad (\Delta i^{\sigma}_{k} \neq 0), \tag{4.31}$$

The curves in Fig. 4.4 evaluate (4.31) for the positive-sequence d-axis ($k = d,\;\; \sigma = +$) of a representative utility-scale converter[4] with a PI ceiling of $M = 0.9$ pu. Five current-loop tunings are compared by sweeping the design time-constant $\tau_c = L_f/K_p \in \{0.5, 1, 2, 3, 5\}$ ms, using the conventional relation $K_i = R_f/\tau_c$. The abscissa is the initial current error $|\Delta i_d^{+}| \in [0.05,\ 1]$ pu; points that violate the positivity condition in (4.31) are omitted.

- *Bandwidth effect.* A larger τ_c (slower loop) lengthens the clamp almost linearly: $\tau_c = 5$ ms keeps the PI saturated for $\approx 4-5$ ms, whereas $\tau_c = 0.5$ ms clears in $0.3-0.5$ ms.

- *Error–size effect.* Along each curve Δt_{PI} decreases as $|\Delta i_d^{+}|$ grows, because a larger step supplies a stronger proportional pull. For the nominal design $\tau_c = 2$ ms the clamp lasts ≈ 1.8 ms at $|\Delta i_d^{+}| = 0.1$ pu but only ≈ 0.4 ms at $|\Delta i_d^{+}| = 0.6$ pu.

---

[4] 690-V, 3-MVA class; $L_f = 1.5$ mH, $R_f = 75$ mΩ.

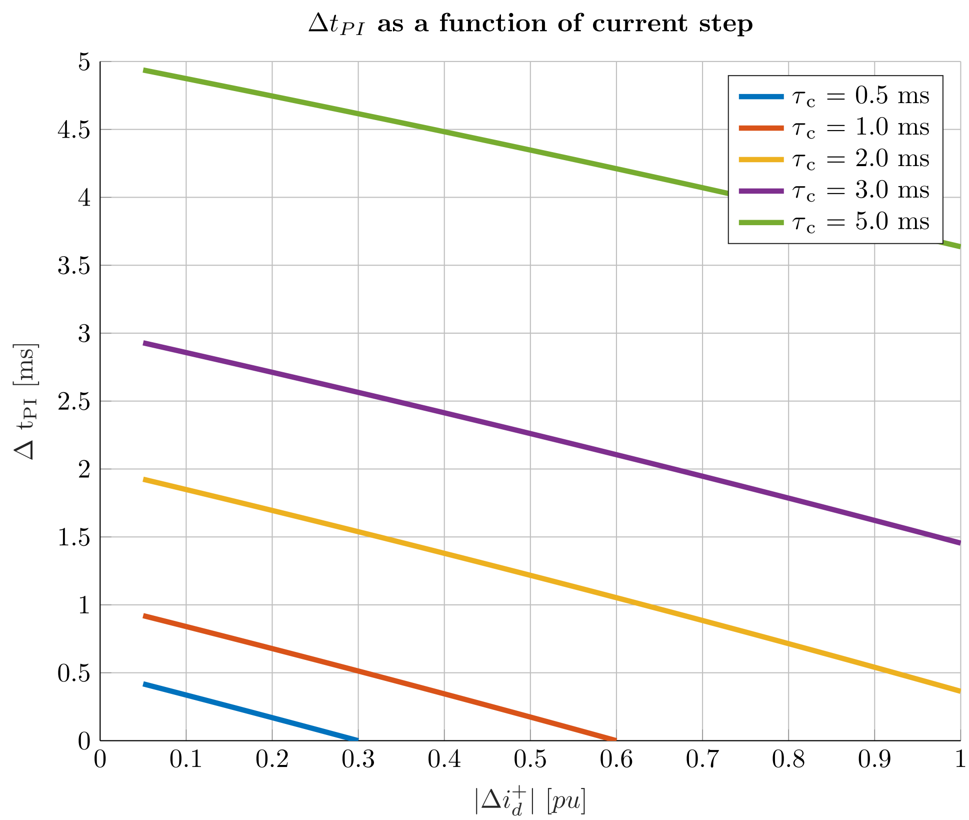

Figure 4.4: Analytical PI–clamp duration Δt_{PI} versus initial current error $|\Delta i_d^+|$ for five current-loop time-constants ($\tau_c = 0.5$–5 ms).

PI saturation is triggered by a sufficiently large current error relative to the chosen gains, whereas PWM saturation depends on the magnitude of the initial voltage overshoot; their practical implications are contrasted in Table 4.1.

4.3.3 Fault–Detection Latency for Ride-Through Transfer

The time between fault inception t_{fault} and the instant the ride-through routine is armed t_{detect} is

$$\Delta t_{\mathrm{detect}} = t_{\mathrm{detect}} - t_{\mathrm{fault}}, \tag{4.32}$$

which defines the pre-detection window in which the current controller still tracks its pre-fault reference.

Intrinsic latency of common detectors

Table 4.1: PI vs. PWM saturation—causes, timing, and dominant factors.

	PI saturation (Δt_{PI})	**PWM saturation** (Δt_{PWM})
Trigger	Current-error step (fault or ref. jump)	$\lVert\tilde{\mathbf{v}}_{dq}^{\mathrm{ctrl}}\rVert > V_{\max}$
Earliest onset	t_{fault}^{+}	t_{fault}^{+}
Second onset	t_{detect}^{+}	–
Exit condition	$\lVert\tilde{\mathbf{v}}_c\rVert \le M$	$\lVert\tilde{\mathbf{v}}_{dq}^{\mathrm{ctrl}}\rVert \le V_{\max}$
Typical duration	0.5–5 ms	1–5 ms
Dominant when	Large $\Delta\mathbf{i}$, high K_i	Deep sag high $V_{\max}/V_g$
Key parameters	$K_p, K_i, M, \lVert\Delta\mathbf{i}\rVert$	$V_{\mathrm{dc}}, L_f, R_f$, SCR

(a) Peak/zero tracking with delayed–signal cancellation issues a preliminary amplitude in 3.5–5 ms and a harmonics-cleansed value in 10–15 ms. [105].

(b) Quadrature Delayed-signal cancellation (DSC) sag detector reaches worst-case detection in $\le$ 3.3 ms while rejecting 6h$\pm$1 harmonics [106].

(c) Fast–amplitude estimation (FAE) for single-phase LVRT converges in 3.9–4.0ms even with THD $\approx$6% and $\pm$1Hz frequency drift [107].

(d) PLL + notch/LPF amplitude extraction (DSOGI-PLL plus 2$^{\mathrm{nd}}$-order notch) typically requires 6–7 ms [106].

(e) Half/full-cycle DFT or RMS windows remain the slowest, 8–20 ms, but need no custom DSP filtering [105].

Additive delay contributors

- *Sensor / ADC* t_{meas}: 0.05-0.5 ms.
- *Digital filtering* t_{filter}: 0.3-2.6 ms (e.g. harmonic DSC adds 2.55 ms).
- *Algorithm run-time* t_{exec}: <0.3 ms on a 150-MHz DSP (FAE benchmark).

- *Qualification / debounce* t_{debounce}: 1-4 ms, grid-code dependent.

Hence

$$\Delta t_{\text{detect}} \approx t_{\text{meas}} + t_{\text{filter}} + t_{\text{alg}} + t_{\text{exec}} + t_{\text{debounce}}. \tag{4.33}$$

Practically this yields $\Delta t_{\text{detect}} \lesssim 5$ ms for DSC-based or FAE schemes, 6-10 ms for PLL–notch implementations, and $\gtrsim 15$ ms when long-window DFT or harmonic-cancellation stages are mandatory. Because modern grid codes (e.g. IEEE 2800) demand the inverter deliver full reactive current within four cycles (66.7 ms at 60 Hz), any additional millisecond of Δt_{detect} proportionally erodes the dynamic current-support margin.

Standards perspective and detection budget IEEE Std 1547-2018 frames latency implicitly: the maximum response time for an inverter to enter its low- or high-voltage ride-through mode is 0.083 s (Category III momentary-cessation band) or 0.16 s (Category II/III voltage-ride-through bands) [95]. IEEE Std 2800-2022 is stricter for transmission-level inverter-based resources: it caps the step response—measured from fault inception to 90 % of the commanded current—at 2.5 cycles ($\approx$ 41.7 ms at 60 Hz) and notes that a one-cycle DFT measurement window (16.7 ms) is already counted in that limit [94, Table 13]. Assuming a typical current-ramp of $\approx$ 25 ms and < 2 ms for control execution, the remainder for detection and qualification is

$$\Delta t_{\text{detect}}^{\max} \;\approx\; 41.7 \text{ ms} - 25 \text{ ms} - 2 \text{ ms} \;\lesssim\; 15 \text{ ms}.$$

Hence, to guarantee compliance with the most demanding clause (IEEE 2800), the detection algorithm—including sensing, filtering and debounce—should complete in $\leq$15 ms.

4.4 Evaluation

EMT simulations and laboratory experiments were conducted to validate the post-fault event sequence and associated timing framework developed in this paper. A detailed Type-IV wind-plant model with fault-ride-through (FRT) functions compliant with IEEE Std 2800 was developed, building on the work in [92]. The inverter connection schematic used in the EMT studies

Table 4.2: Baseline parameters for EMT simulations

Setting	**Description**	**Value**
L_f	Filter inductance	200 µH
R_f	Filter resistance	0.5 mΩ
k	SOGI gain	1
T_i^{PLL}	PLL integral time constant	100
K_p^{PLL}	PLL proportional gain	30
K_1^{FRT}	FRT gain (d to i^+)	1
K_2^{FRT}	FRT gain (d to i^-)	2
K_p^i	d–q current-controller proportional gain	3
K_i^i	d–q current-controller integral gain	0.01
V_{dc}	DC-link voltage set-point	1.5 kV
S_{base}	Apparent power (single inverter)	5.8 MVA
K_p^{dc}	DC-voltage controller proportional gain	4
T_i^{dc}	DC-voltage controller integral time constant	0.02
V_{LVRT}	LVRT threshold	0.9 pu
R_{fault}	Fault resistance	0.01 Ω

is shown in Fig. 4.5. On the DC side, the grid-side converter is supplied by a machine-side converter representing a Type-IV turbine. On the AC side, the inverter feeds a 0.69 kV/33 kV Δ–Y transformer; the secondary voltage is multiplied by a scaling factor N to emulate plant-level power while modeling a single detailed inverter. A 33 kV/138 kV transformer then connects the plant to the transmission grid. Unless otherwise noted in the individual evaluation sections, all EMT cases use the baseline parameters listed in Table 5.2; faults are applied at location F in Fig. 4.5 and the resulting post-fault currents are compared with the analytical predictions.

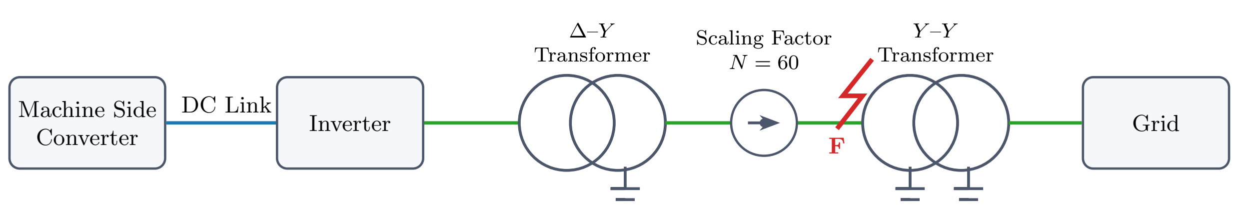

Figure 4.5: Connection schematic of the inverter interfacing a Type-IV wind plant used for EMT simulation-based validation.

4.4.1 PWM Saturation: Evaluation and Validation

The analytical PWM–saturation model (4.3.1–4.3.1) is validated against time–domain simulations by examining (*i*) the entry condition (overshoot) using (4.11)–(4.23), (*ii*) the saturation duration via (4.21), and (*iii*) the validity of the model assumptions (quasi-constant feed-forward, frozen integrator, and negligible cross-coupling) in (4.14)–(4.17). The validation is restricted to stable operating points, i.e., cases without loss of synchronism or sustained oscillations. To capture the main factors that influence overshoot R_{v0} and the current-loop time constant $\tau_c = L_f/R_f$, a structured set of operating points was simulated, as detailed below.

Filter Band-width (τ_c) Sets the Clamp Duration

Figure 4.6 presents results from four EMT simulations in which an A–G fault was applied at location **F** at t =0.0917 s . All simulations used the baseline parameters listed in Table 5.2, except for the filter inductance L_f, which was varied from 175 µH to 300 µH to sweep the electrical time constant $\tau_c = L_f/R_f$. For each case, the inverter three-phase current waveforms and the corresponding modulation indices are shown. The modulation index was constrained to the range [-1, 1]; values clipped at the limits indicate PWM saturation.

As observed in the plots, the duration of PWM saturation increases monotonically with τ_c, in agreement with the analytical prediction $\Delta t_{\mathrm{PWM}} \propto \tau_c$ from (4.21). Specifically, the measured saturation durations were $\Delta t_{\mathrm{PWM}} = \{0, 2.8, 38.4, 91.7\}$ ms for $L_f = \{175, 200, 250, 300\}\,\mu$H, respectively. A similar set of simulations was performed for a B–C fault, and the summary plot in Fig. 4.7 confirms a consistent linear relationship between saturation duration and L_f for both A–G and B–C faults.

Sensitivity to Fault-Inception Angle

To investigate how the fault inception time t_{fault} influences the onset of PWM saturation, we conducted a sweep over t_{fault} within a single fundamental cycle while keeping all other system parameters fixed. The motivation for this test arises directly from the saturation condition in

Eq. (4.11), which states that saturation occurs if the magnitude of the controller-generated voltage vector exceeds the PWM modulation limit: $\|\tilde{\mathbf{v}}_{dq}^{\text{ctrl}}(t_0)\| > V_{\max}$.

The controller voltage reference $\tilde{\mathbf{v}}_{dq}^{\text{ctrl}}(t)$ depends on the instantaneous mismatch between the estimated grid voltage and the inverter current, both of which are sinusoidal in nature and vary continuously over the line cycle. Therefore, even a small change in t_{fault} can significantly alter the initial control response. Specifically, it can either amplify or suppress the transient voltage vector $\tilde{\mathbf{v}}_{dq}^{\text{ctrl}}(t_0)$, determining whether it exceeds $V_{\max}$ and triggers a PWM clamp.

In light of the definition of R_{v0} in Eq. (4.23), which aggregates the initial vector mismatch, we hypothesized that only particular fault-inception angles will result in large enough R_{v0} to cause saturation. These are the angles where the voltage collapse and current mismatch constructively align in the dq frame, maximizing the control action.

Figure 4.8 validates this hypothesis: brief PWM clamps (with $\Delta t_{\text{PWM}} \approx 1.3$ ms) appear only at selective inception times, while most other fault times result in no saturation at all. This selectivity confirms that saturation is not solely a function of system parameters like L_f or R_f, but also of the timing of the fault within the AC waveform—a transient detail often overlooked in traditional fault studies.

Impact of Fault Resistance on PWM Saturation Duration

To further assess the factors influencing PWM saturation, a sweep of the fault resistance R_{fault} was performed while all other parameters were held fixed, except for $K_2^{\text{FRT}} = 0.5$ and SOGI gain $k = 3$. An A–G fault was applied at location **F** at $t = 0.095$ s, and the resulting saturation durations Δt_{PWM} were recorded. Table 4.3 summarizes the observed durations.

These results align with the theoretical expectation that PWM saturation is triggered when the magnitude of the control voltage reference $\|\tilde{\mathbf{v}}_{dq}^{\text{ctrl}}(t_0)\|$ exceeds the hardware-imposed modulation limit $V_{\max}$, as defined by the nonlinear saturation law in (4.11). Smaller fault resistances cause deeper voltage sags at the PCC, increasing the mismatch between the actual and estimated grid voltages. This results in a higher control effort and pushes $\tilde{\mathbf{v}}_{dq}^{\text{ctrl}}$ beyond $V_{\max}$, initiating saturation.

Table 4.3: PWM saturation duration Δt_{PWM} for different fault resistances

Fault Resistance R_{fault} [Ω]	**PWM Clamp Duration** Δt_{PWM} [ms]
0.01	86.06
0.05	84.50
0.08	58.76
0.15	49.66
0.25	35.36

As shown in Table 4.3, the clamp duration Δt_{PWM} decreases significantly as R_{fault} increases, from over 86 ms at $R_{\text{fault}} = 0.01\,\Omega$ to approximately 35 ms at $R_{\text{fault}} = 0.25\,\Omega$. This behavior is consistent with the relationship $\Delta t_{\mathrm{PWM}} \propto \tau_c \left(1 - \frac{V_{\max}}{\|\tilde{\mathbf{v}}_{dq}^{\text{ctrl}}(t_0)\|}\right)$, where fault severity directly influences the magnitude of the initial control overshoot.

These findings highlight the sensitivity of PWM saturation not only to internal control time constants but also to external grid disturbances—particularly the effective fault impedance.

Influence of PLL and SOGI Gains

To decouple control effects from τ_c, L_f is fixed at 200 μH and the PLL proportional gain K_p^{PLL} and SOGI damping k are swept. Fig. 4.9 shows that increasing the PLL bandwidth shortens Δt_{PWM} by at most $\sim$0.8 ms, while changing k leaves the clamp interval essentially unchanged—consistent with the millisecond-scale dominance of τ_c.

Effect of Pre-Fault Current Magnitude Due to Wind Speed Variation

Increasing wind speed elevates the active power output of the wind turbine, thereby raising the pre-fault current magnitude $\|\mathbf{i}_0\|$. This, in turn, amplifies the term $\omega L_f \|\mathbf{i}_0\|$ in the response factor R_{v0}, increasing the likelihood and duration of PWM saturation as predicted by the analytical model.

To examine this effect, EMT simulations were conducted under identical system parameters and fault conditions—an A–G fault with $Z_f = 0.01\,\Omega$—for four wind speeds: $V_w \in \{$ 8, 9, 10, 11$\}$ m/s. The results are summarized in Fig. 4.10. As expected, higher wind speeds generally lead to longer PWM clamp durations due to increased pre-fault current.

However, an exception is observed in the $V_w = 11\,\text{m/s}$ case, where the clamp duration slightly decreases relative to the $V_w = 10\,\text{m/s}$ case. This reduction is attributed to a concurrent drop in the control-generated voltage reference magnitude $\|\tilde{\mathbf{v}}_{dq}^{\text{ctrl}}\|$ at the fault instant t_0. As shown in Fig. 4.12, this voltage term enters the denominator of the PWM saturation condition (4.11) and effectively offsets the impact of the higher current, leading to a shorter clamp duration.

Oscillatory Switching Between Normal and FRT Modes Due to High-Impedance Faults

High-impedance faults can induce nontrivial dynamics in the inverter's ride-through response. In particular, when a fault occurs with moderate resistance (e.g., $R_{\text{fault}} = 1\,\Omega$), the terminal voltage may not fall far below the ride-through threshold, especially once reactive current is injected per FRT logic. This injected reactive current momentarily raises the terminal voltage above the low-voltage threshold, causing the control to switch from fault mode back to normal mode—even though the fault condition physically persists. As the reactive current ceases in normal mode, the terminal voltage drops again, re-triggering fault mode. This back-and-forth toggling leads to an oscillatory behavior.

Figure 4.11 illustrates this behavior by showing the measured terminal RMS voltage used in the FRT detection logic (left y-axis) and the corresponding fault flag (right y-axis). Even though a one-sided hysteresis was implemented in the detection logic to suppress chattering, the inverter enters an oscillatory regime where the voltage fluctuates around the threshold due to the alternating presence and absence of FRT-mode reactive injection. The detection logic repeatedly toggles between normal and FRT modes.

This oscillatory switching has practical implications for the modulation behavior of the inverter. As shown in Fig. 4.13, the inverter modulation index repeatedly enters saturation during this regime, leading to prolonged periods of clamping. The associated phase current becomes highly distorted, evidencing the non-sinusoidal nature of inverter operation under such conditions.

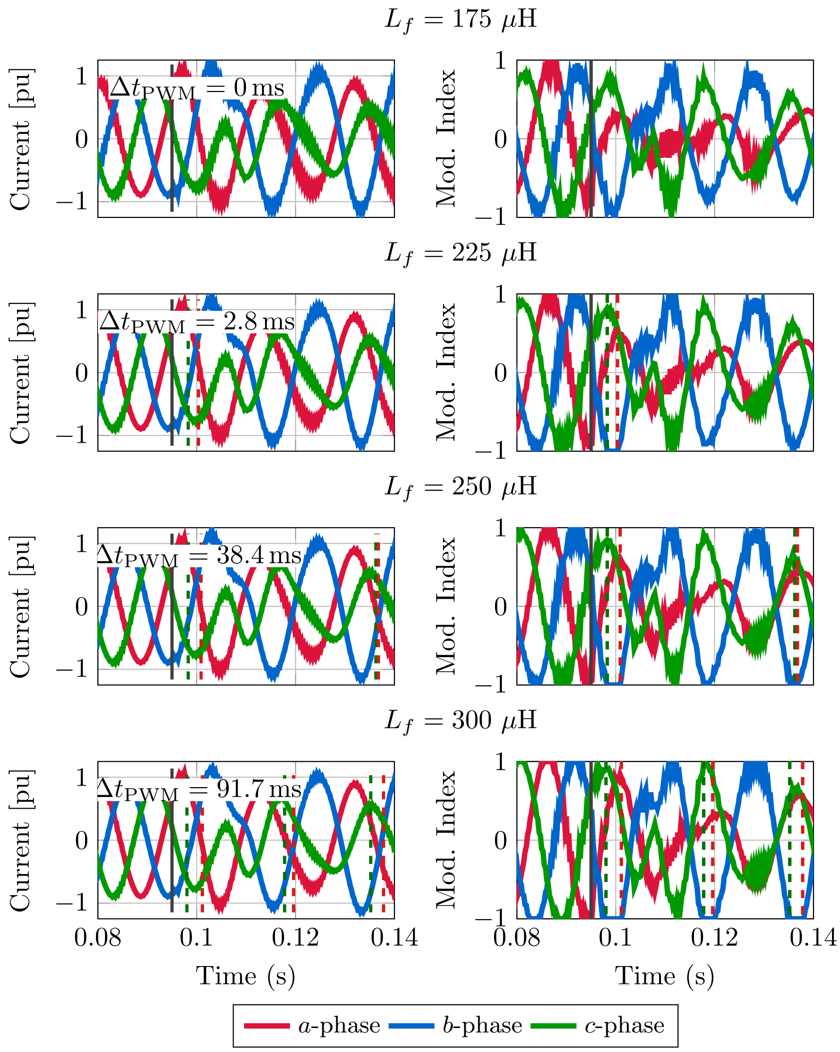

Figure 4.6: PWM-saturation duration as a function of filter inductance L_f.

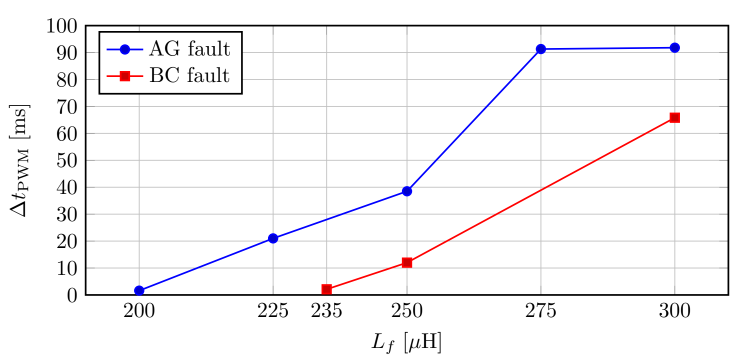

Figure 4.7: Δt_{PWM} vs. L_f. Duration scales nearly linearly with τ_c and collapses as L_f is reduced, consistent with the analytical law.

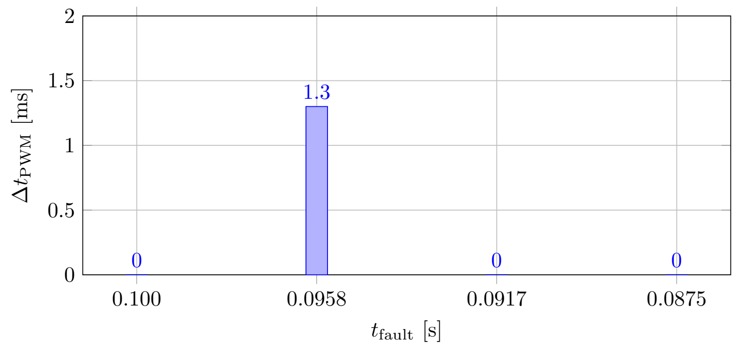

Figure 4.8: Fault-angle selectivity: only the highlighted inception angles enter PWM clamp.

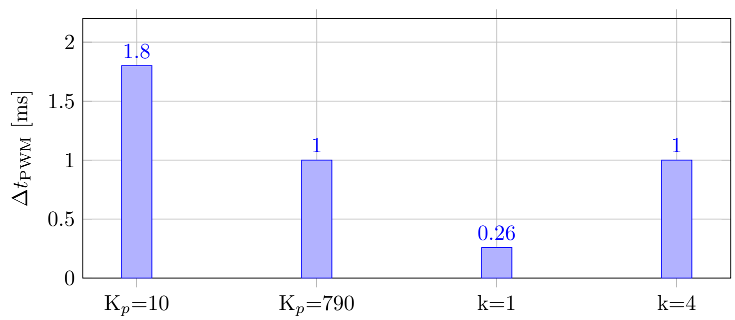

Figure 4.9: Minor influence of PLL bandwidth and SOGI gain on clamp duration.

4.4.2 Experimental Validation

To validate the post-fault timing analysis developed in Section 4.3, we conducted experiments on a commercial 21 kW three-phase grid-following inverter. The experimental setup is shown in Fig. 4.14. On the DC side, the equipment under test (EUT) was supplied by a programmable PV emulator. On the AC side, the EUT was interfaced with a power-hardware-in-the-loop (PHIL) grid simulator running on an OPAL-RT real-time controller. The PHIL simulator imposed both balanced and unbalanced fault scenarios with precise timing and repeatability. Figure 4.15 illustrates the inverter's response to a three-phase-to-ground fault applied at $t = 0.20$ s. The fault was created by reducing the phase voltages from 1 pu to 0.5 pu while the inverter operated at 100% pre-fault power. As shown, the measured positive-sequence current requires approximately 176.9 ms to settle to its post-fault value. Internal controller states (e.g., PI integrator and modulation signal) were not accessible, so all analysis relies on point-of-common-coupling (PCC) voltage

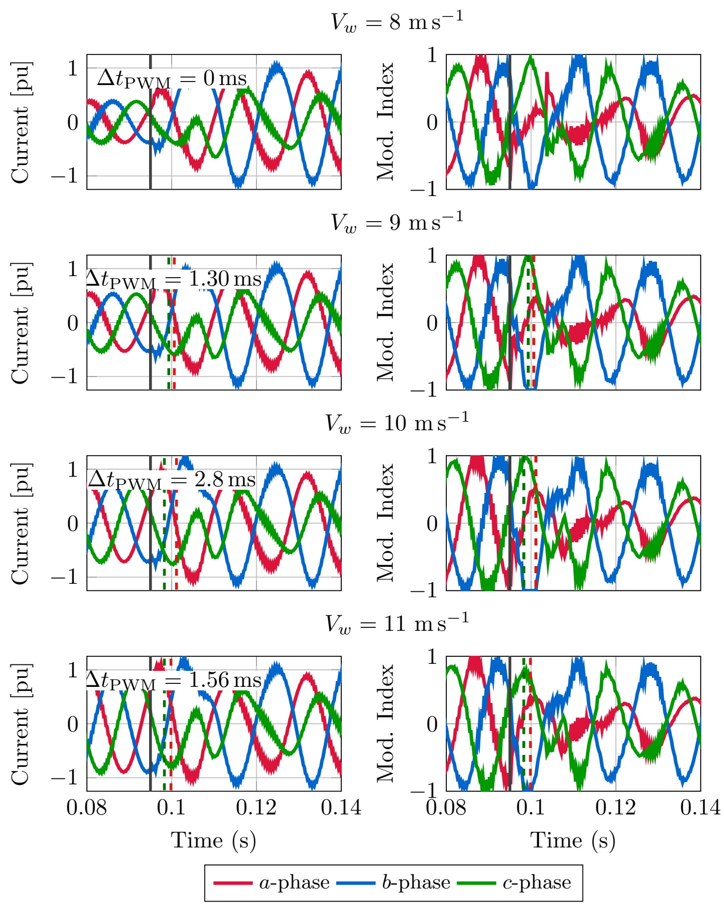

Figure 4.10: PWM saturation evaluation as pre-fault current increases due to wind speed increasing from $V_w = 8$ to $11\ \mathrm{m\,s^{-1}}$.

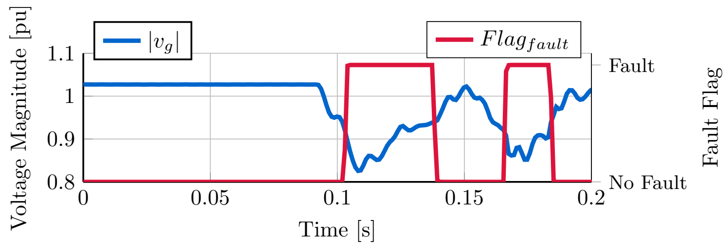

Figure 4.11: Measured voltage magnitude and corresponding fault status over time.

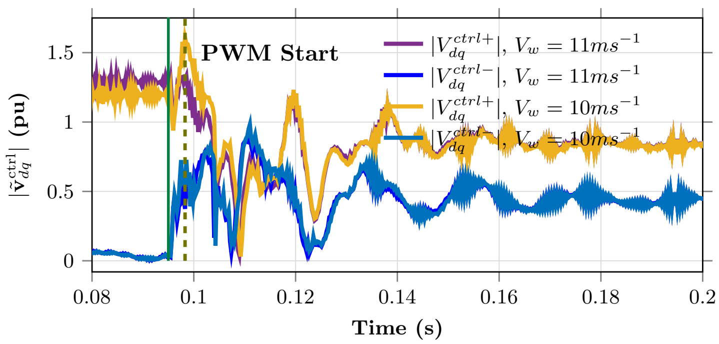

Figure 4.12: Controller-generated positive- and negative-sequence voltage references for $V_w = 10$ and $11\,\mathrm{m\,s^{-1}}$.

and current waveforms. A distinct change in slope of the positive-sequence current is observed at $\Delta t_1 = 30.3$ ms after fault inception, suggesting that the ride-through controller detected the sag and substituted its fault-current reference at that moment. The interval $[0, \Delta t_1]$ corresponds to normal operation where PWM saturation may have been active, while the subsequent $\Delta t_2 = 146.6$ ms interval corresponds to transient settling under the new ride-through regime, likely dominated by PI saturation effects.

To further validate the hypothesis that deeper faults induce longer nonlinear saturation phases, we repeated the three-phase-to-ground test across a range of fault voltages $\{0.2, 0.3, 0.4, 0.5, 0.6\}$ pu. As shown in Fig. 5.6, the settling time increases monotonically with fault severity, ranging from approximately 160 ms to 220 ms.

We also conducted a series of unbalanced fault experiments to observe post-fault current behavior under asymmetrical voltage conditions. Table 5.4 lists the measured post-fault positive- and negative-sequence voltage magnitudes, as well as the corresponding settling times.

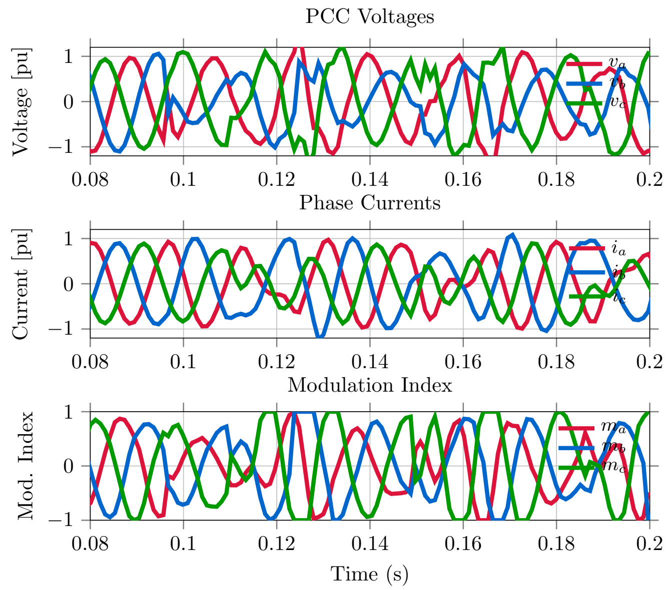

Figure 4.13: PCC voltage, Phase current and modulation index during oscillatory switching regime showing sustained PWM saturation and distorted current.

The results show that test cases with $|v^{+}_{postFault}| \approx$ 0.66 pu and $|v^{-}_{postFault}| \approx$ 0.17 pu exhibit significantly longer settling times (330–360 ms), compared to symmetric faults. Since the inverter's internal parameters remain unchanged across tests, this prolonged duration is attributed to deeper saturation—both in PWM and PI controllers—induced by the unbalanced fault.

In contrast, unbalanced fault cases with higher $|v^{+}_{postFault}| \approx$ 0.87–0.90 pu and relatively low $|v^{-}_{postFault}|$ show much faster settling times (120–150 ms), comparable to those seen in shallow symmetric faults. This reinforces the hypothesis that saturation extent—and thus post-fault settling time—is strongly governed by the depth and asymmetry of the voltage disturbance. These observations corroborate the timing models presented earlier.

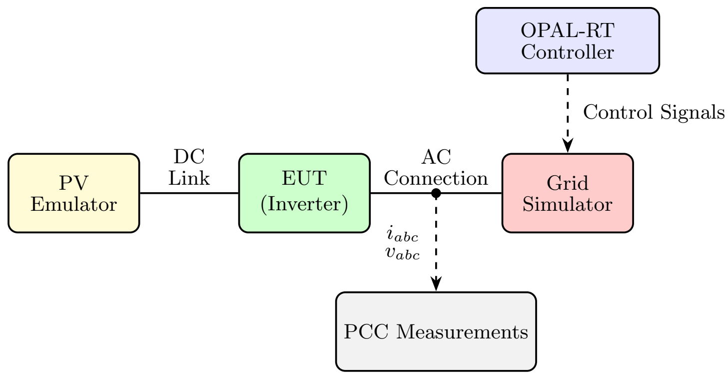

Figure 4.14: Experimental setup comprising a PV emulator connected to the DC side of the EUT (inverter) and a grid simulator on the AC side. PCC measurements are collected at the inverter-grid interface, while the grid simulator is controlled by an OPAL-RT real-time controller.

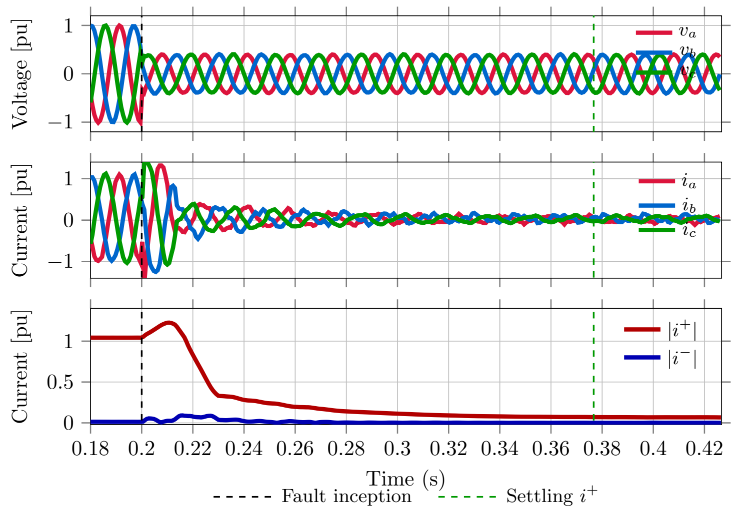

Figure 4.15: Voltages, current, and sequence currents of the commercial inverter for a $3ph - G$ fault resulting in voltage magnbitude to drop to 0.4pu

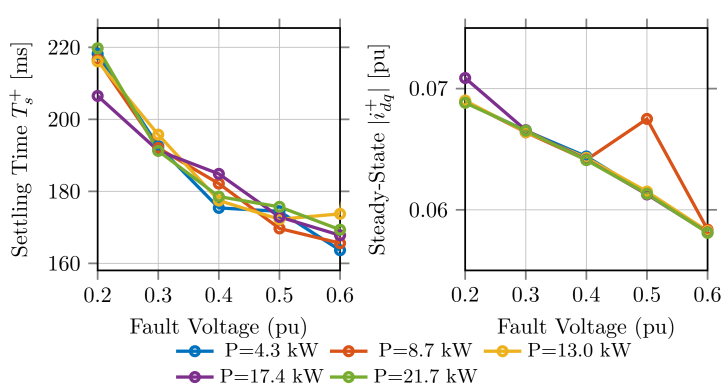

Figure 4.16: Experimental inverter response under three-phase-to-ground faults for multiple pre-fault power levels.

Table 4.4: Measured post-fault voltage sequences and settling times under unbalanced faults.

$\lvert v^{+}_{postFault}\rvert$ (pu)	$\lvert v^{-}_{postFault}\rvert$ (pu)	t^{+}_{s} (s)
0.6658	0.1660	0.3494
0.7496	0.2499	0.3153
0.6658	0.1660	0.3579
0.6663	0.1667	0.3347
0.6658	0.1662	0.3358
0.9000	0.1013	0.1542
0.8668	0.0652	0.1244
0.8673	0.0676	0.1310
0.8664	0.0654	0.1405

Chapter 5

Analysis of IBR Fault Response – Part II: Subsystem-Level Temporal Behavior (Linear Phase)

5.1 Introduction

IBRs have become a dominant source of power generation in modern power systems, propelled by the rapid deployment of wind, solar photovoltaic, and battery energy storage systems. Unlike synchronous machines—characterized by inertia that inherently supports fault current—the response of IBRs to system disturbances relies heavily on high-speed electronic control loops, modulation limits, and PLLs [110–112]. Upon grid faults, IBRs transition through a sequence of non-linear and linear regimes before resuming stable operation. While non-linear mechanisms such as PI output saturation, PWM clipping, and fault ride-through logic are well documented [112–114], the subsequent linear-recovery phase—beginning after clamps clear—has received comparatively less analytical attention, particularly concerning how subsystem interactions shape settling dynamics.

Existing literature has examined specific components influencing post-fault recovery: the L_f–R_f output filter [108], PI-based current regulation with cross-coupling feed-forward [54], and sequence extraction using dual-SOGI filters and SRF–PLL structures [112, 115]. These works have established that each subsystem introduces distinct poles and damping factors that shape the transient decay. However, the majority of prior studies analyze these elements in isolation, focusing either on the power stage, the control loops, or the estimation path separately. This siloed approach omits the dynamic coupling that occurs when these subsystems interact in closed-loop operation, particularly during the linear-recovery phase after clamp clearance.

Furthermore, settling-time predictions in the literature are often derived from empirical simulation sweeps [116] or simplified low-order models [117]. Such approaches, while useful for quick tuning, can obscure the relative contributions of the current loop, sequence extractor, and PLL to the overall recovery timeline. This limitation becomes especially pronounced under unbalanced voltage conditions, where positive- and negative-sequence responses diverge and the negative-sequence dynamics are strongly influenced by PLL bandwidth and filtering characteristics [118, 119]. In these cases, relying solely on low-order approximations can lead to incorrect attribution of the slowest mode, misjudging whether recovery is limited by control, filtering, or estimation dynamics.

This lack of an integrated, physics-informed framework represents a critical gap in the field. For protection engineers and grid code compliance evaluators, accurate prediction of recovery timelines is not merely an academic exercise—it underpins correct relay coordination, FRT compliance, and post-fault stability assessments [120, 121]. Importantly, these assessments depend not only on the positive-sequence current behavior but also on the negative-sequence recovery, which can dominate the total recovery time in weak-grid or unbalanced-fault scenarios [122, 123]. Without analytical tools that explicitly capture the coupled dynamics of the circuit, control, and estimation paths, there is a heightened risk of protection miscoordination, overly conservative FRT margins, or misinterpretation of laboratory and field-test results.

In this work, we address these shortcomings by developing a unified linear time-invariant (LTI) state-space model of the linear-recovery phase. The formulation explicitly combines:

1. The L_f–R_f output filter (circuit path),
2. Positive- and negative-sequence PI current regulators with cross-coupling feed-forward (control path),
3. A dual-SOGI-based SRF–PLL sequence extractor with small-signal modeling of the PLL and Park transformation effects (estimation path).

By deriving closed-form expressions for the characteristic factors of each channel, the model enables analytical estimation of 2% settling times for both positive- and negative-sequence currents.

The results reveal when the recovery is limited by the current loop, the SOGI filter, or the PLL, providing actionable insights for tuning and compliance evaluation under IEEE Std 2800–2022.

The remainder of this paper is organized as follows. Section **??** outlines the IBR control architecture and its behavior during fault conditions. Section 5.3 develops a dynamic model for the linear recovery phase, once nonlinear effects have subsided. Section 5.4 details the sequence of post-fault events and their inter-dependencies. Section 5.5 presents EMT simulations and laboratory experiments used to validate the proposed framework.

5.2 IBR Dynamics During Fault

The detailed grid-following inverter model, including the control architecture, sequence-domain formulation, modulation, filter dynamics, and saturation mechanisms, is developed in Section 4.2.

5.3 Dynamic Model for the Linear-Recovery Phase

This section derives a model for the close-loop recovery phase—the interval that starts once both PI and PWM clamps have cleared and the modulator again operates inside its admissible circle. From that moment the inverter returns to closed-loop operation and its settling speed is governed by the interaction of three subsystems: (*i*) the L_f–R_f output filter (circuit); (*ii*) the dq PI current regulators, including the standard cross-coupling feed-forward terms (control); and (*iii*) the measurement chain that provides voltage in synchronous reference frame and phase angle (estimation). In this paper we adopt an architecture in which the phase angle is supplied by a dual second-order generalized integrator PLL (DSOGI–PLL) and, when negative-sequence control is enabled, the same block delivers separate positive/negative sequence components for the current loops. The state-space formulation below is written for this DSOGI–PLL, but the procedure and the resulting settling-time expressions can be extended to alternative extractors such as notch- filtered or double-decoupled SRF PLLs. Figure 5.1 illustrates these signal-processing components in detail: (*a*) the SOGI-QSG structure for orthogonal voltage generation, (*b*) the SRF-PLL that locks to the positive-sequence component, and (*c*) the complete sequence-extraction path that delivers

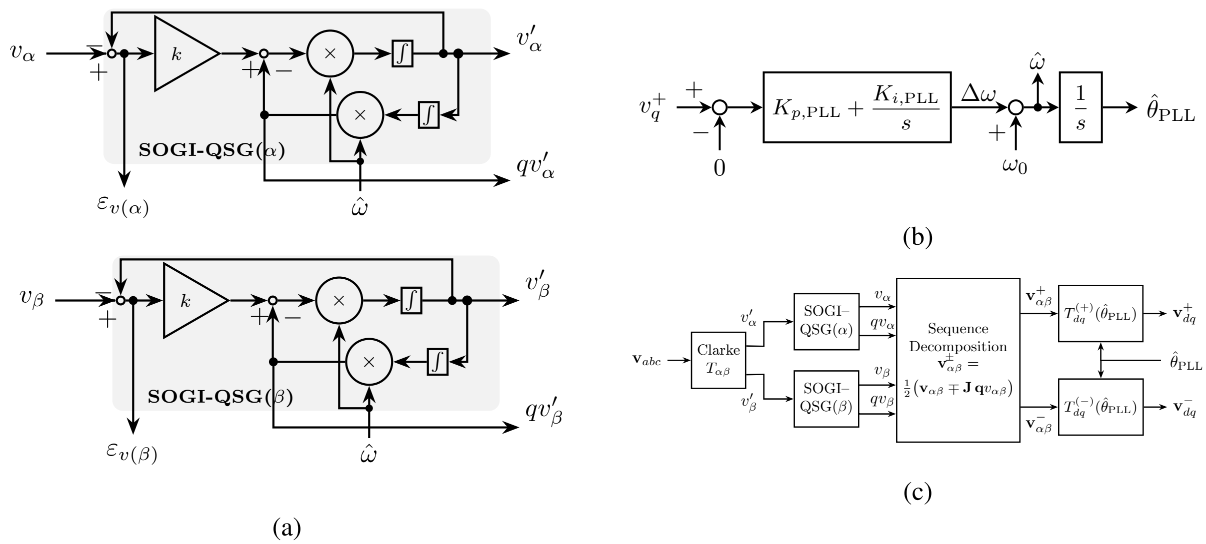

Figure 5.1: Signal-processing stages for sequence-component extraction: (a) Dual-SOGI quadrature–signal generator, (b) SRF-PLL that maintains the synchronous reference frame, and (c) Integrated positive/negative-sequence extraction chain.

$v_{dq}^{\pm}$ to the control loop inputs. All synchronous quantities are expressed in the reference frame of the PLL estimate, $\hat{\theta}_{\mathrm{PLL}}$. By treating the PLL estimated frequency $\hat{\omega}$ as a constant (small-signal perturbations $\Delta\omega$ are considered later), the composite model is LTI.

5.3.1 Dual–SOGI Sequence Extractor (Frozen $\hat{\omega}$)

Let v'_α, v'_β be the raw Clarke voltages obtained from the three–phase set via $\mathbf{v}'_{\alpha\beta} = T_{\alpha\beta}\mathbf{v}_{abc}$. Each component is processed by an identical second–order generalized integrator (SOGI) that produces an in–phase band-pass replica v and a 90°-lead quadrature signal qv. For either Clarke component we employ the realization

$$\dot{x}_1 = -k\hat{\omega}x_1 - \hat{\omega}^2 x_2 + k\hat{\omega}\, v', \tag{5.1a}$$

$$\dot{x}_2 = \quad x_1, \tag{5.1b}$$

$$v = x_1, \quad qv = -\hat{\omega}x_2, \tag{5.1c}$$

where $\hat{\omega}\,[\mathrm{rad/s}]$ is the PLL frequency estimate, and $0 < k \leq 2$ is the damping (or gain) parameter $\zeta = k/2\,(\Rightarrow\ \zeta \in (0{,}1])$. Taking Laplace transforms of (5.1) gives

$$G_d(s) = \frac{v(s)}{v'(s)} = \frac{k\hat{\omega}\, s}{s^2 + k\hat{\omega}\, s + \hat{\omega}^2}, \tag{5.2}$$

$$G_q(s) = \frac{qv(s)}{v'(s)} = \frac{k\hat{\omega}^2}{s^2 + k\hat{\omega}\, s + \hat{\omega}^2}. \tag{5.3}$$

Both G_d and G_q share the pole pair

$$s_{1,2} = -\frac{k\omega}{2} \pm j\,\hat{\omega}\sqrt{1 - \left(\frac{k}{2}\right)^2} \qquad (0 < k < 2), \tag{5.4}$$

Stacking the two identical SOGIs yields

$$\mathbf{x}_{\text{SOGI}} = \left[x_{1\alpha}, x_{2\alpha}, x_{1\beta}, x_{2\beta}\right]^\top, \tag{5.5}$$

$$\dot{\mathbf{x}}_{\text{SOGI}} = A_{\text{SOGI}}\mathbf{x}_{\text{SOGI}} + B_{\text{SOGI}}\mathbf{v}'_{\alpha\beta}, \tag{5.6}$$

with block matrices

$$A_{\text{SOGI}} = \begin{bmatrix} -k\omega & -\omega^2 & 0 & 0 \\ 1 & 0 & 0 & 0 \\ 0 & 0 & -k\omega & -\omega^2 \\ 0 & 0 & 1 & 0 \end{bmatrix}, \quad B_{\text{SOGI}} = \begin{bmatrix} k\omega & 0 \\ 0 & 0 \\ 0 & k\omega \\ 0 & 0 \end{bmatrix}. \tag{5.7}$$

The corresponding 4×2 transfer matrix is

$$T_{\text{SOGI}}(s) = \begin{bmatrix} G_d(s) & 0 \\ G_q(s) & 0 \\ 0 & G_d(s) \\ 0 & G_q(s) \end{bmatrix}. \tag{5.8}$$

Define $\mathbf{v}_{g,\alpha\beta} = [\, v_\alpha,\ v_\beta \,]^\mathsf{T}$ and $\mathbf{q}v_{\alpha\beta} = [\, qv_\alpha,\ qv_\beta \,]^\mathsf{T}$. Following [124] we obtain

$$\begin{aligned} \mathbf{v}_{\alpha\beta}^{+} &= \tfrac{1}{2}\big(\mathbf{v}_{\alpha\beta} - \mathbf{J}\,\mathbf{q}v_{\alpha\beta}\big), \\ \mathbf{v}_{\alpha\beta}^{-} &= \tfrac{1}{2}\big(\mathbf{v}_{\alpha\beta} + \mathbf{J}\,\mathbf{q}v_{\alpha\beta}\big), \end{aligned} . \tag{5.9}$$

$\mathbf{v}_{\alpha\beta}^{+}$ contains only the $+\hat{\omega}$ rotating phasor while $\mathbf{v}_{\alpha\beta}^{-}$ contains only the $-\hat{\omega}$ component—no additional dynamics are introduced. Finally, Park matrices referenced to $\hat{\theta}_{\mathrm{PLL}}$ map the separated $\alpha\beta$ vectors to the synchronous frames:

$$\mathbf{v}_{dq}^{+} = T_{dq}^{(+)}(\hat{\theta}_{\mathrm{PLL}})\,\mathbf{v}_{\alpha\beta}^{+}, \tag{5.10a}$$

$$\mathbf{v}_{dq}^{-} = T_{dq}^{(-)}(\hat{\theta}_{\mathrm{PLL}})\,\mathbf{v}_{\alpha\beta}^{-}, \tag{5.10b}$$

where

$$T_{dq}^{(+)}(\theta) = \begin{bmatrix} \cos\theta & \sin\theta \\ -\sin\theta & \cos\theta \end{bmatrix}, \quad T_{dq}^{(-)}(\theta) = \begin{bmatrix} \cos\theta & -\sin\theta \\ \sin\theta & \cos\theta \end{bmatrix}.$$

Combining the Clarke matrix $T_{\alpha\beta}$, the dual-SOGI band-pass $T_{\mathrm{SOGI}}(s)$, the algebraic sequence splitter $T_{\mathrm{seq}}^{(\pm)}$, and the fixed Park rotation $T_{dq}^{(\pm)}$ yields a single LTI transfer from the raw three-phase PCC voltage $\mathbf{v}_{g,abc}(s)$ to the synchronous dq components supplied to the current loops:

$$\mathbf{v}_{g,dq}^{\pm}(s) = T_{dq}^{(\pm)}\,T_{\mathrm{seq}}^{(\pm)}\,T_{\mathrm{SOGI}}(s)\,T_{\alpha\beta}\,\mathbf{v}_{g,abc}(s). \tag{5.11}$$

with $T_{\mathrm{seq}}^{(+)}$ and $T_{\mathrm{seq}}^{(-)}$ being the first and last two rows, respectively, of $\frac{1}{2}\begin{bmatrix} 1 & 0 & 0 & -1 \\ 0 & 1 & 1 & 0 \\ 1 & 0 & 0 & 1 \\ 0 & 1 & -1 & 0 \end{bmatrix}$.

5.3.2 Composite State–Space Model

The L_f–R_f output filter, dual PI current regulators and the dual–SOGI PLL can be assembled into a single LTI model, expressed in the synchronous frame defined by the PLL angle $\hat{\theta}_{\mathrm{PLL}}$. We collect the positive- and negative-sequence currents ($i^{\pm}_{d/q}$), the corresponding PI-integrator states ($\xi^{\pm}_{d/q}$) and the four internal states ($x_{1\alpha}, x_{2\alpha}, x_{1\beta}, x_{2\beta}$) of the dual SOGI:

$$\mathbf{x} = \left[i_d^+ \, i_q^+ \, \xi_d^+ \, \xi_q^+ \, i_d^- \, i_q^- \, \xi_d^- \, \xi_q^- \, x_{1\alpha} \, x_{2\alpha} \, x_{1\beta} \, x_{2\beta}\right]^\top \in \mathbb{R}^{12}. \tag{5.12}$$

With $I_2 = \begin{bmatrix} 1 & 0 \\ 0 & 1 \end{bmatrix}$, and $0_{m\times n}$ the $m \times n$ zero block, the current-loop sub-matrices are

$$A_{\pm} = -\frac{R_f + K_p}{L_f} I_2 \, \pm \, \frac{\omega}{L_f} J, \qquad B_{\pm,\xi} = \frac{K_i}{L_f} I_2. \tag{5.13}$$

Two disjoint input channels are required:

$$\mathbf{u}_r = \begin{bmatrix} i_d^{*+} \\ i_q^{*+} \\ i_d^{*-} \\ i_q^{*-} \end{bmatrix}, \quad \mathbf{u}_d = \begin{bmatrix} v_{g,d}^+ \\ v_{g,q}^+ \\ v_{g,d}^- \\ v_{g,q}^- \\ v'_\alpha \\ v'_\beta \end{bmatrix}. \tag{5.14}$$

$\mathbf{u}_r \in \mathbb{R}^4$ carries the positive- and negative-sequence current references, whereas $\mathbf{u}_d \in \mathbb{R}^6$ groups the instantaneous dq components of the grid voltage and the raw (α, β) voltages that drive the SOGI. With the SOGI dynamics condensed into the square matrix A_{SOGI} and its input matrix B_{SOGI}, see (5.7) for details, the composite state matrix reads

$$A = \begin{bmatrix} A_+ & B_{+,\xi} & 0 & 0 & 0 \\ -I_2 & 0 & 0 & 0 & 0 \\ 0 & 0 & A_- & B_{-,\xi} & 0 \\ 0 & 0 & -I_2 & 0 & 0 \\ 0 & 0 & 0 & 0 & A_{\text{SOGI}} \end{bmatrix}. \tag{5.15}$$

The reference-input matrix B_r and disturbance-input matrix B_d are, respectively,

$$B_r = \begin{bmatrix} \frac{K_p}{L_f} I_2 & 0 \\ I_2 & 0 \\ 0 & \frac{K_p}{L_f} I_2 \\ 0 & I_2 \\ 0 & 0 \end{bmatrix}, \qquad B_d = \begin{bmatrix} -\frac{1}{L_f} I_2 & 0 & 0 \\ 0 & 0 & 0 \\ 0 & -\frac{1}{L_f} I_2 & 0 \\ 0 & 0 & 0 \\ 0 & 0 & B_{\mathrm{SOGI}} \end{bmatrix}. \tag{5.16}$$

If the measured variables are the four filter currents $\mathbf{y} = \left[i_d^+, i_q^+, i_d^-, i_q^-\right]^\top$, the output matrix is simply

$$C = \begin{bmatrix} I_2 & 0 & 0 & 0 & 0 \\ 0 & 0 & I_2 & 0 & 0 \end{bmatrix}. \tag{5.17}$$

The complete LTI model is therefore

$$\dot{\mathbf{x}} = A\,\mathbf{x} + B_r\,\mathbf{u}_r + B_d\,\mathbf{u}_d, \qquad \mathbf{y} = C\,\mathbf{x}\,. \tag{5.18}$$

In (5.18), rows 1–4 describe the positive-sequence loop, rows 5–8 the negative-sequence loop, and rows 9–12 the dual-SOGI observer.

5.3.3 Closed-Loop Characteristic Factors

Because the composite matrix A in (5.18) is upper block–triangular, states are ordered

$$[\mathbf{i}^+, \boldsymbol{\xi}^+, \mathbf{i}^-, \boldsymbol{\xi}^-, \mathbf{x}_{\mathrm{SOGI}}]^\top,$$

and its characteristic polynomial factorizes:

$$\det(sI - A) = \det\!\big(sI - A^+\big)\,\det\!\big(sI - A^-\big)\,\det\!\big(sI - A_{\mathrm{SOGI}}\big). \tag{5.19}$$

Below, each factor is obtained in closed form.

1. Positive–sequence dq current loop

Consider the d-axis channel; the q-axis is identical. With the SV-PWM operating in its linear region the bridge delivers $\mathbf{v}_{dq} = G_{\text{PWM}}\mathbf{v}_{\text{mod},dq}$. Substituting the PI law and cross–coupling compensation from (4.3) into the filter equation (4.6) (a) gives, in the time domain

$$L_f\dot{i}_d^+ + R_f i_d^+ = G_{\text{PWM}}\Big[K_p\big(i_d^{*+} - i_d^+\big) + K_i\int\big(i_d^{*+} - i_d^+\big)dt\Big] - v_{g,d}^+. \tag{5.20}$$

The grid term $v_{g,d}^+$ acts only as a disturbance; it does not affect the closed-loop poles, so it is dropped for the homogeneous analysis. After differentiation one obtains

$$L_f\ddot{i}_d^+ + \big(R_f + G_{\text{PWM}}K_p\big)\dot{i}_d^+ + G_{\text{PWM}}K_i\, i_d^+ = G_{\text{PWM}}K_i\, i_d^{*+}, \tag{5.21}$$

so the positive–sequence d-axis has the second–order polynomial

$$L_f s^2 + \big(R_f + G_{\text{PWM}}K_p\big)s + G_{\text{PWM}}K_i = 0. \tag{5.22}$$

For compactness we use the effective gains, $\bar{K}_p := G_{\text{PWM}}K_p$, and $\bar{K}_i := G_{\text{PWM}}K_i$, leading to the natural frequency $\omega_n = \sqrt{\bar{K}_i/L_f}$ and damping $\zeta = (R_f + \bar{K}_p)/(2\sqrt{L_f\bar{K}_i})$. So the dominant real part (used later for settling-time estimates) is $\sigma_{\text{cur}} = \zeta\omega_n$.

2. Negative-sequence current loop

The negative channel is identical to the positive one except for the way the grid voltage enters the feed-forward path. Because the SRF–PLL is locked to the positive sequence, $v_{g,q}^+ \approx 0$ in steady state; the PLL transfer function $H_{\text{PLL}}(s) = \frac{\omega_{\text{PLL}}}{s+\omega_{\text{PLL}}}$ therefore multiplies a signal that is essentially zero, so its pole $s + \omega_{\text{PLL}}$ has negligible effect on the positive-sequence dynamics. The negative sequence, however, appears as a $2\omega_s$ disturbance. It is first isolated by the DSOGI band-pass and then attenuated by the same first-order low-pass $H_{\text{PLL}}(s)$; here the pole acts on a non–zero signal and must be retained.

Hence the negative-sequence characteristic polynomial is the current-loop quadratic (5.22) multiplied by the extra first-order factor

$$s + \omega_{\text{PLL}} = 0. \tag{5.23}$$

Its dominant real part is therefore $\sigma_{-} = \min\{\zeta\omega_n, \, \omega_{\text{PLL}}\}$. If the PLL bandwidth is slow ($\omega_{\text{PLL}} < \zeta\omega_n$) the negative-sequence response is PLL-limited; otherwise it is governed by the current-loop damping, similar to as in the positive-sequence channel.

3. Dual-SOGI band-pass

For either Clarke component (α or β) the DSOGI implements the second-order denominator

$$s^2 + k\hat{\omega}\, s + \hat{\omega}^2 = 0, \tag{5.24}$$

The corresponding real part is $\sigma_{\text{SOGI}} = \frac{k}{2}\,\hat{\omega}$

5.3.4 Closed–Loop Characteristic Factors Including SRF–PLL Dynamics

The analysis of Section 5.3.3 treated the PLL center frequency as a fixed constant $\hat{\omega}$. In reality the Dual-SOGI SRF–PLL adjusts its frequency and phase estimate during a transient; both actions feed back into the current regulators through the Park transformations that convert $\alpha\beta \rightarrow dq$.

Small–signal SRF–PLL model

The classical SRF–PLL comprises three non-linear stages: (a) a phase detector, (b) a PI loop filter, and (c) a numerically–integrated VCO. Linearising each block about the synchronous operating point $\theta = \hat{\theta} = \theta_0$, so that $\Delta\theta(t) = \theta(t) - \hat{\theta}_{PLL}(t)$—gives the block diagram in Fig. 5.1b. For the positive-sequence q-axis voltage $v_q^+(t) = V_g^+ \sin(\theta - \hat{\theta})$, a first-order expansion around $\Delta\theta = 0$ yields

$$\Delta v_q^+(t) \;\approx\; V_g^+ \cdot \Delta\theta(t). \tag{5.25}$$

The output of the PI compensator is the frequency deviation:

$$\Delta\omega(s) = \left(K_{p,\mathrm{PLL}} + \frac{K_{i,\mathrm{PLL}}}{s}\right) \Delta v_q^+(s). \tag{5.26}$$

The estimated phase is generated by integration of the frequency command:

$$\Delta\hat{\theta}(s) = \frac{\Delta\omega(s)}{s}. \tag{5.27}$$

Combining (5.25)–(5.27), and closing the unity-feedback loop through the phase detector, PI controller, and integrator, yields the transfer function from the measured voltage error to the frequency deviation [125]:

$$\frac{\Delta\omega(s)}{\Delta v_q^+(s)} = \frac{K_{p,\mathrm{PLL}}s + K_{i,\mathrm{PLL}}}{s^2 + K_{p,\mathrm{PLL}}s + K_{i,\mathrm{PLL}}}. \tag{5.28}$$

This second-order low-pass response is shaped by the pole polynomial, while the zero affects only high-frequency gain. Defining the standard damping parameters $\omega_{\mathrm{PLL}} := \sqrt{K_{i,\mathrm{PLL}}}$, and $\zeta_{\mathrm{PLL}} := \frac{K_{p,\mathrm{PLL}}}{2\sqrt{K_{i,\mathrm{PLL}}}}$, and normalizing the numerator to match the dc gain (unity), gives the compact low-pass model:

$$H_{\mathrm{PLL}}(s) = \frac{\omega_{\mathrm{PLL}}^2}{s^2 + 2\zeta_{\mathrm{PLL}}\omega_{\mathrm{PLL}}s + \omega_{\mathrm{PLL}}^2}. \tag{5.29}$$

This transfer function describes the small-signal dynamics of the SRF–PLL frequency estimate. Only the denominator, the pole set, enters the composite characteristic polynomial and the settling-time analysis.

Impact on the SOGI poles

The dual–SOGI denominator contains the time–varying products $k\hat{\omega}$ and $\hat{\omega}^2$, where the PLL estimate is $\hat{\omega}(t) = \omega_0 + \Delta\omega(t)$. A first-order expansion about the operating value ω_0 gives

$$s^2 + k\hat{\omega}s + \hat{\omega}^2 = \underbrace{\left[s^2 + k\omega_0 s + \omega_0^2\right]}_{\text{nominal quadratic}} + (k\, s + 2\omega_0)\,\Delta\omega(s). \tag{5.30}$$

The square–bracketed term fixes the nominal SOGI poles at $s_{1,2} = -\frac{k\omega_0}{2} \pm j\omega_0\sqrt{1-(k/2)^2}$. The correction $(k\,s + 2\omega_0)\Delta\omega(s)$ is small for two reasons:

(a) it is at most first-order in s, so it can only append additional real roots; and

(b) $\Delta\omega(s)$ is low-pass filtered by the PLL transfer function (5.28), i.e. $\Delta\omega(s) = H_{\text{PLL}}(s)\,\Delta\omega_{\text{grid}}(s)$, with $H_{\text{PLL}}(s)$ strictly proper.

Hence the extra term introduces only higher-order, stable factors that do not influence the dominant dynamics. To first-order accuracy the SOGI poles are therefore retained at $s^2 + k\omega_0 s + \omega_0^2 = 0$.

Settling of the Park transformation

The Park transformation projects the measured $\alpha\beta$ voltages into the synchronous reference frame using the estimated angle $\hat{\theta}_{\text{PLL}}(t)$ provided by the PLL. This mapping is described by (5.10). When the estimated angle differs slightly from the $\theta(t)$, the true (instantaneous) electrical angle of the grid, i.e.,

$$\hat{\theta}_{\text{PLL}}(t) = \theta(t) + \Delta\theta(t), \qquad |\Delta\theta(t)| \ll 1, \tag{5.31}$$

a first-order Taylor expansion of the rotation matrix gives

$$T_{dq}^{(\pm)}\big(\hat{\theta}_{\text{PLL}}\big) \;\approx\; T_{dq}^{(\pm)}(\theta)\,\big(I_2 \mp \Delta\theta\,\mathbf{J}\big). \tag{5.32}$$

Applying the first–order expansion to each sequence channel $\sigma \in \{+,-\}$ gives a compact expression for the small-signal Park-frame voltage error

$$\begin{aligned} \Delta\mathbf{v}_{dq}^{\pm}(t) &:= \mathbf{v}_{dq}^{\pm}(t) - \mathbf{v}_{g,dq}^{\pm}(t) \\ &\approx\; -\kappa_\sigma\,\Delta\theta(t)\,\mathbf{J}\,\mathbf{v}_{g,dq}^{\pm}(t), \end{aligned} \tag{5.33}$$

where the sign factor distinguishes the two sequences $\kappa_+ = +1,\ \kappa_- = -1$. Expressing the small–signal phase relation $\Delta\theta(s) = \dfrac{\Delta\omega(s)}{s}$ in the Laplace domain, the resulting Park-frame voltage error is,

$$\Delta \mathbf{v}_{dq}^{\pm}(s) \;\approx\; -\,\kappa_\sigma\,\mathbf{J}\,\frac{\Delta\omega(s)}{s}\,\mathbf{v}_{g,dq}^{\pm}(s). \tag{5.34}$$

Equation (5.34) illustrates the orthogonal coupling introduced by phase error: a deviation in the q-component of the grid voltage manifests in the d-axis measurement, and vice versa. This cross-coupling arises because the Park transformation is evaluated using the estimated phase angle $\hat{\theta}(t)$, which lags the true grid angle $\theta(t)$ during transients.

In the Laplace domain, the Park-frame voltage error depends on the phase error as $\Delta \mathbf{v}_{dq}^{\pm}(s) = -\Delta\theta(s)\,\mathbf{J}\,\mathbf{v}_{g,dq}^{\pm}(s)$, and since $\Delta\theta(s) = \frac{\Delta\omega(s)}{s}$, it introduces an additional integrator relative to the SRF–PLL frequency response. Consequently, while $\Delta\omega(s)$ follows the second-order dynamics of the PLL transfer function (5.29), the Park-frame voltage error $\Delta \mathbf{v}_{dq}^{\pm}(s)$ inherits a third-order response. The dominant real pole of this composite response still corresponds to the PLL damping rate $\zeta_{\mathrm{PLL}}\omega_{\mathrm{PLL}}$, which governs the rate at which the angle misalignment—and thus the error in dq-coordinates—decays. Therefore, the Park-frame misalignment decays exponentially with time constant $\tau_{\text{Park}} = \frac{1}{\zeta_{\mathrm{PLL}}\omega_{\mathrm{PLL}}}$, and reaches within a 2% tolerance in approximately $t_{s,2\%}^{\text{Park}} \approx \frac{4}{\zeta_{\mathrm{PLL}}\omega_{\mathrm{PLL}}}$. Because the estimated phase angle $\hat{\theta}_{\mathrm{PLL}}$ is shared by both synchronous frames, the Park-frame misalignment caused by PLL transients affects both the positive- and negative-sequence channels whenever the grid is disturbed. In the positive-sequence channel, this angle error perturbs the transformation of $v_{g,dq}^{+}$, but since $v_{g,q}^{+}$ is driven toward zero by the PLL itself, the error signal Δv_q^{+} quickly vanishes in steady state. As a result, the Park-frame error introduces only a mild first-order lag in the positive-sequence channel. In contrast, the negative-sequence channel observes a persistent 2ω component that the PLL must reject. The Park misalignment in this case multiplies a nonzero rotating voltage vector and directly influences the extracted negative-sequence components. This effect is more pronounced and cannot be neglected, which is why the corresponding pole is explicitly retained in the negative-sequence characteristic polynomial derived in Sec. 5.3.3.

5.3.5 Composite Linear Model and Post-Detection Settling Time

Collecting the dominant real parts associated with each block yields candidate time constants that influence the overall post-transient decay:

- Current loop: $\sigma_{\text{cur}} = \zeta\omega_n$, where $\omega_n = \sqrt{\bar{K}_i/L_f}$ and $\zeta = (R_f + \bar{K}_p)/(2\sqrt{L_f\bar{K}_i})$.
- Dual-SOGI filter: $\sigma_{\text{SOGI}} = \frac{k}{2}\hat{\omega}$ from the damping of the band-pass response.
- PLL / Park transformation: $\sigma_{\text{PLL}} = \zeta_{\text{PLL}}\omega_{\text{PLL}}$—the dominant real pole of the second-order small-signal model in (5.29).

These define the effective exponential decay rate of each channel. In the most general case, the slowest decay rate across both positive- and negative-sequence channels is:

$$\sigma_+ = \min\!\big(\sigma_{\text{cur}},\, \sigma_{\text{SOGI}}, ,\sigma_{\text{PLL}}\big), \qquad \sigma_- = \min\!\big(\sigma_{\text{cur}},\, \sigma_{\text{SOGI}},\, \sigma_{\text{PLL}}\big), \tag{5.35}$$

reflecting the fact that the PLL angle estimation directly affects both sequences, but dominates in the negative sequence due to the persistent 2ω content.

Using the classical $4/\sigma$ rule-of-thumb for the 2% settling time [126], we obtain

$$t^+_{s,2\%} \approx \frac{4}{\sigma_+}, \qquad t^-_{s,2\%} \approx \frac{4}{\sigma_-}. \tag{5.36}$$

If the PLL bandwidth is reduced so that $\sigma_{\text{PLL}} = \zeta_{\text{PLL}}\omega_{\text{PLL}}$ becomes the smallest real part, it sets the slowest pole across all channels. In that case, both settling times are approximately equal:

$$t^+_{s,2\%} \approx t^-_{s,2\%} \approx \frac{4}{\zeta_{\text{PLL}}\omega_{\text{PLL}}}. \tag{5.37}$$

In most utility-scale applications, the positive-sequence channel settles faster than the negative-sequence channel. This occurs because the positive-sequence response is primarily shaped by the current controller and SOGI filter—both typically tuned for rapid transient rejection. The PLL contributes little here, as the q-axis voltage is regulated toward zero and hence drives minimal phase error. By contrast, the negative-sequence dynamics are significantly influenced by the PLL, which must reject the persistent 2ω component appearing in unbalanced grid conditions. As a result, the Park-frame misalignment induced by PLL tracking error introduces a slow decay envelope into the negative-sequence response. If the PLL bandwidth is low (i.e., $\zeta_{\text{PLL}}\omega_{\text{PLL}}$ is small), it becomes the dominant limiting factor in the negative-sequence channel.

Post-detection trajectory.

At $t = t_{\text{detect}}$ the ride-through coordinator applies the LVRT reference $i^*_{dq,\text{FRT}}$, respecting $\|i^*_{dq,\text{FRT}}\| \le I_{\max}$ and $\|\tilde{\mathbf{v}}^{\text{ctrl}}_{dq}\| \le V_{\max}$. Any residual voltage or current clamp persists for Δt_{sat}; thereafter the closed-loop error decays exponentially, giving the practical transition time

$$T_{\text{transition}} \simeq \Delta t_{\text{sat}} + \max\bigl(t_s^+,\, t_s^-\bigr). \tag{5.38}$$

Typical parameter ranges reported in the literature are $\tau_c = 0.5\text{–}5$ ms [108], $k \simeq 1$ $(0.7-1.3)$ [104], and $\omega_{\text{PLL}} = 100\text{–}200$ rad/s [109, 112] . Using the settling-time formulas gathered in Sec. 5.3 one obtains

$$\begin{aligned}
t^{\text{cur}}_{s,2\%} &\approx 4\,\tau_c && \Rightarrow \text{2–20 ms},\\
t^{\text{SOGI}}_{s,2\%} &\approx \frac{8}{k\,\hat{\omega}} && \Rightarrow \text{10–25 ms (50/60 Hz grid)},\\
t^{\text{PLL}}_{s,2\%} &\approx \frac{4}{\omega_{\text{PLL}}} && \Rightarrow \text{20–60 ms}.
\end{aligned}$$

Selecting the slowest real part in each sequence gives $t^+_{s,2\%} \approx 4/\sigma_+ \approx$ 10–25 ms, and $t^-_{s,2\%} \approx 4/\sigma_- \approx$ 20–60 ms. Hence, under shallow sags—where the residual clamp interval Δt_{sat} is only a few milliseconds—the PLL pole often dominates the negative-sequence tail, whereas the positive-sequence current is set by the faster of the PI loop or dual-SOGI filter. For severe voltage sags the initial clamp can persist for an extended interval; in that case the saturation window, Δt_{sat}, becomes a dominant contributor to the total post-fault transition time..

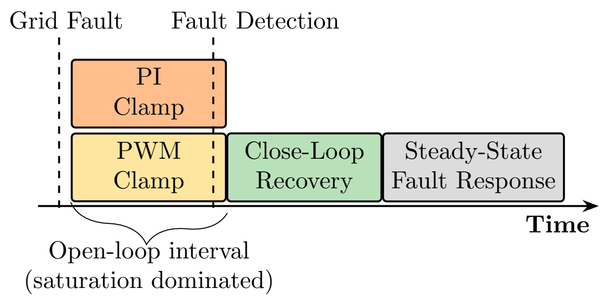

Figure 5.2: Timeline of inverter fault response highlighting PI saturation, PWM saturation, linear recovery and the steady-state faulted regime. Dashed lines mark the grid-fault inception and its subsequent detection by the controller.

Secondary influences.

DC-link droop during deep sags, fast hardware interlocks, up-stream clearing, or weak-grid resonances can lengthen (or shorten) either Δt_{sat} or the linear tail in (5.38).

5.4 Timeline of Post-Fault Events

In the first ∼10–60 ms that follow a grid-fault event, an IBR traverses four generic—and highly non-linear—operating modes:

(i) fault–detection logic,

(ii) PI-output (current-controller) clamping,

(iii) dc-link / SV-PWM clamping, and

(iv) linear closed-loop recovery.

The exact order, possible overlap, and duration of these windows depend on topology, firmware, network strength, and the ride-through policy implemented by the manufacturer. Nevertheless, the four mechanisms above are present in almost every grid-following converter, so the closed-form expressions derived in the previous sections capture a generic IBR response. Figure 5.2 assembles the results into one chronogram; Table 5.1 lists the corresponding numerical ranges for a representative utility-scale unit ($V_{\mathrm{PCC}} = 690\ \mathrm{V_{LL}},\ L_f = 1.5\ \mathrm{mH},\ R_f = 60\ \mathrm{m\Omega},\ \omega_{\mathrm{PLL}} = 100\text{–}200$ rad/s).

Table 5.1: Dominant timing windows after a grid fault (utility-scale, 60 Hz)

Phase / Window	Limit that governs	Typical range
Fault–detector latency	Relay logic	2–20 ms
PI–clamp interval	M limit	0.5–5 ms
PWM–clamp interval	$V_{\max}$ limit	1–5 ms
Linear-recovery phase (closed loop)		
Positive-sequence settling	$\min(\sigma_{\text{cur}}, \sigma_{\text{SOGI}}, \sigma_{\text{PLL}})$	20–60 ms
Negative-sequence settling	$\min(\sigma_{\text{cur}}, \sigma_{\text{SOGI}}, \sigma_{\text{PLL}})$	20–60 ms

5.5 Evaluation

EMT simulations and laboratory experiments were performed to validate the post-fault event sequence and timing framework developed in this paper. A detailed Type-IV wind plant model incorporating FRT functions compliant with IEEE Std 2800 was implemented, extending the work presented in [92].

The inverter connection schematic used in the EMT studies is shown in Fig. 4.5. On the DC side, the grid-side converter is fed by a machine-side converter representing a Type-IV turbine. On the AC side, the inverter is connected to a 0.69kV/33kV Δ–Y transformer; the secondary voltage is scaled by a factor N to emulate plant-level power output while modeling a single detailed inverter. A subsequent 33kV/138kV transformer interfaces the plant with the transmission grid.

Unless otherwise specified in the evaluation sections, all EMT cases use the baseline parameters summarized in Table 5.2. Faults are applied at location **F** in Fig. 4.5, and the corresponding post-fault currents are compared against the analytical predictions.

Table 5.2: Baseline parameters for EMT simulations

Setting	Description	Value
L_f	Filter inductance	200 µH
R_f	Filter resistance	0.5 mΩ
k	SOGI gain	1
T_i^{PLL}	PLL integral time constant	100
K_p^{PLL}	PLL proportional gain	30
K_1^{FRT}	FRT gain ($d \to i^+$)	1
K_2^{FRT}	FRT gain ($d \to i^-$)	2
K_p^i	d–q current-controller K_p	3
K_i^i	d–q current-controller K_i	0.01
V_{dc}	DC-link voltage set-point	1.5 kV
S_{base}	Apparent power (single inverter)	5.8 MVA
K_p^{dc}	DC-voltage controller K_p	4
T_i^{dc}	DC-voltage controller T_i	0.02
V_{LVRT}	LVRT threshold	0.9 pu
R_{fault}	Fault resistance	0.01 Ω

5.5.1 Settling Time Evaluation

To assess the validity of the proposed linear-recovery model, we evaluate the settling time of the inverter's post-fault current response based on EMT simulations.

Validation of Linear-Recovery Model via Current Settling Time

To validate the linear-recovery model developed in Section 5.3, we analyzed the settling behavior of the inverter's fault response by measuring the settling times of the positive- and negative-sequence current magnitudes. The settling time was defined as the time at which each current magnitude remains within a $\pm 2\%$ band around its post-fault steady-state value.

Figure 5.3 presents the simulation results for a representative case using system parameters listed in Table 5.2. For this case, the analytically derived dominant poles were:

$$\sigma_{\text{cur}} = 7501.3, \quad \sigma_{\text{sogi}} = 188.5, \quad \sigma_{\text{pll}} = 123.08.$$

The corresponding measured settling times were:

$$t_s^+ = 28.8\,\text{ms}, \quad t_s^- = 24.8\,\text{ms}.$$

These values closely match the analytical estimate for a second-order settling time, using the standard $4/\sigma$ rule-of-thumb:

$$t_{s,2\%} \approx \frac{4}{\sigma_{\text{PLL}}} = \frac{4}{123.08} \approx 32.5\,\text{ms}.$$

This comparison confirms that the PLL pole, σ_{pll}, is the slowest and thus dominant dynamic in the post-fault recovery. Although the measured settling times are slightly shorter than the analytical prediction, this is expected due to simulation effects such as residual coupling between the PLL and SOGI dynamics not captured in the simplified analytical model. In contrast, the current-control loop and SOGI poles are significantly faster and do not limit the recovery rate.

Overall, the strong agreement between the analytical and simulated results validates the proposed linear-recovery model and confirms that, under the baseline conditions, the inverter's post-fault settling behavior is primarily governed by the PLL dynamics.

Impact of PWM Saturation on Settling Time

To isolate the influence of PWM saturation on the inverter's post-fault recovery, Fig. 5.4 presents results for a case with baseline system parameters, except that the fault was applied at $t = 0.0917$ s—an inception instant previously identified (see Section 4.4.1) to trigger PWM saturation in the simulation model used in this study.

Compared to the non-saturating case, the measured settling times increased significantly: $t_s^+ = 40.6$ ms and $t_s^- = 38.4$ ms. These results confirm that the presence of PWM saturation prolongs the dynamic recovery period, even when all other conditions remain unchanged. The distorted current waveform during the saturation phase delays the return of current magnitudes to their post-fault steady-state values, thereby extending the effective settling time. This highlights the importance of accounting for PWM saturation in protection and control studies involving fast fault-response dynamics.

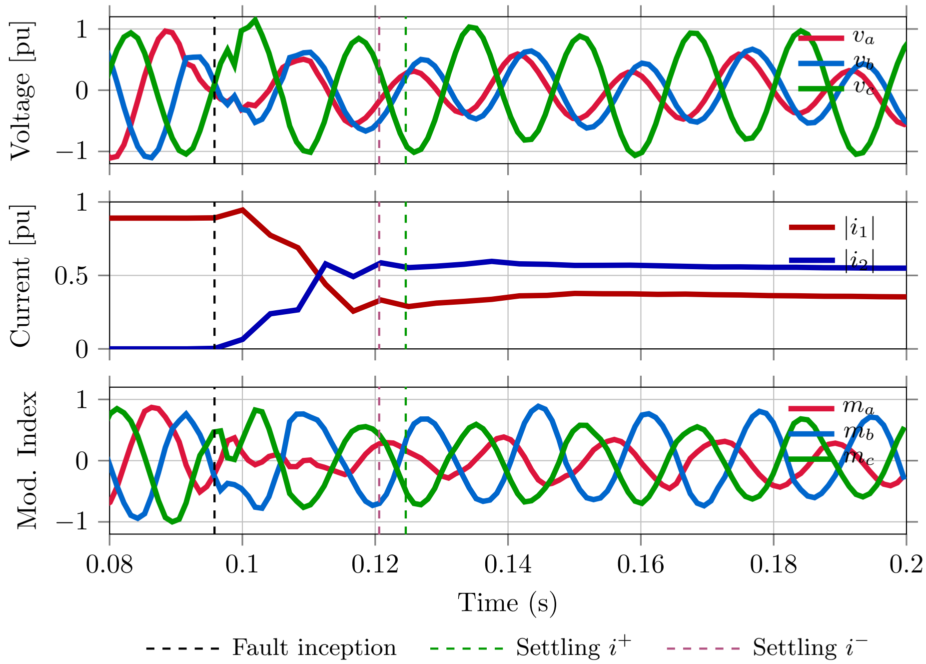

Figure 5.3: Voltages, sequence currents, and modulation index showing settling times without PWM saturation.

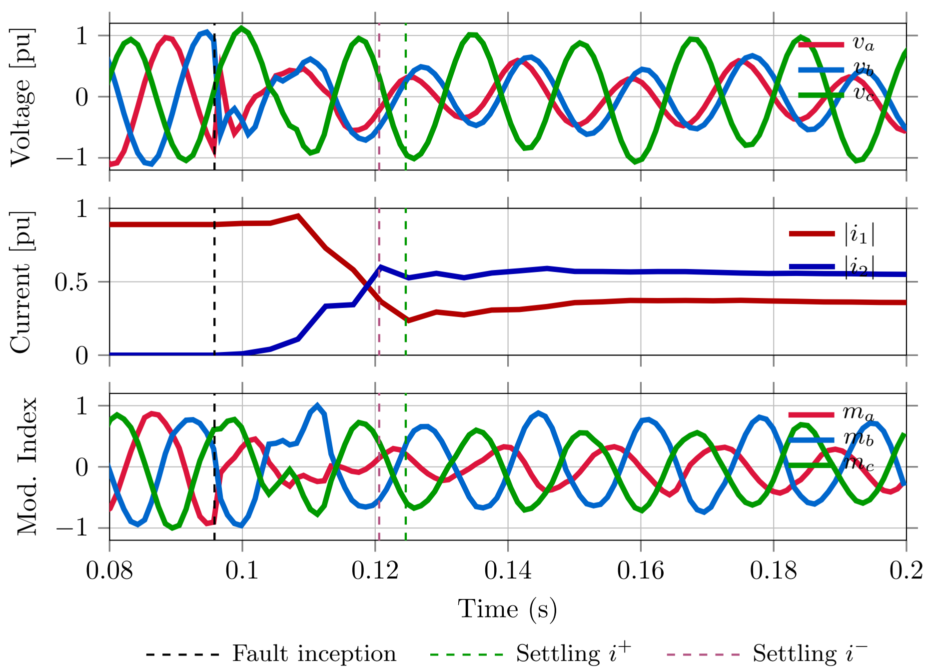

Figure 5.4: Voltages, sequence currents, and modulation index showing settling times under PWM saturation.

Settling trends vs. SOGI gain under BC and AG faults (no PWM clamp)

With the plant and PLL parameters fixed as listed in Table 5.2, the DSOGI gain k was swept, and the resulting positive- and negative-sequence settling times, t_s^+ and t_s^-, were measured. Two analytical references are overlaid in Fig. 5.5: (*i*) the DSOGI benchmark $t_s^{\text{SOGI}} \approx 21.23/k$ ms (for a 60 Hz grid), and (*ii*) the PLL floor $t_s^{\text{PLL}} \approx 4/\sigma_{\text{PLL}}$, where σ_{PLL} is estimated from the measured frequency transient. These curves represent the slowest real poles of the composite model in Sec. 5.3.

In the BC case, t_s^- closely tracks the PLL floor across the sweep, confirming that the negative-sequence channel is typically PLL-limited. t_s^+ is larger for small gains ($k \lesssim 0.8$), indicating a DSOGI-limited tail, and then drops toward the same PLL floor as k increases. For $k \gtrsim 2$ both sequences sit near 20-24 ms, consistent with a dominant PLL pole and a much faster current loop.

The AG case shows the same qualitative transition: small k yields a DSOGI-limited t_s^+, while moderate-to-high k brings both t_s^+ and t_s^- close to the PLL floor. A mild rise of t_s^{PLL} at very large k (caused by a modest reduction of the measured σ_{PLL} as the PLL is excited with increased high-frequency content from a fast DSOGI) produces the slight flattening or increase observed in $t_s^{\pm}$ at the far right of the sweep.

Across both fault types, once k is moderate ($\sim$ 1–2) the post-fault tail is governed by the PLL pole; for very small k the DSOGI pole can become rate-limiting, particularly for t_s^+. These observations match the composite model: the slowest real part among $\{\sigma_{\text{cur}}, \sigma_{\text{SOGI}}, \sigma_{\text{PLL}}\}$ sets the settling; here σ_{PLL} dominates after the DSOGI lag is reduced by increasing k.

PLL Bandwidth Effects on Post-Fault Settling

To investigate the influence of the PLL bandwidth on the post-fault settling behavior, a parameter sweep was performed by varying the proportional (k_p^{PLL}) and integral (T_i^{PLL}) gains of the PLL while maintaining a sufficiently high SOGI gain to reduce the interaction between the DSOGI and the PLL dynamics. As discussed in Section 5.3, the settling time of the inverter current response is expected to reduce with increasing PLL bandwidth since the dominant pole associated with the PLL moves further into the left-half plane, resulting in a faster dynamic response.

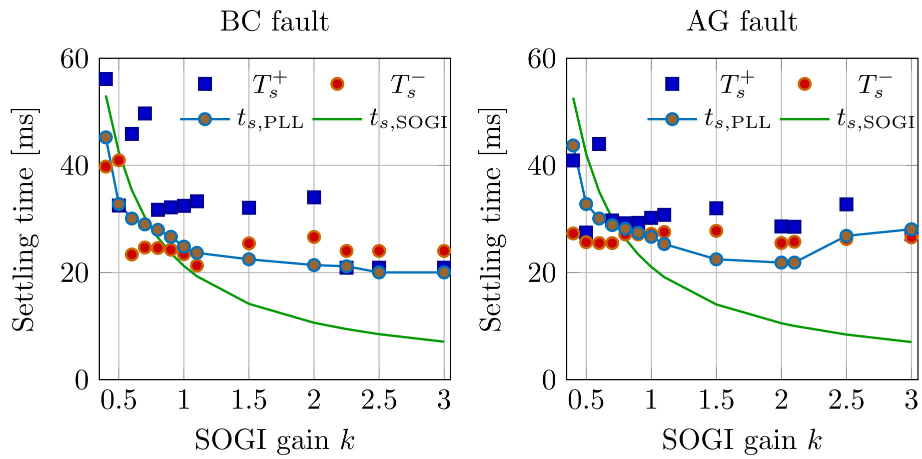

Figure 5.5: Measured settling times $T_s^{\pm}$ vs. SOGI gain, with analytical references: $t_{s,\text{SOGI}} \approx 21.23/k$ and $t_{s,\text{PLL}} \approx 4/\sigma_{\text{PLL}}$ (from measured frequency). For small k the DSOGI pole slows T_s^+; for moderate–high k both sequences become PLL-limited.

Table 5.3: Measured settling times for varying PLL gains (L_f=200 μH, R_f=0.5 mΩ, V_w=11 m/s, SOGI gain = 3 or 4).

Fault	T_p^{PLL}	T_i^{PLL}	T_s^+ [ms]	T_s^- [ms]
AG	100	30	25.9	25.9
AG	150	45	28.2	28.2
AG	200	60	25.4	25.4
BC	100	30	34.8	34.8
BC	150	45	37.6	37.6
BC	200	60	32.1	32.1

Table 5.3 summarizes the measured positive- and negative-sequence settling times (t_s^+ and t_s^-) along with the estimated PLL bandwidth σ_{PLL} for both AG and BC fault scenarios. For BC faults, which do not induce PWM saturation, the results show a clear trend: increasing σ_{PLL} (i.e., reducing T_p^{PLL} and t_i^{PLL}) leads to a decrease in both t_s^+ and t_s^-. This behavior aligns with the analytical relationship $t_s \approx 4/\sigma_{\text{PLL}}$, confirming that, once the DSOGI bandwidth is sufficiently higher than the PLL bandwidth, the PLL pole dominates the post-fault current dynamics.

For AG faults, however, the effect of PWM saturation remains significant despite the increased SOGI gain. PWM saturation introduces nonlinearities that limit the impact of PLL bandwidth improvements. While a slight reduction in t_s^+ and t_s^- is still observed with increasing σ_{PLL}, the improvement is less pronounced due to the saturation-induced current limiting.

Impact of Sustained PWM Saturation under High Fault Impedance

An additional test case was conducted to investigate the inverter behavior under high fault impedance and elevated PLL bandwidth. Specifically, a A–G fault with $R_{\text{fault}} = 1\ \Omega$ was applied—significantly higher than the $0.01\ \Omega$ impedance used in prior cases. As shown in Fig. 4.13, the inverter exhibits sustained PWM saturation throughout the post-fault period. In contrast to earlier cases where saturation was brief and self-clearing, the modulation indices here remain persistently clipped, and the inverter current becomes highly distorted.

While this phenomenon was initially attributed to high PLL gains interacting with the distorted PCC voltage waveform, a deeper analysis revealed that the root cause is oscillatory mode toggling between normal and FRT control modes. This behavior is described in detail in Section 4.4.1. The toggling repeatedly initiates and terminates reactive current injection, producing voltage swings near the detection threshold and causing the modulation to re-enter saturation with each switch. The result is prolonged clamping and loss of current control—despite the presence of only a moderate fault.

5.5.2 Experimental Setup for Validation

To validate the post-fault timing analysis (see Sec. 5.3), we performed experiments on a commercial 21 kW inverter. The test arrangement is shown in Fig. 4.14. On its DC side, the inverter under test (EUT) was fed by a programmable PV emulator; on its AC side it was tied to a power-hardware-in-the-loop grid simulator controlled in real time by an OPAL-RT controller to impose balanced and unbalanced faults. Because this inverter implements only positive-sequence current control during faults, our subsequent evaluation focuses exclusively on the positive-sequence current response.

Figure 4.15 illustrates the inverter's response to a three-phase-to-ground fault applied at t =0.20 s by abruptly reducing all three phase voltages from 1 pu to 0.5 pu while operating at full load (100% pre-fault power). The measured positive-sequence current settling time is 176.9 ms. Internal controller states were not accessible, so all conclusions rely on the point-of-common-coupling

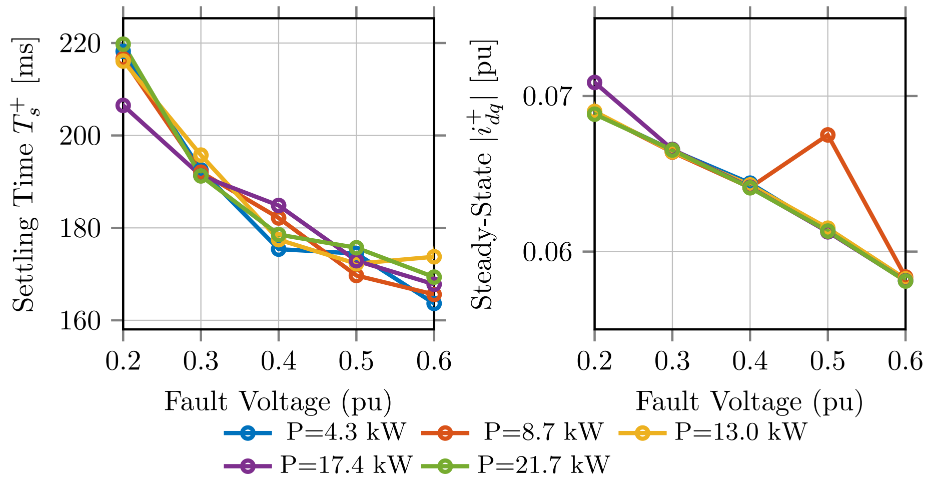

Figure 5.6: Experimental inverter response under three-phase-to-ground faults for multiple pre-fault power levels.

(PCC) measurements in Fig. 4.14. A closer look at the positive-sequence current waveform reveals a distinct change in slope at Δt_1 =30.3 ms after fault inception, suggesting that the inverter's ride-through controller detected the voltage sag and switched to its fault-current reference at that instant. The interval $[0, \Delta t_1]$ corresponds to the normal control mode—during which PWM saturation may have occurred—while the subsequent interval of approximately Δt_2 =146.6 ms is required to reach the new steady-state fault current. Although this total settling time exceeds our nominal simulation predictions, it remains within the range summarized in Table 5.1, and the relatively long tail points to a limited PLL bandwidth as the dominant factor.

To isolate the PLL's influence, we repeated the three-phase-to-ground test for fault voltages {0.2,0.3,0.4,0.5,0.6} pu. As shown in Fig. 5.6, the positive-sequence settling time increases monotonically with deeper voltage sags—a behavior consistent with slower PLL recovery under larger disturbances. Finally, to assess the effect of pre-fault operating point, we ran faults at {100, 80, 60, 40, 20}% of rated inverter power. Figure 5.6 demonstrates that while the steady-state fault current depends primarily on the depth of the voltage sag, it is largely independent of the pre-fault current level; however, in all cases the settling time again grows for deeper sags. These experimental observations corroborate our analytical conclusion (Sec. 5.4) that during the linear-recovery

Table 5.4: Measured faulted positive-sequence voltage ($|v^{+}_{postFault}|$), negative-sequence voltage ($|v^{-}_{postFault}|$), and settling time (t^{+}_{s}) under unbalanced fault conditions.

$\lvert v^{+}_{postFault}\rvert$ (pu)	$\lvert v^{-}_{postFault}\rvert$ (pu)	t^{+}_{s} (s)
0.6658	0.1660	0.3494
0.7496	0.2499	0.3153
0.6658	0.1660	0.3579
0.6663	0.1667	0.3347
0.6658	0.1662	0.3358
0.9000	0.1013	0.1542
0.8668	0.0652	0.1244
0.8673	0.0676	0.1310
0.8664	0.0654	0.1405

phase, the slowest of the three dominant loops—the PI current controller, the dual-SOGI sequence extractor, and the PLL—governs the inverter's current decay back to steady state.

To further evaluate the commercial inverter's post-fault current response, additional experiments were conducted under unbalanced fault conditions at the inverter terminals. The results are summarized in Table 5.4.

The results clearly show that higher $|v^{+}_{postFault}|$ values lead to shorter t^{+}_{s}, consistent with the findings for three-phase-to-ground faults (Fig. 5.6). For cases with $|v^{+}_{postFault}| \approx 0.66$ pu, the settling time is significantly longer ($\approx$ 0.33–0.36 s), whereas for cases with $|v^{+}_{postFault}| \approx 0.87$–0.90 pu, t^{+}_{s} reduces to 0.12–0.15 s. Variations in the negative-sequence voltage $|v^{-}_{postFault}|$ had minimal impact on T^{+}_{s}, as expected since the commercial inverter actively modulated only the positive-sequence current.

These observations further support the conclusion that the inverter's fault current response is primarily governed by the PLL dynamics. The longer settling times observed at deeper voltage dips indicate slower PLL re-synchronization under such conditions. The experimental results are therefore consistent with the analysis, confirming that in the linear recovery mode, the slowest control loop—in this case, the PLL—dominates the inverter's post-fault current response. Finally, we applied a BC fault with a 30° phase step at the fault inception to deliberately stress the inverter's PLL. In this case the commercial unit did not converge to a steady post-fault operating point;

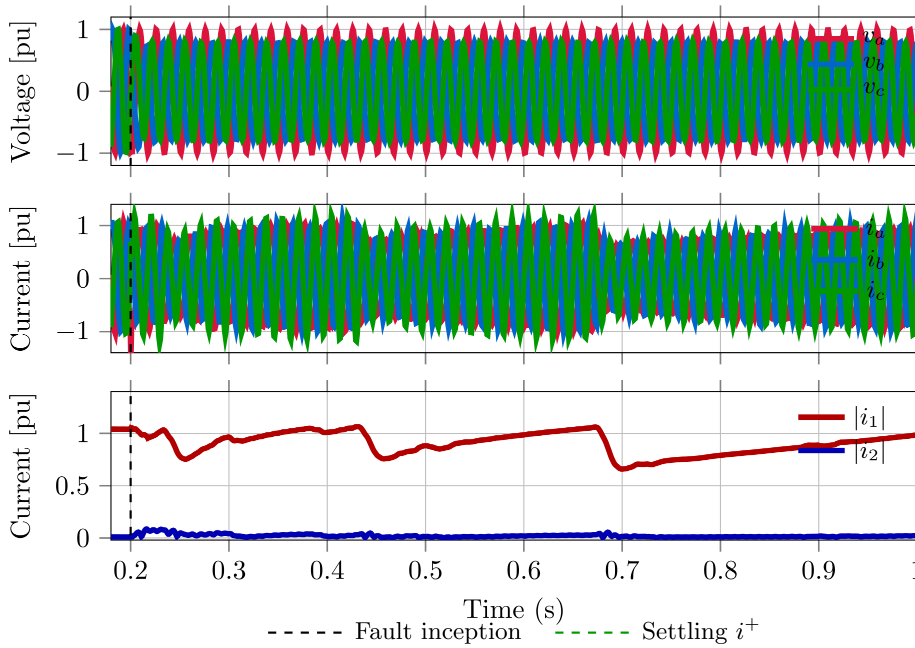

Figure 5.7: Voltages, current, and sequence currents of the commercial inverter for a BC fault with a 30° phase jump

instead, the positive-sequence fault current exhibited a persistent oscillation (no clear decay) as shown in Fig. 5.7.

A plausible mechanism is loss of PLL stability following the abrupt phase jump. The phase step drives the SRF-PLL outside its linear range, producing large phase/frequency errors that push the modulation index to its limits. The resulting PWM saturation distorts the PCC voltage seen by the PLL, which in turn sustains (and potentially amplifies) the oscillation rather than allowing a monotonic return to the steady state. Because the commercial inverter actively regulates only the positive-sequence current, alternative explanations involving negative-sequence control are unlikely. Overall, the experimental behavior is consistent with a PLL-dominated instability reinforced by saturation effects, matching the qualitative features observed in the simulation.

Chapter 6

Characterization of Subsystem Behavior – Part I: Saturation Phase

6.1 Introduction

Grid-connected IBRs such as wind and photovoltaic plants are now dominant contributors to new generation capacity worldwide [127, 128]. Their interconnection to power systems is subject to stringent performance requirements, notably IEEE Std 1547-2018 for distribution systems [95] and IEEE Std 2800-2022 for bulk power systems [94]. These standards mandate precise FRT behavior during grid disturbances. While inverter controls are designed to regulate output current tightly and maintain thermal limits, fault events can still produce momentary current spikes that exceed the rated limit. These spikes, though typically short in duration, can stress semiconductor devices, trip protection, and jeopardize compliance. Multiple mechanisms contribute to such overcurrents, but modulation and controller saturation—particularly SVPWM duty-ratio clipping—are often dominant during deep voltage sags.

When the commanded voltage vector exceeds the modulation boundary, SVPWM saturation clips the duty ratios, partially bypassing the inner current control loop. This distortion produces flat-topped or hexagonally modulated voltage waveforms, alters the instantaneous current trajectory, and increases harmonic distortion [129–132]. The resulting harmonic content, especially in the lower-order odd components, can rise significantly during saturation, with potential impacts on protection coordination and power quality compliance. PWM saturation rarely occurs in isolation—it often coincides with PI-controller saturation, abrupt mode changes after fault detection, and active current-limiting actions [133–135]. The coupled dynamics of these nonlinearities govern the sub-cycle to millisecond-scale post-fault response, ultimately determining whether the plant meets FRT and harmonic compliance thresholds.

Previous work has investigated aspects of IBR fault response such as control reconfiguration strategies [136, 137], current-limiter design [138, 139], and harmonic distortion mechanisms [131, 140]. Analytical models for post-fault transients often rely on low-order approximations or simulation-based parameter sweeps [52, 113, 141–143], which can obscure the individual contributions of modulation saturation, control-loop bandwidth, and sequence interactions. Experimental studies have confirmed that saturation-induced harmonics—especially the 5th and 7th orders—are linked to unbalanced fault conditions and non-fundamental sequence coupling [144, 145]. However, a closed-form framework capable of predicting both transient peak currents and harmonic spectra during PWM saturation has not been established.

Recent research has increasingly addressed how controller and modulation saturation influence both transient overcurrent and harmonic behavior in IBRs. [146] developed a dynamic model capturing current-limiter and PI-controller saturation effects under symmetrical and asymmetrical faults, but did not derive closed-form bounds for peak current magnitude. Similarly, [147] proposed a PI tuning framework with explicit saturation handling to enhance transient performance, yet the focus remained on controller design rather than analytical prediction of current peaks or harmonic spectra. Adaptive saturation strategies, as in [148], dynamically adjust current limits to maintain FRT stability, but stop short of providing parameter-based criteria for overcurrent risk or harmonic distortion.

More recently, [102] examined weak-grid scenarios, showing that sinusoidal PWM saturation combined with parameter uncertainties can significantly impact stability margins; however, their scope excluded explicit prediction of peak currents and harmonic content during faults. In parallel, [149] established a nonlinear systems framework for converters with saturation and bilinear terms, enabling rigorous stability and performance analysis, but without addressing the specific sequence-dependent transient and harmonic phenomena triggered by PWM saturation in grid-connected IBRs.

Earlier foundational work in motor-drive systems [150] demonstrated that over-modulation produces flat-topped voltage waveforms and additional harmonics, but did not address the grid-connected IBR context or the sequence-coupled harmonic generation mechanisms critical during FRT events.

Despite these advances, a closed-form framework that predicts both transient peak currents and the associated harmonic spectrum during PWM saturation—while accounting for PLL and sequence-extractor dynamics—has not yet been established. This gap limits the ability to directly assess whether a given IBR configuration will violate current ratings or harmonic limits under grid fault conditions based solely on controller and plant parameters.

The present work extends existing knowledge by deriving an exact dq-domain solution for inverter current dynamics during PWM saturation. The formulation explicitly accounts for the discontinuous voltage application caused by duty-ratio clipping and incorporates first-order corrections for PLL frequency and phase transients, as well as sequence-extractor settling effects. From this solution, we obtain closed-form expressions for two critical metrics: (*i*) upper and lower bounds on transient peak current, and (*ii*) per-phase magnitudes of dominant harmonics, expressed directly in terms of current controller gains, L_f–R_f filter parameters, pre-fault current magnitude, and grid voltage conditions. This enables rapid, parameter-driven assessment of whether a plant configuration will exceed current ratings or harmonic distortion limits under specified FRT scenarios. The analytical results are verified through EMT simulations using a detailed IEEE Std 2800-compliant Type-IV wind plant model. By directly connecting control-structure dynamics to measurable peak and harmonic behaviors, the proposed framework provides both a rigorous theoretical basis and actionable diagnostic tools for mitigating PWM saturation impacts in modern inverter-based resources.

The remainder of this chapter is organized as follows. Section 6.2 reviews the sequence of events and control actions governing IBR fault dynamics. Section 6.3 formulates the closed-form dq-domain model of PWM saturation, and Section 6.4 establishes existence, uniqueness, and norm estimates for the resulting system. Section 6.5 applies the model to derive analytical bounds on peak current, while Section 6.6 uses the same framework to quantify harmonic content. Section 5.5

validates the predictions through electromagnetic transient simulations. Finally, Section 6.7 summarizes the findings and outlines directions for future work.

6.2 IBR Dynamics During Fault

The detailed grid-following inverter model, including the control architecture, sequence-domain formulation, modulation, filter dynamics, and saturation mechanisms, is developed in Section 4.2.

6.3 Closed-Form dq-Domain Dynamics During PWM Saturation

6.3.1 Setup and Assumptions Over a Clamp Window

During a PWM clamp the converter applies a saturated voltage vector with fixed magnitude $V_{\max}$ and (piecewise) constant direction $\mathbf{e}_v \in \mathbb{R}^2$,

$$\mathbf{v}_{dq}^{\text{sat}} = V_{\max}\, \mathbf{e}_v, \qquad \mathbf{e}_v := \frac{\tilde{\mathbf{v}}_{dq}^{\text{ctrl}}}{\|\tilde{\mathbf{v}}_{dq}^{\text{ctrl}}\|}, \tag{6.1}$$

where $\tilde{\mathbf{v}}_{dq}^{\text{ctrl}}$ is the pre-saturation control voltage vector. The unit vector $\mathbf{e}_v$ encodes only the orientation of the applied saturated voltage in the dq plane; it remains constant within each clamp interval but may change between intervals as the controller updates its saturation direction. Anti-windup freezes the PI integrator so the command direction remains nearly constant until $\|\tilde{\mathbf{v}}_{dq}^{\text{ctrl}}(t)\|$ decays back below $V_{\max}$. Over a single clamp episode (a few ms), we take: (*i*) $\mathbf{e}_v$ constant, (*ii*) the PCC voltage estimate $\mathbf{v}_{g,dq}$ and the PLL speed $\hat{\omega}$ varying slowly (we treat both constant in the base solution and add a first-order correction).

6.3.2 Exact RL Dynamics in the PLL Synchronous Frame

Let $\mathbf{i} = \begin{bmatrix} i_d & i_q \end{bmatrix}^{\mathsf{T}}$ denote the filter current in the frame rotating at the PLL speed $\hat{\omega}$ and angle $\hat{\theta}$. Transforming from $\alpha\beta$ to dq yields the standard inductor dynamics:

$$L_f \dot{\mathbf{i}} \;=\; -R_f \mathbf{i} \;+\; \left(\mathbf{v}_{dq}^{\text{sat}} - \mathbf{v}_{g,dq}\right) \;+\; L_f \hat{\omega}\, \mathbf{J}\, \mathbf{i}, \qquad \mathbf{J} = \begin{bmatrix} 0 & -1 \\ 1 & 0 \end{bmatrix}. \tag{6.2}$$

Hence

$$\dot{\mathbf{i}} \;=\; \underbrace{\left(-\tfrac{R_f}{L_f}\mathbf{I} + \hat{\omega}\, \mathbf{J}\right)}_{\mathbf{A}} \mathbf{i} \;+\; \underbrace{\tfrac{1}{L_f}\left(\mathbf{v}_{dq}^{\text{sat}} - \mathbf{v}_{g,dq}\right)}_{\mathbf{b}}. \tag{6.3}$$

On any interval where $\mathbf{A}$ and $\mathbf{b}$ are constant, the exact solution is

$$\mathbf{i}(t) \;=\; e^{\mathbf{A}(t-t_0)}\, \mathbf{i}(t_0) \;+\; \mathbf{A}^{-1}\left(e^{\mathbf{A}(t-t_0)} - \mathbf{I}\right) \mathbf{b}, \qquad t \in [t_0, t_1]. \tag{6.4}$$

The equilibrium (forced) current is $\mathbf{i}_\infty = -\mathbf{A}^{-1}\mathbf{b}$ and the solution can be written compactly as

$$\mathbf{i}(t) \;=\; \mathbf{i}_\infty \;+\; e^{\mathbf{A}(t-t_0)}\left(\mathbf{i}(t_0) - \mathbf{i}_\infty\right). \tag{6.5}$$

Let $a := -R_f/L_f$. Using $\mathbf{J}^2 = -\mathbf{I}$ and $(a\mathbf{I} + \hat{\omega}\mathbf{J})$ commuting with itself,

$$e^{\mathbf{A}\tau} \;=\; e^{(a\mathbf{I}+\hat{\omega}\mathbf{J})\tau} \;=\; e^{a\tau}\left(\cos(\hat{\omega}\tau)\, \mathbf{I} + \sin(\hat{\omega}\tau)\, \mathbf{J}\right), \qquad \tau := t - t_0. \tag{6.6}$$

Moreover,

$$\mathbf{A}^{-1} \;=\; \frac{1}{a^2 + \hat{\omega}^2}\, (a\mathbf{I} - \hat{\omega}\, \mathbf{J}), \qquad (a, \hat{\omega}) \neq (0, 0). \tag{6.7}$$

Substituting (6.6)–(6.7) into (6.4) gives a fully explicit expression.

6.3.3 First-Order Corrections for PLL Transients

If $\hat{\omega}$ and $\mathbf{v}_{g,dq}$ vary during the clamp, write $\hat{\omega}(t) = \hat{\omega}_0 + \Delta\omega(t)$ and $\mathbf{v}_{g,dq}(t) = \mathbf{v}_{g,dq,0} + \Delta\mathbf{v}_g(t)$. The exact solution of the time-varying system $\dot{\mathbf{i}} = \mathbf{A}(t)\mathbf{i} + \mathbf{b}(t)$ is

$$\mathbf{i}(t) = \Phi(t,t_0)\,\mathbf{i}(t_0) + \int_{t_0}^{t} \Phi(t,\tau)\,\mathbf{b}(\tau)\,d\tau,$$
$$\dot{\Phi} = \mathbf{A}(t)\Phi, \ \ \Phi(t_0,t_0) = \mathbf{I}. \tag{6.8}$$

For small variations, linearize around $\mathbf{A}_0 := a\mathbf{I} + \hat{\omega}_0\mathbf{J}$ and $\mathbf{b}_0$:

$$\mathbf{A}(t) = \mathbf{A}_0 + \Delta\omega(t)\mathbf{J}, \qquad \mathbf{b}(t) = \mathbf{b}_0 - \tfrac{1}{L_f}\Delta\mathbf{v}_g(t).$$

Using variation of constants,

$$\begin{aligned} \mathbf{i}(t) \approx\; & e^{\mathbf{A}_0(t-t_0)}\mathbf{i}(t_0) + \mathbf{A}_0^{-1}\big(e^{\mathbf{A}_0(t-t_0)} - \mathbf{I}\big)\mathbf{b}_0 \\ & + \int_{t_0}^{t} e^{\mathbf{A}_0(t-\tau)} \Big[\Delta\omega(\tau)\,\mathbf{J}\,\mathbf{i}_0(\tau) \;-\; \tfrac{1}{L_f}\Delta\mathbf{v}_g(\tau)\Big]\,d\tau, \end{aligned} \tag{6.9}$$

where $\mathbf{i}_0(\tau)$ denotes the base (constant-parameter) solution (6.5). The integral term is an explicit first-order correction capturing the dynamic lag introduced by PLL and estimator states.

6.3.4 Projection Model: Circle vs. Hexagon

The saturated vector used above can be taken as a circular projection or a more accurate hexagon (sector-wise affine) projection for SVPWM. The closed-form solutions (6.5)–(6.7) remain valid with piecewise constant $\mathbf{b}$; sector transitions induce piecewise intervals $[t_k, t_{k+1})$ with different $\mathbf{e}_v^{(k)}$.

6.3.5 Steady (Forced) Current During Clamp and Unclamp Initial Conditions

For constant parameters on $[t_0, t_1)$, the forced current is

$$\mathbf{i}_\infty = -\mathbf{A}^{-1}\mathbf{b} = -\frac{1}{a^2 + \hat{\omega}^2}\,(a\mathbf{I} - \hat{\omega}\mathbf{J})\,\tfrac{1}{L_f}\big(\mathbf{v}_{dq}^{\text{sat}} - \mathbf{v}_{g,dq}\big). \tag{6.10}$$

The current at unclamp t_1 provides the exact initial condition for the post-clamp linear recovery model: $\mathbf{i}(t_1) = \mathbf{i}_\infty + e^{\mathbf{A}(t_1 - t_0)}\big(\mathbf{i}(t_0) - \mathbf{i}_\infty\big)$. Equations (6.5)–(6.10) furnish: (*i*) exact time-domain currents during clamp, (*ii*) explicit forced (steady) currents under the saturated drive, (*iii*) precise initial conditions for the post-clamp linear recovery, and (*iv*) a principled way to include PLL dynamics via (6.9).

6.4 Existence, Uniqueness and Norm Estimates for Perturbed dq-Domain Clamp Models

We consider the time-varying affine model on a clamp sub-interval $[t_0, t_1]$:

$$\begin{aligned} \dot{\mathbf{i}}(t) &= \mathbf{A}(t)\,\mathbf{i}(t) + \mathbf{b}(t), \\ \mathbf{A}(t) = a\mathbf{I} + \hat{\omega}(t)\mathbf{J}, &\quad \mathbf{b}(t) = \tfrac{1}{L_f}\big(\mathbf{v}_{dq}^{\text{sat}} - \mathbf{v}_{g,dq}(t)\big), \end{aligned} \tag{6.11}$$

Let $\hat{\omega}(t) = \hat{\omega}_0 + \Delta\omega(t)$ and $\mathbf{v}_{g,dq}(t) = \mathbf{v}_{g,dq,0} + \Delta\mathbf{v}_g(t)$, where $\Delta\omega, \Delta\mathbf{v}_g$ are bounded on $[t_0, t_1]$.

Lemma 6.4.1 (Existence & Uniqueness). *Suppose $\hat{\omega}(\cdot)$ and $\mathbf{v}_{g,dq}(\cdot)$ are continuous on $[t_0, t_1]$. Then* (6.11) *admits a unique solution $\mathbf{i}(\cdot) \in C^1([t_0, t_1]; \mathbb{R}^2)$ for any initial condition $\mathbf{i}(t_0) = \mathbf{i}_0$.*

Proof. The right-hand side of (6.11) is affine in $\mathbf{i}$ with continuous coefficients. By the Picard–Lindelöf theorem, linear ODEs with continuous coefficients are globally Lipschitz in $\mathbf{i}$ on compact intervals, hence admit unique solutions. □

Let $\mathbf{A}_0 := a\mathbf{I} + \hat{\omega}_0\mathbf{J}$ and $\mathbf{b}_0 := \frac{1}{L_f}\big(\mathbf{v}_{dq}^{\text{sat}} - \mathbf{v}_{g,dq,0}\big)$. Denote by

$$\mathbf{i}_0(t) = e^{\mathbf{A}_0(t-t_0)}\,\mathbf{i}(t_0) + \mathbf{A}_0^{-1}\big(e^{\mathbf{A}_0(t-t_0)} - \mathbf{I}\big)\mathbf{b}_0 \tag{6.12}$$

the base (constant-parameter) solution on $[t_0, t_1]$ and define the deviation $\mathbf{e}(t) := \mathbf{i}(t) - \mathbf{i}_0(t)$.

Lemma 6.4.2 (Matrix exponential norm)**.** *For $\mathbf{A}_0 = a\mathbf{I} + \hat{\omega}_0\mathbf{J}$ with $a < 0$, we have*

$$e^{\mathbf{A}_0\tau} = e^{a\tau}\big(\cos(\hat{\omega}_0\tau)\mathbf{I} + \sin(\hat{\omega}_0\tau)\mathbf{J}\big), \qquad \big\|e^{\mathbf{A}_0\tau}\big\|_2 = e^{a\tau},\ \ \tau \geq 0. \tag{6.13}$$

Proof. Use $\mathbf{J}^2 = -\mathbf{I}$ to obtain the closed form; the factor multiplying $e^{a\tau}$ is a rotation, which is unitary in the 2-norm. $\square$

Lemma 6.4.3 (First-order deviation bound)**.** *Assume $\Delta\omega, \Delta\mathbf{v}_g$ are bounded on $[t_0, t_1]$ with $\|\Delta\omega\|_\infty := \sup_{t\in[t_0,t_1]} |\Delta\omega(t)|$ and $\|\Delta\mathbf{v}_g\|_\infty := \sup_{t\in[t_0,t_1]} \|\Delta\mathbf{v}_g(t)\|$. Then, to first order (i.e., evaluating the perturbation on the base trajectory), the deviation satisfies*

$$\|\mathbf{e}(t)\| \leq \int_{t_0}^{t} \big\|e^{\mathbf{A}_0(t-\tau)}\big\| \,\Big(\|\Delta\omega(\tau)\|\,\|\mathbf{J}\,\mathbf{i}_0(\tau)\| + \tfrac{1}{L_f}\|\Delta\mathbf{v}_g(\tau)\|\Big)\,d\tau \tag{6.14}$$

$$\leq \underbrace{\left(\sup_{\tau\in[t_0,t]} \|\mathbf{i}_0(\tau)\|\right)}_{M_i(t)} \|\Delta\omega\|_\infty \,\frac{1 - e^{a(t-t_0)}}{-a} \;+\; \frac{\|\Delta\mathbf{v}_g\|_\infty}{L_f}\,\frac{1 - e^{a(t-t_0)}}{-a}. \tag{6.15}$$

Proof. Variation of constants for the time-varying system yields

$$\mathbf{e}(t) = \int_{t_0}^{t} e^{\mathbf{A}_0(t-\tau)}\,\Big(\Delta\omega(\tau)\,\mathbf{J}\,\mathbf{i}_0(\tau) - \tfrac{1}{L_f}\Delta\mathbf{v}_g(\tau)\Big)\,d\tau \tag{6.16}$$

after neglecting higher-order terms (the $\mathbf{e}$ inside the integrand). Taking norms, using Lemma 6.4.2, $\|\mathbf{J}\|_2 = 1$, and the sup bounds gives (6.14). The integral of $e^{a(t-\tau)}$ over $[t_0, t]$ equals $(1 - e^{a(t-t_0)})/(-a)$, yielding (6.15). $\square$

The bound depends on the envelope of the base trajectory. A convenient estimate is obtained from (6.12):

$$\|\mathbf{i}_0(\tau)\| \leq \|\mathbf{i}_\infty\| + \|\mathbf{i}(t_0) - \mathbf{i}_\infty\| \, e^{a(\tau - t_0)}, \qquad \mathbf{i}_\infty = -\mathbf{A}_0^{-1}\mathbf{b}_0, \tag{6.17}$$

so that $M_i(t) \leq \|\mathbf{i}_\infty\| + \|\mathbf{i}(t_0) - \mathbf{i}_\infty\|$.

Corollary 6.4.4 (Small-window approximation)**.** *Let* $\Delta t := t_1 - t_0$*. Then*

$$\sup_{t\in[t_0,t_1]} \|\mathbf{e}(t)\| \;\leq\; \left(M_i \, \|\Delta\omega\|_\infty + \frac{\|\Delta \mathbf{v}_g\|_\infty}{L_f} \right) \frac{1 - e^{a\Delta t}}{-a} \;=\; \mathcal{O}(\Delta t) \quad \textit{as } \Delta t \to 0^+. \tag{6.18}$$

In particular, over millisecond-scale clamp windows with $|a| = \frac{R_f}{L_f} = \tau_c^{-1}$ *in the 100–500* s^{-1} *range, the perturbation is linearly small in* Δt *and suppressed by the stable factor* $1 - e^{a\Delta t}$*.*

Remark 6.4.5 (Piecewise-constant actuator direction)**.** *The same bounds hold when* $\mathbf{v}_{dq}^{sat}$ *is sector-wise constant (SVPWM hexagon). The interval* $[t_0, t_1]$ *is then partitioned into finitely many sub-intervals, and the estimate applies on each, with continuity of* $\mathbf{i}$ *enforced at the switching instants; the global bound is the maximum of the sub-interval bounds.*

Remark 6.4.6 (Interpretation)**.** *Lemma 6.4.3 quantifies the statement that dynamic lag introduced by PLL and estimator states is small over a clamp window: the deviation scales with the sup norms of* $\Delta\omega$ *and* $\Delta\mathbf{v}_g$ *and with the effective window length through* $(1 - e^{a\Delta t})/(-a) \leq \Delta t$*.*

Lemma 6.4.7 (Forced-current norm bound)**.** *Let* $\mathbf{i}_\infty$ *in* (6.10) *denote the forced (steady-state) current for the constant-parameter model on* $[t_0, t_1]$*. Its Euclidean norm satisfies*

$$\|\mathbf{i}_\infty\| = \frac{\left\|\mathbf{v}_{dq}^{\mathrm{sat}} - \mathbf{v}_{g,dq,0}\right\|}{L_f\sqrt{a^2 + \hat{\omega}_0^2}}, \tag{6.19}$$

and, in particular, under a circular projection with $\|\mathbf{v}_{dq}^{\mathrm{sat}}\| = V_{\max}$*,*

$$\|\mathbf{i}_\infty\| \leq \frac{V_{\max} + \|\mathbf{v}_{g,dq,0}\|}{L_f\sqrt{a^2 + \hat{\omega}_0^2}}. \tag{6.20}$$

Proof. Since $\mathbf{A}_0 = a\mathbf{I} + \hat{\omega}_0\mathbf{J}$ is invertible for $(a, \hat{\omega}_0) \neq (0, 0)$, its inverse is

$$\mathbf{A}_0^{-1} = \frac{a\mathbf{I} - \hat{\omega}_0\mathbf{J}}{a^2 + \hat{\omega}_0^2}. \tag{6.21}$$

The matrix $(a\mathbf{I} - \hat{\omega}_0\mathbf{J})$ is orthogonal up to the scale factor $\sqrt{a^2 + \hat{\omega}_0^2}$, so its action preserves vector norms up to that scale. Applying this property to (6.10) gives (6.19). Finally, using the triangle inequality and $\|\mathbf{v}_{dq}^{\text{sat}}\| = V_{\max}$ in the circular-projection case yields (6.20). $\square$

Corollary 6.4.8 (Bound on Current Magnitude)**.** *Under the constant-parameter base model* (6.12)*, the instantaneous current magnitude satisfies*

$$M_i(t) \;\le\; \underbrace{\frac{V_{\max} + \|\mathbf{v}_{g,dq,0}\|}{L_f\sqrt{a^2 + \hat{\omega}_0^2}}}_{\textit{steady–state (forced) term}} \;+\; \underbrace{\|\mathbf{i}(t_0)\|}_{\textit{transient (initial–condition) term}}. \tag{6.22}$$

Here the first term corresponds to the magnitude of the particular solution driven by the saturated and grid voltages, while the second term reflects the homogeneous response from the initial condition.

Worst–case bound: *If no tighter information is available on $\|\mathbf{i}(t_0)\|$, a conservative choice is to bound it by the steady–state term:*

$$\|\mathbf{i}(t_0)\| \;\le\; \frac{V_{\max} + \|\mathbf{v}_{g,dq,0}\|}{L_f\sqrt{a^2 + \hat{\omega}_0^2}}. \tag{6.23}$$

Substituting this into (6.22) *yields*

$$M_i(t) \;\le\; \frac{V_{\max} + \|\mathbf{v}_{g,dq,0}\|}{L_f\sqrt{a^2 + \hat{\omega}_0^2}} + \frac{V_{\max} + \|\mathbf{v}_{g,dq,0}\|}{L_f\sqrt{a^2 + \hat{\omega}_0^2}}. \tag{6.24}$$

In this special case the bound is simply twice the steady–state magnitude. If $\mathbf{i}(t_0) = \mathbf{i}_\infty$, the transient term vanishes and $M_i(t) = \|\mathbf{i}_\infty\|$.

Remark 6.4.9 (Interpretation)**.** *The denominator* $\sqrt{a^2 + \hat{\omega}_0^2}$ *combines the resistive decay rate* $|a| = R_f/L_f$ *and synchronous rotation* $\hat{\omega}_0$*; increasing either reduces the achievable forced current for a given voltage drive.*

6.5 Peak-Current Exceedance Condition During Clamp

During PWM saturation, the dq-frame current evolves according to Lemma 6.4.7, with the steady (forced) value $\mathbf{i}_\infty$ determined by (6.19). Let the initial magnitude at clamp entry be $I_0 = \|\mathbf{i}(t_0)\|$. The exact magnitude trajectory on the clamp interval is

$$\|\mathbf{i}(t)\| = \left\|\mathbf{i}_\infty + e^{\mathbf{A}_0(t-t_0)}\big(\mathbf{i}(t_0) - \mathbf{i}_\infty\big)\right\|, \tag{6.25}$$

where $\mathbf{A}_0$ generates a rotation with decay rate $a = -R_f/L_f$.

6.5.1 Bound and Exceedance Condition

Because the rotation preserves the norm of the offset, the magnitude satisfies

$$\|\mathbf{i}(t)\| \ \leq \ \|\mathbf{i}_\infty\| + e^{a(t-t_0)}\,\|\mathbf{i}(t_0) - \mathbf{i}_\infty\|, \quad a < 0, \tag{6.26}$$

tight at $t = t_0$ and as $t \to \infty$. Over-current is guaranteed if

$$\max\{I_0,\ \|\mathbf{i}_\infty\|\} > I_{\max}, \tag{6.27}$$

in which case the violation occurs immediately (if $I_0 > I_{\max}$) or after a delay

$$t_{\text{exceed}} - t_0 = \frac{1}{|a|}\ln\!\left(\frac{\|\mathbf{i}_\infty\| - I_0}{\|\mathbf{i}_\infty\| - I_{\max}}\right), \quad \|\mathbf{i}_\infty\| > I_{\max} > I_0. \tag{6.28}$$

6.5.2 Worst-Case Peak Envelope

From (6.19) and (6.25)–(6.27), two key observations follow:

- Smaller L_f or larger ΔV_{pu} increases $\|\mathbf{i}_\infty\|_{\text{pu}}$.
- For deep sags with reactive-priority LVRT, $\|\mathbf{i}_\infty\|_{\text{pu}}$ may exceed $I_{\max,\text{pu}}$ even if I_0 was nominal.

This provides a direct parametric test—based on pre-fault current, sag depth, and filter parameters— for whether LVRT operation will transiently violate current ratings during PWM saturation.

6.5.3 Peak Bound and Fault-Type Generalization

The clamp-interval solution is

$$\mathbf{i}(t) = \mathbf{i}_\infty + e^{a(t-t_0)}\, R\big(\omega(t-t_0)\big)\,\big(\mathbf{i}(t_0) - \mathbf{i}_\infty\big), \tag{6.29}$$

where $R(\theta)$ is a 2×2 rotation, $\omega \approx \hat{\omega}_0$. Let

$$c := \|\mathbf{i}_\infty\|, \quad d := \|\mathbf{i}(t_0) - \mathbf{i}_\infty\|, \tag{6.30}$$

and θ_0 be the initial angle between $\mathbf{i}_\infty$ and the offset.

Lemma 6.5.1 (Peak-current bound)**.** *The peak magnitude satisfies*

$$\max\big(c,\, \|\mathbf{i}(t_0)\|\big) \;\le\; \sup_{t \ge t_0} \|\mathbf{i}(t)\| \;\le\; c + d, \tag{6.31}$$

with equality at the first alignment time $t_{\text{align}} = t_0 + \frac{-\theta_0 + 2\pi k}{\omega}$ *for* $\omega \neq 0$*. If* $\omega = 0$*,* $\|\mathbf{i}(t)\|$ *changes monotonically.*

Fig. 6.1 illustrates the geometric interpretation of peak current during PWM clamping: the current vector rotates around $\mathbf{i}_\infty$ as its offset magnitude decays exponentially. The peak occurs when the offset aligns with $\mathbf{i}_\infty$ and depends only on:

- c, determined by $\mathbf{v}_{dq}^{\text{sat}}$, $\mathbf{v}_{g,dq,0}$, and L_f;
- d, representing the pre-fault current offset.

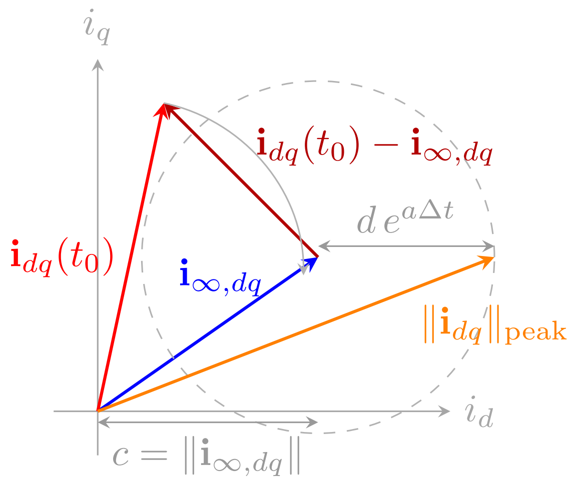

Figure 6.1: Geometric interpretation of peak current during PWM clamp: the current vector rotates around $\mathbf{i}_\infty$ with exponential decay in the offset magnitude. The peak occurs when the decaying offset aligns with $\mathbf{i}_\infty$.

Both c and d are measurable from EMT simulations or experiments, enabling the use of (6.5.1) for any fault type, depth, or power factor without requiring internal control parameters.

6.6 Harmonic Analysis During PWM Saturation Derived from Closed-Form Dynamics

We connect the closed-form dq-domain solution and the perturbation bounds to a constructive harmonics analysis of the line current during the clamp.

6.6.1 Decomposition of the Applied Drive and Solution Structure

Let $v_{a,b,c}(t)$ be the phase-to-neutral voltages applied by the saturated bridge. During clamp, per-phase saturation (duty-ratio clipping) yields a flat-topped waveform, as illustrated in Fig. 6.2, or, in the case of SVPWM, a sector-wise constant hexagon projection, so

$$v_x(t) = \sum_{k\in\mathbb{Z}} V_{x,k}\, e^{\mathrm{j}k\omega t}, \qquad x \in \{a, b, c\}, \tag{6.32}$$

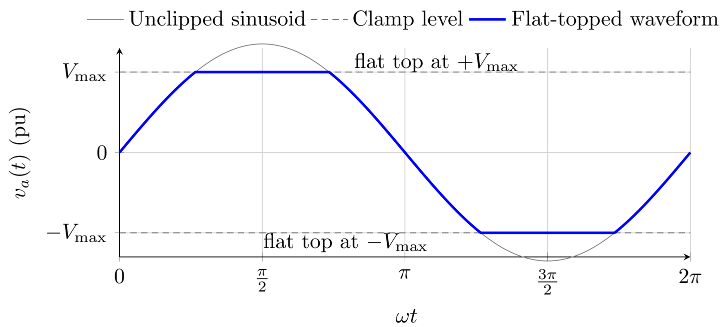

Figure 6.2: Example phase voltage $v_a(t)$ during PWM clamp. Duty-ratio clipping produces a flat-topped waveform: $v_a(t) = \mathrm{sat}_{[-V_{\max},\,V_{\max}]}(\hat{V}\sin(\omega t))$.

with $V_{x,-k} = V_{x,k}^*$ and $V_{x,0} = 0$ (no DC in three-wire). Define the corresponding $\alpha\beta$ series $V_{\alpha\beta,k}$ (Clarke transform) and the dq series $V_{dq,k} := e^{-\mathrm{j}k\hat{\theta}(t)}V_{\alpha\beta,k}$ in the PLL frame. For time-invariant analysis over a clamp sub-interval we treat $\hat{\omega}(t) \approx \hat{\omega}_0$ (steady rotation).

Plant seen by the k-th harmonic.

For a series L_f–R_f filter, the line current in $\alpha\beta$ satisfies (component-wise)

$$L_f\dot{i}_\alpha = -R_f i_\alpha + v_\alpha - v_{g,\alpha}, \qquad L_f\dot{i}_\beta = -R_f i_\beta + v_\beta - v_{g,\beta}. \tag{6.33}$$

At the harmonic frequency $k\omega$ the phasor relation is linear:

$$I_{\alpha\beta,k} \;=\; \frac{V_{\alpha\beta,k} - V_{g,\alpha\beta,k}}{R_f + \mathrm{j}k\omega L_f}. \tag{6.34}$$

For $k \geq 2$, $V_{g,\alpha\beta,k} = 0$ (grid is fundamental-only), so

$$I_{\alpha\beta,k} \;=\; \frac{V_{\alpha\beta,k}}{R_f + \mathrm{j}k\omega L_f}, \quad k \geq 2. \tag{6.35}$$

Equation (6.35) is a direct consequence of the closed-form affine solution (Section 6.3): the forced solution at each excitation frequency is obtained by replacing $\omega \mapsto k\omega$ in the transfer $1/(R_f + \mathrm{j}\omega L_f)$, while the natural term is the exponentially decaying rotation $e^{(a+\mathrm{j}\hat{\omega}_0)t}$ that creates only inter-harmonic leakage (bounded by Lemma 6.4.3).

6.6.2 Fundamental Component from Forced Solution (Link to Lemma 6.4.7)

At $k = 1$, the dq forced current from (6.10) yields the fundamental magnitude

$$\|\mathbf{i}_{\infty,1}\| = \frac{\left\|\mathbf{v}_{dq,1}^{\text{sat}} - \mathbf{v}_{g,dq,1}\right\|}{L_f\sqrt{a^2 + \hat{\omega}_0^2}}, \qquad a = -R_f/L_f. \tag{6.36}$$

In balanced conditions with circular projection, $\mathbf{v}_{dq,1}^{\text{sat}}$ is a constant vector in the PLL frame (magnitude $V_{\max}$), so (6.36) gives the exact fundamental current during clamp. This is precisely the $k = 1$ case of (6.34) written in dq form.

6.6.3 Higher-Order Harmonics from Per-Phase Saturation

Per-phase saturation produces the Fourier coefficients $V_{x,k}$ of a clipped sine. For a symmetric flat-top with clipping angle $\theta_c = \arcsin\left(\frac{V_{\max}}{V_{\text{pk}}}\right)$, only odd k appear in each phase voltage:

$$V_{x,k} \;=\; \frac{1}{\pi}\int_0^{2\pi} v_x(\theta)\, e^{-\mathrm{j}k\theta}\, d\theta, \quad k \in \{1, 3, 5, \dots\}. \tag{6.37}$$

For the symmetric flat-top, evaluating (6.37) yields

$$V_{x,k} = \frac{2V_{\text{pk}}}{k\pi}\left[\sin(k\theta_c) + (\pi/2 - \theta_c)\cos(k\theta_c)\right], \quad k \text{ odd}, \tag{6.38}$$

where V_{pk} is the peak of the unclipped sine. Transforming to $\alpha\beta$ and using (6.35) yields the line-current harmonics:

$$|I_k| \;=\; \frac{|V_{\alpha\beta,k}|}{\sqrt{R_f^2 + (k\omega L_f)^2}}, \qquad k \in \{5, 7, 11, 13, \dots\}. \tag{6.39}$$

Triplen harmonics (3rd, 9th, ...) cancel in line currents of a three-wire system.

6.6.4 SVPWM Hexagon Case (Sector-wise Constant Approximation)

Under deep clamp the SVPWM hexagon projection is well approximated by sector-wise constant phase voltages over 60° intervals, approaching six-step behavior. Then the well-known coefficients (per phase) satisfy $|V_k| \propto 1/k$ for $k = 6m \pm 1$ and $V_k \approx 0$ for $k = 6m$ (ideal six-step, balanced). Consequently, for an L_f–R_f line,

$$|I_k| \;\propto\; \frac{1}{k} \cdot \frac{1}{\sqrt{R_f^2 + (k\omega L_f)^2}} \;\simeq\; \frac{1}{k^2\,\omega L_f} \quad (k\omega L_f \gg R_f), \tag{6.40}$$

with $k \in \{5, 7, 11, 13, \dots\}$ (the $6m \pm 1$ family).

6.6.5 Bounds and Diagnostics via Perturbation Lemmas

The transient term $e^{\mathbf{A}_0(t-t_0)}(\mathbf{i}(t_0) - \mathbf{i}_\infty)$ modulates the periodic steady solution and creates spectral leakage around integer multiples of ω over short windows. Lemma 6.4.3 and Corollary 6.4.4 give

$$\sup_{t\in[t_0,t_1]} \|\mathbf{i}(t) - \mathbf{i}_0(t)\| \;\le\; \left(M_i\,\|\Delta\omega\|_\infty + \frac{\|\Delta \mathbf{v}_g\|_\infty}{L_f}\right) \frac{1 - e^{a\Delta t}}{-a} \;=\; \mathcal{O}(\Delta t), \tag{6.41}$$

so interharmonic sidebands due to dynamic lag introduced by PLL and estimator states are linearly small in the ms-scale clamp window. Thus, the dominant spectral signature during clamp is governed by (6.39) (flat-top or hexagon family), augmented by:

- a step in the fundamental negative-sequence ratio $\kappa_- := |I_1^-|/|I_1^+|$ (from (6.36) under unbalance),
- and weak, window-length–scaled interharmonics near ω (Corollary 6.4.4).

6.6.6 THD and Overcurrent Linked Criteria

Using (6.39),

$$\mathrm{THD}_I = \frac{\sqrt{\sum_{k\in\mathcal{K}} |I_k|^2}}{|I_1^+|} \approx \frac{\sqrt{\sum_{k\in\{5,7,11,13,\dots\}} \frac{|V_{\alpha\beta,k}|^2}{R_f^2+(k\omega L_f)^2}}}{\frac{|V_{\alpha\beta,1}-V_{g,\alpha\beta,1}|}{\sqrt{R_f^2+(\omega L_f)^2}}}, \tag{6.42}$$

where $\mathcal{K}$ excludes triplens in three-wire lines. Moreover, if the forced fundamental magnitude $\|\mathbf{i}_{\infty,1}\|$ exceeds $I_{\max}$ (Lemma 6.4.7), then the peak current will inevitably violate the rating during clamp (Sec. 6.3, (6.26)–(6.28)), and simultaneously the low-order harmonic magnitudes given by (6.39) increase due to deeper flat-topping (smaller θ_c), providing a consistent diagnostic: rising $\{|I_5|, |I_7|\}$, THD_I, and κ_-.

6.7 Evaluation

EMT simulations were carried out to validate the closed-form predictions of peak current and harmonic content during PWM saturation, using a detailed IEEE Std 2800-compliant Type-IV wind plant model under various fault types, depths, and pre-fault operating points. . A detailed Type-IV wind plant model, incorporating IEEE Std 2800-compliant FRT functions, was implemented as an extension of the work in [92].

The EMT setup is illustrated in Fig. 4.5. On the DC side, the grid-side converter is fed by a machine-side converter representing a Type-IV turbine. On the AC side, the inverter is connected to a 0.69kV/33kV Δ–Y transformer; the secondary voltage is scaled by a factor N to emulate plant-level power output while modeling a single detailed inverter. A subsequent 33kV/138kV transformer interfaces the plant with the transmission network.

Unless stated otherwise in the evaluation sections, all EMT cases use the baseline parameters listed in Table 5.2. Faults are applied at location **F** in Fig. 4.5, and the resulting post-fault currents are compared with analytical predictions.

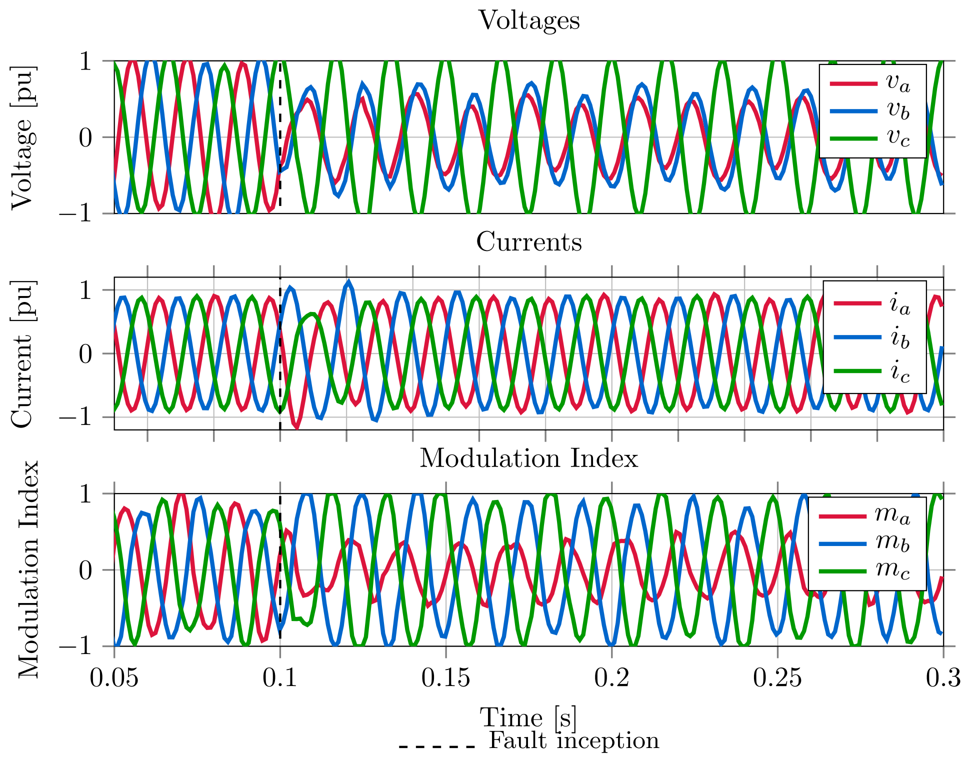

Figure 6.3: Voltages, current, and modulation index under AG fault with PWM saturation

6.7.1 Harmonic Evaluation under PWM Saturation

To investigate the impact of PWM saturation on harmonic distortion during FRT, we performed a controlled study under an AG fault condition. For consistency and to isolate the effect of saturation, all parameters and control settings were kept identical across the two scenarios, except for the K_2^{FRT} setting:

- *Saturation case:* $K_2^{\text{FRT}} = 0$ (allowing full saturation of the modulation signals)
- *Unsaturated case:* $K_2^{\text{FRT}} = 2$ (limiting the modulation index to avoid saturation)

The inverter phase currents for these two cases are shown in Fig. 6.3 and Fig. 6.4, respectively. These waveforms illustrate the more pronounced waveform distortion in the saturated case, particularly visible in the faulted phase during the fault period.

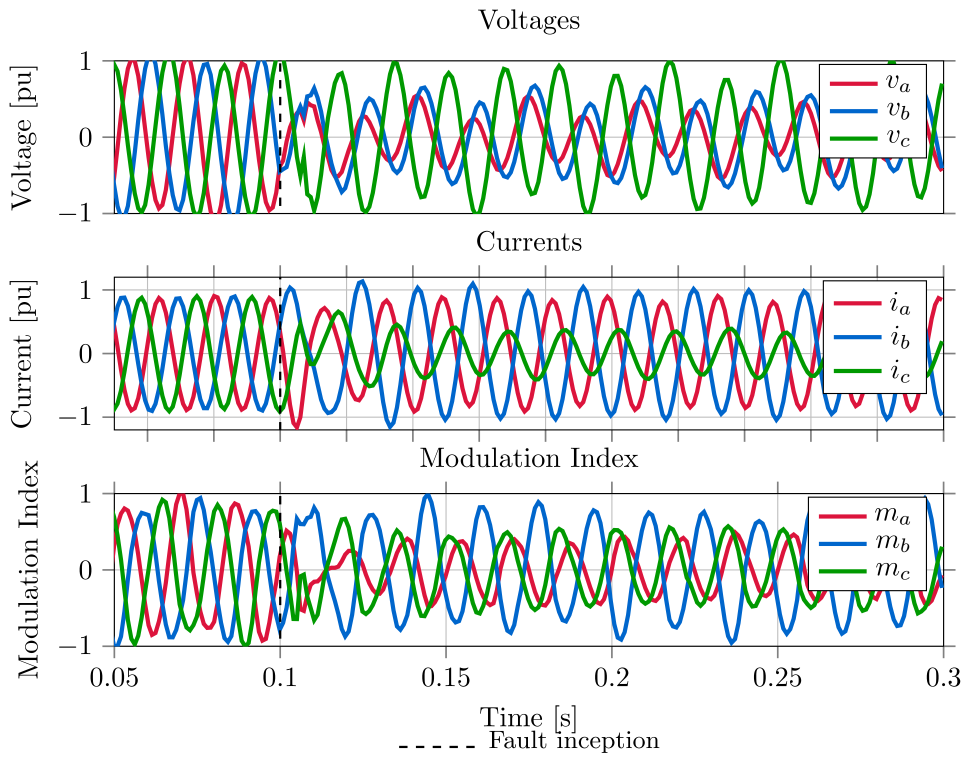

Figure 6.4: Voltages, current, and modulation index under AG fault without PWM saturation

Harmonic Analysis Methodology

The harmonic spectrum was computed from the per-unit phase currents over the steady-state post-fault window using an FFT-based approach. Harmonic magnitudes were extracted for the 5th, 7th, 11th, and 13th orders. The results were normalized with respect to the fundamental magnitude for each phase to yield per-unit harmonic content.

Observed Harmonic Content and Alignment with Analytical Predictions

The measured harmonic magnitudes for each phase under both saturation and non-saturation conditions are summarized in Fig. 6.5. For the 5th harmonic, saturation cases consistently exhibited higher magnitudes across all phases, with increases of approximately 2–3$\times$ compared to the unsaturated cases. For the 7th harmonic, the saturated case showed a 30–140% increase, most significant in Phase B where the fault impact was most direct. Although the 11th and 13th har-

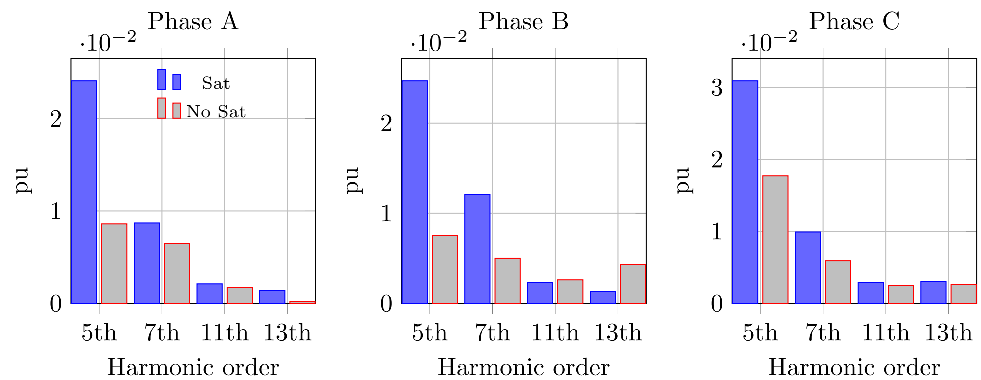

Figure 6.5: Per-unit harmonic magnitudes with and without PWM saturation for each phase.

monics had smaller absolute magnitudes, the saturated case consistently exhibited higher values, confirming increased high-frequency distortion during modulation saturation.

From the closed-form dynamics developed in Section 6.6, it was predicted that during PWM saturation, the inverter control loop is effectively bypassed for portions of the cycle, allowing non-fundamental components introduced by the fault and system asymmetry to propagate into the output current. This effect is particularly pronounced for the 5th and 7th harmonics, which are linked to unbalanced sequence interactions and nonlinear modulation effects. The measured results align closely with this prediction: the magnitude increase in the lower-order harmonics (5th and 7th) matches expectations from the analytical coupling terms, while the presence of elevated 11th and 13th harmonics, though smaller in amplitude, confirms that saturation broadens the harmonic spectrum by introducing sidebands from the nonlinear switching function. In contrast, the unsaturated case, with $K_2^{\mathrm{FRT}} = 2$, preserved current waveform quality.

6.7.2 Evaluation of Peak Current Bounds under BC Fault Conditions

Setup and assumptions.

We evaluate the peak-current envelopes derived in Lemma 6.5.1 and Eqs. (6.26)–(6.28) under a BC fault. During the initial clamp interval the inverter-side voltage vector keeps a fixed direction $\mathbf{e}_v$ equal to the pre-fault positive-sequence angle (reactive priority, $+q$) while its magnitude is clamped; negative-sequence actuation is disabled. Thus the inverter reference is $v_1^{\text{inv}} = 1\angle(\phi_{1,\text{pre}} + 90°)$ p.u., $v_2^{\text{inv}} = 0$. The grid-side post-fault sequences (v_1, v_2) and their angles are measured.

Calculation method.

The net sequence drives are $\Delta\tilde{V}^+ = 1e^{j\phi_{\text{inv}}} - v_1 e^{j\phi_1}$, $\Delta\tilde{V}^- = -v_2 e^{j\phi_2}$, and the per-unit filter impedance is $Z_{\text{pu}} = R_{f,\text{pu}} + jL_{f,\text{pu}}$ with $R_{f,\text{pu}} = R_f/Z_{\text{base}}$, $L_{f,\text{pu}} = \omega_{\text{base}} L_f/Z_{\text{base}}$. The forced sequence-current magnitudes are $I_1 = |\Delta\tilde{V}^+|/|Z_{\text{pu}}|$, $I_2 = |\Delta\tilde{V}^-|/|Z_{\text{pu}}|$, so the forced instantaneous magnitude satisfies $|i_\infty(t)| = \sqrt{I_1^2 + I_2^2 + 2I_1I_2\cos(2\omega t + \delta)}$, with extrema $c_{\max} = I_1 + I_2$ and $c_{\min} = |I_1 - I_2|$. Without entry-phase information, the lemma-compatible bounds are

$$LB = \min\{\, i_{\text{pre}},\ c_{\min}\,\}, \qquad UB = i_{\text{pre}} +\ c_{\max}\,.$$

The observed peak I_{peak} from EMT simulation is expected to satisfy $LB \le I_{\text{peak}} \le UB$.

Test matrix.

We performed two sweeps: (*i*) $R_f \in \{0.0005,\ 0.005,\ 0.05\}\ \Omega$ with $L_f = 200$ µH, and (*ii*) $L_f \in \{150,\ 175,\ 200,\ 250\}$ µH with $R_f = 0.0005\ \Omega$. Each sweep was run for three pre-fault current magnitudes $i_{\text{pre}} \in \{1.00,\ 0.87,\ 0.53027\}$ pu.

Results.

Fig. 6.6 compare I_{peak} against (LB, UB) for the three i_{pre} groups. In all cases the measured peaks lie strictly between the bounds, confirming the correctness of the envelope. For $i_{\text{pre}} =$ 1.00 p.u., the observed peaks ($\approx$ 1.241.31 pu) are much closer to LB than to UB, indicating a small entry offset and dynamics dominated by the forced component. For $i_{\text{pre}} = 0.87$ pu, the same trend holds, with peaks $\approx$ 1.111.28 pu well within the envelope. For $i_{\text{pre}} = 0.53027$ pu, the peaks $\approx$ 0.740.87 p.u. remain well above LB and far below UB, again consistent with the analytical prediction. Across both sweeps, the envelopes exhibit the expected parametric trends: increasing R_f (larger damping) lowers $c_{\max}$ and therefore UB; varying L_f shifts $|Z_{\text{pu}}|$ and the forced term accordingly. That the observed peaks systematically track inside $[LB, UB]$ for all

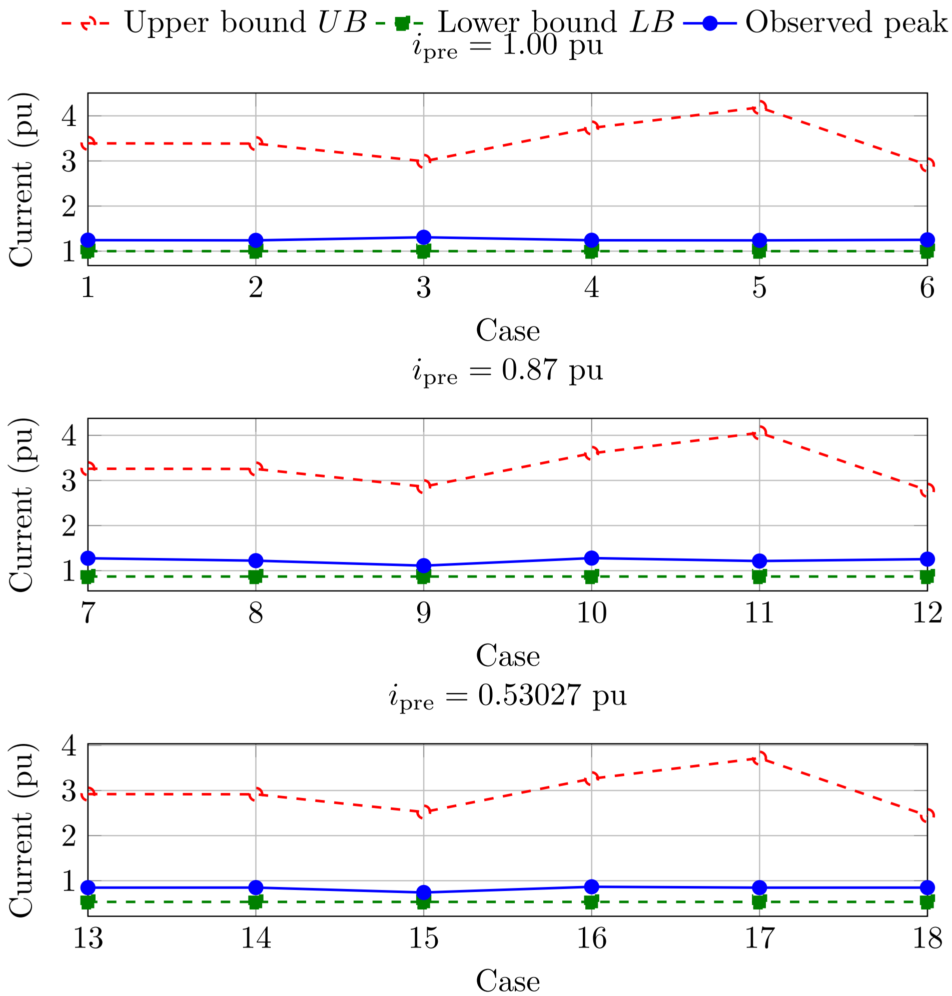

Figure 6.6: BC fault: analytical bounds vs. observed peaks for varying i_{pre}. Observed peaks lie strictly between the predicted lower and upper bounds in all cases.

BC-fault cases provides empirical validation of the lemma-based bounds and the fixed-direction, magnitude-clamped drive model used for the clamp interval.

Chapter 7

Characterization of Subsystem Behavior – Part II: Linear Phase (Trajectory Analysis)

This chapter analyzes the dynamic behavior of the inverter current response during the linear (unsaturated) phase of fault and disturbance events. A per-sequence representation using positive- and negative-sequence synchronous frames is adopted because it enables a clean decoupling of the converter's response to balanced and unbalanced grid conditions [130, 151]. This formulation transparently reveals the role of grid-frequency variations, PLL alignment error, and sequence-extractor artifacts in modulating the current-loop trajectory, and is a standard analytical framework for characterizing IBR short-circuit and ride-through dynamics [152, 153].

The objective of this chapter is to determine how the regulated current vector evolves in time under different perturbations — including phase-angle error, voltage imbalance, and measurement bias — and to quantify the resulting tracking accuracy, settling time, and steady-state deviation. This analysis directly supports later results on peak current prediction, current-envelope modeling, and reduced-order trajectory-based ROM design.

The following sections describe the nominal per-sequence model, introduce PLL- and extractor-induced perturbations, and derive analytical bounds and asymptotic behavior for the closed-loop current dynamics.

7.1 Nominal per-sequence closed-loop model (unified circuit–control)

We model each symmetrical–component channel $\sigma \in \{+,-\}$ in the synchronous dq frame as a combined circuit–control LTI system. The synchronous frame is aligned with the grid under the nominal assumption $\hat{\omega} = \omega_0$ and $\hat{\theta} = \theta_0 + \omega_0 t$. The output stage is an L_f–R_f filter and the inner current controller is PI with gains $K_p > 0$ and $K_i > 0$. For compactness let $a := R_f/L_f$, and let

$$J = \begin{bmatrix} 0 & -1 \\ 1 & 0 \end{bmatrix}, \qquad s_\sigma = \begin{cases} +1, & \sigma = + \\ -1, & \sigma = - \end{cases}, \tag{7.1}$$

so that J generates a 90° rotation in dq and s_σ encodes the sequence rotation. Per sequence we write the filter current $i_\sigma = [\, i_{d\sigma} \;\; i_{q\sigma} \,]^\top$, the commanded inverter terminal voltage $u_\sigma = [\, u_{d\sigma} \;\; u_{q\sigma} \,]^\top$, the PI integrator output $z_\sigma = [\, z_{d\sigma} \;\; z_{q\sigma} \,]^\top$, the current reference $R_\sigma = [\, i_{d\sigma}^{\mathrm{ref}} \;\; i_{q\sigma}^{\mathrm{ref}} \,]^\top$, and the grid voltage expressed in the same frame $V_{g\sigma} = [\, v_{d\sigma} \;\; v_{q\sigma} \,]^\top$. Time derivatives are denoted by dots.

The dq–frame filter dynamics for sequence σ are

$$\dot{i}_\sigma \;=\; -a\, i_\sigma \;+\; \frac{1}{L_f}\big(u_\sigma - V_{g\sigma}\big) \;+\; \omega_0 s_\sigma \, J\, i_\sigma, \tag{7.2}$$

where the last term is the synchronous cross–coupling between the d and q axes. The controller applies grid–voltage feedforward, resistive drop compensation, and synchronous–frame decoupling, together with PI action:

$$u_\sigma = V_{g\sigma} \;+\; R_f\, i_\sigma \;-\; L_f \omega_0 s_\sigma \, J\, i_\sigma \;+\; K_p\big(R_\sigma - i_\sigma\big) \;+\; z_\sigma, \tag{7.3}$$

$$\dot{z}_\sigma = K_i\big(R_\sigma - i_\sigma\big). \tag{7.4}$$

Substituting (7.3) into (7.2) shows that the feedforward and decoupling cancel the corresponding plant terms, giving the nominal closed–loop current channel

$$\dot{i}_\sigma \;=\; -\Big(a + \frac{K_p}{L_f}\Big) i_\sigma \;+\; \frac{1}{L_f} z_\sigma \;+\; \frac{K_p}{L_f} R_\sigma. \tag{7.5}$$

Let $X_\sigma = [\, i_\sigma^\top \; z_\sigma^\top \,]^\top \in \mathbb{R}^4$ denote the state. Then the nominal combined circuit–control model is

$$\dot{X}_\sigma(t) = A_0\, X_\sigma(t) + B_r\, R_\sigma, \tag{7.6}$$

with

$$A_0 = \begin{bmatrix} -\big(a + \frac{K_p}{L_f}\big) I_2 & \frac{1}{L_f} I_2 \\ -K_i I_2 & 0_{2\times 2} \end{bmatrix}, \qquad B_r = \begin{bmatrix} \frac{K_p}{L_f} I_2 \\ K_i I_2 \end{bmatrix}, \tag{7.7}$$

where I_2 is the 2×2 identity and $0_{2\times 2}$ is the 2×2 zero matrix. In the nominal closed loop (7.6), the cross–coupling term is exactly canceled and no $\omega_0 E_\sigma X_\sigma$ term appears.

7.2 Model with PLL and Sequence–Extractor Errors

We extend the nominal per-sequence closed-loop model in (7.6) to capture perturbations introduced by the phase-locked loop (PLL) and the sequence extractor. Let the PLL-estimated frequency be $\hat{\omega}(t) = \omega_0 + \Delta\omega(t)$. Using $\hat{\omega}(t)$ inside the decoupling leaves a residual term in the current channel equal to $-(\Delta\omega) s_\sigma J i_\sigma$, which in compact state form is $-\Delta\omega(t)\, E_\sigma X_\sigma(t)$, where

$$E_\sigma := \mathrm{blkdiag}(s_\sigma J,\ 0_{2\times 2}), \qquad J = \begin{bmatrix} 0 & -1 \\ 1 & 0 \end{bmatrix}. \tag{7.8}$$

Let the sequence extractor provide the measured grid-voltage sequence $V_{g\sigma}^{\mathrm{meas}}(t) = V_{g\sigma}(t) + \varepsilon_{v\sigma}(t)$. Because the feedforward uses $V_{g\sigma}^{\mathrm{meas}}$, the nominal cancellation is imperfect and an additive input remains in the current channel equal to $\frac{1}{L_f}\varepsilon_{v\sigma}(t)$. We represent this with the input matrix

$$B_v \ := \begin{bmatrix} \frac{1}{L_f} I_2 \\ 0_{2\times 2} \end{bmatrix}. \tag{7.9}$$

Applying these perturbations to (7.6) yields the per-sequence perturbed closed-loop model

$$\dot{X}_\sigma(t) = \underbrace{A_0\, X_\sigma(t) + B_r\, R_\sigma}_{\text{nominal}} - \underbrace{\Delta\omega(t)\, E_\sigma X_\sigma(t)}_{\text{PLL residual}} + \underbrace{B_v\, \varepsilon_{v\sigma}(t)}_{\text{sequence-extractor bias}}. \tag{7.10}$$

7.2.1 Analytical Solution via Variation of Constants

For the nominal per–sequence closed-loop model without PLL or sequence–extractor perturbations in (7.6), introduce the nominal state matrix $A_{\sigma,\mathrm{nom}}$, with exact decoupling, no $\omega_0 E_\sigma$ term. Let $\Phi_{\sigma,\mathrm{nom}}(t) := e^{A_{\sigma,\mathrm{nom}} t}$ denote the state–transition matrix of the homogeneous nominal system. With R_σ constant, the nominal forced response for $t \geq t_0$ is

$$X_{\sigma,\mathrm{nom}}(t) = \Phi_{\sigma,\mathrm{nom}}(t - t_0)\, X_\sigma(t_0) + \int_{t_0}^{t} \Phi_{\sigma,\mathrm{nom}}(t - \tau)\, B_r R_\sigma \, d\tau. \tag{7.11}$$

For the perturbed per–sequence model in (7.10), using the same $\Phi_{\sigma,\mathrm{nom}}(\cdot)$ yields

$$\begin{aligned} X_\sigma(t) = \Phi_{\sigma,\mathrm{nom}}(t - t_0)\, X_\sigma(t_0) + \int_{t_0}^{t} \Phi_{\sigma,\mathrm{nom}}(t - \tau)\, B_r R_\sigma \, d\tau \\ + \int_{t_0}^{t} \Phi_{\sigma,\mathrm{nom}}(t - \tau) \big[-\, \Delta\omega(\tau)\, E_\sigma X_\sigma(\tau) + B_v\, \varepsilon_{v\sigma}(\tau) \big]\, d\tau. \end{aligned} \tag{7.12}$$

In (7.12), the first two terms coincide with the nominal response (7.11). The last integral accounts for (*i*) the multiplicative disturbance due to PLL frequency error, $-\Delta\omega(\cdot)\, E_\sigma X_\sigma(\cdot)$, and (*ii*) the additive disturbance introduced by the sequence extractor, $B_v\, \varepsilon_{v\sigma}(\cdot)$.

7.3 Response Characterization under Perturbations: Lemmas and Corollaries

We develop a set of lemmas and corollaries that quantify well-posedness, stability, and tracking-error bounds of the per-sequence closed loop in the presence of the multiplicative PLL term $-\Delta\omega(t) E_\sigma X_\sigma$ and the additive sequence-extractor bias $B_v\, \varepsilon_{v\sigma}(t)$. All proofs are deferred to Appendix A.1.

Lemma 7.3.1 (Well-posedness and uniqueness)**.** *Assume* $\Delta\omega(\cdot),\, \varepsilon_{v\sigma}(\cdot) \in L^\infty([t_0, \infty))$ *and* R_σ *is constant (or, more generally, bounded and measurable). Then for any initial state* $X_\sigma(t_0)$*, the*

Cauchy problem (7.10) *admits a unique solution* $X_\sigma(\cdot) \in AC([t_0,\infty);\mathbb{R}^4)$*, hence* X_σ *is continuous on* $[t_0,\infty)$.

Interpretation: The fault current trajectory is always mathematically defined even when PLL and sequence-extractor imperfections are present, ensuring that subsequent bounds are meaningful.

Lemma 7.3.2 (Nominal exponential stability)**.** *Assume the nominal closed-loop matrix* $A_{\sigma,\mathrm{nom}}$ *(recall* $A_{\sigma,\mathrm{nom}} = A_0$*) is Hurwitz, i.e., all eigenvalues satisfy* $\Re(\lambda) < 0$*. Then there exist constants* $M_\sigma \geq 1$ *and* $\alpha_\sigma > 0$ *such that*

$$\|\Phi_{\sigma,\mathrm{nom}}(t)\| \leq M_\sigma\, e^{-\alpha_\sigma t}, \quad \forall\, t \geq 0, \tag{7.13}$$

where $\Phi_{\sigma,\mathrm{nom}}(t) = e^{A_{\sigma,\mathrm{nom}} t}$ *is the nominal state–transition matrix.*

Interpretation: In the absence of perturbations, the fault current decays exponentially to its steady-state value in the linear range, with rate α set by the control and filter parameters.

Corollary 7.3.3 (Explicit exponential constants from (K_p, K_i, L_f, R_f))**.** *Under the assumptions of Lemma 7.3.2, let* $a := R_f/L_f$ *and define the per-axis closed-loop matrix*

$$A_{\mathrm{ax}} = \begin{bmatrix} -(a + K_p/L_f) & 1/L_f \\ -\,K_i & 0 \end{bmatrix}. \tag{7.14}$$

Let $P_{\mathrm{ax}} \in \mathbb{R}^{2\times 2}$ *be the unique positive-definite solution of the Lyapunov equation*

$$A_{\mathrm{ax}}^\top P_{\mathrm{ax}} + P_{\mathrm{ax}} A_{\mathrm{ax}} = -I_2, \tag{7.15}$$

and set $P = \mathrm{blkdiag}(P_{\mathrm{ax}}, P_{\mathrm{ax}})$*. Then the nominal transition matrix satisfies*

$$\|\Phi_{\sigma,\mathrm{nom}}(t)\|_2 \;\leq\; M_\sigma\, e^{-\alpha_\sigma t}, \tag{7.16}$$

$$M_\sigma := \sqrt{\frac{\lambda_{\max}(P_{\mathrm{ax}})}{\lambda_{\min}(P_{\mathrm{ax}})}}, \quad \alpha_\sigma := \frac{1}{2\,\lambda_{\max}(P_{\mathrm{ax}})}.$$

In particular, M_σ and α_σ are computable functions of (K_p, K_i, L_f, R_f) via P_{ax}.

Corollary 7.3.4 (Uniform boundedness under small PLL/sequence–extractor errors)**.** *Assume Lemma 7.3.2 and consider the perturbed model* (7.10) *with constant R_σ and $\Delta\omega(\cdot),\ \varepsilon_{v\sigma}(\cdot) \in L^\infty([t_0,\infty))$. If*

$$\kappa_\sigma \;:=\; \frac{M_\sigma}{\alpha_\sigma}\,\|E_\sigma\|\,\|\Delta\omega\|_\infty \;<\; 1, \tag{7.17}$$

then $X_\sigma(t)$ is uniformly bounded for all $t \geq t_0$, with

$$\sup_{t\geq t_0}\|X_\sigma(t)\| \;\leq\; \frac{M_\sigma\|X_\sigma(t_0)\| + \frac{M_\sigma}{\alpha_\sigma}\Big(\|B_r\|\,\|R_\sigma\| + \|B_v\|\,\|\varepsilon_{v\sigma}\|_\infty\Big)}{1-\kappa_\sigma}. \tag{7.18}$$

Interpretation: The quantity $\kappa_\sigma = \frac{M_\sigma}{\alpha_\sigma}\|E_\sigma\|\,\|\Delta\omega\|_\infty$ is a small–gain margin: it measures how much PLL frequency error the closed loop can tolerate before losing uniform boundedness. A faster, better–damped nominal current loop (larger α_σ, smaller M_σ) or tighter PLL (smaller $\|\Delta\omega\|_\infty$) enlarges this margin. The bound scales linearly with the sequence–extractor bias $\|\varepsilon_{v\sigma}\|_\infty$ and the setpoint magnitude through $\|B_r\|\,\|R_\sigma\|$, and degrades as $\kappa_\sigma \to 1$.

Lemma 7.3.5 (ISS bound w.r.t. PLL and extractor around the nominal forced model)**.** *Let Lemma 7.3.2 hold and define the deviation from the nominal forced response $\tilde{X}_\sigma(t) := X_\sigma(t) - X_{\sigma,\text{nom}}(t)$, where $X_{\sigma,\text{nom}}(\cdot)$ is given by* (7.11)*. Suppose $\Delta\omega(\cdot),\ \varepsilon_{v\sigma}(\cdot) \in L^\infty([t_0,\infty))$ and*

$$\|\Delta\omega\|_{\infty,[t_0,\infty)} < \frac{\alpha_\sigma}{\|E_\sigma\|\,M_\sigma}. \tag{7.19}$$

Then with $\alpha_{\text{eff}} := \alpha_\sigma - \|E_\sigma\|\,M_\sigma\,\|\Delta\omega\|_{\infty,[t_0,\infty)} > 0$ and

$$C_{\text{nom}} \;:=\; \sup_{t\geq t_0}\|X_{\sigma,\text{nom}}(t)\| \;\leq\; M_\sigma\|X_\sigma(t_0)\| + \frac{M_\sigma}{\alpha_\sigma}\,\|B_r\|\,\|R_\sigma\|, \tag{7.20}$$

the deviation satisfies, for all $t \geq t_0$*,*

$$\|\tilde{X}_\sigma(t)\| \;\leq\; M_\sigma e^{-\alpha_{\mathrm{eff}}(t-t_0)}\|\tilde{X}_\sigma(t_0)\| \\ +\; \frac{M_\sigma}{\alpha_{\mathrm{eff}}}\Big(\|B_v\|\,\|\varepsilon_{v\sigma}\|_{\infty,[t_0,t]} \;+\; \|E_\sigma\|\,\|\Delta\omega\|_{\infty,[t_0,t]}\,C_{\mathrm{nom}}\Big). \tag{7.21}$$

Hence the closed loop is exponentially ISS in the input pair $(\Delta\omega, \varepsilon_{v\sigma})$ *around the nominal forced trajectory.*

Interpretation: The lemma states an eISS property of the closed loop around the nominal forced trajectory: the deviation $\tilde{X}_\sigma$ decays exponentially with rate α_{eff} and is ultimately bounded by a term proportional to the disturbance magnitudes $\|\varepsilon_{v\sigma}\|_\infty$ and $\|\Delta\omega\|_\infty$ (the latter scaled by C_{nom}). The small-gain condition ensures $\alpha_{\mathrm{eff}} > 0$, i.e., that residual PLL coupling cannot overwhelm the nominal damping. When $\varepsilon_{v\sigma} \equiv 0$ and $\Delta\omega \equiv 0$, the deviation vanishes exponentially; with persistent but bounded perturbations, the steady bound is $\mathcal{O}\big((M_\sigma/\alpha_{\mathrm{eff}})\big(\|B_v\|\,\|\varepsilon_{v\sigma}\|_\infty + \|E_\sigma\|\,\|\Delta\omega\|_\infty C_{\mathrm{nom}}\big)\big)$. Design-wise, increasing the nominal decay rate (larger α_σ, smaller M_σ) or reducing PLL error tightens the bound; large setpoints inflate C_{nom} and thus the effect of $\Delta\omega$.

Corollary 7.3.6 (Steady-state error ball: PLL vs. extractor contributions)**.** *Under the hypotheses of Lemma 7.3.5 (so* $\alpha_{\mathrm{eff}} > 0$ *and* C_{nom} *are as defined there), the deviation* $\tilde{X}_\sigma(t) = X_\sigma(t) - X_{\sigma,\mathrm{nom}}(t)$ *satisfies*

$$\limsup_{t\to\infty}\|\tilde{X}_\sigma(t)\| \;\leq\; \underbrace{\frac{M_\sigma}{\alpha_{\mathrm{eff}}}\|B_v\|\,\|\varepsilon_{v\sigma}\|_\infty}_{=:\,r_{\mathrm{ext}}} \;+\; \underbrace{\frac{M_\sigma}{\alpha_{\mathrm{eff}}}\|E_\sigma\|\,\|\Delta\omega\|_\infty\,C_{\mathrm{nom}}}_{=:\,r_{\mathrm{PLL}}}. \tag{7.22}$$

Interpretation: The steady-state deviation from the nominal forced trajectory lies in the Minkowski sum of two balls with radii r_{ext} (extractor bias) and r_{PLL} (PLL error). The extractor term depends only on the bias magnitude, whereas the PLL term scales with the operating-point size via C_{nom}; both shrink with larger α_{eff} (i.e., better damping) and blow up as the small-gain margin tightens ($\alpha_{\mathrm{eff}} \downarrow 0$). If either disturbance is zero, its radius vanishes; if both are zero, the asymptotic error is zero.

Corollary 7.3.7 (ISS about the nominal equilibrium (explicit gains))**.** *Assume Lemma 7.3.2 and constant R_σ, so the nominal equilibrium $X_{\sigma,\infty} = -A_{\sigma,\mathrm{nom}}^{-1} B_r R_\sigma$ exists. For the perturbed model* (7.10)*, let*

$$\kappa_\sigma := \frac{M_\sigma}{\alpha_\sigma} \|E_\sigma\| \, \|\Delta\omega\|_\infty < 1, \tag{7.23}$$

$$\alpha_{\mathrm{eff}} := \alpha_\sigma - M_\sigma \|E_\sigma\| \, \|\Delta\omega\|_\infty > 0. \tag{7.24}$$

Then the deviation $\tilde{X}_\sigma(t) := X_\sigma(t) - X_{\sigma,\infty}$ satisfies, for all $t \geq t_0$,

$$\begin{aligned} \|\tilde{X}_\sigma(t)\| \; &\leq \; \underbrace{M_\sigma e^{-\alpha_{\mathrm{eff}}(t-t_0)} \|\tilde{X}_\sigma(t_0)\|}_{\beta(\|\tilde{X}_\sigma(t_0)\|,\, t-t_0)} \\ &+ \; \underbrace{\frac{M_\sigma}{\alpha_{\mathrm{eff}}} \|B_v\| \, \|\varepsilon_{v\sigma}\|_{\infty,[t_0,t]}}_{\gamma_{\mathrm{ext}}(\|\varepsilon_{v\sigma}\|_{\infty,[t_0,t]})} \; + \; \underbrace{\frac{M_\sigma}{\alpha_{\mathrm{eff}}} \|E_\sigma\| \, \|X_{\sigma,\infty}\| \, \|\Delta\omega\|_{\infty,[t_0,t]}}_{\gamma_{\mathrm{pll}}(\|\Delta\omega\|_{\infty,[t_0,t]})} . \end{aligned} \tag{7.25}$$

Hence the closed loop is exponentially ISS about $X_{\sigma,\infty}$ with explicit gains

$$\beta(r,t) = M_\sigma e^{-\alpha_{\mathrm{eff}} t} r, \quad \gamma_{\mathrm{ext}}(s) = \tfrac{M_\sigma}{\alpha_{\mathrm{eff}}} \|B_v\| \, s, \quad \gamma_{\mathrm{pll}}(s) = \tfrac{M_\sigma}{\alpha_{\mathrm{eff}}} \|E_\sigma\| \, \|X_{\sigma,\infty}\| \, s. \tag{7.26}$$

Interpretation: This ISS bound says deviations from the nominal equilibrium decay exponentially with rate α_{eff} and are ultimately limited by two $L_\infty \to L_\infty$ gains: one from the extractor bias (γ_{ext}) and one from PLL error (γ_{pll}). The PLL contribution scales with the operating point via $\|X_{\sigma,\infty}\|$—so at (or near) zero setpoint it is negligible to first order, while large setpoints amplify PLL-induced error. Improving nominal damping (larger α_σ, smaller M_σ via (K_p, K_i) and filter design) or tightening the PLL (smaller $\|\Delta\omega\|_\infty$) shrinks both terms; as the small-gain margin closes ($\alpha_{\mathrm{eff}} \downarrow 0$), the bound degrades.

Lemma 7.3.8 (Closed-form forced current with estimator bias)**.** *Consider the per-sequence closed-loop model* (7.10) *with zero PLL error and a constant sequence–extractor bias, i.e., $\Delta\omega \equiv 0$ and*

$\varepsilon_{v\sigma}(t) \equiv \bar{\varepsilon}_{v\sigma}$. *For constant* R_σ*, the solution is*

$$X_\sigma(t) \;=\; X_{\sigma,\infty} \;+\; e^{A_0(t-t_0)}\big(X_\sigma(t_0) - X_{\sigma,\infty}\big), \tag{7.27}$$

with equilibrium

$$X_{\sigma,\infty} \;=\; -A_0^{-1}\big(B_r R_\sigma + B_v \bar{\varepsilon}_{v\sigma}\big), \tag{7.28}$$

hence

$$i_{\sigma,\infty} = R_\sigma, \;\; z_{\sigma,\infty} = R_f R_\sigma - \bar{\varepsilon}_{v\sigma}. \tag{7.29}$$

Moreover, for each axis $k \in \{d, q\}$ *define* $\tau := t - t_0$ *and let* $s_{1,2}$ *be the roots of*

$$L_f s^2 + (K_p + aL_f)s + K_i = 0. \tag{7.30}$$

Writing $e_k(\tau) := i_{k\sigma}(t) - R_{k\sigma}$ *and* $\Delta z_k := z_{k\sigma}(t_0) - z_{k\sigma,\infty}$*, the current admits the closed form*

$$i_{k\sigma}(t) = R_{k\sigma} + A_k e^{s_1\tau} + B_k e^{s_2\tau}, \tag{7.31}$$

where

$$e_k(0) = i_{k\sigma}(t_0) - R_{k\sigma}, \qquad \dot{e}_k(0) = -(a + \tfrac{K_p}{L_f})\, e_k(0) + \tfrac{1}{L_f}\Delta z_k, \tag{7.32}$$

and

$$A_k = \frac{\dot{e}_k(0) - s_2 e_k(0)}{s_1 - s_2}, \qquad B_k = \frac{s_1 e_k(0) - \dot{e}_k(0)}{s_1 - s_2}. \tag{7.33}$$

In the critically damped case $s_1 = s_2 =: s$*,*

$$i_{k\sigma}(t) = R_{k\sigma} + \big(e_k(0) + (\dot{e}_k(0) - s\, e_k(0))\, \tau\big)e^{s\tau}. \tag{7.34}$$

Interpretation: For constant extractor bias and no saturation, the PI loop achieves perfect steady-state current tracking: $i_\sigma \to R_\sigma$ while the integrator offsets the bias (Lemma 7.3.8). Thus, the steady-state deviation from the nominal forced trajectory lies entirely in the controller state (and commanded voltage), not in the current. Nonzero steady current error arises only from time-varying bias, PLL mismatch, discretization/delays, or actuator limits/anti-windup.

Remark 7.3.9 (Placement and meaning of the extractor bias (updated))**.** *In the unified closed-loop model* (7.10)*, the sequence–extractor error enters only through the additive term $B_v\,\varepsilon_{v\sigma}(t)$. With the control law* (7.3) *using grid-voltage feedforward, this produces an effective converter-side voltage in the current channel equal to $\frac{1}{L_f}\,\varepsilon_{v\sigma}(t)$, i.e., the filter equation contains $+\frac{1}{L_f}\varepsilon_{v\sigma}(t)$. If a given architecture disables/omits this feedforward (or injects the biased voltage elsewhere), replace B_v accordingly to reflect the actual injection path; no extra bias channel beyond $B_v\,\varepsilon_{v\sigma}$ is needed.*

Lemma 7.3.10 (Peak-current bound in the linear phase)**.** *Assume the unsaturated (linear) operating phase and the small-gain range so that $\alpha_{\text{eff}} > 0$ (cf. Lemma 7.3.5). With constant R_σ and bounded perturbations $\Delta\omega(\cdot), \varepsilon_{v\sigma}(\cdot) \in L^\infty$, the per-sequence current satisfies*

$$\sup_{t\ge t_0}\|i_\sigma(t)\| \;\le\; \underbrace{\|R_\sigma\|}_{\textit{setpoint}} \;+$$

$$\underbrace{M_\sigma\|i_\sigma(t_0)-R_\sigma\|}_{\textit{initial mismatch}} \;+\; \underbrace{\frac{M_\sigma}{\alpha_{\text{eff}}}\big(\|B_v\|\,\|\varepsilon_{v\sigma}\|_\infty + \|E_\sigma\|\,C_{\text{nom}}\,\|\Delta\omega\|_\infty\big)}_{\textit{perturbation leakage}}. \tag{7.35}$$

Sharper nominal (step) bound. In the nominal case $\Delta\omega \equiv 0$, $\varepsilon_{v\sigma} \equiv 0$, each axis obeys $L_f s^2 + (K_p + aL_f)s + K_i = 0$, with natural frequency $\omega_n = \sqrt{K_i/L_f}$ and damping ratio $\zeta = (K_p + aL_f)/(2\sqrt{K_i L_f})$. If R_σ steps at t_0 and $0 < \zeta < 1$, the underdamped step overshoot factor

$$M_{\text{step}} = \exp\Big(-\frac{\pi\zeta}{\sqrt{1-\zeta^2}}\Big) \tag{7.36}$$

yields the axis-wise bound $\sup_{t\ge t_0}|\,i_{k\sigma}(t) - R_{k\sigma}\,| \;\le\; M_{\text{step}}\,|\,i_{k\sigma}(t_0^+) - R_{k\sigma}\,|$ ($k \in \{d,q\}$), and consequently

$$\sup_{t\ge t_0}\|i_\sigma(t)\| \;\le\; \|R_\sigma\| + M_{\text{step}}\,\|i_\sigma(t_0^+) - R_\sigma\|. \tag{7.37}$$

For $\zeta \ge 1$, $M_{\text{step}} = 0$ (no overshoot).

Interpretation: The peak current in the linear (unsaturated) phase is bounded by the nominal steady level plus a nominal transient term and an "error tube" induced by perturbations. Equivalently, the trajectory stays within a tube around the nominal path whose radius is

$$r_\infty = \frac{M_\sigma}{\alpha_{\text{eff}}}\Big(\|B_v\|\,\|\varepsilon_{v\sigma}\|_\infty + \|E_\sigma\|\,C_{\text{nom}}\,\|\Delta\omega\|_\infty\Big), \tag{7.38}$$

with an additional decaying piece $M_\sigma e^{-\alpha_{\text{eff}}(t-t_0)}\|i_\sigma(t_0) - R_\sigma\|$ along the nominal transient. In the ideal nominal case ($\varepsilon_{v\sigma} = \Delta\omega = 0$) the tube collapses and the bound reduces to the classical overshoot determined by ζ; with perturbations, the tube widens proportionally to their magnitudes and shrinks as α_{eff} increases.

Corollary 7.3.11 (Time-to-within-ϵ of steady state)**.** *Assume the hypotheses of Cor. 7.3.7 (so $\alpha_{\text{eff}} > 0$). Let*

$$r_{\text{ss}} \;:=\; \frac{M_\sigma}{\alpha_{\text{eff}}}\Big(\|B_v\|\,\|\varepsilon_{v\sigma}\|_\infty + \|E_\sigma\|\,\|X_{\sigma,\infty}\|\,\|\Delta\omega\|_\infty\Big) \tag{7.39}$$

be the ultimate (state) radius from Cor. 7.3.7. Then for any $\epsilon > 0$,

$$T_\epsilon^{(X)} \;:=\; \frac{1}{\alpha_{\text{eff}}}\ln\!\left(\frac{M_\sigma\,\|\tilde{X}_\sigma(t_0)\|}{\epsilon}\right) \tag{7.40}$$

satisfies, for all $t \ge t_0 + T_\epsilon^{(X)}$,

$$\|\tilde{X}_\sigma(t)\| \;\le\; r_{\text{ss}} + \epsilon.$$

Moreover, for the current output $\tilde{i}_\sigma = C\tilde{X}_\sigma$ the bound

$$T_\epsilon^{(i)} \;:=\; \frac{1}{\alpha_{\text{eff}}}\ln\!\left(\frac{\|C\|\,M_\sigma\,\|\tilde{X}_\sigma(t_0)\|}{\epsilon}\right) \tag{7.41}$$

ensures, for all $t \ge t_0 + T_\epsilon^{(i)}$,

$$\|\tilde{i}_\sigma(t)\| \;\le\; \|C\|\,r_{\text{ss}} + \epsilon. \tag{7.42}$$

Interpretation: The time to enter an ϵ–tube around steady state splits cleanly into two parts: an irreducible radius r_{ss} set by the disturbance levels $(\varepsilon_{v\sigma}, \Delta\omega)$, and an exponential approach governed by α_{eff} and the initial deviation. Larger α_{eff} (stronger nominal damping) shortens the log–time

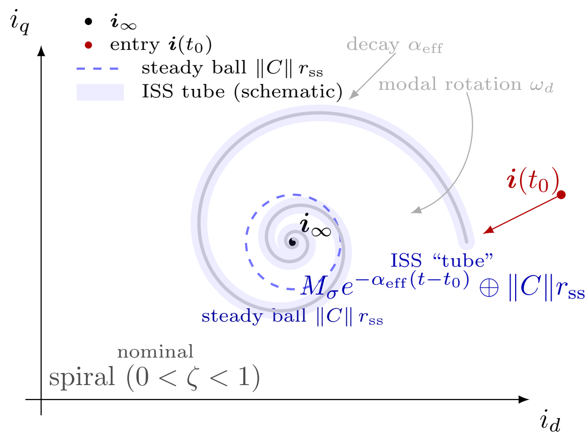

Figure 7.1: Geometric interpretation in the i_d–i_q plane. For an underdamped nominal loop ($0 < \zeta < 1$), the trajectory (gray) spirals toward $\boldsymbol{i}_\infty$ with modal frequency ω_d and decay rate α_{eff}. Perturbations produce a steady current ball of radius $\|C\|\, r_{\text{ss}}$ and a time-varying ISS tube (blue halo) equal to the decaying term $M_\sigma e^{-\alpha_{\text{eff}}(t-t_0)} \|\tilde{X}_\sigma(t_0)\|$ plus the steady radius. For $\zeta \geq 1$, the approach is monotone (no rotation).

$\propto \alpha_{\text{eff}}^{-1} \ln(\cdot)$, while r_{ss} is unaffected by initial conditions and depends only on disturbance magnitudes and gains. For the current, the same conclusions hold up to the output factor $\|C\|$. If disturbances vanish, $r_{\text{ss}} = 0$ and the expressions reduce to the standard settling-time formulas for an exponentially stable linear system.

7.4 Trajectory Patterns in the Linear (Unsaturated) Phase

This section synthesizes the lemma–level results into a compact picture of how the per–sequence current evolves during a fault while the loop remains linear (no saturation/anti–windup) and the small–gain range holds so that $\alpha_{\text{eff}} > 0$ (cf. Lemma 7.3.2, Lemma 7.3.5). We view the response as a nominal backbone (Sec. 7.1, (7.11)) plus a perturbation that is confined to an ISS tube around that backbone (Cor. 7.3.7, Cor. 7.3.6). Figure 7.1 provides a geometric map of the patterns below.

7.4.1 Nominal backbone: monotone vs. ringdown.

With exact decoupling, each axis is a second–order loop with characteristic $L_f s^2 + (K_p + aL_f)s + K_i = 0$. The damping ratio ζ selects the shape: $\zeta \geq 1$ gives a monotone approach to the setpoint, while $0 < \zeta < 1$ yields an underdamped ringdown (a logarithmic spiral in i_d–i_q), with peak set by the standard step–overshoot factor (Lemma 7.3.10). This nominal shape is the trajectory's spine in Fig. 7.1.

7.4.2 Tube around the backbone.

By Lemma 7.3.5 and Cor. 7.3.7, the state and current remain inside a time–varying neighborhood of the nominal path composed of (*i*) a decaying radius $M_\sigma e^{-\alpha_{\text{eff}}(t-t_0)}\|\tilde{X}_\sigma(t_0)\|$ from the entry mismatch and (*ii*) an ultimate radius r_{ss} set by the perturbations. Equivalently,

$$X_\sigma(t) \in X_{\sigma,\text{nom}}(t) \;\oplus\; \mathbb{B}\Big(r_{\text{ss}} + M_\sigma e^{-\alpha_{\text{eff}}(t-t_0)}\|\tilde{X}_\sigma(t_0)\|\Big)\,, \tag{7.43}$$

and the current inherits the same structure via the output map ($\|i_\sigma\| \le \|C\|\,\|X_\sigma\|$). In Fig. 7.1 this appears as the decaying tube around the nominal spiral and the steady ball around $\boldsymbol{i}_\infty$.

7.4.3 Extractor bias: constant vs. time–varying.

A constant sequence–extractor bias does not distort the current trajectory in steady state: the integrator trims and $i_\sigma \to R_\sigma$ (Lemma 7.3.8). In particular, with $R_- = 0$ there is no persistent negative–sequence current (Cor. 8.1.3). Time–varying bias enlarges the tube's ultimate radius in proportion to its magnitude (Cor. 7.3.6, Cor. 7.3.7); the nominal backbone is unchanged, but the halo around it is thicker.

7.4.4 PLL perturbations and operating–point scaling.

PLL frequency error enters multiplicatively via $E_\sigma X_\sigma$, so its effect scales with the operating point: near zero setpoint the tube's steady radius due to PLL is small; at larger commanded currents it grows linearly with $\|X_{\sigma,\infty}\|$ or C_{nom} (Cor. 7.3.6, Cor. 7.3.7). Thus two runs with the same $\Delta\omega$ trace the same backbone but exhibit visibly different halo sizes depending on R_σ.

7.4.5 Peaks and settling.

The peak current in the linear phase is the sum of the nominal peak (set by ζ) and the tube radius induced by perturbations (Lemma 7.3.10); increasing α_{eff} both reduces that radius and attenuates the decaying part. The time to enter an ϵ–neighborhood of steady state separates cleanly into a logarithmic decay term $\alpha_{\text{eff}}^{-1} \ln(\cdot)$ and the irreducible steady radius r_{ss} (Cor. 7.3.11). Design levers are therefore: raise α_{eff} (via (K_p, K_i) and L_f, R_f), and reduce the disturbance magnitudes.

7.4.6 Sequence symmetry and when the picture breaks.

In the nominal model the $+$ and $-$ channels evolve independently with identical tube structure; any apparent cross–sequence effect in the current is attributable to estimator imperfections already accounted for in r_{ss}. The patterns above hold until saturation/anti–windup, coarse discretizations, or unmodeled resonances become active, at which point the linear ISS tube no longer certifies the trajectory and a separate nonlinear analysis is required.

Chapter 8

Characterization of Subsystem Behavior – Part III: Linear Phase (Harmonic Content)

This chapter characterizes the harmonic behavior of IBR during the linear (unsaturated) phase of operation. Whereas prior chapters examined the macroscopic transient response and current-limiting behavior under faulted conditions, the focus here is on the spectral content of the current and voltage waveforms when the modulation index remains within its linear operating region.

The motivation for this analysis arises from the fact that a substantial portion of IBR behavior during faults—even those that ultimately reach PWM saturation—begins in the linear region, where harmonic injection results principally from controller dynamics, PLL behavior, sequence couplings, and converter switching interactions. Understanding this regime enables a clearer attribution of harmonic components to specific subsystems, rather than conflating these effects with nonlinear modulation saturation.

Accordingly, we investigate the frequency content of positive- and negative-sequence current during linear operation, decomposing the observed signal into fundamental and non-fundamental components. The analysis examines:

1. how the PLL and sequence extraction structures contribute to spectral artifacts;
2. how the current regulator dynamics shape harmonic propagation into the terminal currents; and
3. how the electrical filter components (transformer leakage, L_f, C_f, and grid impedance) attenuate or amplify individual frequency components.

These results provide physical insight that informs subsequent reduced-order modeling, parameterization of the fault-response envelopes, and the interpretation of harmonic distortions during both normal and ride-through operating modes.

8.1 Response Characterization under Perturbations

The key well-posedness, nominal exponential stability, and eISS/steady-state tracking-error bounds for the per-sequence closed loop under the multiplicative PLL term $-\Delta\omega(t)E_\sigma X_\sigma$ and the additive sequence-extractor bias $B_v\,\varepsilon_{v\sigma}(t)$ are developed in Section 7.3; see Lemma 7.3.1, Lemma 7.3.2, Lemma 7.3.5, and the associated corollaries therein, with proofs deferred to Appendix A.1. In this section, we build on those results and present additional characterizations that are specific to the analyses in Chapter 8.

8.1.1 Harmonic and Interharmonic Leakage under Perturbations

Assume the hypotheses of Lemma 7.3.5 so that the small-gain range holds and $\alpha_{\text{eff}} > 0$. Let the nominal forced trajectory $X_{\sigma,\text{nom}}(\cdot)$ be defined as in (7.11), and define $C_{\text{nom}} := \sup_{t\geq t_0}\|X_{\sigma,\text{nom}}(t)\|$, which is finite under Lemma 7.3.2. Linearizing the perturbed model (7.10) about $X_{\sigma,\text{nom}}$ yields the following frequency-domain bound on the per-axis current deviation $\tilde{i}_\sigma := i_\sigma - i_{\sigma,\text{nom}}$.

Lemma 8.1.1 (Harmonic and interharmonic leakage bounds under perturbations)**.** *Assume Lemma 7.3.5 and constant R_σ. Then, for $\Omega \geq 0$,*

$$\left\|\widehat{\tilde{i}}_\sigma(j\Omega)\right\| \;\leq\; \underbrace{\left|\frac{s}{L_f s^2 + (K_p + aL_f)s + K_i}\right|_{s=j\Omega}}_{=:\,|G(j\Omega)|} \left(\frac{1}{L_f}\left\|\widehat{\varepsilon}_{v\sigma}(j\Omega)\right\| + \|E_\sigma\|\,C_{\text{nom}}\left|\widehat{\Delta\omega}(j\Omega)\right|\right). \tag{8.1}$$

Consequently, for multi-tone or band-limited $\varepsilon_{v\sigma}$ and $\Delta\omega$, the spectrum of $\tilde{i}_\sigma$ is contained in the union of the input lines/bands and its magnitude at each Ω is bounded by the right-hand side.

Interpretation: The shaping factor $G(j\Omega)$ is high-pass (zero at $\Omega = 0$), so constant extractor bias produces no steady current error (cf. Lemma 7.3.8 in Section 7.3). Only time-varying components of $\varepsilon_{v\sigma}$ and $\Delta\omega$ leak into the current spectrum, with PLL-induced leakage scaling with the operating-point size through C_{nom}.

8.1.2 Short-Window Smear Bound

The following corollary quantifies the energy of mismatch accumulated over a finite window, which is useful when comparing short data records (e.g., relay measurement windows) to nominal trajectories.

Corollary 8.1.2 (Short-window smear)**.** *Assume Lemma 7.3.5 so that $\alpha_{\text{eff}} > 0$. For any window $[t_w, t_w + \Delta t]$ with $\Delta t > 0$, the windowed mean-square deviation between the perturbed and nominal currents satisfies*

$$\begin{aligned}\int_{t_w}^{t_w+\Delta t} \|\tilde{i}_\sigma(t)\|^2 dt \ \le\ \Delta t\, \|C\|^2 M_\sigma^2 \Big(&\|X_\sigma(t_w) - X_{\sigma,\text{nom}}(t_w)\| \\ &+ \alpha_{\text{eff}}^{-1} \big(\|B_v\|\, \|\varepsilon_{v\sigma}\|_{\infty,[t_w,t_w+\Delta t]} + \|E_\sigma\|\, C_{\text{nom}}\, \|\Delta\omega\|_{\infty,[t_w,t_w+\Delta t]} \big) \Big)^2.\end{aligned} \tag{8.2}$$

Interpretation: Over short windows, smear energy scales linearly with window length and quadratically with an effective amplitude formed by instantaneous mismatch at t_w plus disturbance levels weighted by α_{eff}^{-1}.

8.1.3 Spurious Negative-Sequence Current due to Extractor Bias

The negative-sequence channel is particularly sensitive to estimation imperfections. The following result specializes the general eISS bounds from Section 7.3 to the case of nominally zero negative-sequence setpoint.

Corollary 8.1.3 (Spurious negative sequence from extractor bias)**.** *Consider the negative-sequence channel with $R_- = 0$ and $V_{g-} = 0$.*

(a) If $\Delta\omega \equiv 0$ and the extractor bias is constant, $\varepsilon_{v-}(t) \equiv \bar{\varepsilon}_{v-}$, then

$$i_-(t) \ \to\ 0, \qquad z_-(t) \ \to\ -\bar{\varepsilon}_{v-}, \qquad u_-(t) \ \to\ -\bar{\varepsilon}_{v-}, \tag{8.3}$$

i.e., no steady spurious negative-sequence current arises; the PI integrator offsets the bias (cf. Lemma 7.3.8 in Section 7.3).

(b) If $\Delta\omega \equiv 0$ and $\varepsilon_{v-}(\cdot) \in L^\infty([t_0,\infty))$, then the negative-sequence current is eISS with respect to ε_{v-}:

$$\|i_-(t)\| \;\le\; M_- e^{-\alpha_-(t-t_0)}\|i_-(t_0)\| + \frac{M_-}{\alpha_-}\,\|B_v\|\,\|\varepsilon_{v-}\|_{\infty,[t_0,t]}, \tag{8.4}$$

and, in particular,

$$\limsup_{t\to\infty}\|i_-(t)\| \;\le\; \frac{M_-}{\alpha_-}\,\|B_v\|\,\|\varepsilon_{v-}\|_\infty. \tag{8.5}$$

Interpretation: A constant extractor bias does not create persistent negative-sequence current in the ideal linear regime; time-varying bias leaks through with an $L_\infty \to L_\infty$ gain proportional to $(M_-/\alpha_-)\|B_v\|$. In practice, saturation/anti-windup, discretization, and PLL mismatch can create additional leakage mechanisms beyond the assumptions used here.

8.2 Harmonic Content in the Linear (Unsaturated) Phase

In the linear, unsaturated phase (post-clamp), the inner current loop follows the nominal closed-loop dynamics of Sec. 7.1. Grid-voltage feedforward cancels the plant voltage in the nominal channel, while estimator imperfections enter as described in Sec. 7.2. This section characterizes the resulting spectral structure: the baseline harmonic content in the positive-sequence frame and the additional harmonics and interharmonics introduced by PLL and sequence-extractor perturbations. A pathway-level summary is illustrated in Fig. 8.1. All symbols (e.g., J, E_σ, A_0, B_v) follow previous definitions.

8.2.1 Baseline structure in the positive-sequence synchronous frame

Lemma 8.2.1 (Baseline content in the positive-sequence frame)**.** *Under exact alignment ($\hat\omega = \omega_0$, $\hat\theta = \theta_0 + \omega_0 t$), exact decoupling, and constant references:*

(i) If $R_- = 0$, the positive-sequence dq current is purely DC.

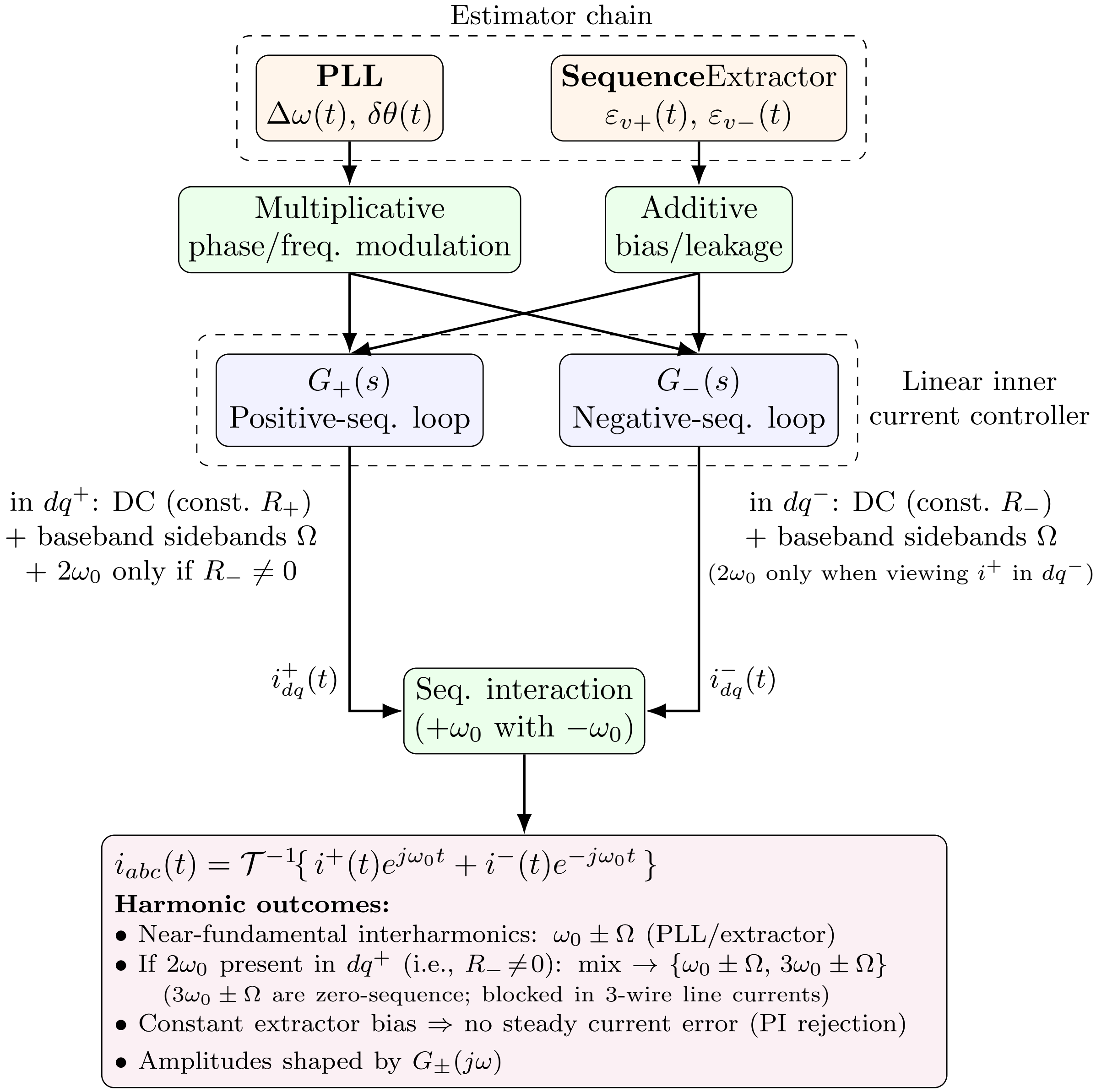

Figure 8.1: Harmonic pathways in the linear (unsaturated) phase. PLL jitter and sequence-extractor ripple inject baseband components in the dq loops; recombination to abc shifts them near the fundamental ($\omega_0 \pm \Omega$). A $2\omega_0$ term in dq^+ (if $R_- \neq 0$) produces additional components near $3\omega_0 \pm \Omega$. All amplitudes are shaped by the closed-loop responses $G_\pm(j\omega)$.

(ii) If $R_- \neq 0$, the positive-sequence frame contains a single $2\omega_0$ component,

$$i_{dq}(t) = i^+_{dq,\mathrm{dc}} + \Re\{\tilde{\imath}_{2\omega} e^{-j2\omega_0 t}\}, \tag{8.6}$$

with $\tilde{\imath}_{2\omega}$ proportional to R_-. No higher harmonics appear in dq under purely fundamental forcing.

Sketch. With exact decoupling and constant R_+, the positive-sequence loop is LTI with a constant equilibrium in its own synchronous frame, producing only DC content. A negative-sequence component rotates at $-\omega_0$ in $\alpha\beta$ and therefore appears at $-2\omega_0$ in the $+$ frame. $\square$

Corollary 8.2.2 (ABC-domain implication)**.** *If i_{dq} contains only DC and $2\omega_0$ components, the abc currents contain only fundamental positive and/or negative sequences, while instantaneous power exhibits a $2\omega_0$ oscillation proportional to $\|\tilde{i}^+\|\,\|\tilde{i}^-\|$.*

8.2.2 Transient envelopes and modal content

Lemma 8.2.3 (Modal content and mapping)**.** *In the linear regime with fixed parameters, each per-sequence loop is second order with poles $s_{\sigma,1,2} = -\sigma_\sigma \pm j\omega_{d,\sigma}$. For piecewise-constant references,*

$$i_{dq}(t) = i^+_{dq,\mathrm{dc}} + \Re\{\tilde{\imath}_{2\omega} e^{-j2\omega_0 t}\} + \sum_{\sigma\in\{+,-\}} e^{-\sigma_\sigma t}\Re\{\tilde{\eta}_\sigma e^{j\omega_{d,\sigma} t}\}. \tag{8.7}$$

Under inverse Park, a transient at $\omega_{d,\sigma}$ in dq maps to abc sidebands at $|\omega_0 \pm \omega_{d,\sigma}|$ with decay rate $e^{-2\sigma_\sigma t}$.

8.2.3 Perturbation-induced harmonics and interharmonics

Define the closed-loop shaping factor (per axis)

$$G(s) = \frac{s}{L_f s^2 + (K_p + aL_f)s + K_i}, \tag{8.8}$$

and recall the leakage mechanism of Lemma 8.1.1.

Lemma 8.2.4 (Sidebands from PLL jitter and extractor ripple)**.** *Let* $\Delta\omega(t) = \sum_\ell w_\ell e^{j\Omega_\ell t}$ *and* $\varepsilon_{v\sigma}(t) = \sum_p e_p e^{j\Omega_p t}$ *over a window where* $X_{\sigma,\mathrm{nom}}$ *is bounded. Then, to first order,*

$$\|\widehat{\tilde{i}}_\sigma(j\Omega)\| \le |G(j\Omega)|\Big(\tfrac{1}{L_f}\|\widehat{\varepsilon}_{v\sigma}(j\Omega)\| + \|E_\sigma\|\,\|X_{\sigma,\mathrm{nom}}\|\,|\widehat{\Delta\omega}(j\Omega)|\Big). \tag{8.9}$$

PLL jitter produces baseband lines in dq *at* Ω_ℓ *and, when* $2\omega_0$ *content exists, additional components at* $2\omega_0 \pm \Omega_\ell$*. Extractor ripple generates analogous baseband and* $2\omega_0 \pm \Omega_p$ *components, all shaped by* G*.*

Corollary 8.2.5 (ABC-domain sideband map)**.** *A* dq *spectral line at* Ω *maps to* abc *tones at* $|\omega_0 \pm \Omega|$*. Thus baseband* dq *interharmonics appear near the fundamental in* abc*, while* $2\omega_0 \pm \Omega$ *components map to* $\{\omega_0 \pm \Omega,\ 3\omega_0 \pm \Omega\}$*.*

Chapter 9

Characterization of Subsystem Behavior – Part IV: Reference Current Policies

This chapter examines the steady–state and dynamic reference–current policies that govern the response of inverter–based resources during grid disturbances. While the preceding chapters focused on subsystem dynamics and linear–phase current behavior, here we turn to the current–command logic that ultimately shapes the external electrical response of the converter. In particular, we analyze how positive– and negative–sequence current injections are synthesized from the instantaneous terminal–voltage measurements and how these reference policies enable voltage support, ride-through compliance, and operational safety.

The motivation for this analysis arises directly from modern grid codes and interconnection standards, which now articulate explicit expectations for reactive and negative-sequence support from grid-connected inverters. Requirements in IEEE Std 2800-2022, and related European and UK practice guidelines, specify not only connectivity obligations during abnormal voltages but also the minimum fault-response current envelopes and coordination rules between active and reactive current components. These policies form an essential layer that bridges low-level current control with grid-level voltage stability.

For these reasons, this chapter formalizes performance-consistent reference–current policies, quantifies their operating envelopes, and examines how positive- and negative–sequence support is coordinated during unbalanced voltage depressions. The following sections dissect the policy structures, limitations, saturation behaviors, and feasibility domains that arise when these policies operate under instantaneous current limits and real converter hardware constraints.

9.1 Reference current policies for fault ride-through in grid-following inverters

This section specifies reference-current policies for voltage support during faults, consistent with major grid codes and interconnection standards. We focus on the steady-state mapping from measured positive-sequence voltage magnitude $V_1 := |\underline{V}_1|$ to the positive-sequence reactive current reference $\underline{I}^{\text{ref}}_{1,Q}$ (and its coordination with active-current references) used by the current controller. Policies are formulated in per-unit (p.u.) on the same base.

9.2 Positive-sequence reactive current versus positive-sequence voltage magnitude

Let $V_{\text{ref}} = 1$ (p.u.) and define the signed deviation

$$\Delta V_1 := V_{\text{ref}} - V_1. \tag{9.1}$$

The core voltage-reactive policy is a monotone map with (*i*) a deadband, (*ii*) a slope (gain) in A/V (p.u./p.u.), and (*iii*) saturation at the admissible current envelope. A canonical form that covers voltage-based functions and European FRT prescriptions is:

$$\begin{aligned} I^{\text{pol}}_{1,Q}(\,V_1\,) &= \text{sat}_{[-I_{Q,\max},\,I_{Q,\max}]}\big(I_{Q,0} \;+\; K_Q\,\mathcal{S}_\epsilon(\Delta V_1)\big)\,, \\ \mathcal{S}_\epsilon(x) &:= \text{sgn}(x)\;\max\{|x| - \epsilon,\,0\}, \end{aligned} \tag{9.2}$$

where $I_{Q,0}$ is the pre-fault reactive current, $\epsilon \in [0,1)$ is a deadband half-width, and $K_Q > 0$ is the reactive-current gain ("K-factor").[5] The complex positive-sequence current reference is then

$$\underline{I}^{\text{ref}}_1 = I^{\text{ref}}_{1,P}\,e^{j\theta_{v1}} \;+\; j\,I^{\text{exec}}_{1,Q}\,e^{j\theta_{v1}}, \qquad \theta_{v1} := \arg\,\underline{V}_1, \tag{9.3}$$

[5] Under-voltage ($\Delta V_1 > 0$) yields capacitive $I^{\text{pol}}_{1,Q} > 0$; over-voltage yields inductive $I^{\text{pol}}_{1,Q} < 0$.

where $I_{1,Q}^{\mathrm{exec}}$ is the allocated reactive current after coordination with limits.

9.2.1 Deadbands, slopes, and saturation limits

9.2.2 Deadband and slope.

Equation (9.2) implements a piecewise-affine law

$$I_{1,Q}^{\mathrm{pol}} = \begin{cases} I_{Q,0} + K_Q(\Delta V_1 - \epsilon), & \Delta V_1 \geq \epsilon, \\ I_{Q,0} - K_Q(\Delta V_1 + \epsilon), & \Delta V_1 \leq -\epsilon, \\ I_{Q,0}, & |\Delta V_1| < \epsilon. \end{cases} \tag{9.4}$$

Values for K_Q and ϵ are prescribed by grid codes. Typical ranges are $K_Q \in [2, 6]$ (pu reactive current per pu voltage drop) with zero or small deadbands $\epsilon \in [0, 0.02]$ for transmission-connected IBRs, and technology-category dependent choices for distribution DERs.[6] Let the instantaneous magnitude envelope be

$$I_{\max}^{\mathrm{env}} := \min\left\{I_{\mathrm{thermal}},\ I_{\mathrm{short}}(\tau),\ I_{\max}^{\mathrm{volt}}(\theta_i, V_{\mathrm{dc}}, V_1)\right\} \tag{9.5}$$

(thermal, short-term, and voltage-feasibility bounds). Define the positive-sequence budget after reserving any mandated negative sequence I_2 (if applicable) as

$$I_{\max,1} := \sqrt{\left(I_{\max}^{\mathrm{env}}\right)^2 - I_2^2}, \qquad I_2 \geq 0. \tag{9.6}$$

The reactive saturation bound for $\underline{I}_1$ is then

$$|I_{1,Q}| \ \leq\ I_{Q,\max} := \sqrt{I_{\max,1}^2 - I_{1,P}^2}\ , \tag{9.7}$$

[6]See citations for ENTSO-E RfG/GB Grid Code FFCI; IEEE 1547-2018 defines voltage-→reactive functions and performance categories.

and the outer saturation in (9.2) guarantees $|\underline{I}_1| \le I_{\max,1}$.

For a worst-case voltage drop to $V_1 = V_{\rm ret}$, nonbinding saturation requires

$$K_Q \max\{0,\, 1-\epsilon-V_{\rm ret}\} \;\le\; I_{Q,\max}, \tag{9.8}$$

which translates into an upper bound on K_Q at a given envelope (and vice versa). If (9.8) is violated, the policy automatically operates on the saturation face $|I_{1,Q}| = I_{Q,\max}$, which is acceptable if the grid code only specifies a minimum response ("at least K_Q") up to the hardware cap.

9.2.3 Active–reactive coordination under a circular limit.

Let $I^\star_{1,P}$ be the pre-fault active current (or an operator-specified target during FRT). Under the instantaneous circle constraint $|\underline{I}_1| \le I_{\max,1}$ the reactive-priority allocation solves

$$\begin{aligned} \min \quad & \big(I_{1,P} - I^\star_{1,P}\big)_+^2 \;+\; \rho\,\big(I_{1,Q} - I^{\rm pol}_{1,Q}\big)_+^2 \\ \text{s.t.} \quad & I_{1,P}^2 + I_{1,Q}^2 \le I_{\max,1}^2, \qquad 0<\rho\ll 1, \end{aligned} \tag{9.9}$$

yielding the radial projection

$$(I^{\rm exec}_{1,P},\, I^{\rm exec}_{1,Q}) = \begin{cases} \Big(I^\star_{1,P},\, I^{\rm pol}_{1,Q}\Big), & \text{if } (I^\star_{1,P})^2 + (I^{\rm pol}_{1,Q})^2 \le I^2_{\max,1}, \\ \left(\dfrac{I_{\max,1}\, I^\star_{1,P}}{\sqrt{(I^\star_{1,P})^2 + (I^{\rm pol}_{1,Q})^2}},\quad \dfrac{I_{\max,1}\, I^{\rm pol}_{1,Q}}{\sqrt{(I^\star_{1,P})^2 + (I^{\rm pol}_{1,Q})^2}}\right), & \\ & \text{otherwise.} \end{cases} \tag{9.10}$$

Equation (9.10) preserves the power-factor angle of the desired $(I^\star_{1,P}, I^{\rm pol}_{1,Q})$ pair while meeting the instantaneous limit.

9.2.4 Ride-through state machine and admissible regions.

Let the voltage ride-through (VRT) region be defined by a no-trip envelope $\mathcal{V}_{\rm NT} \subset \mathbb{R}_{\ge 0} \times \mathbb{R}_{\ge 0}$ in the (V_1, time) plane. During $(V_1, t) \in \mathcal{V}_{\rm NT}$, current injection must continue and the policy (9.2)–

(9.10) is active. Outside $\mathcal{V}_{\mathrm{NT}}$ (extreme low/high voltage regions), cessation or disconnection is permitted/mandated. A minimal state machine is

$$\sigma(t^{+}) = \begin{cases} \textit{RUN}, & (V_1, t) \in \mathcal{V}_{\mathrm{NT}}, \\ \textit{MOM-CEASE}, & (V_1, t) \in \mathcal{V}_{\mathrm{MC}}, \\ \textit{TRIP}, & (V_1, t) \in \mathcal{V}_{\mathrm{TRIP}}, \end{cases} \tag{9.11}$$

$$\mathcal{V}_{\mathrm{NT}} \cup \mathcal{V}_{\mathrm{MC}} \cup \mathcal{V}_{\mathrm{TRIP}} = \mathbb{R}_{\geq 0} \times \mathbb{R}_{\geq 0}$$

with $\mathcal{V}_{\mathrm{MC}}$ a narrow band where momentary cessation may be allowed by local codes. In *RUN*, (9.10) must be respected; in *MOM-CEASE* active and reactive injection may be reduced subject to applicable standards.

9.2.5 Policy–envelope feasibility and guaranteed minimum response.

Combining (9.4) and (9.10), the guaranteed reactive current delivered at a retained voltage V_{ret} is

$$I_{1,Q}^{\min}(V_{\mathrm{ret}}) = \min\left\{ K_Q\,(1 - \epsilon - V_{\mathrm{ret}})_{+},\ \sqrt{I_{\max,1}^{2} - (I_{1,P}^{\star})^{2}} \right\}, \tag{9.12}$$

which meets grid-code minima provided $I_{\max,1}$ (hardware and DC-link) and K_Q satisfy (9.8). If the code additionally caps the total current at the short-term rating I_{short} for a duration τ, replace $I_{\max,1}$ by $\min\{I_{\max,1},\ I_{\mathrm{short}}(\tau)\}$.

9.2.6 Prefault bias removal.

Some grid codes specify that the reactive-current increment is proportional to the change in voltage from the pre-fault level V_{pf}. This is implemented by replacing ΔV_1 with $\Delta V_{\mathrm{pf}} := V_{\mathrm{pf}} - V_1$ and setting $I_{Q,0} \leftarrow I_{Q,\mathrm{pf}}$ (measured just before fault). The policy then responds identically regardless of pre-fault power factor.

9.3 Negative-sequence reactive current versus negative-sequence voltage magnitude

This subsection specifies a steady-state policy for negative-sequence support during asymmetrical faults. Let $V_2 := |\underline{V}_2|$ and $\theta_{v2} := \arg \underline{V}_2$. We define a voltage-proportional policy (consistent with European RfG implementation guidance and GB FFCI developments that explicitly discuss asymmetric support options [154–157])

$$\begin{aligned} \underline{I}_2^{\mathrm{pol}}(V_2) &= K_2\, \mathcal{S}_{\epsilon_2}(V_2)\, e^{j(\theta_{v2}+\phi_{2,\mathrm{pol}})}, \\ \mathcal{S}_{\epsilon_2}(x) &:= \max\{x-\epsilon_2, 0\}, \end{aligned} \tag{9.13}$$

with gain $K_2 > 0$ (pu/pu), deadband $\epsilon_2 \in [0, 1)$, and a policy angle $\phi_{2,\mathrm{pol}}$. The executed reference is the projection of $\underline{I}_2^{\mathrm{pol}}$ onto the instantaneous feasibility envelope:

$$\underline{I}_2^{\mathrm{ref}} = \mathrm{Proj}_{|\underline{I}_1|^2+|\underline{I}_2|^2 \le (I_{\max}^{\mathrm{env}})^2} \left(\underline{I}_1^{\mathrm{ref}}, \underline{I}_2^{\mathrm{pol}}\right)\Big|_{\underline{I}_1^{\mathrm{ref}} \text{ from (9.3)}}, \tag{9.14}$$

where the projection implements either balanced scaling (angle preserving) or reactive-priority allocation. While explicit negative-sequence obligations vary across jurisdictions (some leave them as national options [154, 155]), (9.13) captures the common engineering form used in practice and in testing proposals.

9.3.1 Phase targeting (voltage balancing).

For steady-state voltage balancing, the negative-sequence reactive current should be in quadrature with $\underline{V}_2$. We parameterize

$$\phi_{2,\mathrm{pol}} = \sigma\,\frac{\pi}{2} + \delta\phi_2, \qquad \sigma \in \{+1, -1\}, \tag{9.15}$$

where $\sigma = +1$ ($\sigma = -1$) injects capacitive (inductive) negative-sequence current relative to $\underline{V}_2$. Linearizing the sequence KVL around the PCC (Thévenin negative-sequence source $\underline{V}_{2,\text{th}}$, network $Z_{2,g}$, inverter equivalent $Z_{2,\text{inv}}$) gives

$$\begin{aligned} \underline{V}_2 &= \underline{V}_{2,\text{th}} - (Z_{2,g} + Z_{2,\text{inv}})\, \underline{I}_2 \\ \Rightarrow \quad \left.\frac{dV_2}{dK_2}\right|_{\delta\phi_2=0} &= -\,\Re\big\{(Z_{2,g} + Z_{2,\text{inv}})\, j\, e^{j\theta_{v2}}\big\} \\ &\quad \cdot\, \mathcal{S}_{\epsilon_2}(V_2) \;\leq\; 0, \end{aligned} \tag{9.16}$$

so $\delta\phi_2 = 0$ with $\sigma = +1$ (capacitive) yields the steepest reduction in $|\underline{V}_2|$ for inductive grids ($\Im\{Z_{2,g}\} > 0$). A small policy misalignment $\delta\phi_2$ induces a first-order degradation of voltage balancing $\propto \cos\delta\phi_2$.

9.3.2 Coupled ratio with positive-sequence support.

Let $I_{Q,1}^{\text{pol}}(V_1)$ be the positive-sequence reactive policy from (9.2). A common coordination rule is a share ratio

$$\frac{|\underline{I}_2^{\text{pol}}|}{|I_{Q,1}^{\text{pol}}|} = \rho_2(V_1, V_2) \in [0, \rho_{2,\max}], \qquad \rho_{2,\max} \leq 1, \tag{9.17}$$

selected by the TSO/DSO to prioritize bulk voltage support (often $\rho_{2,\max} \ll 1$) [154, 156]. Implement (9.17) by

$$\begin{aligned} K_2(V_1, V_2) &= \rho_2(V_1, V_2)\, \frac{|I_{Q,1}^{\text{pol}}(V_1)|}{\mathcal{S}_{\epsilon_2}(V_2)}, \\ K_2 &\leq K_{2,\max} \\ &\quad \text{(hardware/DC-link constraint).} \end{aligned} \tag{9.18}$$

Under the instantaneous circle limit $|\underline{I}_1|^2 + |\underline{I}_2|^2 \leq (I_{\max}^{\text{env}})^2$, the reactive-priority projection preserves the power-factor angles of both sequences while meeting the cap, whereas balanced scaling preserves the ratio $|\underline{I}_2|/|I_{Q,1}|$; both are convex and uniquely defined.

9.3.3 Guaranteed minimum and feasibility.

For a retained unbalance $V_{2,\mathrm{ret}}$, the delivered magnitude satisfies

$$|\underline{I}_2^{\mathrm{exec}}| \;\geq\; \min\Big\{ K_2\, \mathcal{S}_{\epsilon_2}(V_{2,\mathrm{ret}}),\; \sqrt{(I_{\max}^{\mathrm{env}})^2 - |\underline{I}_1^{\mathrm{exec}}|^2} \Big\}, \tag{9.19}$$

which is the negative-sequence analogue of (9.12). Equation (9.19) formalizes the trade-off between the share ρ_2, the envelope, and the concurrent $+1$ support mandated by FRT provisions [154, 156].

Chapter 10

Proposed Reduced-Order Model – Part I: Symmetrical Fault Response

10.1 Introduction

The fault response of inverter-interfaced distributed generators (IIDG) is different from that of synchronous generators because the IIDG fault current is limited by the inverter maximum current rating, which is determined by the limited thermal overcurrent capacity of semiconductor devices [158], and the current-control strategies of the IIDGs [159]. Also, the inverter controls can respond faster to faults [160] than synchronous generators. The fault current from conventional generators partially depends on the impedance between the generator terminal and the fault location, whereas the fault current from inverters, which are typically current-regulated sources, shows little or no dependence on network impedance [161]. Hence, traditional generator voltage-source equivalent models for fault analysis are not suitable for modeling IIDGs [160]. Because of the way conventional generators, i.e. synchronous generators, behave during faults, their fault current can be very high. The reason behind the high short-circuit current of synchronous generators is that the initial high reluctance for magnetic flux forces the armature current to be very high to maintain the constant flux linkage. The gradual decrease of reluctance results in gradually decreasing fault current for synchronous generators. But inverter fault currents can change much more quickly and are typically much lower; they can be further limited by the control and protection functions of the inverter, sometimes to values even less than the inverter rated current. Thus, overcurrent-based protection systems that were developed considering conventional generators might not be adequate for networks with high penetration levels of IIDGs [158, 162]. Unlike conventional generators, there is no widely accepted tried-and-tested analytical model that captures the fault response of IIDGs [159, 163]. Generally, studies involving inverter fault response model inverters in three ways: *(i)* complex and full EMT model [164, 165]; *(ii)* constant current model [160, 166]; *(iii)* constant power model [160, 167]. EMT models of inverters are not suitable for large scale protection studies as they are computationally expensive [168] and require information that is confidential (i.e. generally not available outside of inverter manufacturers). On the other hand, approaches *(ii)* and *(iii)* are not robust enough to capture the contribution of fault-current from IIDG as there exists a time-dependency of inverter fault current [169].

Though inverter fault response has been studied extensively with time domain simulations [170] using EMT models of inverters and experimental studies [171, 172], the need of analytical fault models of inverter has been identified by many researchers [160, 173] because accurate and efficient analytical fault models are needed for large-scale protection studies. However, the fault current response of inverters at fundamental frequency after a grid fault cannot be fully explained by models currently available in literature. Authors in [173, 174] have presented an analytical fault model of inverters considering the current limiting approaches to limit inductor current. Taking into account PQ source inverters, the model only considers the controller action on inverter fault response, ignoring the impact of hardware components of the inverter and the standard/grid code requirements. Fault characteristics of IIDGs with two different control modes, current control and voltage control, have been studied in [158]. The impact of different current limiting approaches was also investigated in this research. However, no analytical model was presented by the authors to calculate the fault-current of grid-following inverters. Based on the sequence-current control and reactive power support during grid fault, [160] proposed a short-circuit current calculation method for a multi-IIDG system. The authors assumed the inverters are constant power sources, where the reference power is dependent on reactive power support during grid fault. But, in realty, inverters can also operate in other modes. Moreover, the presented method does not provide any way to calculate different fault current magnitudes observed within the first few cycles after a fault. [169] recommends to model the short-circuit current contribution of a Type IV wind farm as a limited current-source with a current value of $2-3$ pu for the first one to two cycle and 1.5 pu thereafter. This model is quite simple and may not conform to the experimental fault response. In addition, the model does not provide any information about the transition from one fault current level to another fault current level. Using the controller-based equivalent circuit concept, phasor domain short-circuit models have been proposed for Type IV wind turbine generators in [175] and for Type III wind turbine generators in [176]. These models can be used for other IIDGs accounting for different control schemes, transient functionality, decoupled sequence control, and fault ride-through capability. The models provide steady-state fault current via iterative solutions. Some commercial software are using similar models for Type III and Type IV wind turbine generators [177]. However, these models do not give information on how the IIDG current settles from pre-fault current to the steady-state fault current and does not explain the initial current spike during faults typically observed for IIDGs.

The fault responses of grid-forming inverters and grid-following inverters are different. This paper analyzes grid-following inverters because nearly all grid-connected inverters are grid-following at present. The objectives of this paper are to develop an analytical background to characterize the fault behavior of grid-following inverters and to develop a reduced-order parameterized short-circuit current (RPSC) model that explains the most important aspects of inverter fault current magnitude for the purposes of protection and interconnection studies. As such, the model is intentionally relatively simple, and does not reproduce detailed fault current waveforms. The RPSC model of inverters presented in this paper has some similarity with synchronous machine models. To the best of our knowledge, the proposed RPSC model is the first model that addresses the observable high initial spike of inverter fault current and exponential transition to quasi-steady-state fault current magnitude. The model presents mathematical and physical explanations to this behavior. Most of the published relevant models mainly deal with quasi-steady-state fault current, ignoring the transition from sub-transient to transient and finally to steady-state fault current. The rest of the paper is organized as follows: Section 10.2 discusses the typical system description of IIDG, then section 10.3 explores the contribution of different inverter components to the fault current. Based on the analysis carried out in section 10.3, an RPSC model of inverters is proposed in

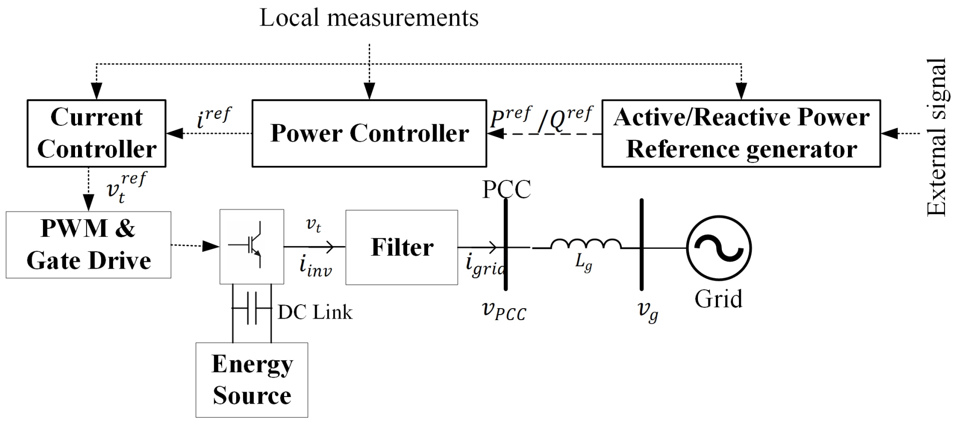

Figure 10.1: Common approach to connect an IIDG with the grid

section 10.4. Validation of the proposed RPSC model through experimental and simulation results is presented in section 10.5 and finally section 10.6 concludes the paper.

10.2 IIDG System Overview

The power delivery capability of IIDG to the grid is determined by the availability of power at the energy source and the power electronics based interfacing units connecting the grid. Fig. 10.1 shows a common approach to connect IIDG with the grid. Because the IIDG is connected with the grid through an inverter, the behavior of the IIDG during a grid fault is largely determined by the inverter. The input energy source dynamics (e.g. photovoltaics or battery systems) typically do not heavily influence AC fault response, so the IIDG fault response is dictated by the inverter controller and the hardware components of inverter. Though actual control strategies and hardware configurations (i.e. power stage, filter etc.) used in inverters vary widely, a general understanding of these blocks will be helpful to design a generic short-circuit model of inverter.

10.3 Factors Affecting Inverter Behavior During Faults

10.3.1 Current Controller and Output Filter

Inverter output current, $i_{grid,k}$, is controlled to track the reference current, i_k^{ref}, by proper selection of current controller compensator, G_i. Here $k \in \{a, b, c\}$ or $k \in \{\alpha, \beta\}$ or $k \in \{d, q\}$, depending on the choice of reference frame for current control. Selection and parameter tuning of G_i depends on the gain of PWM inverter, G_{inv}, sensor gains of measured output current, H_i, inverter output filter, and feedforward voltage passed through feedforward function, G_{fb}. The estimated voltage at point of common coupling (PCC), $\widehat{v}_g$ is often time passed through G_{fb} and applied in the current controller to supress the disturbance of actual PCC voltage, v_g. Fig. 10.2a shows typical current control strategies found in literature, and Fig. 10.2b shows the relationship of output current to input current for a generic current controller [178]. G_{x1} depends on the current controller compensator, and inverter hardware components whereas G_{x2} mainly depends on inverter hardware including filter parameters. For example, Fig. 10.2c shows a basic current controller for an inverter with LCL filter for which G_{x1} and G_{x2} can be calculated as

$$G_{x1} = \frac{G_i G_{inv} Z_{Cf}}{Z_{inv} + Z_{Cf}} \tag{10.1}$$

$$G_{x2} = \frac{Z_{inv} + Z_{grid}}{Z_{inv} Z_{grid} + (Z_{inv} + Z_{grid}) Z_{Cf}} \tag{10.2}$$

where Z_{inv} is the impedance of inverter side L filter, Z_{grid} is the impedance of grid side L filter, and Z_{cf} is the capacitor impedance of the LCL filter.

From Fig. 10.2b, the relation of grid current, $i_{grid,k}$, to the reference current, i_k^{ref}, can be calculated as (10.3).

$$i_{grid,k} = \frac{T}{1+T}\frac{1}{H_i} i_k^{ref} - \frac{G_{x2}}{1+T} v_g \tag{10.3}$$

where T is the loop gain of the current controller and can be expressed as $T = G_{x1} G_{x2} H_i$. Since current controllers are mostly symmetrical, i.e. the transfer functions of d and q axis output currents with respect to corresponding reference currents are the same, for the following discussion, k is discarded for the sake of simplicity. (10.3) indicates that inverter output current not only depends on the reference current, but also on the inverter terminal voltage. Under normal operating condition, the inverter current controllers are designed such a way that the loop-gain T is substantially high to make the contribution of the second part in (10.3) negligible. In some cases, voltage feed-

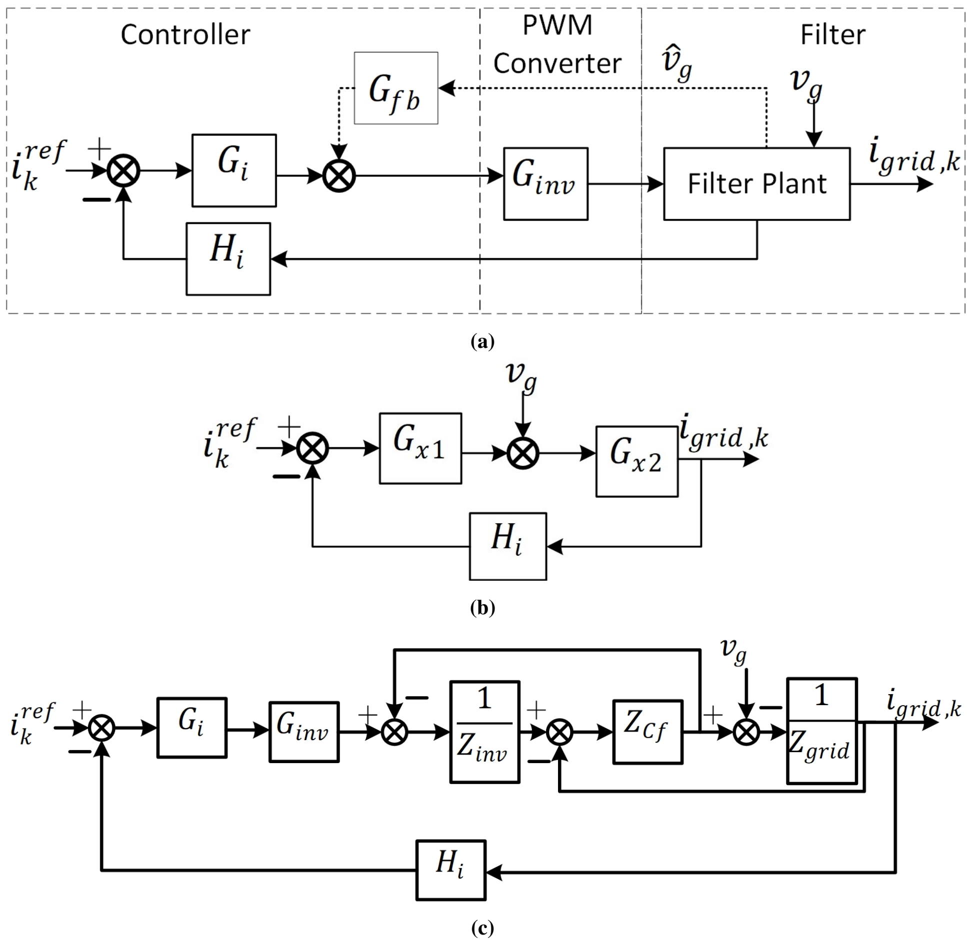

Figure 10.2: Block diagram of typical current-control strategies a) general current controller b) equivalent current controller c) current controller for inverter with LCL filter.

forward terms are added to the inverter current controller to eliminate the impact of grid voltage on inverter output current [178, 179]. The voltage feed-forward term should be theoretically able to suppress the impact of distorted grid-voltage. But, in reality, voltage feed-forward term cannot sufficiently suppress the impact of voltage disturbance on inverter output current [180] as there are errors introduced by signal distortion by the conditioning circuits, digital controller control delay and the pulse-width modulation zero-order hold. When voltage feed-forward terms are used, (10.3) can be updated as (10.4).

$$i_{grid} = \frac{T}{1+T}\frac{1}{H_i}i^{ref} - \frac{G_{x2}}{1+T}v_g + G_{fb}\widehat{v}_g \tag{10.4}$$

if $\widehat{v}_g = G_v v_g$, (10.4) can be updated as

$$i_{grid,k} = \frac{T}{1+T}\frac{1}{H_i}i_k^{ref} - Yv_g \tag{10.5}$$

where $Y = \frac{G_{x2}}{1+T} - G_{fb}G_v$. From (10.5), it is evident that even if voltage feed-forward terms are added in the current controller to eliminate the voltage disturbance, a sudden change in voltage magnitude and phase angle will still have impact on the inverter output current. A close examination of (10.3) and (10.5) reveals that the impact of voltage disturbances on inverter output current is highly dependent on the complexities of the inverter output filter, at least for the initial transient response.

To verify the observations made in this section, four different cases relative to the general inverter current-controller shown in Fig. 10.2a were simulated as shown in Table 10.1. Other parameters common for all cases are shown in Table 10.2. For L filter, the value of filter inductance was calculated as $L = L_{inv} + L_{grid}$. The reference current for all four cases was the same, but the grid voltage magnitude and phase angle were changed at different locations of the voltage waveform. Fig. 10.3 shows the simulation results for two types of grid disturbances: (*i*) change of voltage magnitude from 1 p.u. to 0.2 p.u. and (*ii*) 30° change of phase angle. The responses observed in phase A of the simulated three phase inverters are shown in Fig. 10.3. It can be seen

Table 10.1: Simulated cases

	Case 1	Case 2	Case 3	Case 4
Filter	LCL	LCL	L	L
Voltage FF	None	Yes	None	Yes

Table 10.2: Simulated inverter parameters to evaluate the initial spike of inverter current during fault

Parameter	Value	Parameter	Value
v_g	220V	L_{inv}	600 μH
f_{grid}	60 Hz	C_f	10 μF
P_0	6 kW	L_{grid}	200 μH
f_s	10 kHz		
G_i	$0.1 + \frac{2.5s}{s^2+(31.4)^2}$	G_{fb}	$\frac{1}{120}$
G_{inv}	120	H_i	$\frac{1}{0.0001s+1}$

that the spike of inverter output current after a sudden change of voltage magnitude and phase angle depends on the location on the voltage waveform where the disturbance was applied and on the inverter filter. Other factors, i.e. voltage feed-forward gain, have a small effect compared to the factors previously mentioned. Neglecting the factors with lower impact on the initial spike of inverter fault output current, it can be said that the initial spike of inverter output current after grid fault largely depends on the inverter filters, fault voltage, and point-on-wave timing of the fault. Intuitively, it can be explained as the release of energy stored in the passive components of the inverter filter following a voltage disturbance. Inverter filters will have higher bandwidth than the bandwidth of inverter current-controller to avoid unwanted interactions. So, the time to dissipate the the stored energy in the filter due to voltage disturbance will be lower than the time constant of inverter current controller. The current controller time response is typically in the range of $5 - 50$ ms, depending on the inverter switching frequency and specific requirements [129, 181]. Assuming the filter has ten times higher bandwidth than the current controller, the initial current spike after grid fault is expected to diminish within 0.5 ms-5 ms. The reference current during this period can be safely assumed as constant. From (10.3) and (10.5), it is evident that the relation of voltage disturbance and inverter output current is quite complex. However, based on the previous

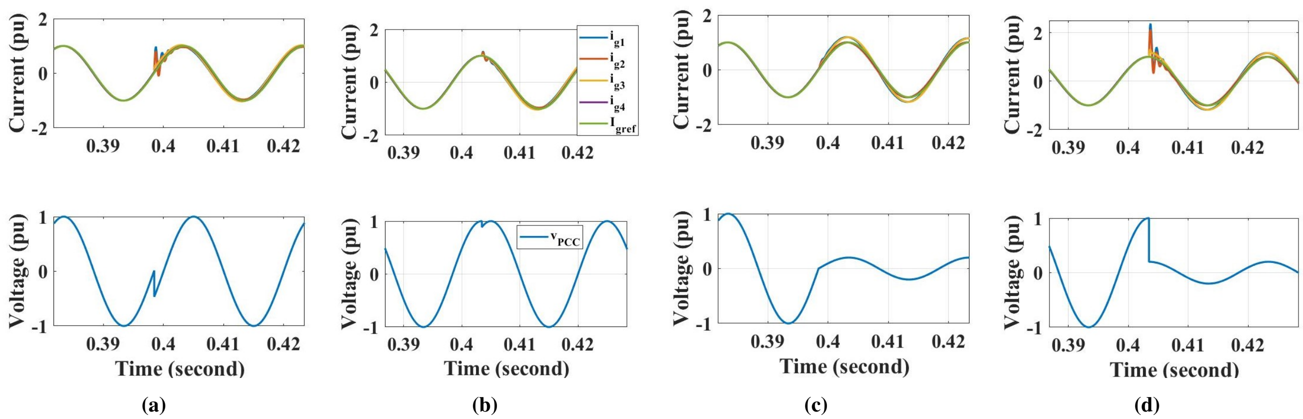

Figure 10.3: Transient inverter current responses to: (a)-(b) change of voltage phase angle at two different points-on-wave; (c)-(d) change in voltage magnitude at two different points-on-wave. I_{g1}-I_{g4} are for the four cases in Table 10.1.

discussion, it can be characterized by an initial spike of output current followed by rapid decay of that initial spike. For most practical purposes, e.g. protection coordination, it is enough to know the approximate magnitude of the initial spike and time to decay that spike. Following this argument, the impact of voltage disturbance on inverter output current can be approximated as

$$I(t) = I_{pre} + I_{spike} e^{\frac{-t}{T''}} \tag{10.6}$$

where $I(t)$ is the magnitude of the output current, I_{pre} is the pre-fault current magnitude, I_{spike} is the magnitude of initial current surge, and $T'' \in [0.5ms, 5ms]$ is the time constant of the exponential decay of I_{spike} if approximated as a first-order response. When using detailed EMT simulation or lab tests to estimate I_{spike}, the fault can be applied near the peak of the voltage waveform to obtain a worst case fault magnitude.

10.3.2 Current Limiters

Grid codes and standards [18] require the inverter to remain connected with the grid during certain voltage disturbances while injecting current, so it is essential to monitor the reference current for any current limit violation. A separate current limit block may be used in the current controller, or the current reference generation algorithm may be designed to prohibit generating any reference current that violates the inverter current rating [167]. During faults, the grid voltage at the PCC changes depending on the severity and nature of the fault. Depending on which grid code and standard is being followed, the inverter response to a grid disturbance will vary widely. For example, for an inverter that conforms to IEEE 1547-2018, if the grid voltage falls within the continuous operation region, the inverter current must be adjusted to maintain the same pre-fault power or prorated power. Thus, in this range, the IIDG system can be considered a current-limited power source. Outside the continuous operation region, the IIDG has more flexibility to regulate its output current [182] so that the inverter power electronic switches are protected from overcurrent. The IIDG can employ any of the following mechanisms to provide this protection [158, 162, 173]:

Instantaneous saturation limit on reference current

This approach limits the instantaneous magnitude of the reference current whenever the current tends to exceed the acceptable current threshold value, I_{max}, of the inverter. This approach can be expressed as:

$$I_{ssf}^{ref} = \begin{cases} I_{PQ}^{ref} & V_{cl} \leq v_{PCC} & (10.7a) \\ I_{PQ}^{ref} & I_{PQ}^{ref} < I_{max} \text{ and } v_{PCC} \leq V_{cl} & (10.7b) \\ I_{max} & others & (10.7c) \end{cases}$$

where v_{PCC} is the voltage at PCC, V_{cl} is the lower voltage limit of continuous operation region, I_{PQ}^{ref} is the reference current required to maintain constant reference output power and I_{ssf}^{ref} is the quasi-steady-state reference current after the fault. When the current hits the saturation limit, the phase angle of fault current depends on the active power or reactive power priority settings of the inverter.

Predefined fault current

In this case, the reference current will be changed to a predefined fault current to avoid damaging the inverter during a fault. Predefined fault current may be defined in two ways:

(a) A fixed predefined fault current, $I_{ssf,pd0}^{ref}$, may be used for any fault that results in a grid voltage disturbance beyond the continuous operation region. This approach can be expressed as follows:

$$I_{ssf}^{ref} = \begin{cases} I_{PQ}^{ref} & V_{cl} \leq v_{PCC} \quad (10.8a) \\ I_{ssf,pd0}^{ref} & \text{others} \quad (10.8b) \end{cases}$$

(b) A variable predefined fault current, $I_{ssf,pd}$, based on fault voltage or other parameters can be used. This approach to the predefined fault current can be expressed as follows:

$$I_{ssf}^{ref} = \begin{cases} I_{PQ}^{ref} & V_{cl} \leq v_{PCC} \quad (10.9a) \\ I_{ssf,pd}^{ref}(v_{PCC}, I_{pre}) & \text{others} \quad (10.9b) \end{cases}$$

where I_{pre} is the pre-disturbance inverter output current.

The inverter reference current gets updated once a voltage disturbance has been detected and the pre-disturbance reference current, $I_{pre\_f}^{ref}$, gets changed to the I_{ssf}^{ref} after detection of fault. The transition from $I_{pre\_f}^{ref}$ to I_{ssf}^{ref} tends to happen in an approximately exponential manner because of the presence of a low-pass filter [174, 183, 184] in the power controller and in the current reference generator to eliminate higher order harmonics. The cutoff frequency of the low-pass filter in the power controller needs to be low enough to eliminate the unwanted terms and high enough to meet design requirements on power response time [184]. Several values appear in the literature for the cutoff frequency for this low-pass filter. Reference [185] recommended a transient response time for the power controllers on the order of 100 ms to provide a slowly changing reference current to ensure a high-quality inverter output current. It was recommended in [186] to fix the cutoff frequency of the low-pass filter one decade below the fundamental frequency. IEEE 1547-2018 contains some requirements that might influence the low-pass filter design. For example, following the restoration of the voltage to the mandatory operation region, the inverter must restore the active current to 80% of the pre-disturbance value within 0.4 s, and the inverter must be able to meet the response time requirements for the frequency-power droop and other grid support functions. In most cases, this low-pass filter is first order, but a higher order filter could also be used. For the purpose of generalization, a first-order low-pass filter with a cutoff frequency of ω_c can be assumed, which will result in an exponential transition from $I^{ref}_{pre\_f}$ to I^{ref}_{ssf}. Assuming the current controller tracks reference current with sufficiently high accuracy, inverter output current magnitude, I, during fault will be a time-dependent variable and can be expressed as (10.10).

$$I(t) = I^{ref}_{ssf} + (I^{ref}_{pre\_f} - I^{ref}_{ssf})e^{-\omega_c t} \tag{10.10}$$

10.3.3 Grid-support Functions

Grid support functions will not have any impact on the maximum fault current from the inverter because the current limiter will clip any attempt to increase the fault current beyond the acceptable value. The voltage support functions in IEEE 1547-2018 have relatively slow response times because they are designed to support steady-state voltage, so the effect on the fault current will be minimal. In some regions following other interconnection standards, inverters may directly adjust current magnitude or phase angle to support voltage during faults. In such cases, the response depends on the specific grid code being followed, but is still constrained by the inverter current limit. To obtain an RPSC model that accounts for the effects of standards requirements such as continuous current production, momentary cessation, or fast dynamic voltage support, the relevant functions should be enabled during the simulation or testing used to produce the RPSC model. RPSC model parameters may be different for different inverter settings configurations.

10.4 Reduced-order Parameterized Short-circuit Current (RPSC) Model

Discussion in Section 10.3 showed that the inverter fault current has at least three components that are time dependent. (10.6) - (10.10) describe these time-dependent components. These time-dependent components of the inverter fault current can be considered analogous to the sub-transient, transient, and steady-state reactance of the synchronous generators during transient conditions [187]. But unlike synchronous generators, these components refer to the inverter current instead of the reactance. Another key difference between the three-phase fault current transients in synchronous generators and the IIDG is that the former has a DC component but the IIDG does not have significant DC component in the fault current. At the moment of voltage dip during fault, there could be some DC current due to interactions of flux linkages in the filter inductors. However, this DC component will die out quickly as the time response of the inverter current controller takes effect.

Inverter fault behavior can be modeled in three distinct time periods:

Subtransient period, $T^{''}$

During this period, there is an initial spike of inverter fault current after the grid fault, as discussed in section 10.3.1. The magnitude of the initial spike largely depends on the inverter filter and the point-on-wave of the grid voltage where the fault happened. The duration of this period is expected to be less than the time constant of the inverter current controller. Based on the published literature on current-controller time constants, it can be assumed that $T^{''} \leq 5ms$. The maximum current magnitude, $I^{''}$, in this very brief period could be as high as 200% to 300% of nominal current [187–189] for typical off-the-shelf inverters.

Transient period, $T^{'}$

This is the period when the inverter output current transitions to steady-state fault current from the pre-fault current as described by (10.10) and discussed in Section 10.3.2. This transition from pre-fault current to steady-state fault current may last between 15ms to 500ms. At the beginning of this period, the inverter output current, $I^{'}$, is approximately equal to the pre-fault current, i.e. $I^{'} = I_{pre}$, and the period ends when the inverter output current reaches close to the steady-state fault current.

Steady-state period

This is the final stage of inverter fault response when the inverter reaches a quasi-steady state. The fault current during this period can be denoted as a steady-state current, I^{ssf}. The value of

Table 10.3: Range of the proposed RPSC model parameters

Parameter	Range	Parameter	Range
$I^{''}$	$1-3$ p.u.	$T^{''}$	$0.5ms-5ms$
$I^{'}$	I_{pre}	$T^{'}$	$15ms-500ms$
I^{ssf}	<1.5 p.u.	T^{ss}	Clearing time

I^{ssf} will be limited by (10.7), (10.8) or (10.9). Inverters exhibiting steady state fault response as described by (10.9) need additional consideration since the steady state fault current is a function of fault voltage at PCC and pre-fault current. In time-domain simulation, a lookup table can be used for those inverters to set the steady state fault current. For more accurate analysis, a power flow study can be done to get an estimate of the fault voltage at PCC to set the steady state fault current level, perhaps using iterative power flow solution techniques as in [175] and [176].

Immediately after a grid fault, the IIDG can be modeled as a current source as shown in Fig. 10.4a. Fig. 10.4b graphically shows the three distinct periods of inverter current response after a grid fault. Mathematically, the proposed RPSC model can be expressed as (10.11).

$$I_f(t) = (I^{''} - I^{'})e^{\frac{-t}{T^{''}}} + (I^{'} - I^{ssf})e^{\frac{-t}{T^{'}}} + I^{ssf}f(t), \tag{10.11}$$

where $I_f(t)$ is the IIDG fault current and $f(t)$ is a step function which can be defined as

$$f(t) = \begin{cases} 1 & t \leq T^{ss} \quad (10.12a) \\ 0 & t > T^{ss} \quad (10.12b) \end{cases}$$

where T^{ss} is the clearing time of the fault. The expected range of the parameters of the proposed inverter fault current model is presented in Table 10.3. Most commercially available inverters control their output current in positive sequence only, without contributing to negative- and zero-sequence currents. In those cases, the RPSC model developed in this paper can be applied to positive sequence only. However, the model can be easily extended to negative and zero sequence currents if the inverter also contributes to negative and zero-sequence currents. Note that the proposed RPSC model covers fault current magnitude, so the model can be used of the model can be

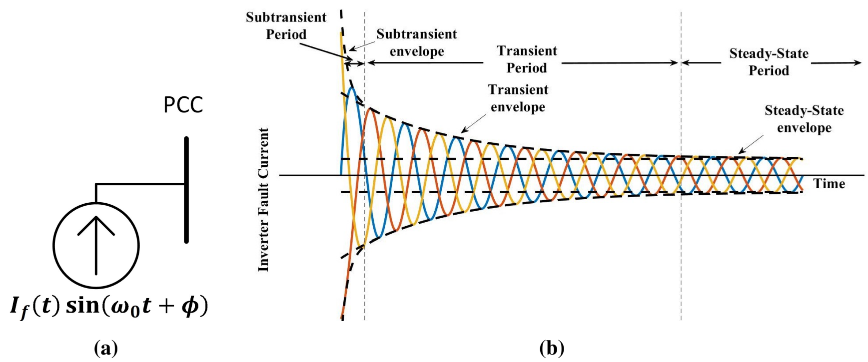

Figure 10.4: Visual illustration of the RPSC model of inverters a) inverter fault model b) inverter fault current

in overcurrent protection analysis. The phase angle of the fault current is not currently modeled; the model could be expanded to include phase angle in future work. The phase angle will be determined by many factors, including availability of the primary energy source, the control structure of the inverter, and the standards the inverter conforms to. Once the fault current envelop is known, by considering the factors effecting phase angle, the RPSC model can be used for setting other protective relays, e.g. distance relays.

10.4.1 Model Parameter Fitting

Fig. 10.5 shows the steps developed to fit the RPSC model to experimental data. Inverter fault response is recorded via laboratory experiment (or via detailed electromagnetic transient simulation if available). The envelope of the fault current curve can be detected using available envelope detection algorithms, for example, the function *envelope* in Matlab. The envelope may be passed through a low-pass filter to remove components at frequencies above those of interest. Using a filter may add additional time delay in the detected envelope which may negatively impact fitting the model to data. To mitigate this, it is necessary to time shift the fault current envelope to align with the fault start time.

After the fault current envelope is obtained, an appropriate form of the RPSC model needs to be selected. In the first iteration, the basic form as shown in (10.11) can be chosen. The RPSC model response in the transient period can be easily updated with an appropriate higher order response if capturing the higher-order response is important for any specific application. In that case, the first order decay term $e^{\frac{-t}{T'}}$ in can be replaced with a second order decay term $d(t)$. Equations (10.13) and (10.14) show the expressions for $d(t)$ and $D(s)$, the second order responses to a unit step change in the time domain and frequency domain, respectively.

$$d(t) = e^{\frac{-\zeta t}{\tau_s}} \left(cos\left(t\omega_d\right) + \frac{\zeta}{\sqrt{1-\zeta^2}} sin\left(t\omega_d\right) \right) \tag{10.13}$$

$$D(s) = \frac{1}{\tau_s^2 s^2 + 2\zeta\tau_s s + 1} \tag{10.14}$$

Here τ_s is second order time constant, ζ is damping factor and $\omega_d = \frac{1}{\tau_s}\sqrt{1-\zeta^2}$. An example of the inclusion of higher order terms is demonstrated in the next section.

Before the model and envelope data can be used in a curve fitting algorithm, initial estimates of the model parameters are required if a least-squares curve-fitting algorithm is used. The approximate values of $I^{''}$, $I^{'}$ and I^{ssf} can be directly measured from the inverter fault response. It was found that setting $T^{''} = 0.002$ and $T^{'} = 0.02$ as starting points gives good convergence using a lease-squares curve fitting algorithm. Once the model is fitted, the r-squared value is calculated as an indicator of goodness of fit (GoF). If the GoF of the fitted model is acceptable, the fitted model can be accepted. Otherwise, the process is repeated with with different starting points (or higher order equations) until an acceptable GoF is reached.

10.5 Experimental and Simulation Results

The proposed inverter fault current model presented in this paper was validated with experimental and simulation results.

10.5.1 Experimental Setup

The inverter fault test setup shown in Fig. 10.6 was developed at the Energy Systems Integration Facility (ESIF) of the National Renewable Energy Laboratory (NREL). The test setup consists of a PV simulator, commercial off-the-shelf inverter (equipment under test (EUT) in Fig. 10.6),

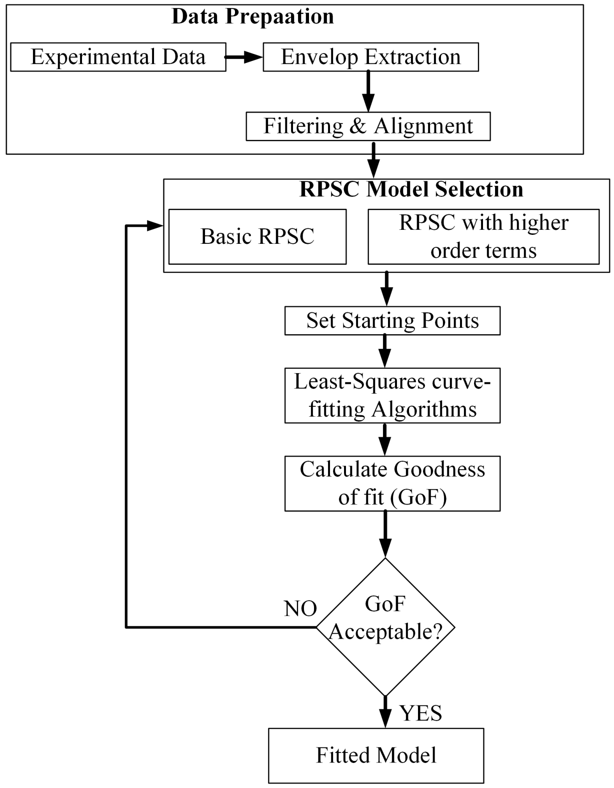

Figure 10.5: Algorithm to fit the model with experimental data

and a grid simulator (programmable AC voltage source). The grid simulator output voltage was controlled by an OPAL-RT to generate test voltage waveforms. The grid simulator was used to change the grid voltage from nominal to non-nominal voltages to simulate grid disturbances. The OPAL-RT provides flexibility to create different grid fault scenarios using the grid simulator. Two off-the-shelf PV inverters with a rated powers of 20 kVA and 550 kVA from two different manufacturers were used in the experimental evaluations. Both inverters were three-phase, three-wire

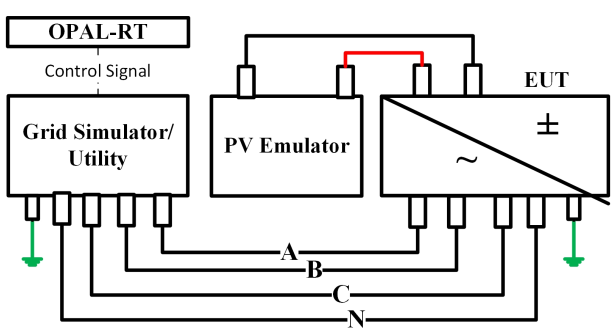

Figure 10.6: Inverter fault test setup at NREL's ESIF

Table 10.4: Simulated inverter parameters to validate the proposed RPSC model

Parameter	Inverter 1	Inverter 2
$v_g(rms)$	277 V	277 V
f	60 Hz	60 Hz
f_s	5 kHz	5kHz
S_{rating}	550 kVA	22 kVA
L_{inv}	2.08 mH	5.72 mH
L_{grid}	3.54 mH	9.74 mH
C_f	3.35 μF	12.12 μF
R_f	0.1 Ω	2.7 Ω
G_i	$0.243 + \frac{20}{s}$	$6.7 + \frac{20}{s}$
G_{fb}	1	1

inverters (with neutral connections present for measurement only, as is typical). To complement the experimental results, a detailed EMT model similar to the test setup shown in Fig. 10.6 was developed in MATLAB/Simulink for time domain simulation. Two separate three-phase inverter models were developed with ratings of 20 kVA and 550 kVA. The inverters were modeled with a damping resistor R_f in series with the capacitor in the LCL filter to damp the resonance associated with LCL filters. The LCL filter parameters of these inverters were determined following the filter design procedure presented in [190], and the current controller in the synchronous reference frame was designed following the steps shown in [129]. Thus, the modeled inverters represent generic inverters rather than manufacturer-specific models, allowing the time-domain simulation results to be compared to hardware tests to validate the inverter fault-response model developed in this paper. Table 10.4 lists the key parameters used in the time domain simulation to validate the proposed inverter fault current model.

10.5.2 Steady-State Fault Current

The 20-kVA and 550-kVA inverters were subjected to different low and high impedance grid fault conditions by changing the AC-side voltage from its nominal value to a reduced value representing the residual voltage during the fault. Both inverters were tested for fault response at

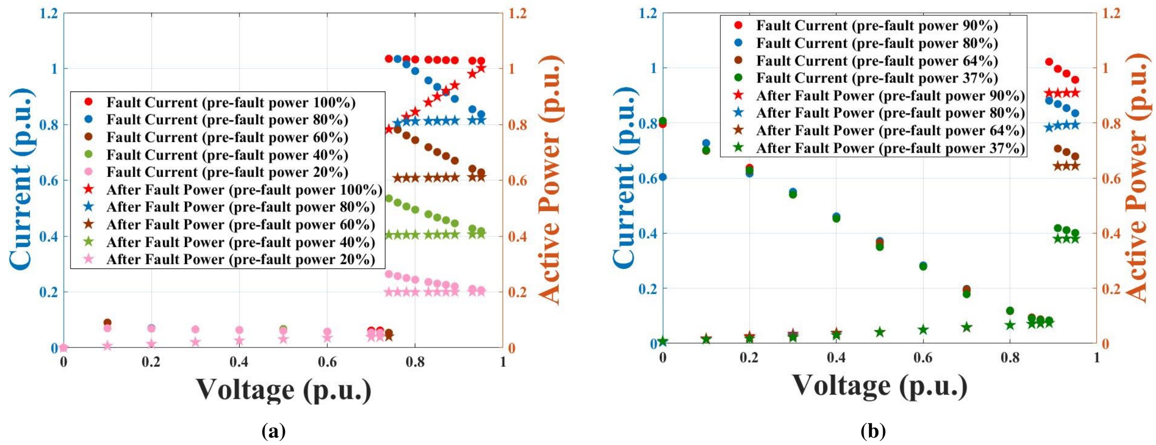

Figure 10.7: Steady-state experimental fault current during three-phase-to-ground faults a) 20-KVA inverter b) 550-KVA inverter

different pre-fault power levels. Fig. 10.7 shows the measured steady-state fault currents (I_{ssf}) for three-phase-to-ground faults with various residual voltages. During the tests, the low-voltage trip times for both inverters were set to the maximum allowed values to better observe the steady-state fault current.

For pre-fault power levels of 80% and below, the 20-kVA inverter maintained the pre-fault power level down to 0.74 p.u. voltage. When the fault current reached I_{max}, in this case 1.031 p.u., the inverter maintained that current by prorating the power, even in the continuous operation region. Below 0.74 p.u., it switched to a predefined fault current, $I_{ssf,pd0}^{ref}$, which was same for all fault levels regardless of pre-fault power or current (the fault currents are staked on top of each other in the figure). The 550-kVA inverter behaved differently than the 20-kVA inverter. The test results show that for voltages above 0.88 p.u., the 550-kVA inverter maintained the pre-fault power level by increasing its current. The inverter no longer maintained the pre-fault power level when the grid voltage dropped to less than 0.88 p.u. For the voltages $\leq$ 0.88 p.u., the inverter output current transitioned to a predefined steady-state fault current, $I_{ssf,pd}^{ref}(v_{PCC})$, which is a function of the fault voltage and does not depend to the pre-fault power or current. These results validate the assumptions on quasi-steady-state fault current of IIDG made in section 10.3.2.

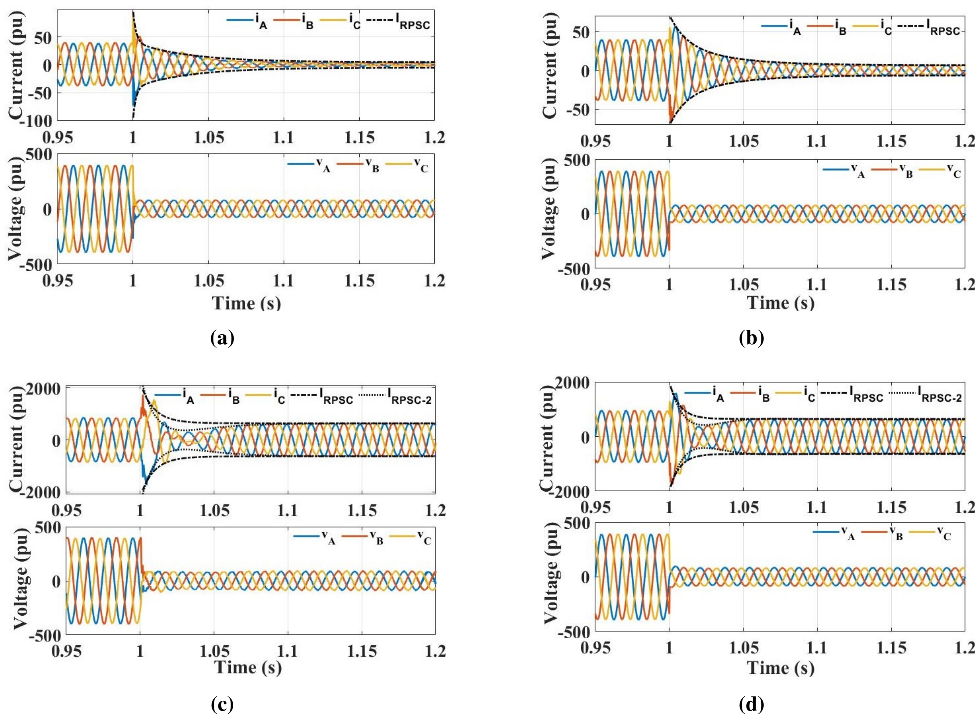

Figure 10.8: Fitting of the proposed RPSC with experimental and simulation results: (a) experimental result for 20-kVA inverter, (b) simulated result for 20-kVA inverter, (c) experimental result for 550-kVA inverter, (d) simulated result for 550-kVA inverter.

10.5.3 Transient Periods of Inverter Fault Current

Experimental studies and time domain simulations were performed to verify the proposed RPSC model. Due to space constraints, test results of selected cases are presented here in Fig. 10.8 showing the fault responses of the 20-kVA and 550-kVA inverters along with their counterpart EMT models and the RPSC current envelope, I_{RPSC}. For the cases shown here, the inverter pre-fault current was 1 p.u., and at time $t = 1s$, a three-phase balanced fault was applied that resulted in sudden drop of grid voltage to 0.2 p.u. The off-the-shelf inverters were found to have three distinct transient periods when they were subjected to this fault. The envelope of the fault currents for both of the off-the-shelf inverters and corresponding EMT models were fitted with the proposed RPSC model. Examining the fitted model in Fig. 10.8, it can be said that the proposed model traces the inverter fault current envelope with accuracy acceptable for most applications. The 550-kVA inverter has a second-order response during the transient period instead of a first-order response as

Table 10.5: RPSC model parameters found for the off-the-shelf inverters

Parameters for (11)	20-kVA inverter	550-kVA inverter
$I^{''}$	2.318 p.u.	2.317 p.u.
$I^{'}$	1	1
I^{ssf}	0.1207 p.u.	0.7605 p.u.
$T^{''}$	8.52 ms	2.022 ms
$T^{'}$	15 ms	35.9 ms

proposed in (10.10). In order to capture the second order response seen in the 550 kVA inverter more accurately, the first order decay term $e^{\frac{-t}{T'}}$ during transient period was replaced with a second order decay term, (10.13). The model fitting algorithm presented in section 10.4 was used to fit the model to experimental and EMT simulated fault responses observed for both of the inverters. Parameters calculated for the RPSC model are presented in Table 10.5 for both of the inverters. As shown, the parameter values are consistent with the expected values presented in Table 10.3. Fig. 10.8a and Fig. 10.8c show the fitting of the RPSC model for the physical inverters. In Fig. 10.8, the curves indicated by I_{RPSC} show the fitted model when (10.6) is directly used and the curves indicated by I_{RPSC-2} show the fitted model when (10.6) is updated with the second order response expressed by (10.13). The maximum current magnitude in the subtransient period, $I^{''}$, was somewhat higher for both of the off-the-shelf inverters than their counterpart EMT models. The reason for this mismatch is that the actual filter configuration and corresponding parameters along with control strategies for the off-the-shelf inverters are not known. Fig. 10.8b and Fig. 10.8d illustrate the concept of fitting the RPSC to match an EMT simulation rather than test data.

10.6 Chapter Summary

A reduced-order parameterized fault current model for inverter interfaced distributed generation is presented in this paper. It is shown here that inverter current after a fault undergoes three distinctive periods. Analogous to synchronous machine behavior, these periods were defined here as subtransient, transient and steady-state period. But unlike synchronous machines, instead of reactance, inverter output current has different magnitudes during these periods. The initial high spike of current after the fault was found to depend mostly on the inverter output filter and the grid voltage point-on-wave where the fault occurs. This initial spike lasts for a very short duration (less than one cycle). After the fault, the inverter may take up to several cycles to reach a new quasi-steady state fault current. The magnitude of this quasi-steady-state current partly depends on the grid code or standard that the inverter conforms to and may vary widely from manufacturer to manufacturer. For typical inverters, the quasi-steady-state fault current is not expected to be much higher than the rated current of the inverter. Experimental and simulation results were presented to verify the model. The model is expected to be useful for fault response analysis of distribution networks containing inverter-coupled generation, such as utility protection coordination studies. Future work could extend the model to include fault current phase angle and sequential components.

Chapter 11

Proposed Reduced-Order Model – Part II: Asymmetrical Fault Response

11.1 From Theoretical Fault-Response Analysis to the Proposed Reduced-Order Model

The reduced-order model (ROM) developed in this dissertation is not an empirical approximation but a direct abstraction of the underlying physics and control dynamics governing IBR fault response. The model architecture and parameterization arise from a sequence of analytical studies that examined the behavior of grid-following inverters under saturation, current limiting, sequence interactions, estimator imperfections, and ride-through policies. Across six complementary investigations, a consistent view emerged: IBR fault currents evolve through a structured series of event-driven dynamic regimes, each characterized by distinct mathematical behavior. The ROM generalizes these dynamics into a compact parametric form whose components correspond directly to the physical mechanisms identified in the theoretical analysis.

11.1.1 Event-Driven Structure of IBR Fault Response.

The analytical studies demonstrate that IBRs do not respond to grid faults in an arbitrary manner; rather, the response progresses through four dominant stages: (*i*) a subtransient interval governed by PWM saturation and instantaneous voltage depression; (*ii*) a transient recovery interval dominated by current controller dynamics, anti-windup behavior, and filter interactions; (*iii*) a composite settling interval in which PLL and sequence-extractor effects shape multi-rate exponential envelopes; and (*iv*) a steady-state injection interval determined by grid-code reference-current policies and circular current limits. This natural partitioning motivates the ROM's additive structure, which decomposes the total current into subtransient, transient, and steady-state components.

11.1.2 PWM Saturation and Subtransient Dynamics.

Temporal saturation analyses reveal that during the first few hundred microseconds, the inverter bypasses PI control and behaves as a clipped voltage source filtered through the L_f–R_f network. The resulting current trajectory follows a rapidly decaying exponential modulated by the grid frequency and initial voltage depression. This justifies the ROM's transient term of the form

$$i_{\text{sub}}(t) = A_0 e^{-t/\tau_0} \sin(\omega_f t + \phi_0), \tag{11.1}$$

with parameters tied to saturation-induced voltage deficits and filter constants.

11.1.3 Composite Transient Behavior.

Post-saturation analysis shows that the inverter enters a region where the current controller, dc-link dynamics, PLL, and sequence extractor interact to produce a multi-rate exponential decay. Closed-form dq-domain expressions and simulation evidence confirm that two to three dominant dynamic modes describe this interval. This motivates the ROM's transient component:

$$i_{\text{tr}}(t) = \sum_k A_k e^{-t/\tau_k} \cos(\omega_k t + \phi_k), \tag{11.2}$$

which captures underdamped oscillations, overshoot, and rate variations observed in EMT simulations and theoretical derivations.

11.1.4 PLL and Sequence-Extractor Imperfections.

Closed-loop analyses with PLL and sequence-extractor imperfections show that, once outside the saturation region, the dq-domain current converges exponentially toward an equilibrium reference. Imperfect phase tracking produces bounded harmonic and interharmonic leakage but does not change the dominant exponential envelope. This motivates the ROM's steady-state term:

$$i_{\text{ss}}(t) = I_\infty + A_\infty e^{-t/\tau_\infty}, \tag{11.3}$$

representing the long-term convergence to the grid-code-mandated reference current.

11.1.5 Harmonic and Interharmonic Leakage.

Analytical results show that harmonic leakage arises from PLL phase error and dq–$\alpha\beta$ coupling, but these effects remain small and exponentially bounded. Consequently, they can be captured implicitly through the phase terms ϕ_0 and ϕ_k of the ROM, avoiding the need for dedicated harmonic states and preserving model compactness.

11.1.6 Reference-Current Policies and Steady-State Targets.

Grid-code-mandated positive- and negative-sequence current policies define the steady-state injection following a fault. These policies produce the equilibrium value I_∞ that the ROM's steady-state term must asymptotically reach. Thus, the theoretical mapping from (V_1, V_2) to $(I_1^{\mathrm{ref}}, I_2^{\mathrm{ref}})$ directly informs the ROM's steady-state target.

11.2 Overview of the Proposed ROM Approach

The proposed ROM is a parametric representation of an IBR's short-circuit behavior. It is derived from high-fidelity EMT simulations or field-test measurements, but formulated for efficient use within conventional short-circuit and protection-study environments.

At its core, the ROM expresses the per-sequence, per-axis fault current response $i_\nu^\sigma(t)$, for $\sigma \in \{+,-\}$ and $\nu \in \{d,q\}$, as a compact sum of physically meaningful components [52, 191]:

$$i_\nu^\sigma(t) = A_{0,\nu}^\sigma + A_{1,\nu}^\sigma e^{-\alpha_\nu^\sigma t} + A_{2,\nu}^\sigma e^{-\gamma_\nu^\sigma t} + \sum_{k=1}^{2} B_{k,\nu}^\sigma e^{-\beta_{k,\nu}^\sigma t} \cos\bigl(\omega_{k,\nu}^\sigma t + \phi_{k,\nu}^\sigma\bigr), \tag{11.4}$$

where $A_{0,\nu}^\sigma$ denotes the steady-state current for each axis and sequence, $A_{1,\nu}^\sigma$ and $A_{2,\nu}^\sigma$ represent the subtransient and transient exponential envelopes, and the oscillatory terms $B_{k,\nu}^\sigma, \beta_{k,\nu}^\sigma, \omega_{k,\nu}^\sigma, \phi_{k,\nu}^\sigma$ capture dynamics primarily shaped by PLL behavior and sequence-extraction effects.

The model captures the sequence-domain fault current response as a function of:

1. *Pre-fault operating point:* The pre-fault positive-sequence current magnitude I^{+}_{pre}, determined by the active and reactive power setpoints $(P_{\mathrm{ref}}, Q_{\mathrm{ref}})$.

2. *Voltage depression during fault:* Positive- and negative-sequence voltage drops $\Delta V^{+}, \Delta V^{-}$ at the point of common coupling (PCC), which govern current limiting and control-mode transitions.

3. *Dynamic control response:* Effects of current limiting, PLL dynamics, anti-windup logic, and gain scheduling activated during the fault.

The ROM structure is intentionally compact, with parameters directly linked to physical and control-relevant quantities (e.g., effective impedance, current limits, control gains). This enables:

- *Parameter portability:* The same parametric form can be used across different short-circuit tools by exchanging parameter files, without rewriting model code.

- *Scalability:* Multiple units or plants can be represented by scaling and aggregating parameter sets.

- *Transparency:* Parameters can be shared and verified without exposing proprietary controller implementations.

Unlike traditional fixed voltage-source–behind–impedance models, the ROM explicitly reproduces control-driven effects such as current saturation, positive/negative-sequence coupling, and trajectory shaping caused by PLL dynamics and sequence-component estimation errors during the fault. Compared with tabular voltage–current lookup models, the continuous-time formulation in (11.4) preserves subcycle dynamics and the smooth evolution of currents from fault inception through steady state.

In practice, the parameter identification workflow proceeds as follows:

1. Run EMT simulations or use field-test data for representative pre-fault conditions and fault types.

2. Extract positive- and negative-sequence dq current trajectories.

3. Fit the trajectories to (11.4) to obtain the parameter sets.

4. Validate the ROM against independent EMT or measurement cases within required protection-study tolerances.

Once the sequence-domain currents are predicted, the three-phase currents are reconstructed using the inverse symmetrical-component and inverse Park transformations (Fig. 11.1):

$$\mathbf{i}_{abc}(t) = T_{\text{sym}}^{-1} \begin{bmatrix} i_d^+(t) + j\, i_q^+(t) \\ i_d^-(t) + j\, i_q^-(t) \\ 0 \end{bmatrix}. \tag{11.5}$$

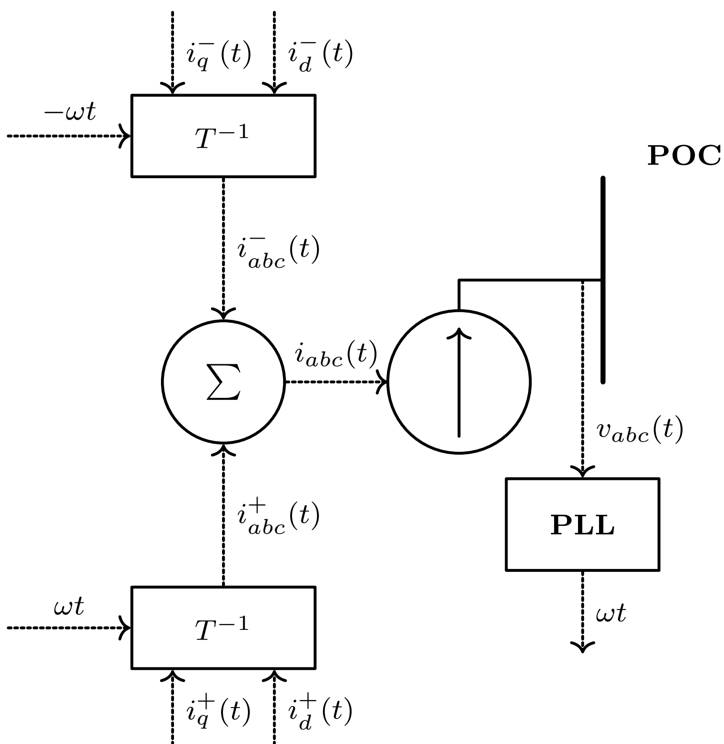

Figure 11.1: Base reduced-order model workflow showing the transformation of positive- and negative-sequence dq currents back to three-phase abc currents via the inverse symmetrical component and inverse Park transformations.

11.3 Data-Driven Generalizability Layer

While the core ROM structure provides a compact and physically interpretable short-circuit model, industrial deployment requires robustness across loading levels, voltage-sag severity, and inverter operating conditions. To achieve this, a data-driven generalizability layer is integrated into the ROM framework to preserve model fidelity across a wide range of operating scenarios.

The generalizability layer extends the base parameter set through simple, physically motivated adjustment rules applied on a per-sequence, per-axis basis. Specifically, each ROM parameter C_{ν}^{σ} for $\sigma \in \{+,-\}$ and $\nu \in \{d,q\}$ is adjusted according to

$$C_{\mathrm{adj},\nu}^{\sigma} = C_{\mathrm{base},\nu}^{\sigma} + k_{I,\nu}^{\sigma} I_{\mathrm{pre}}^{\sigma} + k_{V,\nu}^{\sigma} \Delta V_{\sigma}, \tag{11.6}$$

where:

- I_{pre}^{+} is the pre-fault positive-sequence current magnitude (with $I_{\mathrm{pre}}^{-} = 0$ under balanced operating conditions),
- $\Delta V_{\sigma} = V_{\sigma,\mathrm{pre}} - V_{\sigma,\mathrm{fault}}$ is the sequence-specific voltage depression,
- $k_{I,\nu}^{\sigma}$ and $k_{V,\nu}^{\sigma}$ are sensitivity coefficients identified during ROM parameter fitting.

The adjusted parameters $C_{\mathrm{adj},\nu}^{\sigma}$ are then used directly in the parametric ROM formulation of Sec. 11.2. For balanced faults, only the positive-sequence adjustments $C_{\mathrm{adj},\nu}^{+}$ are active, while negative-sequence adjustments $C_{\mathrm{adj},\nu}^{-}$ become effective during unbalanced faults when $\Delta V^{-} > 0$.

This generalizability mechanism provides several key advantages:

- *Smooth parameter evolution:* Continuous dependence on I_{pre} and ΔV ensures realistic current trajectories between tested operating points.
- *Minimal data requirement:* A relatively small set of EMT simulations or field tests is sufficient to calibrate the adjustment coefficients.

- *Operational adaptability:* The same ROM structure remains valid across fault severities, loading conditions, and inverter operating regimes.

- *Preserved interpretability:* The adjustment maintains physical meaning of the base ROM parameters while enabling practical operational flexibility.

The generalizability layer is technology-agnostic in structure but technology-specific in its fitted coefficients. For example, in IBRs with fast current-limiting control, the dependence on I_{pre} may be weak ($k^{\sigma}_{I,\nu} \approx 0$), whereas systems exhibiting stronger control–hardware coupling often require both I_{pre} and ΔV terms for accurate fault-current representation.

11.4 Multi-Platform Implementation

The ROM framework was designed as a modular, cross-platform workflow to enable consistent model generation, tuning, and validation across multiple EMT simulation environments. Its architecture integrates data acquisition, scenario simulation, parameter extraction, and post-processing within a unified automation pipeline that can interface with PSCAD, MATLAB/Simulink, and Python environments. The goal is to allow users—ranging from inverter manufacturers and researchers to utilities—to apply the same workflow whether the source data originate from detailed EMT simulations, hardware-in-the-loop (HIL) experiments, or field measurements.

11.4.1 Workflow Overview

The end-to-end process begins with available measurements or detailed simulation outputs in the three-phase (i_{abc}, v_{abc}) domain. Each dataset is tagged with metadata describing the operating condition, control mode, and applied fault scenario. These data are then processed through three major functional layers: simulation and extraction, processing and analysis, and output and validation. The complete workflow is illustrated in Fig. 11.2.

Data Preparation.

The workflow accepts inputs from either measured or simulated inverter responses. For simulated cases, the EMT environment (e.g., PSCAD or Simulink) produces time-domain voltage and current waveforms for each test condition. Each case is indexed by a scenario list that defines pre-fault power flow, fault type, location, and control mode.

Simulation and Extraction.

Fault scenarios are executed in the detailed EMT model to generate voltage and current time series. The raw three-phase quantities are converted into synchronous reference-frame components (d–q) using Python or MATLAB utilities embedded in the extraction module. This conversion isolates positive- and negative-sequence components required for parameter fitting and performance comparison.

Processing and Analysis.

The extracted sequence currents are analyzed over multiple cycles to separate subtransient, transient, and steady-state segments. A scenario loop function enables serial or parallel execution of multiple cases, with automatic saving of intermediate results. Signal processing techniques such as the Fourier transform, Hilbert transform, or Prony analysis are optionally applied to compute frequency and damping characteristics. For each case, the ROM parameters are estimated using an iterative identification routine that fits the simplified dynamic equations to the extracted currents.

Parameter Generation and Sensitivity Computation.

Once fitted, all parameters are stored in a centralized database that includes metadata such as controller type and operating point. A post-processing stage performs sensitivity analysis and k-factor computation to determine the dependency of ROM coefficients on pre-fault current and voltage sag magnitude. This step enables dynamic parameter adjustment during subsequent simulations, ensuring that the ROM captures variations in fault severity and control strategy.

Output and Validation.

The generated parameter sets are formatted for direct use in Simulink and PSCAD environments. A validation module automatically compares ROM responses against detailed EMT results using quantitative metrics—RMSE, cumulative error, phase shift, and relay timing deviation—and compiles composite performance plots. This unified workflow allows the same ROM to be validated across platforms, promoting repeatability and transparency in the model-development process.

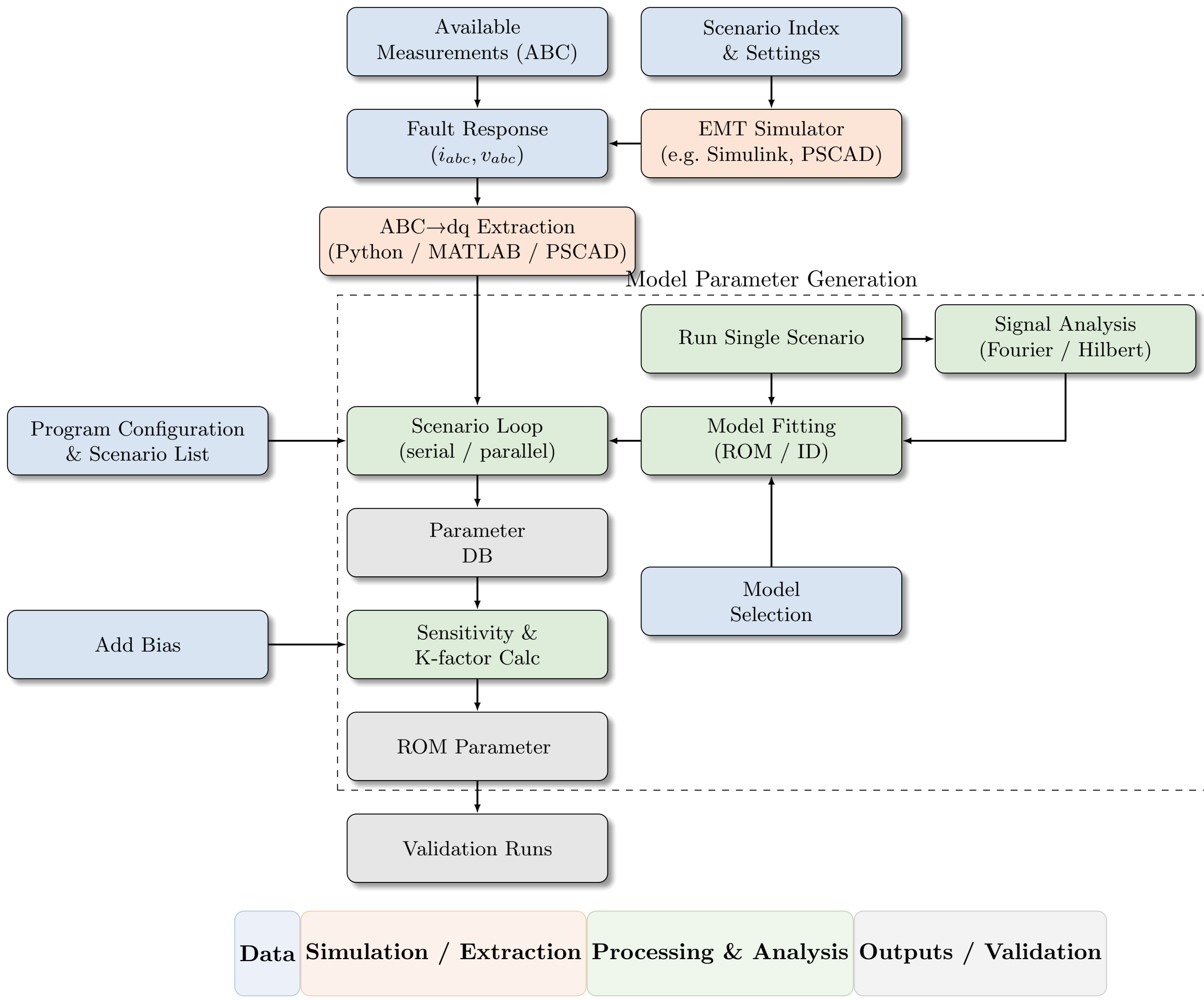

Figure 11.2: Multi-platform workflow for ROM generation, parameter fitting, and validation across PSCAD, Simulink, and Python environments.

This architecture ensures that ROM development is both platform-agnostic and data-driven. The modular design supports rapid testing of new scenarios, automatic feature extraction, and cross-validation with experimental data. It also enables end users to contribute additional data for model refinement without modifying the core structure. Ultimately, this multi-platform implementation bridges detailed inverter modeling with system-level protection studies, facilitating widespread adoption and benchmarking of the ROM across research and industry applications.

11.4.2 Applicability and Model-Fitting Workflow

A key design objective of the proposed reduced-order modeling framework is broad practical applicability. The model-fitting process is not restricted to any specific simulation environment, data source, or user type. Instead, the framework is designed to be usable by a wide range of stakeholders involved in inverter modeling and protection studies.

The proposed approach can be employed by any user with access to inverter fault-response data in the three-phase *abc* reference frame. This includes equipment manufacturers, consultants, utilities, system planners, and academic researchers. Data for model fitting may originate from field measurements, laboratory experiments, hardware-in-the-loop testing, or detailed electromagnetic transient (EMT) simulation models.

In practice, however, utilities and system operators are rarely provided with full internal control and firmware details of commercial inverters. Although vendors are typically required to supply validated EMT models for interconnection and compliance studies, these models are commonly delivered as compiled black-box implementations that obscure internal controller structure and parameters. This lack of transparency significantly limits independent verification, cross-tool portability, and protection-oriented analysis. As a result, an external model-extraction process becomes essential for developing protection-relevant representations of inverter fault behavior that do not rely on proprietary control information.

Users with access to detailed inverter models may apply the accompanying software tool developed in this dissertation to automatically execute multiple fault scenarios, extract fault-response data, and perform systematic parameter identification for the reduced-order model. This capability enables rapid exploration of operating conditions, fault types, and control settings, significantly reducing the effort required to construct and validate protection-oriented inverter models.

The overall workflow is intentionally flexible. It supports both measured and simulated data, and it integrates seamlessly with commonly used platforms including PSCAD, MATLAB/Simulink, and Python-based processing pipelines. This flexibility ensures that the proposed framework can be incorporated into existing utility and research workflows without requiring proprietary software dependencies or modifications to established simulation infrastructures.

Chapter 12

Proposed Reduced-Order Model – Part III: Validation

12.1 Validation of the Reduced-Order Model (ROM)

12.1.1 Objective and Scope

The validation focuses on evaluating the fidelity, robustness, and scalability of the developed ROM for IBRs. The ROM aims to replicate the short-circuit and post-fault current behavior of IBRs through a physics-informed, data-driven formulation that captures subtransient, transient, and steady-state components.

The validation activities were designed to confirm the model's ability to reproduce key characteristics observed in detailed EMT simulations and measured laboratory data. The main objectives included:

- Quantitative comparison of ROM and EMT responses in terms of current magnitude, phase, and relay decision logic.
- Verification of relay element trigger timing accuracy.
- Evaluation of model generalizability across control modes, fault types, and network conditions.

12.1.2 Validation Framework and Methodology

The validation of the ROM leverages its multi-platform implementation to ensure performance consistency across simulation environments, control modes, and data sources. Because the ROM was developed to be platform-agnostic, its behavior can be directly compared against EMT-generated waveforms in both Simulink and PSCAD, as well as against laboratory experimental measurements. This multi-platform capability forms the foundation of a comprehensive validation framework.

Multi-Platform Capability.

The ROM is implemented in Python, Simulink, and PSCAD-compatible forms, enabling a unified evaluation workflow. In the first stage of validation, ROM-generated currents were compared directly with inverter currents from both experimental tests and simulation environments. These comparisons were performed in:

- the ABC frame, to assess raw waveform fidelity during fault inception and recovery,
- the sequence domain, evaluating positive- and negative-sequence current magnitudes and corresponding phase-angle trajectories.

This dual-frame comparison allowed the ROM to be evaluated not only on amplitude accuracy but also on its ability to preserve the correct dynamic phasor evolution following unbalanced faults.

Data Sources. Two categories of reference data were used:

- *Experimental measurements*, obtained from the hardware test platform described in Section 10.5.1, including ABC voltages and currents under staged fault events.
- *Detailed EMT simulation data*, generated using high-fidelity models of the IBR in both Simulink and PSCAD. The Simulink EMT implementation is documented in [75, 92, 93], while the PSCAD model is detailed in [192].

These EMT models support multiple control strategies—such as synchronous-reference-frame (dq) current control and stationary-frame negative-sequence suppression—allowing the ROM to be validated across diverse control architectures commonly employed in modern grid-following and grid-forming inverters.

Simulation-Based Verification. For simulation-based verification, identical fault scenarios were executed in both the detailed EMT models and the ROM environment. This included:

- AG and BC faults,
- faults at multiple electrical distances,
- variations in IBR control mode and operating point.

This ensured that differences between ROM and EMT outputs arose solely from the modeling approach rather than from discrepancies in the signal-processing pipeline.

Quantitative Performance Evaluation.

Beyond qualitative waveform inspection, the ROM was subjected to a structured set of quantitative accuracy assessments. For every EMT–ROM pair of waveforms, multi-cycle error metrics were computed using the definitions provided in Section 12.1.3. These include the cycle-specific Cumulative Error (CE), Root Mean Square Error (RMSE), and phase-shift error for both positive- and negative-sequence currents. By evaluating these metrics over the first three cycles following the fault, the framework captures the ROM's ability to reproduce subtransient, transient, and early steady-state dynamics. A Composite Performance Metric (CPM) further condenses these results into a single normalized score, enabling rapid comparison across fault types, control modes, and electrical distances. This quantitative layer ensures that ROM fidelity is measured consistently and objectively across all test cases, complementing both waveform-level and relay-level validation stages.

Relay-Based Performance Evaluation.

Because the long-term objective of the ROM is to support large-scale protection studies, the final stage of validation analyzed relay behavior when driven by ROM versus EMT waveforms. To achieve this, fault responses from both the ROM and PSCAD EMT model were passed through a detailed distance and overcurrent relay model, following the methodology described in [12, 193]. Relay elements—including TRIP, Z1G, XAG, MAG, F32, and FIDEN—were monitored for:

- element pickup timing,
- zone misalignment or premature pickup,
- changes in negative-sequence directional behavior,
- consistency across cycles and control schemes.

This relay-focused evaluation provides a direct measure of whether the ROM maintains sufficient fidelity for its intended application in protection studies.

End-to-End Validation.

The complete validation workflow therefore integrates:

1. experimental and EMT waveform acquisition,
2. multi-platform dq and sequence-domain extraction,
3. direct waveform-to-waveform comparison,
4. multi-cycle performance metrics (CE, RMSE, phase error, CPM),
5. relay decision-path validation.

12.1.3 Performance Evaluation Metrics

To assess the accuracy of the ROM in comparison to the detailed simulation model, we define several evaluation metrics. These metrics quantify the error in current magnitude and phase angle responses over multiple cycles following a disturbance. Additionally, a CPM is introduced to provide a single-score evaluation of model accuracy.

Cumulative Error (CE)

The CE measures the total accumulated deviation between the ROM and the detailed model over a given time window. It is computed for both the positive- and negative-sequence current magnitudes (I_1, I_2) as:

$$CE = \int_{t_0}^{t_f} \left| I_{\text{detailed}}(t) - I_{\text{ROM}}(t) \right| dt, \tag{12.1}$$

where t_0 and t_f define the integration window for each cycle. To normalize the error, we express it as a percentage relative to the integral of the peak current magnitude over the same period:

$$CE_{\%} = \frac{CE}{\int_{t_0}^{t_f} |I_{\text{peak}}(t)| dt} \times 100, \tag{12.2}$$

where $I_{\text{peak}}(t)$ represents the estimated three-phase peak current magnitude.

Root Mean Square Error (RMSE)

The RMSE quantifies the average deviation between the ROM and detailed model. It is computed as:

$$RMSE = \sqrt{\frac{1}{N} \sum_{i=1}^{N} \left(I_{\text{detailed},i} - I_{\text{ROM},i} \right)^2}, \tag{12.3}$$

where N is the number of time samples in the cycle. Similar to CE, RMSE is expressed as a percentage relative to the maximum peak current magnitude:

$$RMSE_{\%} = \frac{RMSE}{\max(I_{\text{peak}})} \times 100, \tag{12.4}$$

where I_{peak} represents the estimated three-phase peak current magnitude during the same time window.

Phase Shift Error

The Phase Shift Error quantifies the misalignment between the phase angles of the positive- and negative-sequence currents. The relative shift between the detailed and ROM models is computed using cross-correlation:

$$\Delta\theta = \arg\max_{\tau} \left(\sum_{i} I_{\text{detailed},i} I_{\text{ROM},i+\tau} \right), \tag{12.5}$$

where τ represents the time lag that maximizes the correlation. The phase shift score is then normalized using the maximum possible shift within one cycle:

$$\theta_{\text{score}} = 1 - \frac{\min(|\Delta\theta|, 1)}{1}, \tag{12.6}$$

ensuring that a perfect alignment results in a score of 1.

Composite Performance Metric (CPM)

To provide a single performance indicator, we define the CPM as a weighted combination of the normalized scores for cumulative error, RMSE, and phase shift:

$$CPM = w_1 \cdot CE_{\text{score}} + w_2 \cdot RMSE_{\text{score}} + w_3 \cdot \theta_{\text{score}}, \tag{12.7}$$

where:

- $w_1 = 0.4$ (Cumulative Error weight),
- $w_2 = 0.4$ (RMSE weight),
- $w_3 = 0.2$ (Phase Shift weight).

Each component is normalized as:

$$CE_{\text{score}} = 1 - \frac{\min(CE, 100)}{100}, \tag{12.8}$$

$$RMSE_{\text{score}} = 1 - \frac{\min(RMSE, 100)}{100}, \tag{12.9}$$

$$\theta_{\text{score}} = 1 - \frac{\min(|\Delta\theta|, 1)}{1}, \tag{12.10}$$

ensuring that a CPM value close to 1 indicates high model accuracy, while a lower CPM signifies a greater deviation from the detailed model.

12.2 Performance Evaluation Across Different Data Sources

This section presents representative waveform used for the validation of the ROM. While the detailed PSCAD and Simulink implementation procedures are documented in other sections, the figures included here illustrate the key input signals, reference frames, and inverter response characteristics that form the basis for the ROM parameter extraction and multi-platform interoperability.

12.2.1 PSCAD EMT Simulation

The proposed ROM was validated against a detailed PSCAD model of the IBR. Both models were subjected to identical unbalanced fault conditions, with the voltage and current at Bus 3 (PCC) recorded for comparison, as shown in Fig. 12.1.

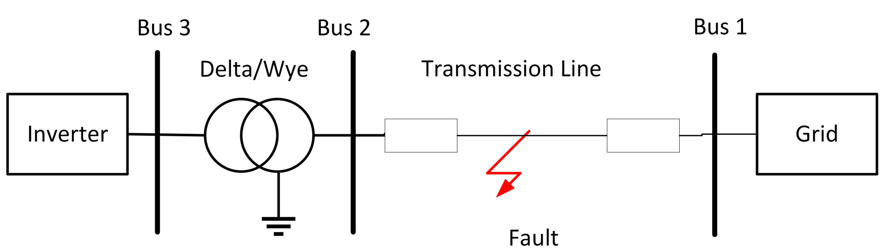

Figure 12.1: Simulation setup.

The reference model was a PSCAD EMT representation including full converter, control, and network detail. The ROM was tuned using a diverse set of scenarios spanning multiple fault types, locations, and pre-fault current levels, all with active negative-sequence control in the dq frame. Parameters obtained from these cases leveraged the ROM's ability to generalize inverter fault response across operating conditions. Figure. 12.2 and 12.3 show representative comparisons between the ROM and detailed EMT model for AG and BC faults, respectively, both using the same tuned parameter set without further adjustment. For the AG fault (Fig. 12.2), the ROM closely reproduces the EMT model's transient and steady-state current waveforms, capturing magnitude, phase, and oscillatory content within 1.5 cycles after fault inception. The EMT response for the AG

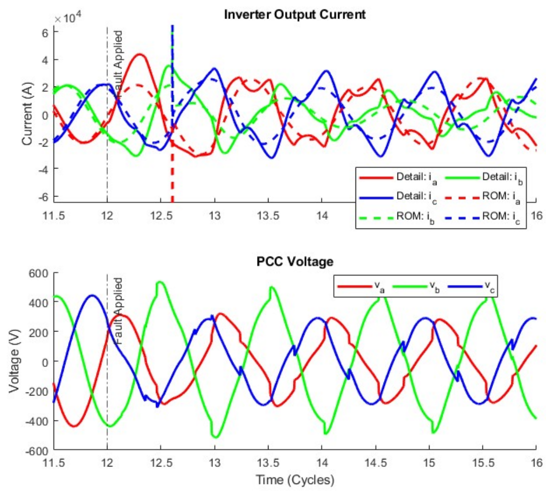

Figure 12.2: AG fault response comparison between detailed EMT model and ROM.

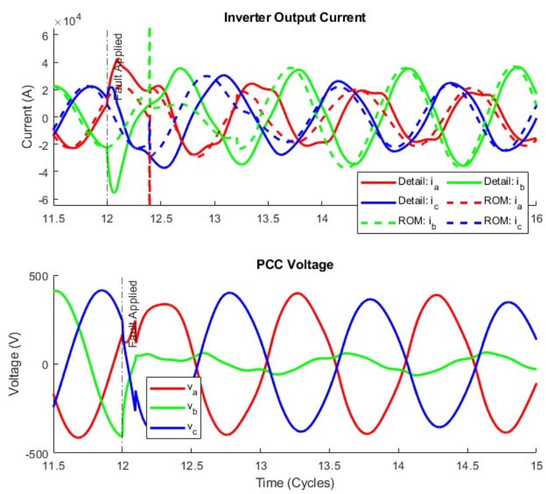

Figure 12.3: BC fault response comparison between detailed EMT model and ROM.

fault also exhibits pronounced harmonic distortion; however, since the ROM is designed to represent only the fundamental-frequency behavior, these high-frequency components are not present in the ROM output. A similarly high level of agreement is observed for the BC fault case (Fig. 12.3), demonstrating the ROM's accuracy across different fault types.

12.2.2 Simulink-Based EMT Simulation

To support cross-platform ROM deployment, the same fault conditions and input signals were replicated using Simulink-based reduced-order modeling frameworks. Figures 12.4 and 12.5 capture the core subsystems used to process ABC-domain inputs into synchronous and stationary reference frames.

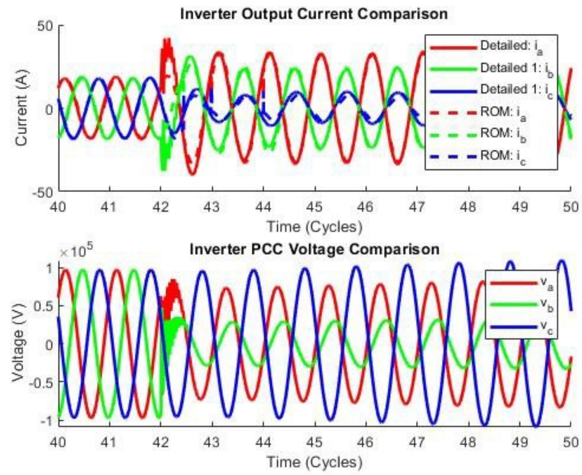

Figure 12.4: Simulink synchronous reference-frame model used for dq transformation and filtering.

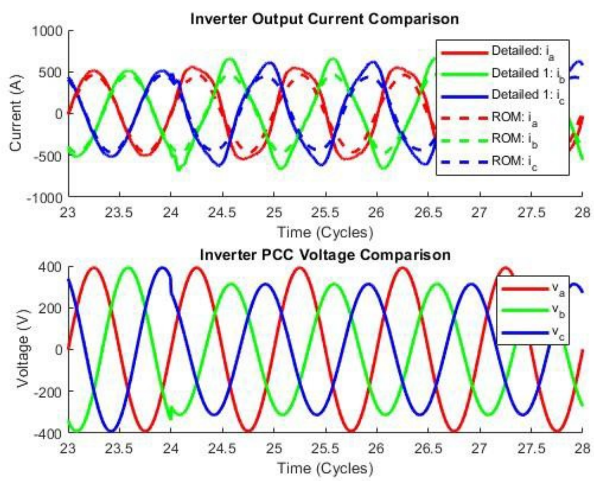

Figure 12.5: Simulink stationary-frame ($\alpha\beta$) model for alternative sequence extraction and control validation.

12.2.3 Commercial Off-the-Shelf (COTS) Inverter

Finally, Figure 12.6 illustrates the performance of the ROM in replicating the fault response of a COTS inverter. The experimental setup used to obtain the COTS inverter waveforms was described in Section 10.5.1. These measured responses were used to tune the ROM parameters, after which the same fault conditions were applied to the tuned ROM to assess its ability to reproduce the COTS behavior. As shown in the figure, the ROM closely matches the measured COTS fault response, achieving very high accuracy within the first cycle following fault inception.

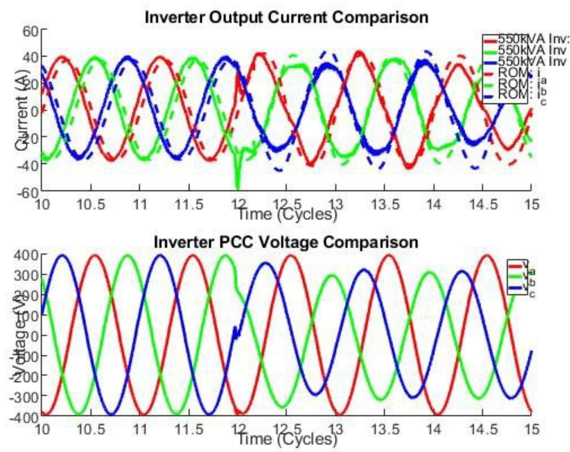

Figure 12.6: Snapshot of the COTS environment used for multi-platform ROM validation.

12.3 Relay-Based Performance Evaluation

To establish whether the ROM is suitable for protection studies, this section summarizes the approach used to compare relay responses driven by ROM-generated currents against those obtained from detailed EMT simulations.

12.3.1 Test System and Fault Scenarios

The validation of the ROM was performed using the simplified transmission corridor shown in Fig. 12.7. This network represents a generic medium-voltage transmission path between a main grid source and an IBR connected through a step-up transformer. The model preserves the essential impedance partitions and transformer interfaces required to reproduce the voltage and current profiles that strongly influence inverter short-circuit behavior and protection system response. On the left side of Fig. 12.7, the grid is represented by a Thévenin equivalent source feeding the corridor through an equivalent impedance Z_{eq}. Downstream of this point, the line is divided into multiple segments:

- $0.15Z_{12}$: an initial short section from the grid to the first bus,
- $(m-1)Z_{12}$: an adjustable intermediate section,
- mZ_{12}: the final segment leading into the IBR interconnection.

Here, Z_{12} is the line impedance, and the parameter m determines the effective electrical distance between buses, enabling systematic variation of fault severity and negative-sequence voltage levels along the feeder. Two sources supply the reduced network:

1. A hydro generator connected to the first bus through a step-up transformer (TF1, Yg–Δ),
2. The primary grid feeding through Z_{eq}.

The IBR under study is connected at Bus 3 through transformer TF2 (Yg–Δ), representing typical grounding and harmonic-separation characteristics observed in utility-scale PV, wind, or storage systems. Four designated fault points are available in the model:

- f_1: grid-side bus fault,
- f_2: fault at the intermediate bus near the hydro generator,
- f_3: line fault between the two primary buses (used extensively for EMT–ROM comparisons),
- f_4: fault at the bus feeding the IBR transformer.

Fault location f_3 is particularly useful because varying the parameter m shifts the electrical distance from the IBR to the fault. Across this network, the following fault scenarios were evaluated:

- *Fault Types:* AG (single line-to-ground) and BC (line-to-line),
- *Fault Locations:* 5%, 50%, and 80% of the electrical distance between the two main buses (implemented by scaling m),

- *IBR Control Modes:*

    1. dq-frame negative-sequence current suppression,
    2. $\alpha\beta$-frame negative-sequence current suppression,
    3. $\alpha\beta$-frame negative-sequence current injection,

- *Operating Points:* Zero active/reactive power flow (baseline), with selected cases including nonzero pre-fault current to evaluate sensitivity.

These scenarios collectively exercise the ROM across a wide range of electrical distances, sequence-voltage levels, and converter control modes. A complete summary of all evaluated test

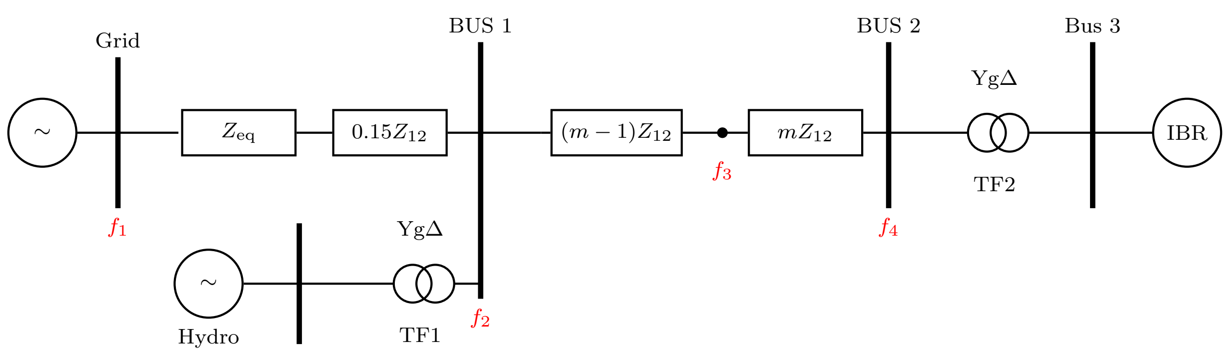

Figure 12.7: Single-line diagram of the reduced generic transmission corridor used for ROM and EMT validation. The model includes multiple fault points (f_1–f_4), transformer interfaces, and adjustable line impedance sections.

conditions—including fault types, locations, control modes, and operating points—is provided in Table 12.1, which defines the full scenario space used throughout the ROM–EMT validation.

12.3.2 Impedance Trajectories in the R–X Plane

Figures 12.8 and 12.9 show the R–X trajectories for AG and BC faults. Protection elements were evaluated by plotting the dynamic impedance seen from the relay location. The ROM-generated impedance trajectories closely reproduce those from the EMT simulation.

- Zone 1 and Zone 2 reach boundaries are crossed at nearly the same time.

Table 12.1: Summary of Test Scenarios Used for ROM Validation

Scenario Category	Options / Variations	Notes	Purpose
Fault Types	AG (Single Line-to-Ground) BC (Line-to-Line)	Covers both zero-sequence and negative-sequence rich events	Evaluate ROM performance under different sequence-voltage conditions
Fault Locations	f_3 (primary analysis at 5%, 50%, 80% of line to BUS 2)	Implemented by varying parameter m in line impedance partitions	Assess sensitivity to electrical distance and grid strength
Current Control Modes	dq-frame neg. seq. suppression $\alpha\beta$-frame neg. seq. suppression/injection	Represents common IBR control strategies under unbalanced faults	Test robustness of ROM across control architectures
Operating Conditions	Zero P/Q (baseline) Selected cases with nonzero pre-fault current	Nonzero pre-fault current used for sensitivity and k-factor extraction	Examine impact of operating point on ROM accuracy

- The shape and direction of the trajectory—particularly the negative-resistance swing characteristic during unbalanced faults—match strongly between EMT and ROM.
- Any deviations are confined to the first 3–5 ms of the subtransient period and do not affect relay decision paths.

12.3.3 Directional and Distance Protection Elements

Figures Figures 12.8 and 12.9 illustrate the directional (32QG) responses for selected AG and BC faults. The directional logic (zero-sequence or negative-sequence based) shows consistent forward-fault indication between the two models.

- The 32QG element in the ROM activates within one cycle of EMT.
- Mho elements (MAG1/MAG2) show nearly identical entry and exit times relative to zone boundaries.

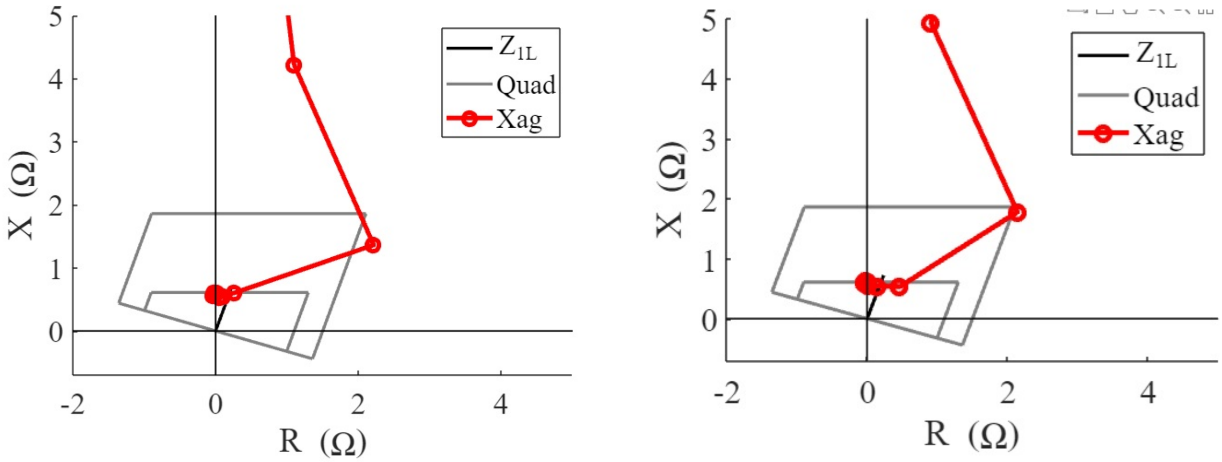

(a) AG Fault – EMT

(b) AG Fault – ROM

Figure 12.8: R–X plane impedance trajectories for AG fault.

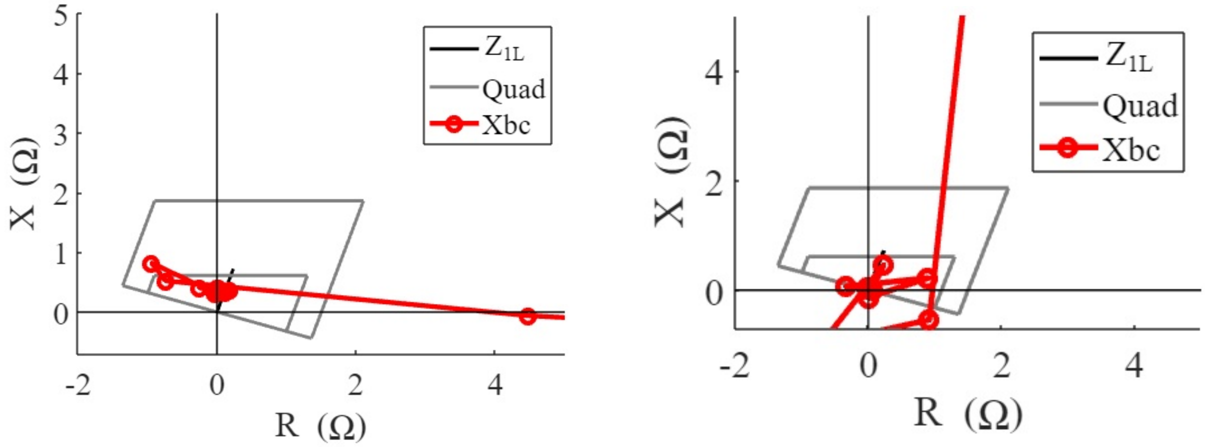

(a) BC Fault – EMT

(b) BC Fault – ROM

Figure 12.9: R–X plane impedance trajectories for BC fault.

- The ROM is able to reproduce complex relay logic ordering: TRIP $\rightarrow$ Z1G $\rightarrow$ MAG $\rightarrow$ F32V, maintaining proper event sequencing.

12.3.4 Mho Element Response

Figures 12.12 show the mho-element reach (MAG) comparison. The ROM correctly reproduces the zone entry/exit behavior observed in EMT.

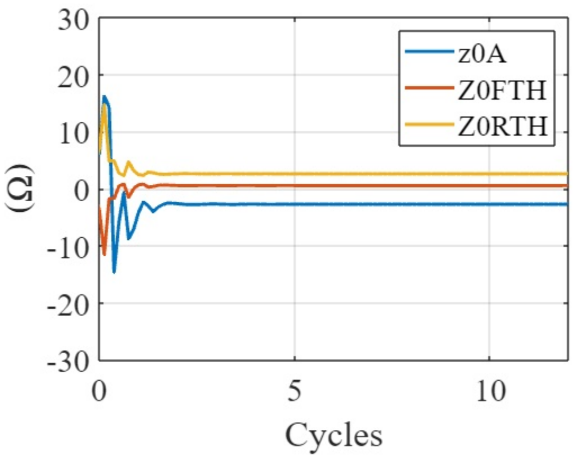

(a) AG Fault – EMT

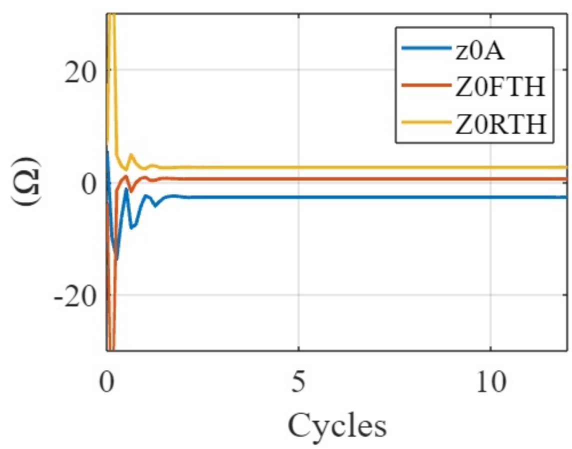

(b) AG Fault – ROM

Figure 12.10: Directional element (32Q) response for AG fault.

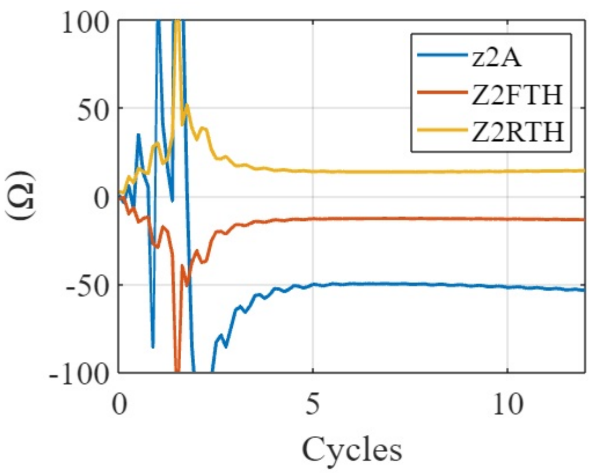

(a) BC Fault – EMT

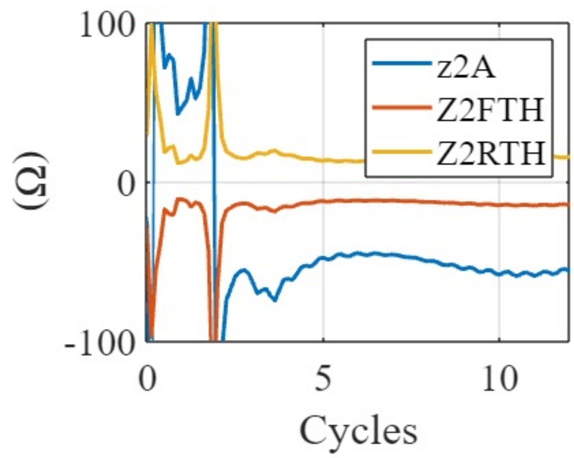

(b) BC Fault – ROM

Figure 12.11: Directional element (32Q) response for BC fault.

12.3.5 Relay Timing Comparison

Relay element trigger timing is one of the most important benchmarks for validating the ROM, because protection decisions depend not only on the magnitude and direction of measured quantities but also on the precise ordering and timing of relay element activation. To evaluate this, relay firing instants were extracted for six representative cases (Cases 13–18), covering a range of fault types, fault locations, and inverter control modes. Both the EMT model (serving as the reference)

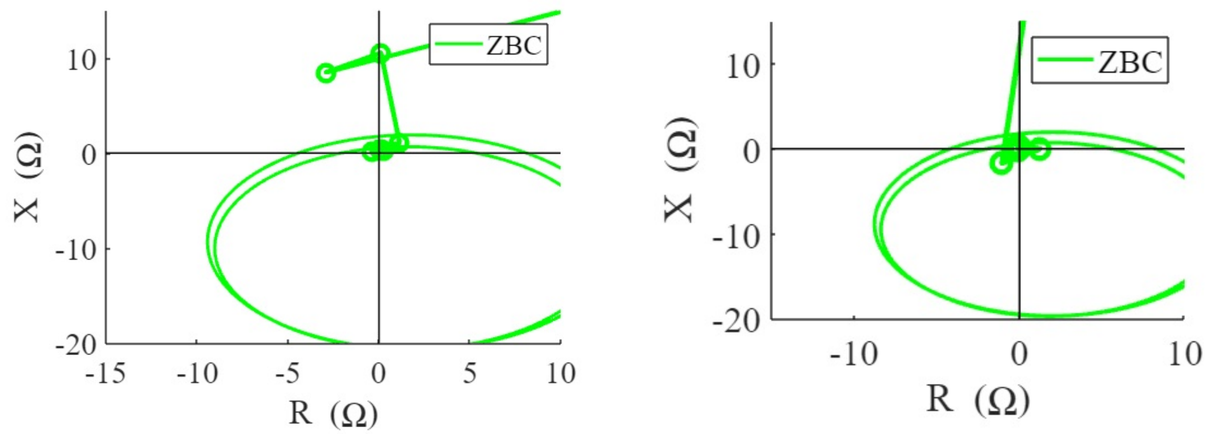

(a) BC Fault – EMT

(b) BC Fault – ROM

Figure 12.12: Mho element reach comparison for BC fault.

and the ROM were subjected to identical scenarios, and protection element activation times were recorded in cycles from the instant of fault inception.

Table 12.2 presents the full relay-element timing matrix. Across all cases, the ROM closely reproduces the timing of key elements—TRIP, Z1G, XAG, MAG, F32V, and FIDEN—typically within 0.25 to 1.0 cycles of the EMT reference. Such deviations fall well within industry-accepted tolerances for protection studies, particularly for inverter-based resources whose responses exhibit rapidly decaying subtransient components not fully modeled in simplified representations.

Several important trends emerge:

- *Primary protection elements*: TRIP, Z1G, and XAG exhibit consistent ordering between EMT and ROM across all six cases.
- *Directional and voltage-dependent elements*: the ROM activates F32V and F32QG slightly earlier due to smoother negative-sequence profiles, but never produces a false activation.
- *Distance/mho elements*: MAG1, MAG2, and XBC1/XBC2 show small timing offsets (typically 0.25–0.50 cycles), but preserve correct reach and direction behavior.
- *Stability elements*: FIDEN matches exactly between EMT and ROM in all scenarios.

Overall, the results demonstrate that the ROM is sufficiently accurate for relay time-coordinated studies, ensuring correct element sequence, correct zone entry/exit, and acceptable timing fidelity for EMT-to-ROM substitution in large-scale studies.

Across all cases evaluated:

- No element that remained inactive in EMT was falsely activated in ROM.
- Deviations larger than one cycle were not observed.
- All deviations fall within typical industry tolerances for protection studies (1–1.5 cycles).

12.4 Quantitative Performance Evaluation

Using the metrics defined in Section 12.1.3, the accuracy of the ROM was evaluated against the detailed EMT simulation across multiple unbalanced-fault scenarios.

12.4.1 Multi-Cycle Error Metrics

Table 12.3 summarizes the CE, RMSE, and phase-shift values for the positive- and negative-sequence currents across three consecutive cycles following fault inception. These metrics are provided for Cases 13–18, covering variations in fault type, location, and inverter control mode. Consistent with expectations, the largest deviations appear during Cycle 1, where fast EMT-only subtransient effects dominate. Errors decrease sharply in Cycle 2, and by Cycle 3 both CE and RMSE fall within low single-digit percentages across all cases. The negative-sequence phase shift shows small signs of misalignment during Cycle 1 for certain cases but converges rapidly by Cycle 3, often reaching perfect alignment ($\Delta\theta = 0$). These results confirm that the ROM accurately captures the dominant sequence currents that govern relay behavior once the initial subtransient distortion diminishes.

12.4.2 Composite Performance Metric (CPM)

While the multi-cycle error metrics in Table 12.3 provide detailed insight into the ROM performance for each cycle and sequence component, it is often useful to have a single scalar indicator that summarizes overall accuracy. The CPM defined in Section 12.1.3 serves this purpose by combining normalized CE, RMSE, and phase-shift scores into one value between 0 and 1. Figure 12.13 shows the CPM values for all eighteen test cases. For Cases 1–12, which span a range of AG and BC faults and operating conditions, CPM remains consistently high, typically between about 0.985 and 0.995. Cases 13–18 correspond to the more challenging scenarios summarized in Table 12.3; even in these cases, CPM never drops below approximately 0.96. Overall, all eighteen cases satisfy the target acceptance threshold of CPM > 0.95, confirming that the ROM delivers a high level of fidelity across different fault types, locations, and control modes.

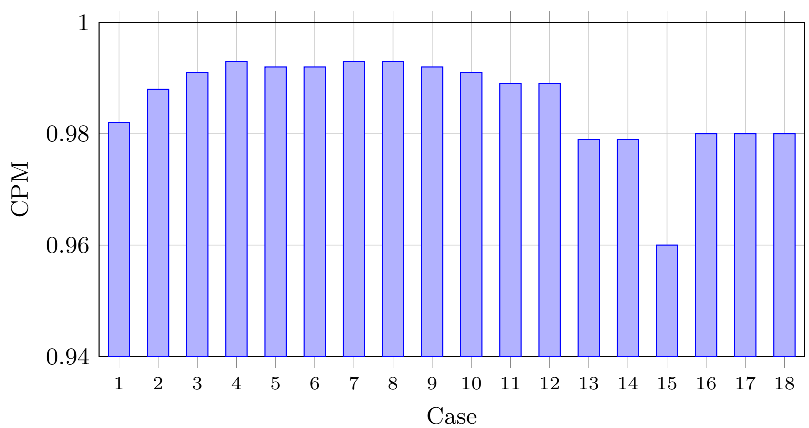

Figure 12.13: Composite Performance Metric (CPM) for all 18 test cases. A value of 1 corresponds to perfect agreement between the ROM and the detailed EMT model.

12.4.3 Satisfaction of ROM Requirements

The developed reduced-order model satisfies the derived requirements of Section 2.4.4 through its formulation, implementation, and multi-platform validation. A concise summary of requirement fulfillment is provided below.

Outputs

The ROM natively produces the required sequence-domain quantities $\{|I_1|, \angle I_1, |I_2|, \angle I_2\}$ as functions of the corresponding voltage sequences. These outputs retain EMT-level temporal resolution and accurately reproduce subtransient, transient, and early steady-state behavior, as demonstrated through the CE, RMSE, phase-shift, and CPM metrics across all test scenarios.

Behaviors

Key inverter behaviors relevant to protection performance are embedded directly in the model: current limiting with I_q/I_p priority, negative-sequence suppression or injection (depending on control mode), and the ride-through logic involving timers, hysteresis, and setpoint freeze. Sensitivity to grid strength and operating point is captured through parameter regression and K-factor tuning. These features allow the ROM to reflect the dominant control, electrical, and sequence-coupling dynamics governing IBR fault response.

Interfaces

The ROM supports export of parameter tables and sequence-resolved surfaces for use in short-circuit and protection-coordination tools. Metadata, scenario identifiers, and verification artifacts are included for traceability. Cross-validation utilities allow users to directly compare ROM and EMT outputs in Python, Simulink, or PSCAD environments.

Quality Targets

Quantitative evaluation confirms that the ROM meets the accuracy targets established for protection applications. Multi-cycle error metrics show low steady-state error and good phase alignment, with subtransient deviations limited to the first cycle. Relay-based validation demonstrates timing differences typically within 0.25–0.5 cycles for primary protection elements, indicating that the ROM preserves the timing, magnitude, and sequence characteristics needed for reliable use in protection studies.

Overall, the ROM satisfies the outputs, behaviors, interfaces, and quality requirements and demonstrates robust performance across platforms, operating conditions, and data sources, including EMT simulations and COTS inverter measurements.

Table 12.2: Relay Element Trigger Timing Table (Cycles From Fault Inception)

Relay Model	IBR Model	Case 13	Case 14	Case 15	Case 16	Case 17	Case 18
TRIP	Full Model	1.375	2	1.375	2.125	2.125	2
	ROM Model	1.625	1.375	1.5	3	3	3
Z1G	Full Model	1.375	2.25	1.375	2.125	2.125	2
	ROM Model	1.625	1.375	1.5	3	3	3
Z2GT	Full Model						
	ROM Model						
XAG1	Full Model	2	2				
	ROM Model	1.625	1.5	1.5			
XAG2	Full Model	2	2.125	2.125			
	ROM Model	1.625	1.5	1.5			
MAG1	Full Model	2	2	2.75			
	ROM Model	1.625	1.375	1.5			
MAG2	Full Model	2	2	2.125			
	ROM Model	1.625	1.375	1.375			
F32QG	Full Model						
	ROM Model	0	0	0			
F32V	Full Model	0.75	0.75	0.75			
	ROM Model	0.625	0.625	0.625			
FSA	Full Model	2	2	2.125			
	ROM Model	1	1.375	1.375			
FSB	Full Model						
	ROM Model						
FSC	Full Model						
	ROM Model						
FIDEN	Full Model	1	1	1			
	ROM Model	1	1	1			
XBC1	Full Model				2.125	2.125	2.5
	ROM Model				3	3	3
XBC2	Full Model				2.125	2.125	2.125
	ROM Model				3	3	3
MBC1	Full Model				2.125	2.125	2
	ROM Model				3	3	3

Table 12.3: Multi-Cycle Error Metrics for Test Cases 13–18

Case	Cycle	I1 CE	I2 CE	I1 RMSE	I2 RMSE	I1 Phase Shift	I2 Phase Shift
13	1	25.33	5.46	14.13	3.40	0	-0.22
	2	19.39	6.10	18.80	6.13	0	0.31
	3	4.71	9.49	5.68	9.57	0	0
14	1	25.07	6.28	14.01	3.82	0	-0.22
	2	19.16	6.31	18.62	6.48	0	0.31
	3	4.71	7.96	5.68	8.03	0	0
15	1	25.15	6.98	14.03	4.15	0	-0.22
	2	19.06	6.50	18.55	6.83	0	0.30
	3	4.74	6.96	5.72	7.04	0	0
16	1	30.63	13.46	20.62	9.30	0	0.61
	2	21.03	6.28	20.32	6.77	0	-0.14
	3	4.93	2.44	6.68	2.90	0	0
17	1	30.56	13.49	20.59	9.35	0	0.61
	2	20.93	6.37	20.25	6.93	0	-0.15
	3	4.90	2.47	6.66	2.93	0	0
18	1	30.50	13.50	20.56	9.38	0	0.58
	2	20.96	6.24	20.29	6.96	0	-0.21
	3	4.94	2.53	6.77	3.03	0	0

Chapter 13

Conclusions and Future Work

This dissertation presented a comprehensive and systematic investigation into the fault response of IBRs and the development of a ROM suitable for large-scale protection studies. Motivated by the growing penetration of IBRs and the resulting challenges in protection coordination and fault analysis, the work established a full end-to-end framework that combines requirements engineering, detailed modeling, theoretical characterization, and multi-platform validation.

The research began with an in-depth requirements analysis to identify the essential behaviors and output characteristics an IBR model must exhibit to be useful for protection studies. This analysis defined the need to capture subtransient, transient, and steady-state current behavior; negative-sequence phenomena; current-limiting logic; ride-through characteristics; and sequence-domain outputs compatible with relay algorithms. Based on these requirements, high-fidelity EMT models were developed in Simulink and PSCAD to generate accurate IBR fault responses across a range of control modes, grid strengths, and fault locations.

A detailed theoretical investigation of inverter fault response was then carried out to understand the sequence of events following a disturbance. This included a temporal analysis of subtransient and transient intervals, current-trajectory patterns in the dq and sequence frames, and harmonic content arising from voltage imbalance and control saturation. These theoretical insights provided the foundation for deriving a physics-informed, data-driven ROM capable of reproducing the dominant dynamics of IBR short-circuit currents while maintaining interpretability and computational efficiency.

The central contribution of this dissertation is the formulation of this physics-informed ROM and its implementation across multiple platforms, demonstrating both accuracy and portability. A comprehensive validation campaign was performed using detailed EMT simulations and experimental measurements from a COTS inverter. The evaluation included waveform-level comparisons in the ABC and sequence domains, quantitative analysis using CE, RMSE, phase-shift error, and the CPM, and relay-based assessments using a detailed distance and overcurrent relay model. Across all test scenarios, the ROM demonstrated strong agreement with EMT and experimental results, with especially tight alignment after the first cycle. Relay timing deviations were generally within 0.25–0.5 cycles, confirming that the ROM preserves the timing, magnitude, and sequence characteristics relevant for protection performance.

Beyond accuracy, the ROM satisfies practical interface and usability requirements through its ability to model parameter, generate sequence-resolved response surfaces, embed scenario metadata for traceability, and support structured cross-validation workflows in Python, Simulink, and PSCAD. This ensures that the model can integrate directly into utility short-circuit and protection coordination tools and can be maintained and extended in alignment with PPMV (performance, provenance, maintenance, validation) practices.

While the ROM captures the dominant dynamics governing grid-following IBR fault response, certain limitations remain. The model does not explicitly represent switching-scale oscillations or high-frequency control effects inherent to EMT models. Furthermore, although validated across multiple control modes, additional testing under grid-forming control schemes, hybrid inverter architectures, and more complex network conditions would broaden its applicability. Maintaining and updating the model as inverter control strategies evolve is also essential.

Overall, this dissertation advances the state of the art in reduced-order modeling for modern power systems. By combining theoretical insight, high-fidelity simulation, laboratory measurements, and protection-oriented metrics, this work provides a validated and practical ROM suitable for large-scale short-circuit and protection studies. The research framework developed herein establishes a strong foundation for continued innovation in modeling, analyzing, and protecting grids with high levels of inverter-based resources.

13.1 Contribution Statement

This dissertation provides several original contributions to the understanding, modeling, and application of IBR fault behavior for protection studies. The work spans requirements analysis, theoretical characterization, high-fidelity simulation, and reduced-order modeling, resulting in a cohesive framework for short-circuit analysis in power systems with high IBR penetration. The key contributions are as follows:

- *Requirements-Guided Framework for IBR Fault Modeling:* A systems engineering based requirements assessment was developed to identify the essential behaviors, outputs, interfaces, and performance targets for a protection-oriented IBR short-circuit model. This analysis integrates standards (IEEE 2800, IEEE 1547), protection principles, and inverter control limitations, providing a structured foundation for ROM formulation.

- *Theoretical Characterization of IBR Fault Dynamics:* A sequence of analytical investigations was conducted to describe the subtransient, transient, and steady-state processes governing inverter fault response, including: (*i*) PWM saturation onset and recovery, (*ii*) settling characteristics of dq-current controllers, (*iii*) PLL distortions and sequence-extraction effects, (*iv*) harmonic and interharmonic components during unbalanced faults. These analyses collectively provide a coherent theoretical representation of the dynamic stages present during IBR short-circuit events.

- *High-Fidelity EMT Modeling and Data Generation:* EMT models of modern grid-following IBRs were implemented in both Simulink and PSCAD to produce simulation data for analysis and validation purposes. The models support multiple control modes and realistic grid conditions, enabling fault responses to be evaluated over a broad operating domain.

- *Physics-Informed, Data-Supported Reduced-Order Model:* Using the theoretical insights, a ROM was developed that represents the principal physical stages of inverter fault behavior while remaining computationally efficient. The model captures subtransient magnitude changes, transient decay patterns, steady-state current limits, positive/negative sequence interactions, and dependencies on operating conditions.

- *Parameter Adaptation Across Operating and Grid Conditions:* A data-based parameter adjustment methodology was introduced to extend the ROM applicability across varying pre-fault operating points, grid strengths, controller parameters, and negative-sequence voltage magnitudes. This enables accurate representation without requiring exhaustive enumeration of simulation scenarios.

- *Validation Across Modeling Platforms and Protection Contexts:* The ROM was compared against PSCAD/Simulink EMT simulations, laboratory measurements, and relay models. The results indicate that the ROM reproduces IBR fault current characteristics and protection-relevant quantities with sufficient accuracy for short-circuit analysis and protection coordination studies.

13.1.1 Limitations

While the proposed reduced-order modeling framework provides a practical and protection-oriented representation of inverter fault response, several limitations of the present study should be acknowledged.

First, the model focuses on the dominant electromechanical and control-driven dynamics relevant to short-circuit and protection studies, and therefore does not explicitly capture high-frequency switching harmonics or electromagnetic phenomena above the fundamental-frequency range. Such effects, while important for electromagnetic compatibility and power-quality analysis, fall outside the intended scope of protection-oriented fault modeling.

Second, the current framework has been developed and validated primarily for grid-following inverter architectures. Grid-forming inverters, which exhibit fundamentally different control structures and fault-response mechanisms, are not explicitly addressed in this work and constitute an important direction for future extension.

Third, the proposed model is intended to represent inverter behavior at the device level or at the level of multiple closely coupled inverters (e.g., within a plant or feeder section). It is not designed to replace full network-wide EMT simulation of large interconnected power systems. This design choice reflects a deliberate and reasonable modeling scope: the model captures detailed inverter dynamics where they matter most for protection behavior, while enabling efficient integration into broader system studies through established short-circuit and protection analysis tools.

13.2 Future Work

Several opportunities exist to extend and apply the modeling framework developed in this dissertation:

- *Positive-sequence reduced-order model for large-scale studies.* Extending the approach to develop a planning-grade positive-sequence ROM would allow system-wide screening, faster relay coordination studies, and integration into existing transmission-level short-circuit and dynamic simulation tools.

- *Reduced-order model for grid-forming inverters.* As grid-forming inverters become increasingly common, a complementary ROM capturing their voltage-forming behavior, inertia emulation, and distinct short-circuit characteristics will be critical for future protection and stability studies.

- *Deployment in real-world protection applications.* Applying the ROM in utility environments—including protection coordination, misoperation analysis, and field event reconstruction—will further validate its practicality and accelerate adoption in operational and planning workflows.

- *AI-assisted parameter extraction and data processing.* Future work may explore the integration of artificial intelligence and machine-learning techniques to enhance the parameter-identification process, particularly when large volumes of measured or simulated fault data are available. AI-based methods could assist with automated event segmentation, noise filtering, feature extraction, operating-mode classification, and anomaly detection, improving the robustness and scalability of ROM calibration while preserving the underlying physics-based model structure.

Bibliography

[1] U. Karaagac, J. Mahseredjian, R. Gagnon, H. Gras, H. Saad, L. Cai, I. Kocar, A. Haddadi, E. Farantatos, S. Bu, K. W. Chan, and L. Wang, "A generic EMT-type model for wind parks with permanent magnet synchronous generator full size converter wind turbines," *IEEE Power and Energy Technology Systems Journal*, vol. 6, no. 3, pp. 131–141, 2019.

[2] R. Mahmud, A. Hoke, and J. White, "Impact of aggregated pv on subsynchronous torsional interaction," in *2020 47th IEEE Photovoltaic Specialists Conference (PVSC)*, 2020, pp. 0342–0347.

[3] International Energy Agency, "Renewables 2024: Analysis and forecast to 2029," IEA, Paris, France, Tech. Rep., 2024, accessed 8 June 2025. [Online]. Available: https://www.iea.org/reports/renewables-2024

[4] U.S. Energy Information Administration, "Electric power monthly: Data for march 2025," U.S. Department of Energy, Washington, DC, Tech. Rep., May 2025, release 22 May 2025; accessed 8 June 2025. [Online]. Available: https://www.eia.gov/electricity/monthly/

[5] California ISO. (2024, June) New renewables records — what they mean for the grid and its carbon-free future. Energy Matters Blog; accessed 8 June 2025. [Online]. Available: https://www.caiso.com/about/news/energy-matters-blog/new-renewables-records-what-they-mean-for-the-grid-and-its-carbon-free-future

[6] Electric Reliability Council of Texas, "Ercot monthly — april 2024," ERCOT, Austin, TX, Tech. Rep., 2024, accessed 8 June 2025. [Online]. Available: https://www.ercot.com/files/docs/2024/04/30/ERCOT-Monthly-April-2024.pdf

[7] *IEEE Standard for Interconnection and Interoperability of Inverter-Based Resources (IBRs) Interconnecting with Associated Transmission Electric Power Systems*, IEEE Std. IEEE Std 2800-2022, 2022. [Online]. Available: https://standards.ieee.org/standard/2800-2022.html

[8] "Inverter-based resource model quality deficiencies — level 2 industry recommendation," North American Electric Reliability Corporation (NERC), Tech. Rep., June 2024. [Online]. Available: https://www.nerc.com/pa/rrm/bpsa/Alerts%20DL/NERC%20Alert%20Level%202%20-%20Inverter-Based%20Resource%20Model%20Quality%20Deficiencies.pdf

[9] "Inverter-based resource performance issues — public report," North American Electric Reliability Corporation, Tech. Rep., 2023, includes discussion of Level 2 alert in March 2023.

[10] North American Electric Reliability Corporation, "Level 3 alert: Essential actions to industry—inverter-based resource performance and modeling," NERC, Atlanta, GA, Tech. Rep., May 2025, initial distribution 20 May 2025; accessed 8 June 2025. [Online]. Available: https://www.nerc.com/pa/rrm/bpsa/Alerts%20DL/Level%203%20Alert%20Essential%20Actions%20IBR%20Performance%20and%20Modeling.pdf

[11] Electric Power Research Institute, "Inverter-based resource short-circuit modeling — 2024 research summary," EPRI, Palo Alto, CA, Tech. Rep. Product ID 3002030170, 2024, accessed 8 June 2025. [Online]. Available: https://www.epri.com/research/products/3002030170

[12] S. Chakraborty, P. H. Pinheiro, G. B. Romulo, H. Lei, B. K. Johnson, S. Manson, J. Wang, R. Mahmud, A. Hoke, and C. J. Kruse, "Studying the impact of IBR modeling on the commonly applied transmission line protective elements," in *2024 IEEE Energy Conversion Congress and Exposition (ECCE)*, 2024, pp. 4238–4245.

[13] North American Electric Reliability Corporation, "Reliability guideline: Recommended practices for performing emt system studies for inverter-based resources," NERC, Atlanta, GA, Tech. Rep., December 2024, approved by Reliability and Security Technical Committee; accessed 8 June 2025. [Online]. Available: https://www.nerc.com/comm/RSTC_Reliability_Guidelines/Reliability_Guideline_Recommended_Practices_for_EMT_Studies_for_IBR_Approved.pdf

[14] North American Electric Reliability Corporation and Texas Reliability Entity, "Odessa ii: Disturbance report—loss of solar photovoltaic resources on 4 june 2022," NERC, Atlanta, GA, Tech. Rep., 2023, accessed 8 June 2025. [Online]. Available: https://www.nerc.com/comm/RSTC/IRPS/2022_Odessa_Disturbance_Webinar.pdf

[15] TRC Companies. (2024, May) Insights from the odessa ii power system disturbance. Blog article; accessed 8 June 2025. [Online]. Available: https://www.trccompanies.com/insights/insights-from-the-odessa-ii-power-system-disturbance/

[16] S. Rahman, J. Kim, and M. Reza, "Investigating disturbance-induced misoperation of grid-following inverter-based resources," *IET Generation, Transmission & Distribution*, vol. 19, no. 4, pp. 456–468, 2025.

[17] U.S. Department of Energy, "i2X Forum: Meeting synopses on implementing ieee 2800-2022," DOE, Washington, DC, Tech. Rep., January 2025, accessed 8 June 2025. [Online]. Available: https://www.energy.gov/sites/default/files/2025-01/i2x%20Forum%20Meeting%20Synopses%20%285%29.pdf

[18] ENTSO-E, "Commission regulation (eu) 2016/631—requirements for generators," 2016, official Journal of the European Union L112/1; accessed 8 June 2025. [Online]. Available: https://eur-lex.europa.eu/eli/reg/2016/631/oj

[19] Western Electricity Coordinating Council, "2024 anchor data set and 2032 reference case overview," WECC, Salt Lake City, UT, Tech. Rep., 2024, accessed 8 June 2025. [Online]. Available: https://www.wecc.org/Administrative/2032-Reference-Case-Overview.pdf

[20] W. F. Holmgren, C. W. Hansen, and M. A. Mikofski, "pvlib python: a python package for modeling solar energy systems," *Journal of Open Source Software*, vol. 3, no. 29, 9 2018.

[21] B. Kroposki and A. Hoke, "A path to 100 percent renewable energy: Grid-forming inverters will give us the grid we need now," *IEEE Spectrum*, vol. 61, no. 5, pp. 50–57, 2024.

[22] Oak Ridge National Laboratory. (2024, August) 2024 Electromagnetic transient (EMT) simulation workshop. Workshop summary; accessed 8 June 2025. [Online]. Available: https://www.energy.gov/eere/solar/2024-electromagnetic-transient-emt-simulation-workshop

[23] Electric Power Research Institute, "2025 Research portfolio—P174 DER integration," EPRI, Palo Alto, CA, Tech. Rep., 2025, product overview; accessed 8 June 2025. [Online]. Available: https://restservice.epri.com/publicattachment/92812

[24] North American Electric Reliability Corporation (NERC), "Short-circuit modeling and system strength," NERC, Tech. Rep., 2018. [Online]. Available: https://www.nerc.com

[25] I. P. T. Force and N. J. W. Group, "Impact of inverter-based generation on bulk power system dynamics and short-circuit performance," IEEE Power & Energy Society, Tech. Rep. PES-TR68, 2018.

[26] Z. Javid, F. Ul Nazir, W. Zhu, D. Chakravorty, A. Aboushady, and M. Galeela, "A new paradigm in IBR modeling for power flow and short circuit analysis," *IEEE Transactions on Power Systems*, vol. 40, no. 6, pp. 5459–5471, 2025.

[27] L. R. Tuladhar and K. Banerjee, "Grid of the Penetration of Inverter-Based Systems on Grid Protection," *CIGRE US National Committee 2019 Grid of the Future Symposium*, 2019. [Online]. Available: http://www.cigre.org

[28] R. Furlaneto, I. Kocar, A. Grilo-Pavani, U. Karaagac, A. Haddadi, and E. Farantatos, "Short circuit network equivalents of systems with inverter-based resources," *Electric Power Systems Research*, vol. 199, p. 107314, 2021. [Online]. Available: https://www.sciencedirect.com/science/article/pii/S0378779621002959

[29] M. Cespedes and J. Sun, "Impedance modeling and analysis of grid-connected voltage-source converters," *IEEE Transactions on Power Electronics*, vol. 29, no. 3, pp. 1254–1261, 2014.

[30] S. Prakash, O. A. Zaabi, R. K. Behera, K. A. Jaafari, K. A. Hosani, and U. R. Muduli, "Modeling and dynamic stability analysis of the grid-following inverter integrated with photovoltaics," *IEEE Journal of Emerging and Selected Topics in Power Electronics*, vol. 11, no. 4, pp. 3788–3802, 2023.

[31] M. Ghazavi Dozein, B. C. Pal, and P. Mancarella, "Dynamics of inverter-based resources in weak distribution grids," *IEEE Transactions on Power Systems*, vol. 37, no. 5, pp. 3682–3692, 2022.

[32] I. Kim, "Short-circuit analysis models for unbalanced inverter-based distributed generation sources and loads," *IEEE Transactions on Power Systems*, vol. 34, no. 5, pp. 3515–3526, 2019.

[33] N. Baeckeland, D. Venkatramanan, M. Kleemann, and S. Dhople, "Fault behavior of inverter-based resources: A comparative study for grid-forming and grid-following control paradigms," in *IECON 2022 – 48th Annual Conference of the IEEE Industrial Electronics Society*, 2022, pp. 1–6.

[34] M. C. Vargas, O. E. Batista, and Y. Yang, "Estimation method of short-circuit current contribution of inverter-based resources for symmetrical faults," *Energies*, vol. 16, no. 7, 2023. [Online]. Available: https://www.mdpi.com/1996-1073/16/7/3130

[35] Z. Cheng, T. R. Patel, J. Holbach, M. J. Reno, C. Weldy, T. Nguyen, and Y. Alkraimeen, "Assessing inverter-based resources modeling gaps in commonly used short-circuit programs," in *2025 78th Annual Conference for Protective Relay Engineers (CFPR)*, 2025, pp. 1–13.

[36] J. Matevosyan, H. Soltani, M. Gordon, A. Shattuck, S. Grogan, D. Ramasubramanian, and S. Goyal, "Electromagnetic transient modeling for connection studies: High-fidelity models are key [feature]," *IEEE Power and Energy Magazine*, vol. 23, no. 4, pp. 66–80, 2025.

[37] F. V. Lopes, M. J. B. B. Davi, M. Oleskovicz, and G. B. Fabris, “Importance of EMT-type simulations for protection studies in power systems with inverter-based resources,” in *2022 Workshop on Communication Networks and Power Systems (WCNPS)*, 2022, pp. 1–6.

[38] R. W. Kenyon, A. Sajadi, A. Hoke, and B.-M. Hodge, “Criticality of inverter controller order in power system dynamic studies – case study: Maui island,” *Electric Power Systems Research*, vol. 214, p. 108789, 2023. [Online]. Available: https://www.sciencedirect.com/science/article/pii/S0378779622008434

[39] North American Electric Reliability Corporation (NERC), “Electromagnetic transient analysis in operations planning,” NERC, Tech. Rep., 2024.

[40] N. Crooks, Y. Cheng, A. Harjula, E. Kuhlmann, and N. Qin, “Large-scale EMT model examples for high-share IBR systems: Using large-scale EMT models for operations and planning power systems with a high share of IBRs [feature],” *IEEE Power and Energy Magazine*, vol. 23, no. 4, pp. 40–52, 2025.

[41] North American Electric Reliability Corporation (NERC), “Reliability guideline – electromagnetic transient modeling for BPS-connected inverter-based resources : Recommended model requirements and verification practices,” NERC, Atlanta, GA, USA, Tech. Rep., 2023. [Online]. Available: https://www.nerc.com/globalassets/who-we-are/standing-committees/rstc/irps/reliability_guideline-emt_modeling_and_simulations.pdf

[42] R. Yao, Q. Chen, H. Bai, C. Liu, T. Liu, Y. Luo, and W. Yang, “A multi-rate simulation strategy based on the modified time-domain simulation method and multi-area data exchange method of power systems,” *Electronics*, vol. 13, no. 5, 2024. [Online]. Available: https://www.mdpi.com/2079-9292/13/5/884

[43] K.-C. Hsu, J. Choi, and S. Debnath, “Sparse linear solvers for large-scale electromagnetic transient simulations,” in *IECON 2024 - 50th Annual Conference of the IEEE Industrial Electronics Society*, 2024, pp. 1–6.

[44] North American Electric Reliability Corporation (NERC), "EMT modeling adoption for interconnection and planning studies," NERC, Tech. Rep., 2025, draft white paper, June 2025.

[45] M. Xiong, B. Wang, D. Vaidhynathan, J. Maack, Y. Liu, S. Abhyankar, B. Palmer, R. Henriquez-Auba, A. Hoke, K. Sun, V. Vittal, M. Sajjadi, M. Khamees, K. Huang, D. Ramasubramanian, V. Verma, M. Reynolds, and J. Tan, "EMT-TS hybrid simulation for large power grids considering IBR-driven dynamics," in *IECON 2024 - 50th Annual Conference of the IEEE Industrial Electronics Society*, 2024, pp. 1–6.

[46] Z. Dong, A. Ingalalli, M. Al Mamun, G. Bharati, S. Kamalasadan, S. Chakraborty, S. Paudyal, and A. Ashok, "An EMT-phasor co-simulation setup for studying reconfiguration of distribution system with inverter based resources," in *2024 IEEE Power & Energy Society General Meeting (PESGM)*, 2024, pp. 1–5.

[47] L. Orellana, L. Sainz, E. Prieto-Araujo, M. Cheah-Mané, H. Mehrjerdi, and O. Gomis-Bellmunt, "Study of black-box models and participation factors for the positive-mode damping stability criterion," *International Journal of Electrical Power & Energy Systems*, vol. 148, p. 108957, 2023. [Online]. Available: https://www.sciencedirect.com/science/article/pii/S0142061523000145

[48] Electric Power Research Institute (EPRI), "Inverter-based resource short-circuit modeling," EPRI, Palo Alto, CA, USA, Tech. Rep., 2023.

[49] A. Haddadi, E. Farantatos, J. C. Boemer, M. Patel, and W. W. Baker, "Inverter-based resource short circuit model–considerations for VCCS tabular model," in *Proceedings of the Western Protective Relay Conference*, Nov. 2023, pp. 1–6.

[50] Electric Reliability Council of Texas (ERCOT) and ASPEN Inc., "Update on inverter-based resource (IBR) modeling and simulation in aspen oneliner," Proceedings of the ERCOT System Planning Working Group (SPWG) meeting, July 17, 2024, 2024.

[Online]. Available: https://www.ercot.com/files/docs/2024/07/24/ASPEN%20Update%20On%20IBR%20Modeling%20For%20ERCOT_SPWG2024_07-_17.pdf

[51] A. Haddadi, X. Chen, E. Farantatos, and I. Kocar, "A robust solver for phasor-domain short-circuit analysis with inverter-based resources," *IEEE Transactions on Power Delivery*, vol. 40, no. 4, pp. 2181–2193, 2025.

[52] R. Mahmud, D. Narang, and A. Hoke, "Reduced-order parameterized short-circuit current model of inverter-interfaced distributed generators," *IEEE Transactions on Power Delivery*, vol. 36, no. 6, pp. 3671–3680, 2021.

[53] Q. Liu, K. Jia, B. Yang, L. Zheng, and T. Bi, "Fault analysis of inverter-interfaced RESs considering decoupled sequence control," *IEEE Transactions on Industrial Electronics*, vol. 70, no. 5, pp. 4820–4830, 2023.

[54] ——, "Analytical model of inverter-interfaced renewable energy sources for power system protection," *IEEE Transactions on Power Delivery*, vol. 38, no. 2, pp. 1064–1073, 2023.

[55] H. Ma, T. Zheng, T. Zhang, and Z. Hao, "A fault calculation method for large-scale photovoltaic integrated transmission systems," *International Journal of Electrical Power & Energy Systems*, vol. 165, p. 110504, 2025. [Online]. Available: https://www.sciencedirect.com/science/article/pii/S0142061525000559

[56] E. Kaufhold, S. Grandl, J. Meyer, and P. Schegner, "Feasibility of black-box time domain modeling of single-phase photovoltaic inverters using artificial neural networks," *Energies*, vol. 14, no. 8, 2021. [Online]. Available: https://www.mdpi.com/1996-1073/14/8/2118

[57] K. A. Kharusi, A. E. Haffar, and M. Mesbah, "Adaptive machine-learning-based transmission line fault detection and classification connected to inverter-based generators," *Energies*, vol. 16, no. 15, 2023. [Online]. Available: https://www.mdpi.com/1996-1073/16/15/5775

[58] D. D. Walden, G. J. Roedler, and K. Forsberg, *INCOSE Systems Engineering Handbook: A Guide for System Life Cycle Processes and Activities*, 5th ed. Hoboken, NJ: Wiley, 2023.

[59] ISO/IEC/IEEE, *Systems and Software Engineering — System Life Cycle Processes (ISO/IEC/IEEE 15288:2023)*, IEEE Standards Association Std., May 16 2023, supersedes ISO/IEC/IEEE 15288:2015. [Online]. Available: https://standards.ieee.org/ieee/15288/10424/

[60] IEEE PES Power System Relaying and Control Committee (PSRC), "Protection challenges and practices for interconnecting inverter-based resources to utility transmission systems," https://www.pes-psrc.org/kb/report/109.pdf, Tech. Rep., 2020.

[61] North American Electric Reliability Corporation (NERC), "Reliability guideline: Electromagnetic transient modeling and simulations for BPS studies," https://www.nerc.com/comm/RSTC_Reliability_Guidelines/Reliability_Guideline-EMT_Modeling_and_Simulations.pdf, Feb. 2023.

[62] ——, "Reliability guideline: Recommended practices for performing EMT system studies for inverter-based resources," https://www.nerc.com/comm/RSTC_Reliability_Guidelines/Reliability_Guideline_Recommended_Practices_for_EMT_Studies_for_IBR_Approved.pdf, Tech. Rep., Dec. 2024.

[63] IEEE/EPRI/NAGF/NATF/NERC, "IEEE std 2800-2022 overview (joint webinar slides)," https://sagroups.ieee.org/2800/wp-content/uploads/sites/336/2022/06/ieee28002022jointieeeesigpserccurentwebinarmay22022165227217277l.pdf, May 2022.

[64] A. Haddadi, I. Kocar, J. Mahseredjian, U. Karaagac, and E. Farantatos, "Negative sequence quantities-based protection under inverter-based resources challenges and impact of the german grid code," *Electric Power Systems Research*, vol. 188, p. 106573, 2020. [Online]. Available: https://www.sciencedirect.com/science/article/pii/S0378779620303771

[65] ERCOT Inverter-Based Resource Task Force (IBRTF), “Reliability guideline: Electromagnetic transient (EMT) modeling and simulation for inverter-based resources,” Electric Reliability Council of Texas (ERCOT), Tech. Rep., January 2023, prepared by the ERCOT IBRTF and EMT Task Force. [Online]. Available: https://www.ercot.com/files/docs/2023/01/20/RG%20-%20EMT%20Modeling%20and%20Simulation%20-%20EMT%20TF%20-%20ERCOT%20IBRTF%202023.pdf

[66] A. Haddadi, E. Farantatos, J. C. Boemer, M. Patel, and W. W. Baker, “Inverter-based resource short circuit model — considerations for VCCS tabular model,” *Electric Power Research Institute (EPRI) / Southern Company technical publication*, October 2023, presented via WPRC archives, 6 pp. [Online]. Available: https://wprcarchives.org/wp-content/uploads/2024/03/Haddadi_Aboutaleb_Inverter-Based-Resource-Short-Circuit-Model-%E2%80%92-Considerations-for-VCCS-Tabular-Model_20231012.pdf

[67] North American Electric Reliability Corporation (NERC), “Level 3 alert: Essential actions for IBR performance and modeling,” https://www.nerc.com/pa/rrm/bpsa/Alerts%20DL/Level%203%20Alert%20Essential%20Actions%20IBR%20Performance%20and%20Modeling.pdf, May 2025.

[68] R. Mahmud, L. Yu, and A. Hoke, “Characterization of DER momentary cessation and rate-of-change-of-frequency response,” in *2022 IEEE 49th Photovoltaics Specialists Conference (PVSC)*, 2022, pp. 1000–1002.

[69] North American Electric Reliability Corporation (NERC), “State of reliability 2025 – overview,” https://www.nerc.com/pa/RAPA/PA/Performance%20Analysis%20DL/NERC_SOR_2025_Overview.pdf, Jun. 2025.

[70] Federal Energy Regulatory Commission (FERC), “Reliability standards to address inverter-based resources (order no. 901),” https://www.federalregister.gov/documents/2023/10/30/2023-23581/reliability-standards-to-address-inverter-based-resources, Oct. 2023.

[71] ——, “FERC approves grid reliability standards applicable to inverter-based generators,” https://www.ferc.gov/news-events/news/ferc-approves-grid-reliability-standards-applicable-inverter-based-generators, Jul. 2025.

[72] North American Electric Reliability Corporation (NERC), “Reliability guideline: Electromagnetic transient modeling and simulations for BPS studies,” https://www.nerc.com/comm/RSTC_Reliability_Guidelines/Reliability_Guideline-EMT_Modeling_and_Simulations.pdf, Tech. Rep., Feb. 2023.

[73] ——, “Electromagnetic transient modeling task force (EMTTF) — scope and deliverables,” https://www.nerc.com/comm/RSTC/EMMTF/EMTTF%20Scope.pdf, 2023.

[74] ——, “Integrating inverter-based resources into low short-circuit strength systems,” https://www.nerc.com/comm/RSTC_Reliability_Guidelines/Item_4a._Integrating%20_Inverter-Based_Resources_into_Low_Short_Circuit_Strength_Systems_-_2017-11-08-FINAL.pdf, Tech. Rep., Nov. 2017.

[75] R. Mahmud, A. Hoke, J. Keen, and J. Cale, “Developing IEEE std 2800-compliant algorithms for transmission-connected inverter based resources,” in *2024 IEEE 52nd Photovoltaic Specialist Conference (PVSC)*, 2024, pp. 1170–1175.

[76] IEEE 2800 Working Group, “IEEE 2800 overview (SEIA–ACP joint webinar slides),” https://sagroups.ieee.org/2800/wp-content/uploads/sites/336/2022/06/IEEE-2800-2022-SEIA-ACP-May-31-2022-Joint-Webinar.pdf, May 2022.

[77] ERCOT Inverter-Based Resource Task Force (IBRTF), “EMT modeling and simulation: Adoption guidance and model quality expectations,” https://www.ercot.com/files/docs/2023/01/20/RG%20-%20EMT%20Modeling%20and%20Simulation%20-%20EMT%20TF%20-%20ERCOT%20IBRTF%202023.pdf, Jan. 2023.

[78] ERCOT, “ERCOT planning guide (December 1, 2024 edition),” https://www.ercot.com/files/docs/2024/11/26/December%201%2C%202024%20Planning%20Guide.pdf, Dec. 2024.

[79] A. Haddadi-Aboutaleb and colleagues, “Inverter-based resource short-circuit model: Considerations for VCCS tabular model,” https://wprcarchives.org/wp-content/uploads/2024/03/Haddadi_Aboutaleb_Inverter-Based-Resource-Short-Circuit-Model-%E2%80%92-Considerations-for-VCCS-Tabular-Model_20231012.pdf, Western Protective Relay Conference (WPRC), Tech. Rep., 2023, rev. 2024.

[80] Z. Cheng, T. R. Patel, J. Holbach, M. J. Reno, C. Weldy, T. Nguyen, and Y. Alkraimeen, “Assessing inverter-based resources modeling gaps in commonly used short-circuit programs,” in *2025 78th Annual Conference for Protective Relay Engineers (CFPR)*, 2025, pp. 1–13.

[81] Electric Power Research Institute (EPRI), “Short-circuit modeling and protection system performance with high penetration of inverter-based resources,” https://restservice.epri.com/publicdownload/000000003002028606/0/Product, Tech. Rep., Jul. 2025.

[82] ERCOT, “Update on inverter-based resource (IBR) modeling and simulation in aspen,” https://www.ercot.com/files/docs/2024/07/24/ASPEN%20Update%20On%20IBR%20Modeling%20For%20ERCOT_SPWG2024_07-_17.pdf, Jul. 2024.

[83] M. J. Davi, M. Oleskovicz, and F. V. Lopes, “Study on IEEE 2800-2022 standard benefits for transmission line protection in the presence of inverter-based resources,” *Electric Power Systems Research*, vol. 220, p. 109304, 2023. [Online]. Available: https://www.sciencedirect.com/science/article/pii/S0378779623001931

[84] D. Wu, G.-S. Seo, L. Xu, C. Su, L. Kocewiak, Y. Sun, and Z. Qin, “Grid integration of offshore wind power: Standards, control, power quality and transmission,” *IEEE Open Journal of Power Electronics*, vol. 5, pp. 583–604, 2024.

[85] A. Hansen and G. Michalke, "Multi-pole permanent magnet synchronous generator wind turbines' grid support capability in uninterrupted operation during grid faults," *IET Renewable Power Generation*, vol. 3, pp. 333–348, 2009. [Online]. Available: https://digital-library.theiet.org/doi/abs/10.1049/iet-rpg.2008.0055

[86] V. Akhmatov, A. H. Nielsen, J. K. Pedersen, and O. Nymann, "Variable-speed wind turbines with multi-pole synchronous permanent magnet generators. Part I: Modelling in dynamic simulation tools," *Wind Engineering*, vol. 27, no. 6, pp. 531–548, 2003.

[87] L. Barros and C. Barros, "An internal model control for enhanced grid-connection of direct-driven PMSG-based wind generators," *Electric Power Systems Research*, vol. 151, pp. 440–450, 2017. [Online]. Available: https://www.sciencedirect.com/science/article/pii/S0378779617302638

[88] S. Grabic, N. Celanovic, and V. A. Katic, "Permanent magnet synchronous generator cascade for wind turbine application," *IEEE Transactions on Power Electronics*, vol. 23, no. 3, pp. 1136–1142, 2008.

[89] V. Yaramasu, A. Dekka, M. J. Durán, S. Kouro, and B. Wu, "PMSG-based wind energy conversion systems: survey on power converters and controls," *IET Electric Power Applications*, vol. 11, no. 6, pp. 956–968, 2017. [Online]. Available: https://ietresearch.onlinelibrary.wiley.com/doi/abs/10.1049/iet-epa.2016.0799

[90] X. Song, Y. Chen, S. Qu, C. Wang, D. Wang, and S. Gao, "Evaluation and control of voltage support capability in wind-storage grid-connected systems based on entropy weight method," *Energy Reports*, vol. 13, pp. 3442–3455, 2025. [Online]. Available: https://www.sciencedirect.com/science/article/pii/S2352484725001477

[91] X. He, H. Geng, and G. Mu, "Modeling of wind turbine generators for power system stability studies: A review," *Renewable and Sustainable Energy Reviews*, vol. 143,

p. 110865, 2021. [Online]. Available: https://www.sciencedirect.com/science/article/pii/S1364032121001593

[92] R. Mahmud, L. He, and J. Cale, "A generic FSC wind park EMT model with IEEE std 2800-compliant fault ride-through capability." University of Illinois Chicago, 10 2025. [Online]. Available: https://www.osti.gov/biblio/2563315

[93] R. Mahmud, J. Cale, and L. He, "Adapting inverter-based resources with current limiting techniques for asymmetrical fault compliance according to new standards," 04 2025. [Online]. Available: https://www.osti.gov/biblio/2563316

[94] *IEEE Standard for Interconnection and Interoperability of Inverter-Based Resources Interconnecting with Associated Transmission Electric Power Systems*, Std. IEEE Std 2800-2022, 2022, doi:10.1109/IEEESTD.2022.9745671.

[95] "IEEE Standard for Interconnection and Interoperability of Distributed Energy Resources with Associated Electric Power Systems Interfaces," 2018.

[96] S. Xu, Y. Xue, and L. Chang, "Review of power system support functions for inverter-based distributed energy resources- standards, control algorithms, and trends," *IEEE Open Journal of Power Electronics*, vol. 2, pp. 88–105, 2021.

[97] I. Khan and S. Doolla, "Improved fault ride-through response of grid forming inverters under symmetrical and asymmetrical faults," *IEEE Transactions on Energy Conversion*, vol. 40, no. 1, pp. 394–408, March 2025.

[98] T. Hu, "A nonlinear-system approach to analysis and design of power-electronic converters with saturation and bilinear terms," *IEEE transactions on power electronics*, vol. 26, no. 2, pp. 399–410, 2010.

[99] C. Cheng, S. Xie, Q. Qian, J. Xu, B. Zeng, and J. Lv, "On stability of time-invariant current controlled weak-grid-tied inverters considering sinusoidal pulsewidth modulation saturation

and parameter uncertainties," *IEEE Transactions on Industrial Electronics*, vol. 69, no. 11, pp. 11 359–11 369, 2021.

[100] R. Mahmud, A. Hoke, and D. Narang, "Validating the test procedures described in UL 1741 SA and IEEE P1547.1," in *2018 IEEE 7th World Conference on Photovoltaic Energy Conversion (WCPEC) (A Joint Conference of 45th IEEE PVSC, 28th PVSEC & 34th EU PVSEC)*, June 2018, pp. 1445–1450.

[101] T. Hu, "A nonlinear-system approach to analysis and design of power-electronic converters with saturation and bilinear terms," *IEEE Transactions on Power Electronics*, vol. 26, no. 2, pp. 399–410, Feb 2011.

[102] C. Cheng, S. Xie, Q. Qian, J. Xu, B. Zeng, and J. Lv, "On stability of time-invariant current controlled weak-grid-tied inverters considering sinusoidal pulsewidth modulation saturation and parameter uncertainties," *IEEE Transactions on Industrial Electronics*, vol. 69, no. 11, pp. 11 359–11 369, 2022.

[103] N. Bottrell and T. Green, "Comparison of current-limiting strategies during fault ride-through of inverters to prevent latch-up and wind-up," *IEEE Transactions on Power Electronics*, vol. 29, no. 7, pp. 3786–3797, 2014.

[104] W. Xu, Y. Li, C. Liu, Z. Xiang, and B. Han, "Peak short-circuit current calculation of PMSG considering PI controller saturation characteristic," *CSEE Journal of Power and Energy Systems*, pp. 1–11, 2024.

[105] C. Ma, F. Gao, G. He, and G. Li, "A voltage detection method for the voltage ride-through operation of renewable energy generation systems under grid voltage distortion conditions," *IEEE Transactions on Sustainable Energy*, vol. 6, no. 3, pp. 1131–1140, 2015.

[106] J. Roldán-Pérez, A. García-Cerrada, M. Ochoa-Giménez, and J. L. Zamora-Macho, "Delayed-signal-cancellation-based sag detector for a dynamic voltage restorer in distorted grids," *IEEE Transactions on Sustainable Energy*, vol. 10, no. 4, pp. 2015–2025, 2019.

[107] J. Zhang, P. Zhao, Z. Zhang, Y. Yang, F. Blaabjerg, and Z. Dai, "Fast amplitude estimation for low-voltage ride-through operation of single-phase systems," *IEEE Access*, vol. 8, pp. 8475–8484, 2020.

[108] A. Yazdani and R. Iravani, *Voltage-sourced converters in power systems: modeling, control, and applications*. John Wiley & Sons, 2010.

[109] B. Li, G. Zheng, Q. Zhong, S. Wang, and B. Li, "Analysis of transient characteristics of asymmetric fault current in offshore wind power system based on positive and negative sequence decoupling control," *IET Generation, Transmission & Distribution*, vol. 19, no. 1, p. e70081, 2025. [Online]. Available: https://ietresearch.onlinelibrary.wiley.com/doi/abs/10.1049/gtd2.70081

[110] T. Bi, B. Yang, K. Jia, L. Zheng, Q. Liu, and Q. Yang, "Review on renewable energy source fault characteristics analysis," *CSEE Journal of Power and Energy Systems*, vol. 8, no. 4, pp. 963–972, July 2022.

[111] J. Song, M. Cheah-Mane, E. Prieto-Araujo, and O. Gomis-Bellmunt, "Short-circuit analysis of grid-connected PV power plants considering inverter limits," *International Journal of Electrical Power & Energy Systems*, vol. 149, p. 109045, 2023. [Online]. Available: https://www.sciencedirect.com/science/article/pii/S0142061523001023

[112] B. Li, R. Mu, J. He, W. Wang, C. Yao, and Y. Zhang, "Transient fault current calculation method for the PV grid-connected system considering dynamic response of PLL," *IEEE Transactions on Industry Applications*, vol. 60, no. 5, pp. 7537–7547, Sep. 2024.

[113] K. Jia, Q. Liu, B. Yang, L. Zheng, Y. Fang, and T. Bi, "Transient fault current analysis of iiress considering controller saturation," *IEEE Transactions on Smart Grid*, vol. 13, no. 1, pp. 496–504, Jan 2022.

[114] Z. Yang, Q. Zhang, Z. Liu, and Z. Chen, “Fault current calculation for inverter-interfaced power sources considering saturation element,” in *2021 IEEE 4th International Electrical and Energy Conference (CIEEC)*, May 2021, pp. 1–5.

[115] Y. Han, M. Luo, X. Zhao, J. M. Guerrero, and L. Xu, “Comparative performance evaluation of orthogonal-signal-generators-based single-phase PLL algorithms—a survey,” *IEEE Transactions on Power Electronics*, vol. 31, no. 5, pp. 3932–3944, May 2016.

[116] Z. Shuai, C. Shen, X. Yin, X. Liu, and Z. J. Shen, “Fault analysis of inverter-interfaced distributed generators with different control schemes,” *IEEE Transactions on Power Delivery*, vol. 33, no. 3, pp. 1223–1235, June 2018.

[117] B. Popadic, B. Dumnic, and L. Strezoski, “Modeling of initial fault response of inverter-based distributed energy resources for future power system planning,” *International Journal of Electrical Power & Energy Systems*, vol. 117, p. 105722, 2020. [Online]. Available: https://www.sciencedirect.com/science/article/pii/S0142061519334556

[118] H. Guo, “Sequence-impedance modeling of voltage source converter interconnection under asymmetrical grid fault conditions,” *IEEE Transactions on Industrial Electronics*, vol. 68, no. 2, pp. 1332–1341, Feb 2021.

[119] Z. Xie, W. Wu, Y. Chen, S. Cao, and Y. Xu, “Sequence-admittance measurement method of grid-connected inverter with its control system disturbance,” *IEEE Transactions on Industrial Electronics*, vol. 70, no. 8, pp. 8598–8602, Aug 2023.

[120] North American Electric Reliability Corporation (NERC), “Integrating inverter-based resources into low short circuit strength systems,” 2017, emphasizes importance of accurate inverter modeling and coordination in weak-grid protection design. [Online]. Available: https://www.nerc.com/comm/RSTC_Reliability_Guidelines/Item_4a._Integrating_Inverter-Based_Resources_into_Low_Short_Circuit_Strength_Systems_-_2017-11-08-FINAL.pdf

[121] Electric Power Research Institute (EPRI), "Fault-ride through performance analysis of grid-forming inverter-based resources," EPRI, Tech. Rep., 2024, highlights the need for accurate characterization of IBR fault current and recovery behavior for reliable protection design. [Online]. Available: https://restservice.epri.com/publicdownload/000000003002029578/0/Product

[122] A. Camacho, M. Castilla, J. Miret, L. G. de Vicuña, and R. Guzman, "Positive and negative sequence control strategies to maximize the voltage support in resistive–inductive grids during grid faults," *IEEE Transactions on Power Electronics*, vol. 33, no. 6, pp. 5362–5373, June 2018.

[123] X. Li, Z. Wang, L. Zhu, L. Guo, and C. Wang, "Analytical dual-sequence current injections feasible region of weak-grid connected VSC under asymmetric grid faults," *IEEE Transactions on Power Systems*, vol. 38, no. 6, pp. 5546–5559, Nov 2023.

[124] M. Rocabert, A. Luna, F. Blaabjerg, and P. Rodriguez, "Control of power converters in AC microgrids," *IEEE Trans. Power Electronics*, vol. 27, no. 11, pp. 4734–4749, 2012, sequence-component transformations and DSOGI implementation, see eq. (8.23).

[125] S. Golestan, J. M. Guerrero, and J. C. Vasquez, "Three-phase PLLs: A review of recent advances," *IEEE Transactions on Power Electronics*, vol. 32, no. 3, pp. 1894–1907, 2017.

[126] B. C. Kuo and F. Golnaraghi, *Automatic Control Systems*, 8th ed. Hoboken, NJ: John Wiley & Sons, 2003.

[127] International Energy Agency, "Renewables 2023: Analysis and forecast to 2028," https://www.iea.org/reports/renewables-2023, 2023, accessed: 2025-08-11.

[128] REN21, "Renewables 2024 global status report," https://www.ren21.net/gsr-2024/, 2024, accessed: 2025-08-11.

[129] A. Yazdani and R. Iravani, *Voltage-sourced converters in power systems : modeling, control, and applications*. IEEE Press/John Wiley, 2010. [Online]. Available: https://www.wiley.com/en-us/Voltage+Sourced+Converters+in+Power+Systems+{\%}3A+Modeling{\%}2C+Control{\%}2C+and+Applications-p-9780470521564

[130] R. Teodorescu, M. Liserre, and P. Rodríguez, *Grid Converters for Photovoltaic and Wind Power Systems*, 2011.

[131] B. P. McGrath, D. G. Holmes, and T. Meynard, "Reduced PWM harmonic distortion for multilevel inverters operating over a wide modulation range," *IEEE Transactions on Power Electronics*, vol. 21, no. 4, pp. 941–949, July 2006.

[132] A. Hava, R. Kerkman, and T. Lipo, "Carrier-based PWM-VSI overmodulation strategies: analysis, comparison, and design," *IEEE Transactions on Power Electronics*, vol. 13, no. 4, pp. 674–689, July 1998.

[133] A. Rini Ann Jerin, P. Kaliannan, U. Subramaniam, and M. Shawky El Moursi, "Review on FRT solutions for improving transient stability in DFIG-WTs," *IET Renewable Power Generation*, vol. 12, no. 15, pp. 1786–1799, 2018. [Online]. Available: https://ietresearch.onlinelibrary.wiley.com/doi/abs/10.1049/iet-rpg.2018.5249

[134] A. Abdelrahim, M. Smailes, K. H. Ahmed, P. Mckeever, and A. Egea-Àlvarez, "New fault detection algorithm for an improved dual VSM control structure with FRT capability," *IEEE Access*, vol. 9, pp. 125 134–125 150, 2021.

[135] M. A. Awal and I. Husain, "Transient stability assessment for current-constrained and current-unconstrained fault ride through in virtual oscillator-controlled converters," *IEEE Journal of Emerging and Selected Topics in Power Electronics*, vol. 9, no. 6, pp. 6935–6946, Dec 2021.

[136] N. Baeckeland, D. Chatterjee, M. Lu, B. Johnson, and G.-S. Seo, "Overcurrent limiting in grid-forming inverters: A comprehensive review and discussion," *IEEE Transactions on Power Electronics*, vol. 39, no. 11, pp. 14 493–14 517, Nov 2024.

[137] A. Pal, P. D. Achlerkar, and B. K. Panigrahi, "Fault-induced current limitation control for grid-forming inverters: A framework for rapid grid code compliance," *Electric Power Systems Research*, vol. 242, p. 111471, 2025. [Online]. Available: https://www.sciencedirect.com/science/article/pii/S0378779625000641

[138] B. Fan, T. Liu, F. Zhao, H. Wu, and X. Wang, "A review of current-limiting control of grid-forming inverters under symmetrical disturbances," *IEEE Open Journal of Power Electronics*, vol. 3, pp. 955–969, 2022.

[139] R. S. Gonzalez, V. A. Aryasomyajula, K. S. Ayyagari, N. Gatsis, M. Alamaniotis, and S. Ahmed, "Modeling and studying the impact of dynamic reactive current limiting in grid-following inverters for distribution network protection," *Electric Power Systems Research*, vol. 224, p. 109609, 2023. [Online]. Available: https://www.sciencedirect.com/science/article/pii/S0378779623004984

[140] Y. Du, D. D.-C. Lu, G. James, and D. J. Cornforth, "Modeling and analysis of current harmonic distortion from grid connected PV inverters under different operating conditions," *Solar Energy*, vol. 94, pp. 182–194, 2013. [Online]. Available: https://www.sciencedirect.com/science/article/pii/S0038092X1300193X

[141] D. Pal and B. K. Panigrahi, "Reduced-order modeling and transient synchronization stability analysis of multiple heterogeneous grid-tied inverters," *IEEE Transactions on Power Delivery*, vol. 38, no. 2, pp. 1074–1085, April 2023.

[142] N. Mohammed, W. Zhou, D. Ramasubramanian, B. Bahrani, S. Dutta, and M. Bello, "Data-driven estimation of impedance of inverter-based resources for efficient stability

evaluation," *Electric Power Systems Research*, vol. 244, p. 111559, 2025. [Online]. Available: https://www.sciencedirect.com/science/article/pii/S0378779625001518

[143] S. Shah, P. Koralewicz, V. Gevorgian, and R. Wallen, "Sequence impedance measurement of utility-scale wind turbines and inverters – reference frame, frequency coupling, and mimo/siso forms," *IEEE Transactions on Energy Conversion*, vol. 37, no. 1, pp. 75–86, March 2022.

[144] E. Zhao, Y. Han, X. Lin, E. Liu, P. Yang, and A. S. Zalhaf, "Harmonic characteristics and control strategies of grid-connected photovoltaic inverters under weak grid conditions," *International Journal of Electrical Power & Energy Systems*, vol. 142, p. 108280, 2022. [Online]. Available: https://www.sciencedirect.com/science/article/pii/S0142061522003027

[145] Z. Jia, S. Xiao, and Y. Huang, "Mechanism and quantitative analysis of harmonics for grid-connected inverter during asymmetrical grid fault," in *2018 2nd IEEE Conference on Energy Internet and Energy System Integration (EI2)*, Oct 2018, pp. 1–5.

[146] K. Jia, Q. Liu, B. Yang, L. Zheng, Y. Fang, and T. Bi, "Transient fault current analysis of iiress considering controller saturation," *IEEE Transactions on Smart Grid*, vol. 13, no. 1, pp. 496–504, Jan 2022.

[147] R. Errouissi, A. Al-Durra, and M. Debouza, "A novel design of PI current controller for PMSG-based wind turbine considering transient performance specifications and control saturation," *IEEE Transactions on Industrial Electronics*, vol. 65, no. 11, pp. 8624–8634, Nov 2018.

[148] H. A. Pereira, R. M. Domingos, L. S. Xavier, A. F. Cupertino, V. F. Mendes, and J. O. Paulino, "Adaptive saturation for a multifunctional three-phase photovoltaic inverter," in *2015 17th European Conference on Power Electronics and Applications (EPE'15 ECCE-Europe)*. IEEE, 2015, pp. 1–10.

[149] T. Hu, "A nonlinear-system approach to analysis and design of power-electronic converters with saturation and bilinear terms," *IEEE Transactions on Power Electronics*, vol. 26, no. 2, pp. 399–410, 2011.

[150] E. Y. Y. Ho and P. C. Sen, "Digital simulation of PWM induction motor drives for transient and steady-state performance," *IEEE Transactions on Industrial Electronics*, vol. IE-33, no. 1, pp. 66–77, Feb 1986.

[151] M. Reyes, P. Rodriguez, S. Vazquez, A. Luna, R. Teodorescu, and J. M. Carrasco, "Enhanced decoupled double synchronous reference frame current controller for unbalanced grid-voltage conditions," *IEEE Transactions on Power Electronics*, vol. 27, no. 9, pp. 3934–3943, 2012.

[152] S. Li, W. Lu, S. Yan, and Z. Zhao, "Improving dynamic performance of boost PFC converter using current-harmonic feedforward compensation in synchronous reference frame," *IEEE Transactions on Industrial Electronics*, vol. 67, no. 6, pp. 4857–4866, 2020.

[153] F. Blaabjerg and K. Ma, "Future on power electronics for wind turbine systems," *IEEE Journal of Emerging and Selected Topics in Power Electronics*, vol. 1, no. 3, pp. 139–152, 2013.

[154] "Implementation guidance document: Fault current contribution from PPMs and HVDC," ENTSO-E, Tech. Rep., 2017, discusses asymmetric (negative-sequence) reactive current contribution options. [Online]. Available: https://consultations.entsoe.eu/system-development/entso-e-connection-codes-implementation-guidance-d-3/user_uploads/igd-fault-current-contribution.pdf

[155] "Implementation guideline for network code requirements for generators (NC RfG)," ENTSO-E, Tech. Rep., 2013. [Online]. Available: https://www.entsoe.eu/fileadmin/user_upload/_library/resources/RfG/131016_-_NC_RfG_implementation_guideline.pdf

[156] "Grid code modification gc0111: Fast fault current injection — specification text and workgroup material," National Grid ESO, Tech. Rep., 2018. [Online]. Available: https://www.nationalgrid.com/sites/default/files/documents/GC0111%20Workgroup%20Presentation.pdf

[157] "Fast fault current injection (GC0048) — background and proposals," National Grid ESO, Tech. Rep., 2016. [Online]. Available: https://www.nationalgrid.com/sites/default/files/documents/8589936564-GC0048-T%20Presentation%201%20June%2016%20-%20Fast%20Fault%20Current%20Injection.pdf

[158] Z. Shuai, C. Shen, X. Yin, X. Liu, and Z. J. Shen, "Fault Analysis of Inverter-Interfaced Distributed Generators With Different Control Schemes," *IEEE Transactions on Power Delivery*, vol. 33, no. 3, jun 2018. [Online]. Available: https://ieeexplore.ieee.org/document/7953685/

[159] C. A. Plet, M. Brucoli, J. D. F. McDonald, and T. C. Green, "Fault models of inverter-interfaced distributed generators: Experimental verification and application to fault analysis," in *2011 IEEE Power and Energy Society General Meeting*. IEEE, jul 2011, pp. 1–8. [Online]. Available: http://ieeexplore.ieee.org/document/6039183/

[160] Q. Wang, N. Zhou, and L. Ye, "Fault Analysis for Distribution Networks With Current-Controlled Three-Phase Inverter-Interfaced Distributed Generators," *IEEE Transactions on Power Delivery*, jun 2015. [Online]. Available: http://ieeexplore.ieee.org/document/7051243/

[161] L. Wieserman and T. McDermott, "Fault current and overvoltage calculations for inverter-based generation using symmetrical components," in *2014 IEEE Energy Conversion Congress and Exposition (ECCE)*. IEEE, sep 2014, pp. 2619–2624. [Online]. Available: http://ieeexplore.ieee.org/document/6953752/

[162] I. Sadeghkhani, M. E. Hamedani Golshan, A. Mehrizi-Sani, J. M. Guerrero, and A. Ketabi, "Transient Monitoring Function-Based Fault Detection for Inverter-Interfaced Microgrids," *IEEE Transactions on Smart Grid*, pp. 1–1, 2016. [Online]. Available: http://ieeexplore.ieee.org/document/7562364/

[163] G. Kou, L. Chen, P. VanSant, F. Velez-Cedeno, and Y. Liu, "Fault characteristics of distributed solar generation," *IEEE Transactions on Power Delivery*, vol. 35, no. 2, 2020.

[164] S. P. Pokharel, S. M. Brahma, and S. J. Ranade, "Modeling and simulation of three phase inverter for fault study of microgrids," in *2012 North American Power Symposium (NAPS)*. IEEE, sep 2012, pp. 1–6. [Online]. Available: http://ieeexplore.ieee.org/document/6336325/

[165] A. Borghetti, R. Caldon, S. Guerrieri, and F. Rossetto, "Dispersed generators interfaced with distribution systems: Dynamic response to faults and perturbations," in *2003 IEEE Bologna Power Tech Conference Proceedings,*, vol. 2. IEEE, pp. 438–443. [Online]. Available: http://ieeexplore.ieee.org/document/1304590/

[166] A. Mathur, B. Das, and V. Pant, "Fault analysis of unbalanced radial and meshed distribution system with inverter based distributed generation (IBDG)," *International Journal of Electrical Power & Energy Systems*, vol. 85, pp. 164–177, feb 2017. [Online]. Available: http://linkinghub.elsevier.com/retrieve/pii/S0142061516306202

[167] J. Miret, M. Castilla, A. Camacho, L. G. de Vicuña, and J. Matas, "Control Scheme for Photovoltaic Three-Phase Inverters to Minimize Peak Currents During Unbalanced Grid-Voltage Sags," *IEEE Transactions on Power Electronics*, vol. 27, no. 10, pp. 4262–4271, oct 2012. [Online]. Available: http://ieeexplore.ieee.org/document/6171862/

[168] S. Chiniforoosh, J. Jatskevich, A. Yazdani, V. Sood, V. Dinavahi, J. A. Martinez, and A. Ramirez, "Definitions and Applications of Dynamic Average Models for Analysis of Power Systems," *IEEE Transactions on Power Delivery*, vol. 25, no. 4, pp. 2655–2669, Oct 2010. [Online]. Available: http://ieeexplore.ieee.org/document/5440017/

[169] T. Wijnhoven, J. Tant, and G. Deconinck, "Inverter modelling techniques for protection studies," in *IEEE International Symposium on Power Electronics for Distributed Generation Systems (PEDG)*, jun 2012. [Online]. Available: http://ieeexplore.ieee.org/document/6253999/

[170] D. Turcotte and F. Katiraei, "Fault contribution of grid-connected inverters," in *IEEE Electrical Power & Energy Conference (EPEC)*, oct 2009. [Online]. Available: http://ieeexplore.ieee.org/document/5420365/

[171] J. Keller, B. Kroposki, R. Bravo, and S. Robles, "Fault current contribution from single-phase PV inverters," in *2011 37th IEEE Photovoltaic Specialists Conference*. IEEE, Jun 2011, pp. 001 822–001 826. [Online]. Available: http://ieeexplore.ieee.org/document/6186307/

[172] M. Ropp, A. Hoke, S. Chakraborty, D. Schutz, C. Mouw, A. Nelson, M. McCarty, T. Wang, and A. Sorenson, "Ground Fault Overvoltage With Inverter-Interfaced Distributed Energy Resources," *IEEE Transactions on Power Delivery*, vol. 32, no. 2, pp. 890–899, apr 2017. [Online]. Available: http://ieeexplore.ieee.org/document/7486059/

[173] C. A. Plet and T. C. Green, "Fault response of inverter interfaced distributed generators in grid-connected applications," *Electric Power Systems Research*, jan 2014. [Online]. Available: https://www.sciencedirect.com/science/article/pii/S0378779613001946

[174] C. A. Plet, M. Graovac, T. C. Green, and R. Iravani, "Fault response of grid-connected inverter dominated networks," in *IEEE PES General Meeting*. IEEE, Jul 2010, pp. 1–8. [Online]. Available: http://ieeexplore.ieee.org/document/5589981/

[175] T. Kauffmann, U. Karaagac, I. Kocar, S. Jensen, E. Farantatos, A. Haddadi, and J. Mahseredjian, "Short-Circuit Model for Type-IV Wind Turbine Generators with Decoupled Sequence Control," *IEEE Transactions on Power Delivery*, vol. 34, no. 5, pp. 1998–2007, oct 2019.

[176] T. Kauffmann, U. Karaagac, I. Kocar, S. Jensen, J. Mahseredjian, and E. Farantatos, "An Accurate Type III Wind Turbine Generator Short Circuit Model for Protection Applications," *IEEE Transactions on Power Delivery*, vol. 32, no. 6, pp. 2370–2379, dec 2017.

[177] "GM 2019 - Modeling of Converter-Interfaced Renewable Sources for Short Circuit Studies." [Online]. Available: https://resourcecenter.ieee-pes.org/conference-videos-and-slides/general-meeting/PES{_}CVS{_}GM19{_}0805{_}309{_}1{_}3.html

[178] X. Wang, X. Ruan, S. Liu, and C. K. Tse, "Full Feedforward of Grid Voltage for Grid-Connected Inverter With LCL Filter to Suppress Current Distortion Due to Grid Voltage Harmonics," *IEEE Transactions on Power Electronics*, vol. 25, no. 12, pp. 3119–3127, dec 2010. [Online]. Available: http://ieeexplore.ieee.org/document/5580125/

[179] X. Li, J. Fang, Y. Tang, X. Wu, and Y. Geng, "Capacitor-Voltage Feedforward with Full Delay Compensation to Improve Weak Grids Adaptability of LCL-Filtered Grid-Connected Converters for Distributed Generation Systems," *IEEE Transactions on Power Electronics*, 2018.

[180] Q. Yan, X. Wu, X. Yuan, and Y. Geng, "An Improved Grid-Voltage Feedforward Strategy for High-Power Three-Phase Grid-Connected Inverters Based on the Simplified Repetitive Predictor," *IEEE Transactions on Power Electronics*, vol. 31, no. 5, pp. 3880–3897, 2016.

[181] M. Zhao, X. Yuan, J. Hu, and Y. Yan, "Voltage Dynamics of Current Control Time-Scale in a VSC-Connected Weak Grid," *IEEE Transactions on Power Systems*, vol. 31, no. 4, pp. 2925–2937, 2016.

[182] R. Mahmud, A. Hoke, and D. Narang, "Fault Response of Distributed Energy Resources Considering the Requirements of IEEE 1547-2018," in *IEEE PES General Meeting*, Montreal, 2020.

[183] D. Van Tu, S. Chaitusaney, and A. Yokoyama, "Fault current calculation in distribution systems with inverter-based distributed generations," *IEEJ Transactions*

on Electrical and Electronic Engineering, sep 2013. [Online]. Available: http://doi.wiley.com/10.1002/tee.21882

[184] S. M. S. M. Sharkh, M. A. M. A. Abusara, G. I. G. I. Orfanoudakis, and B. Hussain, *Power electronic converters for microgrids*.

[185] M. Prodanovic, T. C. T. Green, M. Prodanović, and T. C. T. Green, "Control and filter design of three-phase inverters for high power quality grid connection," *IEEE Transactions on Power Electronics*, jan 2003. [Online]. Available: http://ieeexplore.ieee.org/lpdocs/epic03/wrapper.htm?arnumber=1187456

[186] J. Guerrero, L. GarciadeVicuna, J. Matas, M. Castilla, and J. Miret, "A Wireless Controller to Enhance Dynamic Performance of Parallel Inverters in Distributed Generation Systems," *IEEE Transactions on Power Electronics*, vol. 19, no. 5, pp. 1205–1213, sep 2004. [Online]. Available: http://ieeexplore.ieee.org/document/1331481/

[187] T. Kai, N. Takeuchi, T. Funabashi, and H. Sasaki, "A simplified fault currents analysis method considering transient of synchronous machine," *IEEE Transactions on Energy Conversion*, vol. 12, no. 3, 1997. [Online]. Available: http://ieeexplore.ieee.org/document/629707/

[188] A. Hoke, A. Nelson, B. Miller, S. Chakraborty, F. Bell, and M. McCarty, "Experimental Evaluation of PV Inverter Anti-Islanding with Grid Support Functions in Multi-Inverter Island Scenarios," National Renewable Energy Laboratory (NREL), Golden, CO, Tech. Rep., jul 2016. [Online]. Available: http://www.osti.gov/servlets/purl/1265055/

[189] A. Nelson, G. Martin, and J. Hurtt, "Experimental evaluation of grid support enabled PV inverter response to abnormal grid conditions," in *2017 IEEE Power & Energy Society Innovative Smart Grid Technologies Conference (ISGT)*. IEEE, apr 2017, pp. 1–5. [Online]. Available: http://ieeexplore.ieee.org/document/8086016/

[190] A. Reznik, M. G. Simoes, A. Al-Durra, and S. M. Muyeen, "LCL Filter Design and Performance Analysis for Grid-Interconnected Systems," *IEEE Transactions on Industry Applications*, mar 2014. [Online]. Available: http://ieeexplore.ieee.org/lpdocs/epic03/wrapper.htm?arnumber=6571219

[191] R. Mahmud, O. Cornmesser, S. Chakraborty, J. Wang, A. Hoke, J. Cale, B. K. Johnson, P. H. Pinheiro, and R. G. Bainy, "A parametric reduced-order model for inverter short-circuit response in protection studies," in *2026 IEEE Transmission and Distribution Conference and Exposition (T&D)*, 2026.

[192] S. Chakraborty, J. Wang, R. Mahmud, A. Hoke, B. Johnson, R. G. Bainy, and H. Lei, "Design of multifunctional electromagnetic transient model for grid-forming inverters," in *IECON 2024 - 50th Annual Conference of the IEEE Industrial Electronics Society*, 2024, pp. 1–6.

[193] P. H. Pinheiro, B. W. França, Y. Lopes, S. Chakraborty, R. G. Bainy, H. Lei, B. K. Johnson, S. Manson, J. Wang, R. Mahmud, A. Hoke, and C. J. Kruse, "Analysis of line distance elements for various ibr controllers and system conditions," *Electric Power Systems Research*, vol. 252, p. 112370, 2026. [Online]. Available: https://www.sciencedirect.com/science/article/pii/S0378779625009575

Appendix A

Proofs

A.1 Proofs of Lemmas and Corollaries of Chapter 7

Proof of Lemma 7.3.2. By the Hurwitz assumption on $A_{\sigma,\mathrm{nom}}$ (Lemma 7.3.2), the standard bound on the matrix exponential gives $\|\Phi_{\sigma,\mathrm{nom}}(t)\| \le M_\sigma e^{-\alpha_\sigma t}$ for all $t \ge 0$. Hence the homogeneous nominal system $\dot{X}_\sigma = A_{\sigma,\mathrm{nom}} X_\sigma$ is exponentially stable.

For constant R_σ, the equilibrium $X_{\sigma,\infty} = -A_{\sigma,\mathrm{nom}}^{-1} B_r R_\sigma$ exists (cf. (7.6)). Let $\tilde{X}_\sigma := X_\sigma - X_{\sigma,\infty}$; then $\dot{\tilde{X}}_\sigma = A_{\sigma,\mathrm{nom}} \tilde{X}_\sigma$, so $\|\tilde{X}_\sigma(t)\| \le M_\sigma e^{-\alpha_\sigma (t-t_0)} \|\tilde{X}_\sigma(t_0)\|$, which proves exponential convergence. $\square$

Proof of Corollary 7.3.3. We first isolate the per–axis closed loop. With $a := R_f/L_f$ the nominal 4×4 matrix admits the Kronecker form

$$A_{\sigma,\mathrm{nom}} \;=\; A_0 \;=\; A_{\mathrm{ax}} \otimes I_2, \tag{A.1}$$

$$A_{\mathrm{ax}} = \begin{bmatrix} -(a + K_p/L_f) & 1/L_f \\ -\,K_i & 0 \end{bmatrix}$$

Consider the 2×2 Lyapunov equation

$$A_{\mathrm{ax}}^\top P_{\mathrm{ax}} + P_{\mathrm{ax}} A_{\mathrm{ax}} = -I_2, \tag{A.2}$$

with symmetric $P_{\text{ax}} = \begin{bmatrix} p_{11} & p_{12} \\ p_{12} & p_{22} \end{bmatrix}$. Expanding (A.2) entrywise yields a linear system in (p_{11}, p_{12}, p_{22}) whose unique solution is

$$p_{12} = -\frac{L_f}{2}, \qquad p_{11} = \frac{L_f\,(K_i L_f + 1)}{2\,(K_p + aL_f)}, \tag{A.3}$$

$$p_{22} = \frac{1}{2K_i}\left(\frac{K_i L_f + 1}{K_p + aL_f} + K_p + aL_f\right). \tag{A.4}$$

Since $K_p > 0$, $K_i > 0$, $L_f > 0$, and $a \geq 0$, we have $p_{11} > 0$ and $p_{22} > 0$. Moreover,

$$\det P_{\text{ax}} = \frac{L_f\big(K_i^2 L_f^2 + 2K_i L_f + K_p^2 + 2K_p L_f a + L_f^2 a^2 + 1\big)}{4K_i\,(K_p + aL_f)^2} > 0, \tag{A.5}$$

so $P_{\text{ax}} \succ 0$.

Now define $P := \operatorname{blkdiag}(P_{\text{ax}}, P_{\text{ax}})$. Using $A_0 = A_{\text{ax}} \otimes I_2$ and the mixed–product property,

$$A_0^\top P + PA_0 = (A_{\text{ax}}^\top P_{\text{ax}} + P_{\text{ax}} A_{\text{ax}}) \otimes I_2 = -I_2 \otimes I_2 = -I_4. \tag{A.6}$$

For any trajectory $\dot{X} = A_0 X$, the Lyapunov function $V(X) := X^\top P X$ satisfies

$$\dot{V}(X) = X^\top (A_0^\top P + PA_0) X = -\|X\|_2^2 \tag{A.7}$$

$$\leq -\frac{1}{\lambda_{\max}(P)}\, V(X), \tag{A.8}$$

where we used $V(X) \leq \lambda_{\max}(P)\|X\|_2^2$. Grönwall's inequality gives

$$V(t) \leq e^{-(t-t_0)/\lambda_{\max}(P)}\, V(t_0). \tag{A.9}$$

Since $\lambda_{\min}(P)\|X\|_2^2 \le V(X) \le \lambda_{\max}(P)\|X\|_2^2$, we obtain

$$\|X(t)\|_2 \ \le \ \sqrt{\frac{\lambda_{\max}(P)}{\lambda_{\min}(P)}}\, e^{-(t-t_0)/(2\lambda_{\max}(P))}\, \|X(t_0)\|_2. \tag{A.10}$$

This implies the operator–norm bound on the transition matrix (2–norm):

$$\|\Phi_{\sigma,\text{nom}}(t)\|_2 \ = \ \|e^{A_0 t}\|_2 \ \le \ \sqrt{\frac{\lambda_{\max}(P)}{\lambda_{\min}(P)}}\, e^{-t/(2\lambda_{\max}(P))}. \tag{A.11}$$

Finally, because P is block diagonal with two identical blocks, $\lambda_{\max}(P) = \lambda_{\max}(P_{\text{ax}})$ and $\lambda_{\min}(P) = \lambda_{\min}(P_{\text{ax}})$. Hence the claimed explicit constants

$$M_\sigma := \sqrt{\frac{\lambda_{\max}(P_{\text{ax}})}{\lambda_{\min}(P_{\text{ax}})}}, \qquad \alpha_\sigma := \frac{1}{2\,\lambda_{\max}(P_{\text{ax}})}, \tag{A.12}$$

with P_{ax} given by (A.4). □

Proof of Corollary 7.3.4. Starting from the variation–of–constants representation (7.12) and the bound $\|\Phi_{\sigma,\text{nom}}(t)\| \le M_\sigma e^{-\alpha_\sigma t}$ (Lemma 7.3.2), take norms and use submultiplicativity to obtain, for all $t \ge t_0$,

$$\begin{aligned} \|X_\sigma(t)\| \le M_\sigma \|X_\sigma(t_0)\| + \frac{M_\sigma}{\alpha_\sigma}\|B_r\|\,\|R_\sigma\| \\ + \frac{M_\sigma}{\alpha_\sigma}\|B_v\|\,\|\varepsilon_{v\sigma}\|_\infty + \frac{M_\sigma}{\alpha_\sigma}\|E_\sigma\|\,\|\Delta\omega\|_\infty \sup_{s\in[t_0,t]} \|X_\sigma(s)\|. \end{aligned} \tag{A.13}$$

Let $g(t) := \sup_{s\in[t_0,t]} \|X_\sigma(s)\|$ and $\kappa_\sigma := \frac{M_\sigma}{\alpha_\sigma}\|E_\sigma\|\,\|\Delta\omega\|_\infty$. Then

$$g(t) \le M_\sigma \|X_\sigma(t_0)\| + \frac{M_\sigma}{\alpha_\sigma}\big(\|B_r\|\,\|R_\sigma\| + \|B_v\|\,\|\varepsilon_{v\sigma}\|_\infty\big) + \kappa_\sigma\, g(t). \tag{A.14}$$

If $\kappa_\sigma < 1$, rearranging yields the claimed uniform bound, hence $X_\sigma(t)$ is bounded for all $t \ge t_0$. □

Proof of Lemma 7.3.5. Subtract (7.11) from (7.12) to obtain

$$\tilde{X}_\sigma(t) = \int_{t_0}^{t} \Phi_{\sigma,\mathrm{nom}}(t-\tau)\Big[-\Delta\omega(\tau)\, E_\sigma X_\sigma(\tau) + B_v\, \varepsilon_{v\sigma}(\tau)\Big]\, d\tau. \tag{A.15}$$

Take norms, use $\|\Phi_{\sigma,\mathrm{nom}}(t)\| \le M_\sigma e^{-\alpha_\sigma t}$ and the triangle inequality, and split $X_\sigma = X_{\sigma,\mathrm{nom}} + \tilde{X}_\sigma$:

$$\|\tilde{X}_\sigma(t)\| \le \frac{M_\sigma}{\alpha_\sigma}\|B_v\|\,\|\varepsilon_{v\sigma}\|_{\infty,[t_0,t]} + \frac{M_\sigma}{\alpha_\sigma}\|E_\sigma\|\,\|\Delta\omega\|_{\infty,[t_0,t]}\Big(\sup_{\tau\in[t_0,t]}\|X_{\sigma,\mathrm{nom}}(\tau)\| \quad + \sup_{\tau\in[t_0,t]}\|\tilde{X}_\sigma(\tau)\|\Big). \tag{A.16}$$

Let $g(t) := \sup_{\tau\in[t_0,t]}\|\tilde{X}_\sigma(\tau)\|$. Then

$$\begin{aligned} g(t) \;&\le\; \frac{M_\sigma}{\alpha_\sigma}\|B_v\|\,\|\varepsilon_{v\sigma}\|_{\infty,[t_0,t]} \\ &+\frac{M_\sigma}{\alpha_\sigma}\|E_\sigma\|\,\|\Delta\omega\|_{\infty,[t_0,t]}\, C_{\mathrm{nom}} + \frac{M_\sigma}{\alpha_\sigma}\|E_\sigma\|\,\|\Delta\omega\|_{\infty,[t_0,t]}\, g(t). \end{aligned} \tag{A.17}$$

By the small-gain condition, $\frac{M_\sigma}{\alpha_\sigma}\|E_\sigma\|\,\|\Delta\omega\|_{\infty,[t_0,\infty)} < 1$, so

$$g(t) \;\le\; \frac{M_\sigma}{\alpha_{\mathrm{eff}}}\Big(\|B_v\|\,\|\varepsilon_{v\sigma}\|_{\infty,[t_0,t]} + \|E_\sigma\|\,\|\Delta\omega\|_{\infty,[t_0,t]}\, C_{\mathrm{nom}}\Big). \tag{A.18}$$

Finally, the homogeneous deviation $\dot{\tilde{X}}_\sigma = A_{\sigma,\mathrm{nom}}\tilde{X}_\sigma$ contributes the decaying term $M_\sigma e^{-\alpha_\sigma(t-t_0)}\|\tilde{X}_\sigma(t_0)\|$, which under the same small-gain bound yields the stated $M_\sigma e^{-\alpha_{\mathrm{eff}}(t-t_0)}\|\tilde{X}_\sigma(t_0)\|$. Combining terms gives the claim. □

Proof of Corollary 7.3.2. From Lemma 7.3.6,

$$\|\tilde{X}_\sigma(t)\| \le M_\sigma e^{-\alpha_{\mathrm{eff}}(t-t_0)}\|\tilde{X}_\sigma(t_0)\| + \frac{M_\sigma}{\alpha_{\mathrm{eff}}}\Big(\|B_v\|\,\|\varepsilon_{v\sigma}\|_{\infty,[t_0,t]} + \|E_\sigma\|\,\|\Delta\omega\|_{\infty,[t_0,t]}\, C_{\mathrm{nom}}\Big). \tag{A.19}$$

Taking $\limsup_{t\to\infty}$ eliminates the decaying term and replaces the truncated sup-norms by global ones on $[t_0,\infty)$, yielding the stated bound. □

Proof of Lemma 7.3.8. Set $\Delta\omega \equiv 0$ and $\varepsilon_{v\sigma}(t) \equiv \bar{\varepsilon}_{v\sigma}$ in (7.10). Then

$$\dot{X}_\sigma(t) = A_0 X_\sigma(t) + B_r R_\sigma + B_v \bar{\varepsilon}_{v\sigma}. \tag{A.20}$$

Since A_0 is Hurwitz (Lemma 7.3.2), the LTI system with constant input admits the standard closed form

$$X_\sigma(t) = e^{A_0(t-t_0)} X_\sigma(t_0) + \int_{t_0}^{t} e^{A_0(t-\tau)} \big(B_r R_\sigma + B_v \bar{\varepsilon}_{v\sigma}\big)\, d\tau = X_{\sigma,\infty} + e^{A_0(t-t_0)}\big(X_\sigma(t_0) - X_{\sigma,\infty}\big), \tag{A.21}$$

with equilibrium $X_{\sigma,\infty} = -A_0^{-1}(B_r R_\sigma + B_v \bar{\varepsilon}_{v\sigma})$.

Writing the closed-loop blocks (cf. (7.5) and $\dot{z}_\sigma = K_i(R_\sigma - i_\sigma)$) and setting $\dot{i}_\sigma = \dot{z}_\sigma = 0$ gives

$$i_{\sigma,\infty} = R_\sigma, \qquad 0 = -(a + \tfrac{K_p}{L_f}) R_\sigma + \tfrac{1}{L_f} z_{\sigma,\infty} + \tfrac{K_p}{L_f} R_\sigma + \tfrac{1}{L_f} \bar{\varepsilon}_{v\sigma}, \tag{A.22}$$

hence $z_{\sigma,\infty} = R_f R_\sigma - \bar{\varepsilon}_{v\sigma}$.

For the axis-wise closed form, define the errors $e_k := i_{k\sigma} - R_{k\sigma}$ and $w_k := z_{k\sigma} - z_{k\sigma,\infty}$ ($k \in \{d, q\}$). From $\dot{i}_\sigma = -(a + \frac{K_p}{L_f}) i_\sigma + \frac{1}{L_f} z_\sigma + \frac{K_p}{L_f} R_\sigma + \frac{1}{L_f} \bar{\varepsilon}_{v\sigma}$ and $\dot{z}_\sigma = K_i(R_\sigma - i_\sigma)$, subtracting the equilibrium relations yields

$$\dot{e}_k = -\Big(a + \frac{K_p}{L_f}\Big) e_k + \frac{1}{L_f} w_k, \qquad \dot{w}_k = -K_i e_k. \tag{A.23}$$

Eliminating w_k gives the second-order homogeneous ODE

$$L_f \ddot{e}_k + (K_p + a L_f)\dot{e}_k + K_i e_k = 0, \tag{A.24}$$

whose characteristic roots $s_{1,2}$ satisfy $L_f s^2+(K_p+aL_f)s+K_i=0$. Thus $e_k(\tau)=A_k e^{s_1\tau}+B_k e^{s_2\tau}$, $\tau:=t-t_0$, with initial data

$$e_k(0)=i_{k\sigma}(t_0)-R_{k\sigma}, \tag{A.25}$$

$$\dot e_k(0)=-\Big(a+\frac{K_p}{L_f}\Big)e_k(0)+\frac{1}{L_f}\Delta z_k, \tag{A.26}$$

$$\Delta z_k:=z_{k\sigma}(t_0)-z_{k\sigma,\infty}, \tag{A.27}$$

and coefficients

$$A_k=\frac{\dot e_k(0)-s_2e_k(0)}{s_1-s_2},\qquad B_k=\frac{s_1e_k(0)-\dot e_k(0)}{s_1-s_2}. \tag{A.28}$$

Therefore $i_{k\sigma}(t)=R_{k\sigma}+A_ke^{s_1\tau}+B_ke^{s_2\tau}$. In the critically damped case $s_1=s_2=:s$, $i_{k\sigma}(t)=R_{k\sigma}+\big(e_k(0)+(\dot e_k(0)-se_k(0))\,\tau\big)e^{s\tau}$. □

Sketch of Lemma 7.3.10. From Lemma 7.3.5 with $X=i_\sigma$ extracted by C, we have for $t\ge t_0$:

$$\|i_\sigma(t)-R_\sigma\|\le M_\sigma e^{-\alpha_{\text{eff}}(t-t_0)}\|i_\sigma(t_0)-R_\sigma\|+\frac{M_\sigma}{\alpha_{\text{eff}}}\left(\|B_v\|\,\|\varepsilon_{v\sigma}\|_\infty+\|E_\sigma\|\,C_{\text{nom}}\,\|\Delta\omega\|_\infty\right). \tag{A.29}$$

Taking $\sup_{t\ge t_0}$ and using $e^{-\alpha_{\text{eff}}(t-t_0)}\le 1$ gives (7.35). For the nominal step case, the two axes are decoupled, each a standard second-order loop with damping ratio ζ; the classical step overshoot bound gives the axis-wise result and the vector bound (7.37) follows by norm subadditivity. □

Proof of Corollary 7.3.11. From Cor. 7.3.7,

$$\|\tilde X_\sigma(t)\|\le M_\sigma e^{-\alpha_{\text{eff}}(t-t_0)}\|\tilde X_\sigma(t_0)\|+\underbrace{\frac{M_\sigma}{\alpha_{\text{eff}}}\Big(\|B_v\|\,\|\varepsilon_{v\sigma}\|_\infty+\|E_\sigma\|\,\|X_{\sigma,\infty}\|\,\|\Delta\omega\|_\infty\Big)}_{=:\,r_{\text{ss}}}. \tag{A.30}$$

To ensure $\|\tilde{X}_\sigma(t)\| \le r_{\text{ss}} + \epsilon$, it suffices to make the decaying term $M_\sigma e^{-\alpha_{\text{eff}}(t-t_0)}\|\tilde{X}_\sigma(t_0)\| \le \epsilon$. Solving for t gives $t - t_0 \ge \frac{1}{\alpha_{\text{eff}}} \ln\bigl(\frac{M_\sigma\|\tilde{X}_\sigma(t_0)\|}{\epsilon}\bigr)$, which yields $T_\epsilon^{(X)}$ in the statement (take $T_\epsilon^{(X)} := \max\{0, \frac{1}{\alpha_{\text{eff}}} \ln(\frac{M_\sigma\|\tilde{X}_\sigma(t_0)\|}{\epsilon})\}$ if desired).

For the current output $\tilde{i}_\sigma = C\tilde{X}_\sigma$, we have

$$\|\tilde{i}_\sigma(t)\| \le \|C\|\,\|\tilde{X}_\sigma(t)\| \le \|C\|\,r_{\text{ss}} + \|C\|M_\sigma e^{-\alpha_{\text{eff}}(t-t_0)}\|\tilde{X}_\sigma(t_0)\|. \tag{A.31}$$

Requiring $\|C\|M_\sigma e^{-\alpha_{\text{eff}}(t-t_0)}\|\tilde{X}_\sigma(t_0)\| \le \epsilon$ gives $t - t_0 \ge \frac{1}{\alpha_{\text{eff}}} \ln\bigl(\frac{\|C\|M_\sigma\|\tilde{X}_\sigma(t_0)\|}{\epsilon}\bigr)$, which is $T_\epsilon^{(i)}$. $\square$